



**University of  
Nottingham**

UK | CHINA | MALAYSIA

# **An investigation into the thermal management and control of ceramic injection moulding die-tools**

Submitted in partial fulfillment of  
the conditions for the award of the degree **PhD Mechanical  
Engineering.**

**Maria Floriana Bianchi**  
**4261573**

**Supervised by Prof. Dragos Axinte, Dr. Andres  
Gameros**

Department of Mechanical, Materials and Manufacturing Engineering  
University of Nottingham

I hereby declare that this dissertation is all my own work, except as  
indicated in the text:

Signature \_\_\_\_\_

Date \_\_\_\_ / \_\_\_\_ / \_\_\_\_

## Abstract

Ceramic Injection Moulding (CIM) is an extensively used process in the mass production of complex components, consisting of three stages: injection moulding, debinding (i.e. binder removal) and sintering. In the aerospace industry, CIM is employed to make ceramic cores, which are sacrificial components used to shape the internal cooling channels of high-pressure turbine blades and vanes, manufactured by investment casting. The injection moulding of cores presents significant challenges due to their geometry, characterised by adjoined features having uneven wall thickness: this determines differential cooling rates along the part arising throughout the moulding process, which, in turn, cause several flaws in finished cores (e.g. warpage, cracking and poor surface quality). Even higher mouldability challenges are brought by the increasing requirements of turbine working temperatures, calling for higher complexity of core geometries. To cope with this, suitable die-tool thermal control approaches have to be employed. However, state-of-the-art temperature control methods present strong limitations, as they aim at achieving a uniform cavity temperature, which do not prevent the development of uneven cooling rates in parts with differential wall thickness.

To address these shortcomings, the aim of this project is to develop and demonstrate a novel thermal control system for die-tools to improve the capability of manufacturing complex components characterised by uneven wall thickness through CIM. To achieve this, the present work addresses the following objectives: (i) to develop a methodology to analyse the performance of thermal control systems for CIM; (ii) to explore the effects of state-of-the-art thermal control approaches upon the quality of features having different wall thickness; (iii) to design and demonstrate a novel die-tool with a tailored and optimised temperature control system; (iv) to construct guidelines for applying and operating the novel proposed thermal management system with generic complex components.



In the first part of the work, a methodological framework for the performance evaluation of thermal control systems for CIM die-tools was developed. This methodology relates macro- and micro-structural outcomes observed in green and sintered components to the heat transfer phenomena occurring while employing a thermal control system. This was achieved with the support of a developed simulation of the injection moulding filling process. Then, a novel study was carried out to analyse the performance of Rapid Heat Cycle Moulding (RHCM) applied to CIM. The RHCM approach was found to promote a more uniform microstructure, in terms of particle orientation and packing, compared to the use of a constant ambient mould temperature. However, the RHCM approach determines an increase of mould-part adhesion, thus compromising the demoulding process. Based on the understanding achieved from these studies, a novel system was developed, having a regional control of die-tool temperatures. This was achieved through the development of a thermal control model, having the objective to minimise cooling rate gradients in the part, and demonstrated using a prototype mould equipped with actively controlled thermoelectric elements. The novel system ensures simultaneous solidification of features having different thicknesses, hence promoting higher dimensional accuracy compared to the RHCM approach, while keeping its advantages related to feature replication capability and surface integrity. Finally, the thermal model was applied to a case study core geometry and guidelines for the were elaborated for the use of the novel proposed system in industrial contexts.

The work developed in this thesis hence contributes to the understanding of how heat transfer phenomena in CIM affect the quality of ceramic moulded components. Moreover, the development and validation of moulds with regional temperature control push the boundaries of injection moulding to manufacture components characterised by uneven wall thickness, which has the potential of highly expanding the process flexibility and its possible fields of application.

## Acknowledgements

These past years of PhD have been a bit like a "coming of age" story, in which I felt both the writer and the main character. Since a writer and a main character are not nearly enough to make a good story, I believe there are some people that deserve my acknowledgements, for their help and contribution to my work and life throughout these years.

I would first like to thank Prof Dragos Axinte and Dr Andres Gameros for supervising my PhD. Thanks for pushing me to be curious, for the interesting discussions and for all the time you dedicated to support my work. My acknowledgements go also to Dr Stewart Welch, Dr Alex Cendrowicz and Mr Peter Winton, for providing me supervision and guidance throughout these years and for sharing your knowledge and experience. I would like to express my gratitude to Dr Stewart Lowth, for supervising my work and contributing to it with a vivid creativity. I wish also to thank Dr Christopher Bennett, for the interesting and stimulating discussion during my annual review.

My acknowledgements go to Mrs Cecilia Flores, for the precious support on the administrative side of the research work within our group. I would like to thank all the colleagues and friends within and outside the UTC, who have contributed to make these years interesting, intense and enjoyable.

Then there are some "special characters", who I think deserve particular acknowledgement, for sharing with me the perks and pitfalls encountered along the way. To Oriol, who started with me from day one, for your precious advices, and for being a great colleague and friend. To Guillaume and Sophie, for being a family away from home. To Jorge, for your friendship, support and chats, which are always fun and helpful. To Irati, for sharing our common interests and our huge amount of words-per-minute. To Luca, for your support throughout my work and for being an irreplaceable friend,

I owe you a lot. To my "soulmates" Gaia, Simo and Claudia, for being always by my side, each in your unique way, despite the long distance and short available time to spend together. To my aunt Silvia, for being close to me with endless love and affection. To Alessandro, for your complicity and support, which is worth even more, coming from my "little brother". To my parents, for teaching me the importance of hard work and for always encouraging me to think in my own way. To David, for all the fun time, your patience and understanding, for challenging and supporting me every day, personally and professionally. For being my friend, my partner, my colleague.

# Contents

<b>Abstract</b>	<b>i</b>
<b>Acknowledgements</b>	<b>iii</b>
<b>1 Introduction</b>	<b>1</b>
1.1 Motivation . . . . .	1
1.2 Research problem . . . . .	6
1.3 Objectives of the study . . . . .	11
<b>2 Literature Review</b>	<b>14</b>
2.1 Injection moulding . . . . .	15
2.1.1 Injection moulding machines . . . . .	15
2.1.2 Injection moulding materials . . . . .	16
2.1.3 Injection moulding process stages . . . . .	27
2.2 Ceramic injection moulding . . . . .	33
2.2.1 Feedstock preparation . . . . .	34
2.2.2 Injection moulding . . . . .	36
2.2.3 Debinding and sintering . . . . .	37
2.3 Tooling for injection moulding . . . . .	38
2.3.1 Injection moulding die-tools components . . . . .	38
2.3.2 Mould heating and cooling technologies . . . . .	40
2.4 Outcomes of ceramic injection moulding . . . . .	43
2.4.1 Feature replication capability and lack-of-fill . . . . .	44

2.4.2	Weld lines . . . . .	45
2.4.3	Shrinkage-related defects . . . . .	46
2.4.4	Demoulding issues . . . . .	57
2.5	Injection moulding process modelling . . . . .	59
2.5.1	Thermal control models and optimisation for injection moulding die-tools . . . . .	60
2.6	Summary of the literature . . . . .	64
2.7	Research challenges from Literature Review . . . . .	67
2.7.1	Research challenges – Methodology for the evaluation of thermal systems performances in CIM . . . . .	67
2.7.2	Research challenges – Effect of RHCM on outcomes of CIM . . . . .	68
2.7.3	Research challenges – Novel thermal system and con- trol optimisation for CIM die-tools . . . . .	69
2.7.4	Industrial challenges – Application of novel thermal control models and optimisation to generic complex ceramic components . . . . .	70
<b>3</b>	<b>Methodology</b>	<b>72</b>
3.1	Introduction . . . . .	72
3.2	Materials used in the study . . . . .	74
3.2.1	Wax feedstock . . . . .	74
3.2.2	Ceramic feedstocks . . . . .	77
3.3	Injection moulding equipment . . . . .	79
3.3.1	Laboratory equipment . . . . .	79
3.3.2	Industrial equipment . . . . .	92
3.4	Materials analysis and characterisation techniques . . . . .	95
3.4.1	Microstructural characterisation . . . . .	95
3.4.2	Density characterisation . . . . .	98

3.4.3	Surface integrity and dimensional control . . . . .	99
3.5	Modelling and optimisation methods and equipment . . . . .	102
3.5.1	Modelling of the injection moulding process . . . . .	102
3.5.2	Mould temperature optimisation . . . . .	104
<b>4</b>	<b>Methodology for the evaluation of thermal systems perfor-</b>	
	<b>mances in CIM</b>	<b>107</b>
4.1	Introduction . . . . .	108
4.2	Reference geometries for model development and analysis of	
	IM outcomes . . . . .	111
4.3	Step I: Development of a filling simulation . . . . .	114
4.3.1	Model setup . . . . .	115
4.3.2	Model validation . . . . .	120
4.4	Step II: Analysis of IM outcomes from green components . .	138
4.5	Step III: Analysis of IM outcomes from sintered components	147
4.6	Conclusions . . . . .	153
<b>5</b>	<b>Application of rapid thermal cycling to CIM</b>	<b>155</b>
5.1	Introduction . . . . .	156
5.2	Effect of RHCM on ceramic particle orientation and packing	158
5.2.1	Experimental methodology . . . . .	159
5.2.2	Main findings of the study . . . . .	164
5.2.3	Conclusions . . . . .	181
5.3	Effect of RHCM on the part-mould adhesion behaviour . . .	183
5.3.1	Experimental setup . . . . .	183
5.3.2	Results and discussion . . . . .	186
5.3.3	Conclusions . . . . .	192
<b>6</b>	<b>Novel thermal control system for CIM die-tools</b>	<b>194</b>
6.1	Introduction . . . . .	195

6.2	Novel mould and temperature control concepts . . . . .	196
6.3	Materials and methods . . . . .	200
6.3.1	Novel die-tool: reference geometries and mould design	201
6.3.2	Characterisation methods . . . . .	205
6.4	Thermal control model and optimisation . . . . .	206
6.4.1	Optimisation of mould temperatures . . . . .	209
6.4.2	Numerical modelling of the IM process . . . . .	212
6.5	Results and discussion . . . . .	217
6.5.1	Optimisation results and thermal analysis . . . . .	217
6.5.2	Performance evaluation of the novel thermal control approach: effects on injection moulded parts . . . . .	225
6.6	Conclusions . . . . .	236
<b>7</b>	<b>Application of the novel thermal control system to generic complex components</b>	<b>239</b>
7.1	Introduction . . . . .	240
7.2	Ceramic cores for high-pressure turbines . . . . .	241
7.3	Application of thermal control model to core geometry . . .	243
7.3.1	Selection of sample geometries . . . . .	243
7.3.2	Filling model validation . . . . .	245
7.3.3	Thermal control model and optimisation setup for core geometry . . . . .	252
7.3.4	Results and discussion . . . . .	257
7.4	Novel prototype mould for a production machine . . . . .	260
7.5	Industrialisation of die-tools with regional temperature control	264
7.6	Conclusions . . . . .	267
<b>8</b>	<b>Conclusions</b>	<b>270</b>
8.1	Methodology for the evaluation of thermal systems perfor- mances in CIM . . . . .	272

8.2	Application of rapid thermal cycling to CIM . . . . .	273
8.3	Novel thermal control system for CIM die-tools . . . . .	276
8.4	Application of the novel system to generic complex components	278
8.5	Future work . . . . .	279
<b>Bibliography</b>		<b>281</b>
<b>Appendices</b>		<b>303</b>
<b>A Engineering Drawings</b>		<b>303</b>



# List of Tables

3.1	Particle size distribution for the analysed ceramic feedstock .	78
3.2	Summary of the moulds designed for the laboratory rig through- out this PhD work. . . . .	85
4.1	Material properties used for mould plates in the filling model	116
4.2	Cross-Exp model parameters for wax and ceramic feedstocks	117
4.3	Tait model parameters for wax and ceramic feedstocks . . .	118
4.4	Process parameters for ceramic block injection moulding . .	149
5.1	Average shrinkage measured in the green ceramic bars . . . .	177
5.2	Stiffness modulus values for main analysed cases. Calculated standard deviations for the moduli are of the order of 20 MPa.	181
6.1	PSO parameters . . . . .	211
6.2	Height difference among Feature 1 (farther from the gate) in Cavity B, moulded in SS configuration . . . . .	228
7.1	Main dimensions of cavity features . . . . .	245
7.2	Injection moulding process parameters . . . . .	248
7.3	Main dimensions of core features . . . . .	253
7.4	Main dimensions of core features . . . . .	253
7.5	Optimal injection temperature ( $T(Q_1)$ ) and time for the cav- ity to cool down to 35°C ( $t(Q_2)$ ) for each core feature and Peltier module. . . . .	257

# List of Figures

1.1	Schematic of the CIM process. (a) Feedstock preparation. (b) Injection moulding. (c) Debinding. (d) Sintering. . . . .	2
1.2	Schematic of the investment casting process. (a) Core injection moulding. (b) Core encapsulation in wax pattern. (c) Shell and de-waxing. (d) Casting. (e) Shell removal. (f) Core removal. . . . .	3
1.3	Cores for investment casting of turbine blades. (a) Example of core geometry (representative model design, provided by Rolls-Royce plc). (b) Cooling channels in a blade (Rolls-Royce, 2015). . . . .	4
1.4	Evolution and future trends of turbine entry temperature in aero engines (Kyprianidis, 2012). . . . .	5
2.1	Schematics of a screw-type injection moulding machine (Chen, 2016). . . . .	16
2.2	Molecular morphologies of thermoplastic materials (Malloy, 2010). . . . .	18
2.3	Schematic of simple shear flow (Kennedy, 2013). . . . .	20
2.4	Types of pseudoplastic material flow as a function of shear rate (Zhou, 2013). . . . .	21
2.5	Viscosity behaviour of shear thinning polymeric fluids (Zhou, 2013). . . . .	22

2.6	Example PVT diagram for a semicrystalline polymer (Zheng, 2011). . . . .	25
2.7	Cavity pressure profile at the nozzle during injection moulding (Zhou, 2013) . . . . .	27
2.8	Volume shrinkage development during injection moulding (Zhou, 2013) . . . . .	31
2.9	Binder content in CIM feedstocks (Mannschatz, 2010) . . . .	35
2.10	Generic mould configuration (Rosato, 2000) . . . . .	39
2.11	Feedstock solidification in cavities of different thickness $th_1 > th_2$ : (a) instant $t_0$ in which material enters the cavity; (b) instant $t_1$ , end of filling . . . . .	41
2.12	Shaped baffles for conformal cooling (Wang, 2014a) . . . . .	42
2.13	SEM micrographs of a V-notch (a) and weld line (b) in a polypropylene specimen (Wu, 2005) . . . . .	45
2.14	Formation of flow-induced residual stresses (Guevara-Morales, 2014) . . . . .	49
2.15	Formation of thermal residual stresses (Guevara-Morales, 2014). Left: Temperature profile across part thickness. Centre: Schematics of residual stress sign in across part thickness. Right: Schematics of stress magnitude across part thickness. . . . .	50
2.16	Powder-binder separation due to geometrical configurations (German, 1997; Karatas, 2008) . . . . .	52
2.17	Powder distribution in a complex shape with convex and concave shapes (Greiner et al., 2011). (a) Schematics of the part. (b) Particle distribution at early stage of filling. (c) Particle distribution at a later stage of filling. . . . .	53
2.18	Evolution of cracks in ceramic moulded parts from green to sintered state (Mannschatz, 2011). Note: the arrows show cracks and voids observed in the injection moulded parts. . .	55

2.19 Particle orientation in feedstock during filling (Mannschatz, 2011) . . . . .	55
2.20 Temperature distribution in a cross section of a case study component, with two temperature profiles, with respect to the neutral axis of the part (Nian, 2015). . . . .	63
3.1 Flow diagram defining the main steps involved in the presented research. . . . .	73
3.2 SEM micrograph of fracture surface for the wax feedstock. .	75
3.3 Material properties of the wax feedstock. (a) Viscosity behaviour. (b) PVT behaviour. . . . .	75
3.4 SEM micrograph of fracture surface for the ceramic feedstock.	77
3.5 Material properties of the ceramic feedstock. (a) Viscosity behaviour. (b) PVT behaviour. . . . .	78
3.6 Test rig used for injection moulding experiments. . . . .	80
3.7 Heated aluminium tank: main dimensions and locations of Peltier modules and temperature sensors. . . . .	81
3.8 Nozzle: main dimensions and o-rings housings. . . . .	81
3.9 Schematic diagram of the pneumatic system employed in the laboratory rig. . . . .	82
3.10 Schematics of thermoelectric modules. (a) Working principle of a single thermocouple (Enescu and Virjoghe, 2014). (b) Schematic representation of a whole thermoelectric module. .	83
3.11 Cross-channels mould: main dimensions. . . . .	86
3.12 Parallel channels mould: main dimensions of mould and Peltier module. . . . .	87
3.13 Adhesion tests mould: main dimensions of mould and Peltier module. . . . .	88

3.14	Regional controlled mould: main dimensions of mould and Peltier modules. . . . .	89
3.15	Schematic diagram of the effect of pneumatic cylinder movement on the pressure drop across the aluminium tank. . . .	91
3.16	Picture of the injection moulding machine used in the conducted experiments. . . . .	92
3.17	Regional controlled mould (industrial): main dimensions of mould and Peltier modules. . . . .	93
3.18	Regional controlled mould (industrial): main dimensions of mould and Peltier modules. . . . .	94
3.19	Picture of Gatan Microtest 200VT tensile-compressive stage.	97
3.20	Picture of the Alicona InfiniteFocus G5. . . . .	100
3.21	Schematics of filling model BCs. . . . .	103
3.22	Schematics of thermal model BCs. . . . .	104
4.1	Flow-chart of the followed approach to develop a methodology for the evaluation of thermal systems performance for CIM die-tools. . . . .	109
4.2	<i>Cross-channels</i> reference component . . . . .	112
4.3	<i>Parallel-channels</i> reference component. (a) Main dimensions for the component in the "disconnected channels" configuration. (b) Component in the "connected channels" configuration. . . . .	113
4.4	Modelled assemblies for the filling simulation. (a) Cross-channels mould. (b) Parallel-channels mould. . . . .	116
4.5	Exploded view of the <i>Cross-channels</i> mould. . . . .	121
4.6	<i>Parallel-channels</i> mould. (a) Picture of the assembly. (b) Exploded view. . . . .	122

4.7	Mould temperature profiles during ambient temperature and RHCM trials, controlled through the Peltier element . . . . .	123
4.8	Flow rate calibration, $T_{melt}=65$ °C: Experiment versus simulated flow length over time for different channel thicknesses of the Cross-channels mould. . . . .	125
4.9	Flow rate calibration, $T_{melt}=70$ °C: Experiment versus simulated flow length over time for different channel thicknesses of the Cross-channels mould. . . . .	126
4.10	Filling model validation, wax feedstock, $T_{melt} = 65$ °C. Experiment versus simulated flow length over time for different channel thicknesses of the Parallel-channels mould in disconnected channels configuration. The error bars represent the standard deviation over the five experimental measurements. . . . .	127
4.11	Filling model validation, wax feedstock, $T_{melt} = 75$ °C. Experiment versus simulated flow length over time for different channel thicknesses of the Parallel-channels mould in disconnected channels configuration. The error bars represent the standard deviation over the five experimental measurements. . . . .	127
4.12	Filling model validation, $T_{melt} = 65$ °C. Experiment versus simulated flow length over time for different channel thicknesses of the Parallel-channels mould in connected channels configuration - Visual comparison. . . . .	129
4.13	Filling model validation, wax feedstock, $T_{melt} = 65$ °C. Experiment versus simulated flow length over time for different channel thicknesses of the Parallel-channels mould in connected channels configuration. Note: results for the $th_{04}$ channel are plotted only for the first part of the process, as the feature is eventually filled from the largest channels through the machined passages. . . . .	130

4.14 Filling model validation, $T_{melt} = 70\text{ }^{\circ}\text{C}$ . Experiment versus simulated flow length over time for different channel thicknesses of the Parallel-channels mould in connected channels configuration - Visual comparison. . . . .	131
4.15 Filling model validation, wax feedstock, $T_{melt} = 70\text{ }^{\circ}\text{C}$ . Experiment versus simulated flow length over time for different channel thicknesses of the Parallel-channels mould in connected channels configuration. Note: results for the $th_{04}$ channel are plotted only for the first part of the process, as the feature is eventually filled from the largest channels through the machined passages. . . . .	132
4.16 Filling model validation, $T_{melt} = 75\text{ }^{\circ}\text{C}$ . Experiment versus simulated flow length over time for different channel thicknesses of the Parallel-channels mould in connected channels configuration - Visual comparison. . . . .	133
4.17 Filling model validation, wax feedstock, $T_{melt} = 75\text{ }^{\circ}\text{C}$ . Experiment versus simulated flow length over time for different channel thicknesses of the Parallel-channels mould in connected channels configuration. Note: results for the $th_{04}$ channel are plotted only for the first part of the process, as the feature is eventually filled from the largest channels through the machined passages. . . . .	134
4.18 Filling model validation, ceramic feedstock, $T_{mould} = 30\text{ }^{\circ}\text{C}$ . Experiment versus simulated flow length over time for different channel thicknesses of the Parallel-channels mould in disconnected channels configuration. The error bars represent the standard deviation over the five experimental measurements. . . . .	136

4.19	Pictures of mould filling, ceramic feedstock, $T_{mould} = 30\text{ }^{\circ}\text{C}$ , at different time steps. (a) $t = 0.1\text{ s}$ . (b) $t = 0.2\text{ s}$ . (c) End of filling. . . . .	137
4.20	Filling model validation, ceramic feedstock, RHCM. Experiment versus simulated flow length over time for different channel thicknesses of the Parallel-channels mould in disconnected channels configuration. The error bars represent the standard deviation over the five experimental measurements.	138
4.21	Pictures of mould filling, ceramic feedstock, RHCM, at different time steps. (a) $t = 0.4\text{ s}$ . (b) $t = 0.8\text{ s}$ . (c) End of filling. . . . .	139
4.22	Sink marks at the end of the thickest channels, $T_{melt} = 70\text{ }^{\circ}\text{C}$	140
4.23	Filler exposure. (a) Simulation results for melt front temperature, $T_{melt} = 75\text{ }^{\circ}\text{C}$ . (b) SEM micrograph of the top surface of the $th_{04}$ channel, showing exposed fillers, $T_{melt} = 75\text{ }^{\circ}\text{C}$ . (c) Simulation results for melt front temperature, $T_{melt} = 70\text{ }^{\circ}\text{C}$ . (d) SEM micrograph of the top surface of the $th_{04}$ channel, showing exposed fillers, $T_{melt} = 70\text{ }^{\circ}\text{C}$ . (e) Simulation results for melt front temperature, $T_{melt} = 65\text{ }^{\circ}\text{C}$ . (b) SEM micrograph of the top surface of the $th_{04}$ channel, showing covered fillers, $T_{melt} = 65\text{ }^{\circ}\text{C}$ . . . . .	141
4.24	Weld lines morphology. (a) Simulation results for melt front temperature, $T_{melt} = 70\text{ }^{\circ}\text{C}$ . (b) SEM micrograph of the top surface of the $th_{04}$ channel, showing a visible weld line $T_{melt} = 70\text{ }^{\circ}\text{C}$ . (c) SEM micrograph of the top surface of the $th_{04}$ channel, showing a well merged weld line $T_{melt} = 70\text{ }^{\circ}\text{C}$ .	142



4.25	Fillers packing. (a) Schematics of samples location in the component. (b) Simulation results for shear rates, $T_{melt} = 70\text{ }^{\circ}\text{C}$ . (c) SEM micrograph of the top surface of the $th_{04}$ channel at bridge location, $T_{melt} = 65\text{ }^{\circ}\text{C}$ . (d) SEM micrograph of the top surface of the $th_{04}$ channel at bridge location, $T_{melt} = 70\text{ }^{\circ}\text{C}$ . (e) SEM micrograph of the top surface of the $th_{04}$ channel at bridge location, $T_{melt} = 75\text{ }^{\circ}\text{C}$ . . . . .	144
4.26	Fillers packing. (a) Schematics of samples location in the component. (b) SEM micrograph of the cross section of the bridge between the $th_{04}$ and $th_2$ channels, $T_{melt} = 75\text{ }^{\circ}\text{C}$ . (c) SEM micrograph of the cross section of the $th_{04}$ channel, $T_{melt} = 75\text{ }^{\circ}\text{C}$ . . . . .	145
4.27	Ceramic block used for the study (Step III). (a) 3D view. (b) Main dimensions. . . . .	148
4.28	Sample location in the ceramic block. (a) Sample mapping in the block. (b) Example of samples location at the beginning of the block. . . . .	148
4.29	Defects at the beginning of the block. (a) Sample location legend. (b) S1b: SEM micrograph of a voids. (c) Simulation results for air trapped. (d) S2b: SEM micrograph of a crack around location hole. (e) Simulation showing mould filling and weld line creation around the location hole. . . . .	149
4.30	Defects at the centre of the block. (a) Sample location legend. (b) S4c: SEM micrograph of a flow line at the bottom surface of the block. (c) Simulation results showing melt front temperature and subsequent flow line creation. . . . .	150
4.31	Defects at the centre of the block (II). (a) Separation line close to the top surface of the block; (b) Sample location legend. . . . .	151

4.32	Defects at the beginning of the block. (a) Sample location legend. (b) S5a: SEM micrographs of voids. (c) Simulation results showing turbulences in flow. . . . .	153
5.1	<i>Parallel-channels</i> reference component. . . . .	159
5.2	SEM micrograph of fracture surface for the ceramic feedstock, showing the presence of elongated particles. . . . .	160
5.3	Schematics of samples cut for microstructural analysis to investigate particle orientation and packing . . . . .	161
5.4	Setup for uniaxial micro-compression tests under SEM - Part thickness in the y-axis of the reference coordinate system. (a) Moulded part. (b) Samples location. (c) Stage mounted within the SEM (top view). (d) Specimen. . . . .	163
5.5	Example of cavity filling and temperature distribution (0.933 sec after the beginning of injection) for conventional and RHCM approaches. (a) Injection moulded part, $T_{mould} = 30^{\circ}$ C. (b) Melt front time, $T_{mould} = 30^{\circ}$ C. (c) Temperature distribution inside the thinnest (0.4 mm) channel, $T_{mould} = 30^{\circ}$ C. (d) Melt front time, RHCM. (e) Temperature distribution inside the thinnest (0.4 mm) channel, RHCM. . . . .	165
5.6	Examples of orientation distribution in ceramic injection moulded green samples, ambient temperature - Part thickness in the y-axis of the reference coordinate system. (a) Schematics of the microstructure. (b) Moulded part. (c) Samples location. (d) 0.4 mm channel. (e) 2 mm channel. (f) 4 mm channel. (g) 6 mm channel. Note: Various magnifications have been used to represent different scales of phenomena. (h) Chart summarising layers distribution. . . . .	167

- 5.7 Examples of orientation distribution in ceramic injection moulded green samples, RHCM - Part thickness in the y-axis of the reference coordinate system. (a) Schematics of the microstructure. (b) Moulded part. (c) Samples location. (d) 0.4 mm channel. (e) 2 mm channel. (f) 4 mm channel. (g) 6 mm channel. Note: Various magnifications have been used to represent different scales of phenomena. (h) Chart summarising layers distribution. . . . . 168
- 5.8 Temperature along channel thickness during mould filling from Moldex3D simulation - Part thickness in the y-axis of the reference coordinate system. (a) Part isometric view of part for  $T_{mould} = 30^{\circ}$  C. (b) Section of 2 mm channel for  $T_{mould} = 30^{\circ}$  C. (c) Part isometric view of part for RHCM. (d) Section of 2 mm channel for RHCM. . . . . 170
- 5.9 Maximum shear rate along channel thickness from mould wall to the centre during mould filling from Moldex3D simulation. In the case of the thinnest bar (0.4 mm), two RHCM shear rate profiles are depicted in Figure (a): the maximum shear rate at the filling stage corresponding to the maximum filled length at ambient mould temperature  $l_0$  (yellow) and the maximum shear rate at the end of filling (red). . . . . 171

5.10	Examples of particle orientation in a 6 mm thick bar. (a) $T_{mould} = 30^{\circ} \text{ C}$ , 950 $\mu\text{m}$ from mould surface, micrograph taken at a higher magnification than the others because of lower particle size in this analysed area. (b) $T_{mould} = 30^{\circ} \text{ C}$ , centre of the moulding. (c) RHCM, 950 $\mu\text{m}$ from mould surface. (d) RHCM, centre of the moulding. (e) Feret angle distribution, 950 $\mu\text{m}$ from mould surface. (f) Feret angle distribution, centre of the moulding. Note: at least 70 platelets was $^{\circ}$ in the samples. . . . .	173
5.11	Example of particle size distribution in a $th_4$ bar. (a) $T_{mould}=30^{\circ} \text{ C}$ . (b) RHCM. . . . .	174
5.12	Average density of ceramic samples moulded at ambient temperature and RHCM. The error bars represent standard deviation calculated for five samples. . . . .	175
5.13	Simulation results for shear rates at the gate of the thinnest (0.4 mm) channel from the beginning of injection time to the completion of the filling stage. (a) Location of the measurement mesh node. (b) Shear rate over normalised time, where $t=0$ is the beginning of injection and $t=1$ the time at which the three thicker channels are completely filled. . . . .	176
5.14	Examples stress-strain curves before sample failure for the three reference cases: 2 mm channel, $T_{mould}=30^{\circ} \text{ C}$ ; 6 mm channel, RHCM and 6 mm channel, $T_{mould}=30^{\circ} \text{ C}$ . . . . .	178
5.15	Examples of cracked samples under uniaxial compression - Part thickness in the y-axis of the reference coordinate system. (a) Moulded part. (b) Samples location. (c) 2 mm channel, $T_{mould}=30^{\circ} \text{ C}$ . (d) 6 mm channel, RHCM. (e) 6 mm channel, $T_{mould}=30^{\circ} \text{ C}$ . . . . .	179

5.16	Setup for the adhesion tests. (a) Exploded view. (b) Drawing and main dimensions. (c) Picture of the setup. . . . .	185
5.17	Main temperature profiles used for the adhesion tests. The graph show the temperature measured by the two used thermistors, which were respectively 1 mm distant from the Peltier module (Peltier Temperature) and 1 mm distant from the mould cavity surface (Cavity Temperature). (a) Profile 1: Constant mould temperature ( $T_{mould}=35\text{ }^{\circ}\text{C}$ ). (b) Profile 2: RHCM. . . . .	187
5.18	Third temperature profile, of "alternative RHCM" used for the adhesion tests. The graph show the temperature measured by the two used thermistors, which were respectively 1 mm distant from the Peltier module (Peltier Temperature) and 1 mm distant from the mould cavity surface (Cavity Temperature) . . . . .	187
5.19	Absolute value of ejection force for the three temperature profiles. Prof. 1: $T_{mould}=35\text{ }^{\circ}\text{C}$ ; Prof. 2: RHCM; Prof. 3: Alternative RHCM. The error bars represent the standard deviation over three carried out measurements. . . . .	188
5.20	SEM micrographs of part and mould cavity surfaces after component ejection. (a) Part surface, Profile 1. (b) Mould surface, Profile 1. (c) Part surface, Profile 2. (d) Mould surface, Profile 2. (e) Part surface, Profile 3. (f) Mould surface, Profile 3. . . . .	189
5.21	Schematics of part-mould adhesion behaviour at different stages of the IM process for the three analysed mould temperature profiles. . . . .	190

5.22	Ejection temperature versus the characteristic DSC output curve of normalised heat flow rate for the green ceramic feed-stock and versus peak force during ejection. The graph shows correlation between the glass transition temperature ( $T_g$ ) of the binder, corresponding to the flex in the blue curve, and the drop in ejection force when the part is de-moulded at a mould temperature $\geq T_g$ . . . . .	191
6.1	Concept of the novel thermal control system. (a) Generic component, isometric view. (b) Schematics of Peltier configuration and positioning, showing the independent control for the two features and the location of temperature sensors for closed-loop control of the thermoelectric modules. (c) Schematics of the control approach for RHCM. (d) Schematics of the novel regional control approach. Note: Whole Peltier modules are larger than those displayed, as they occupy the whole feature thickness. . . . .	197
6.2	Example temperature cycle using the novel approach. (a) Filling stage. (b) End of filling. (c) Packing phase, Peltier 1 switches from heating to cooling. (d) Packing phase, Peltier 2 switches from heating to cooling. (e) End of cooling phase. (f) Ejection phase, Peltier 2 swaps to heating again to facilitate part ejection. (g) Thermal profile of the two Peltier modules shown in the schematics. Note: the graph shows hypothetical temperatures, which do not correspond to any specific thermal cycle. . . . .	199
6.3	Sample components. (a) Component A. (b) Component B. .	202

6.4	Prototype of the novel mould tool. (a) Exploded view of the assembly. (b) Main dimensions. (c) Mould cavity, main dimensions. (d) Cross section of the mould, showing Peltier modules and thermistor housings locations. . . . .	203
6.5	Mould unit, injection configurations. (a) Schematics of possible configurations (b) Example configuration for Cavity B SS. . . . .	204
6.6	Example temperature profiles for the three employed thermal control approaches, showing the Peltier temperatures corresponding to the thin and thick features of the mould. (a) Ambient mould temperature. (b) RHCM. (c) Regional control approach. . . . .	205
6.7	Flow chart of the thermal control model. . . . .	207
6.8	Example process window used for FE-PSO variable definition, for a single Peltier (P1). Note: a different set of parameters is valid per each Peltier. . . . .	209
6.9	Example of solution convergence over iteration number. . . .	212
6.10	Assembly modelled in Moldex3D filling simulation. . . . .	213
6.11	Example of ABAQUS-modelled assembly (Cavity B) (a) CAD model of the assembly. (b) Schematics of the model setup, showing the used mesh and temperature distribution. . . .	215
6.12	Results from the thermal control model and optimisation. (a) 3D mesh, Cavity A. (b) 3D mesh, Cavity B. (c) Optimal Peltier temperature profiles, Cavity A. (d) Optimal Peltier temperature profiles, Cavity B. (e) Optimal temperature profiles in the centre of Feature 1 and Feature 2, Cavity A. (f) Optimal temperature profiles in the centre of Feature 1 and Feature 2, Cavity B. . . . .	218

6.13	Results from the thermal control model: example for Cavity A in DS configuration. (a) 3D mesh, RHCM. (b) 3D mesh, optimised regional. (c) Peltier temperature profile, RHCM. (d) Peltier temperature profile, optimised regional. (e) Feature cooling rate profile (node sets A and B), RHCM. (f) Feature cooling rate profile (node sets A and B), optimised regional. (g) Feature temperature profile (node sets A and B), RHCM. (h) Feature temperature profile (node sets A and B), optimised regional. . . . .	220
6.14	Schematics of lack of packing during single sprue moulding with RHCM approach compared to the optimal case. (a) Schematics of the analysed sample and detailed of the magnified area. (b) Filling stage, RHCM. (c) Packing stage, RHCM. (d) Filling stage, optimised regional. (c) Packing stage, optimised regional. . . . .	221
6.15	Validation of the thermal control model: example for Cavity B in SS configuration. (a) Schematics of the component and location of the sensor in the cavity. (b) Validation, RHCM. (c) Validation, optimised regional control. . . . .	223
6.16	Measured temperature inside Feature 1b and in the centre of Feature 2 for Cavity B injected in DS configuration, using the regional optimised temperature approach. Note: the exact location of the thermistor inside Feature 1b could not be determined, but the figure show that similar cooling rates occur in the two features using the optimised control. . . . .	224



6.17	Enhancement of feature replication capability using RHCM and regional control approach. (a) Schematics of the phenomenon. (b) Cavity A DS, $T_m = 35^\circ C$ . (c) Cavity A DS, RHCM and optimal cases. (d) Cavity B SS, $T_m = 35^\circ C$ . (e) Cavity B SS, RHCM and optimal cases. Note: as the same flow length, during filling, was achieved in the RHCM and optical case, only one picture for both approaches is displayed for simplicity. . . . .	226
6.18	Dimensional accuracy analysis (a) Schematics of the analysed sample features (b) Schematics of the setup for dimensional accuracy measurements. . . . .	228
6.19	CIM outcome: Dimensional control. (a) Schematics of the phenomenon, mould filling, RHCM. (b) Schematics of the phenomenon, packing phase, RHCM. (c) Schematics of the phenomenon, mould filling, optimal. (d) Schematics of the phenomenon, packing phase, optimal. (e) Schematic of the phenomenon, part after cooling, RHCM and optimal. (f) Example of PVT behaviour. . . . .	229
6.20	CIM outcome: Weld lines in the ambient temperature case. (a) Schematics of the phenomenon, filling phase. (b) Schematics of the phenomenon, part after ejection. (c) Example of analysed component, Cavity B in DS configuration. (d) SEM micrograph of weld line. (e) Surface topography of weld line. . . . .	231
6.21	CIM outcome: Weld lines in the high temperature case. (a) Schematics of the phenomenon, filling phase. (b) Schematics of the phenomenon, part after ejection. (c) Example of analysed component, Cavity A in DS configuration. (d) SEM micrograph of weld line. (e) Surface topography of weld line. (f) SEM micrograph of the side of the top surface. . . . .	232

6.22	CIM outcome: surface quality on the thin feature in the ambient temperature case. (a) Schematics of the phenomenon, filling phase. (b) Schematics of the phenomenon, part after ejection. (c) SEM micrograph showing different orientation layers in the part cross section. (d) Example of analysed component, Cavity B in DS configuration. (e) SEM micrograph of shear-induced layer separation. (f) Surface topography of shear-induced layer separation. . . . .	234
6.23	CIM outcome: surface quality on the thick feature in the RHCM and regional control temperature cases. (a) Schematics of the phenomenon, filling phase, RHCM. (b) Schematics of the phenomenon, filling phase, optimal. (c) Schematics of the phenomenon, part after ejection, with highlighted area of the surface. (d) SEM micrograph of feature surface, RHCM. (e) SEM micrograph of feature surface, optimal. . . . .	235
7.1	Ceramic core example geometry and main features. Note: this reference core is a model geometry provided by Rolls-Royce plc, which has representative features to real ceramic cores for high pressure turbine blades. . . . .	242
7.2	Feature thickness in a core geometry. (a) Core top view. (b) Schematics of width and thickness directions. (c) Section A.	244
7.3	Isometric view of cavity features . . . . .	245
7.4	Mould inserts for injection moulding experiments. (a) Bottom plate, isometric view. (b) Bottom plate, main dimensions. (c) Top plate, isometric (d) Top plate, main dimensions.	246
7.5	Injection configurations: (a) single sprue injection (b) double sprue injection . . . . .	247

7.6	Thermocouple locations in the mould: (a) holes location, (b) thermocouple probe location . . . . .	248
7.7	Flow length vs flow rate in calibration experiments. (a) Low flow rate, SS configuration. (b) High flow rate, SS configuration. (c) Low flow rate, DS configuration. (d) High flow rate, DS configuration. . . . .	249
7.8	Experimental vs modelled flow length for the 9 cavities injected in SS configuration. (a) Mould temperature 35°C, experimental. (b) Mould temperature 35°C, simulation. (c) Mould temperature 50°C, experimental. (d) Mould temperature 50°C, simulation. . . . .	251
7.9	Reference core geometries used for the application of thermal control model and optimisation. . . . .	252
7.10	Application of filling model to core geometry and determination of Peltier and weld line locations. (a) Prediction of cavity filling over time. (b) Peltier regions in the core, based on filling patterns and features thickness, and location of weld lines. . . . .	254
7.11	Example process window for each Peltier, used for the implementation of the thermal control model and optimisation to core geometry. . . . .	255
7.12	Temperature profiles at the centre of each core feature using different thermal control approaches. (a) Core feature mapping. (b) Temperature profiles using constant ambient mould temperature. (c) Temperature profiles using RHCM. (d) Temperature profiles using the regional optimised temperature control. . . . .	259

7.13	Prototype mould for production IM machine with regionally controlled temperature. (a) Exploded assembly for the bottom half of the mould. (b) Main dimensions of the whole assembly. (c) Cross section of the bottom cavity showing Peltier module location. . . . .	261
7.14	Results from the FE simulation, to verify stresses and displacements on the insulation sheet of the mould. . . . .	263
7.15	Example concept of mould with arrays of Peltier modules, selectively controlled. . . . .	266
7.16	Example concept of mould with layer of multi-conductivity materials. . . . .	267

# Chapter 1

## Introduction

### 1.1 Motivation

Ceramic materials are extensively used in several high value industries, such as aerospace, power generation, automotive and healthcare. Thanks to their properties, in particular high temperature resistance, excellent thermal as well as electric insulation, mechanical strength and chemical inertness, they are employed in a wide range of applications, including but not limited to coatings, investment casting cores, kiln furniture, fuel cell components, as well as sealing and insulation for sensors (e.g. thermocouples). Several manufacturing methods are usually employed to produce ceramic components, including casting (e.g. slip or tape casting), hot pressing and ceramic injection moulding (CIM). A significant advantage of CIM as a manufacturing route for the production of ceramic parts, compared to the other processes, is that it enables a large scale and high throughput automated production of complex macro and micro components at a low cost per unit.

The CIM process chain consists of four distinct stages (Figure): (i) feed-stock preparation, (ii) injection moulding, (iii) firing (or debinding) and (iv) sintering (Rahaman, 2007).

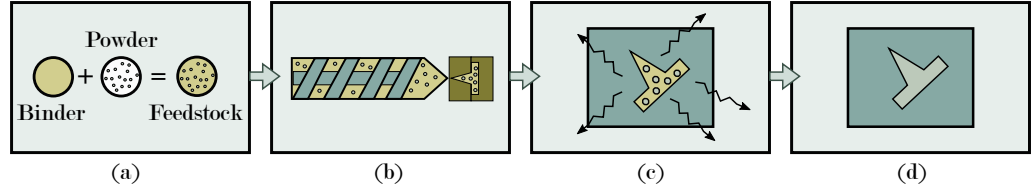


Figure 1.1: Schematic of the CIM process. (a) Feedstock preparation. (b) Injection moulding. (c) Debinding. (d) Sintering.

The first stage, consists in the creation of the feedstock by mixing ceramic powder or granules with a polymer- or wax-based binder. This step is of uttermost importance, as the material behaviour for subsequent stages of CIM is highly influenced by the particle content of the mixture (i.e. solid loading), powder morphology, as well as rheological, thermodynamic and mechanical properties of the binder. In the injection moulding stage, similarly to plastic processing applications, the feedstock is firstly molten and then injected at high pressure into a mould cavity having the negative shape of the component that needs to be manufactured. The material then undergoes rapid cooling inside the die-tool and, during solidification, the moulded component will shrink according to both feedstock thermodynamic properties and the processing conditions, in particular pressure and temperature the feedstock is subjected to. Hence, to compensate for shrinkage, further material is injected at a high pressure, in the so-called packing phase. In this stage of the CIM process, injection moulding die-tools play a fundamental role for obtaining defect-free parts and their thermal control systems need to be tailored and optimised based on the parts that need to be manufactured. After cooling, the as-moulded (so-called green) part is then ejected from the die-tool and transferred to a kiln where the binder is firstly removed and then the remaining ceramic powder is sintered to achieve the required porosity level. During the firing and sintering stages, the moulded components undergo further volume contraction, with shrinkage rates up to 20 volume % (Krug, Evans, and Ter Maat, 2002a).

The remarkable consequentiality and interdependency among these stages makes the whole CIM process highly complex and challenging to analyse and optimise, as quality outcomes visible on finished components do not only depend on material properties and sintering conditions, but also on the part macro- and micro-structural properties achieved within each single process step.

A relevant application where CIM is often employed is the manufacture of ceramic cores, which are sacrificial components used to shape complex internal cavities in hollowed parts through investment casting (Gromada et al., 2015). A schematic of the metal investment casting process is displayed in Figure 1.2.

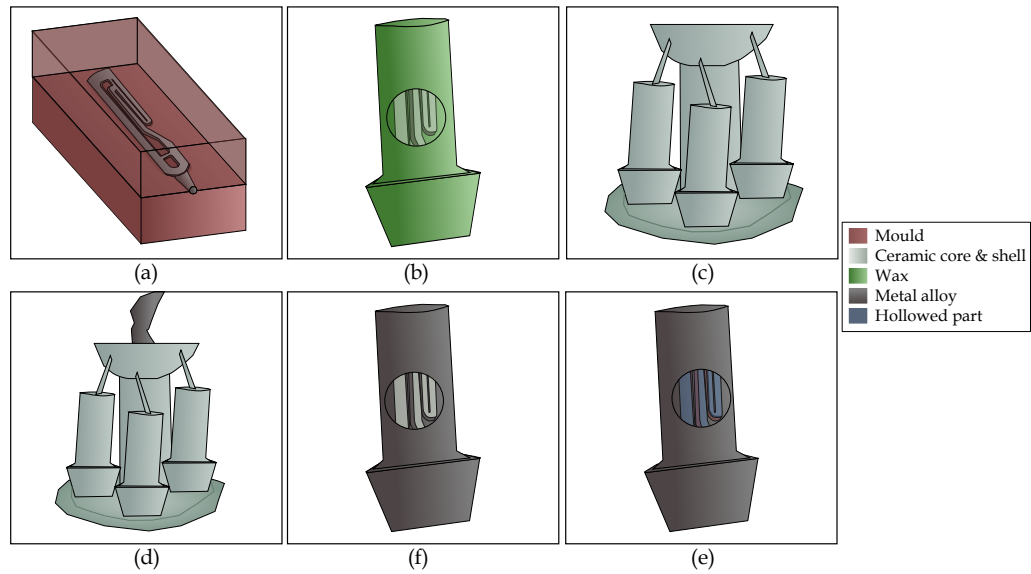


Figure 1.2: Schematic of the investment casting process. (a) Core injection moulding. (b) Core encapsulation in wax pattern. (c) Shell and de-waxing. (d) Casting. (e) Shell removal. (f) Core removal.

After being moulded (Figure 1.2a) and sintered, cores are usually encapsulated in wax patterns, through a further injection moulding process (Fig-

ure 1.2b); the resultant part, including core and wax pattern, is often assembled to form an investment casting tree and then coated with a ceramic shell (Figure 1.2c) , which will form the actual casting mould. Once the whole casting tree assembly is ready, it is placed in a furnace and undergoes the de-waxing process, where patterns are fired to obtain the final investment casting die, comprising cores and shells. Following this, the metal pouring process step is carried out (Figure 1.2d), after which the casting is released from the shell (Figure 1.2e) and the cores are removed (Figure 1.2f), usually by chemical leaching, to leave the hollowed cavity in the casted component.

A significant example of this application comes within the aerospace industry where, in turbo-fan engines, cores (Figure 1.3a) are used to shape internal cooling channels in high pressure turbine blades and nozzle guide vanes (Figure 1.3b), manufactured by investment casting. These cavities are needed to withstand the high operating temperatures these components are subjected to, as well as to reduce their weight (Rolls-Royce, 2015).

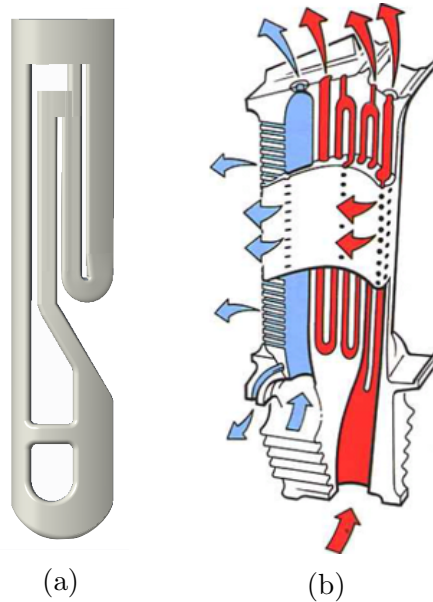


Figure 1.3: Cores for investment casting of turbine blades. (a) Example of core geometry (representative model design, provided by Rolls-Royce plc). (b) Cooling channels in a blade (Rolls-Royce, 2015).



To allow the higher working temperatures of blades and vanes, their cooling efficiency must be enhanced through an optimum coolant flow. Therefore, the internal hollowed channels, and hence the cores, must follow the airfoil shape of the blade and are usually characterised by a serpentine-like geometry with variable thickness. Future trends in the aerospace industry call for rapidly increasing requirements of higher turbine inlet temperatures (Figure 1.4), which are already close to the melting point of the Nickel-based super-alloys blades and vanes are made of. To meet these requirements, industrial and research efforts are needed to enhance cooling performance, hence demanding advances in core design, including an increased amount of fine features and reduced trailing edge sections, as well as tighter tolerances to be achieved.

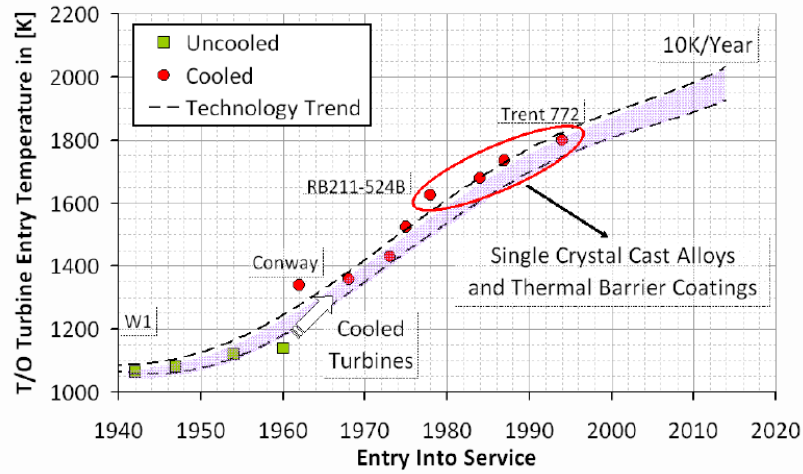


Figure 1.4: Evolution and future trends of turbine entry temperature in aero engines (Kyprianidis, 2012).

Despite the aforementioned advantages of CIM, its manufacturing capability is significantly limited to mouldings having fairly uniform wall thickness (Fischer, 2013). This brings challenges to aerospace companies for the manufacturing of ceramic cores, as they need to develop their current manufacturing procedures and equipment in order to meet the new stringent requirements.

The present PhD work has been granted by a Rolls-Royce CASE award scheme, moved by an interest in research on how to boost internal capability to produce ceramic cores through CIM. The focal point in this improvement process is not only oriented towards the formulation of new feedstock materials and the optimisation of processing conditions, but it entails an effort into the development of new smart mould heating and cooling technologies capable to improve thermal control of the process and cope with increasingly complex geometries. This is not trivial as, being CIM a mass production process, large investment costs in terms of die-tools are required. For this reason, there is a need for a structured research approach that can promote the development of effective and long-lasting mould tooling technologies. This strategy, developed for the present work, can be summarised as follows: (i) the development of a methodology to assess the effect of heat transfer phenomena on the quality of ceramic moulded parts, (ii) the achievement of a deep understanding on how state-of-the-art thermal control approaches affect quality outcomes from the moulding process, (iii) the design of a mould tool with suitable heating and cooling technologies and the joint development of a thermal control model and (iv) the application of the proposed tool and generation of guidelines for generic complex components. Strong academic and industrial challenges need to be addressed and overcome to enable the development of novel thermal control systems for CIM throughout the described research strategy. These challenges are presented and discussed in the following section.

## **1.2 Research problem**

The use of CIM for the manufacturing of complex geometries such as ceramic cores presents several challenges, which are mostly related to mouldability

issues intrinsically linked to design requirements that must be fulfilled to preserve part functionality.

The first challenging aspect relates to the uneven thickness of these components, which is usually avoided in conventional injection moulding. This requirement of constant wall thickness is due to the fact that differential feature size causes uneven cooling rates along the part, during and after the filling stage of the process, as the molten feedstock solidifies faster at thinner sections. This, in turn, generates major mouldability issues. First of all, during mould filling, the feedstock can solidify at thin sections, hence causing lack of fill (i.e. short-shots) in the mould. Even if this does not occur and the cavity can be successfully filled, quicker solidification rates at thin features will cause differential shrinkage in the part, which will provoke component warpage and cracking.

Differential shrinkage, as a consequence of uneven cooling rates, can be attributed to factors related to pressure-temperature conditions during solidification and to the binder microstructure developing throughout the process. When thick features are more distant from the gate than thin ones (which solidify first), lack of packing can occur at the former sections. Considering binder morphology, thicker features shrink more due to higher stress relaxation and a more random molecular orientation developing because of lower cooling rates (Krug, Evans, and Ter Maat, 2000); in the case of semi-crystalline binders, this effect is even more relevant as their ordered crystalline structure will further promote shrinkage (De Santis, Pantani, Speranza, and Titomanlio, 2010). Differential shrinkage defects may appear in green parts or directly after sintering, due to stress relaxation at high temperatures. This makes it challenging to attribute these defects to the injection moulding process or to flaws within firing and sintering. Fur-

thermore, in the particular case of CIM, the presence of ceramic powder further complicates these effects, due to particle orientation and packing: these two phenomena are mainly caused by uneven shear rates along the part and cause microstructural anisotropy which, in turn, will affect shrinkage behaviour during firing and sintering and ultimately promote part cracking and distortion (Krug, Evans, and Ter Maat, 2002a).

The second challenging aspect concerns the intricate shape of the components: complex geometries cause convoluted filling patterns to arise, where multiple flow fronts meet, thus creating weld lines. These defects on components surface represent preferential locations for crack initiation, especially when the flow fronts do not merge properly. As weld lines cannot sometimes be avoided, is preferable that flow fronts join at a high temperature to ensure a lower viscosity and promote a stronger bonding.

The third aspect is related to abrupt changes in thickness of the part, as these variations cause high shear rate areas during filling, where often segregation between particles and binder occurs, since ceramic powder tends to be present at higher concentrations at low shear rate regions. This phenomenon causes major defects in finished components, as it determines the creation of areas with excess of binder, which will be removed and leave "eroded" regions in the part after the processes of debinding and sintering.

To prevent these issues, when part design cannot be simplified (such as in the case of ceramic cores), process optimisation and effective mould tooling technologies are vital. A conventional "constant mould temperature" approach throughout the process will imply a trade-off between part quality at thick and thin sections: in case of a "too cold" mould cavity, lack of fill is likely to arise, as well as surface defects and weld lines cracking;

instead, if the mould is kept at a higher temperature, shrinkage-related defects, such as sink marks are more likely to appear, as well as longer cycle times. Moreover, in both cases, thin features will solidify sooner rather than thicker ones, thus causing lack-of-packing defects at thick sections farther from the gate.

State-of-the-art research on innovative die-tools for injection moulding, which has been mainly carried out for plastic applications, is currently focussing on rapid heat cycle moulding (RHCM) and conformal cooling (Shayfull et al., 2014). The RHCM approach consists of rapidly heating the mould cavity to keep low feedstock viscosity, hence ensuring complete filling and reducing surface defects, such as flow and weld lines. Conformal cooling is based on the manufacturing of moulds having shaped cooling channels that follow the geometry of the mould cavity to allow for uniform and fast part cooling.

Whilst these techniques are effective in ensuring a complete cavity filling, while maintaining short cycle times and attaining high surface quality, they are oriented towards the achievement of a uniform mould temperature at the cavity surface (Wang, Zhao, Guan, and Hui, 2015). This averts shrinkage-related defects for parts having a uniform wall thickness, as is the case of a wide range of plastic components. Nevertheless, in case of parts with the aforementioned mouldability challenges, i.e. uneven thickness, intricate filling patterns and abrupt variations in cross section, these approaches will not prevent differential cooling rate effects. Hence, mould tools with smarter thermal control strategies must be developed, alongside customised temperature profiles for different feature thicknesses, in order to prevent differential cooling rates during the IM process.

The design and development of these new die-tools for ceramic injection

moulding, with tailored temperature control presents several challenges for the following reasons:

- Novel approaches to mould thermal control must allow a uniform microstructure at sections having different wall thickness. This is important because microstructural anisotropy developing during the injection moulding process leads to the formation of defects that are often not evident in the green part, but appear post-sintering. Hence, a thorough understanding of the phenomena of orientation and packing in relation to cavity temperature is required.
- The heat transfer phenomena taking place during injection moulding differ between thick and thin features. Energy transfer mechanisms are not restricted to the cooling phase but also involve viscous heating dissipation and heat conduction as well as convection within the part, whose extent highly depends on features thickness (Yao and Kim, 2004). This needs to be taken into account when developing moulds with optimised thermal control management systems.
- The temperature control system must account for the distance of the features from the gate. As stated previously, this aspect is critical especially for parts having adjoined features, where the molten feedstock might prematurely solidify at thinner sections. The novel thermal control must then ensure features closer to the gate to be held at higher temperature than those farther, especially when they are thinner.
- Mould temperature affects part adhesion to the die tool. This aspect cannot be overlooked, as ejection issues are likely to cause part warpage, cracking (Delaney, Bissacco, and Kennedy, 2012a) or defects such as ploughing, i.e. local plastic deformation of the part surface from shear contact with the mould. Therefore, temperature optimi-

sation must be constrained to a process window that allows for the secure ejection of the moulding from the die-tool.

- Being that CIM a mass production process, cycle times should be minimised. Therefore, short cooling times must be achieved and mould heating-up should be averted. This represents a strong design challenge, as the thermal control system must be developed in a way that the mould is shortly heated during the filling stage only in proximity to the cavity and that heat is quickly dissipated to gain a steady moulding cycle from a temperature point of view.

All these aspects make the development of novel thermal control approaches for ceramic injection moulding an intricate research problem. Some of the aforementioned challenges require a thorough understanding of phenomena occurring during injection moulding that still need to be further investigated; others call for smart design approaches and choices in both the heating and cooling technologies to be employed.

### 1.3 Objectives of the study

The aim of this study is to develop and demonstrate a thermal management system for die-tools able to improve the capability of manufacturing complex components characterised by uneven cross section thickness through CIM.

To achieve this aim, the following research objectives are set:

- To develop a methodology to analyse the effect of heat transfer phenomena on the quality of ceramic injection moulded parts. As the three steps of moulding, debinding and sintering are closely interrelated to each other, a structured approach is essential to study compo-

nents quality. This methodology was developed through the analysis of macro and micro-structural outcomes from the Injection Moulding (IM) process in green and sintered components. The correlation between the observed outcomes and IM was achieved with the support of a numerical simulation of the injection process, which captures the effect of different thermal control approaches on mould cavity filling.

- To explore and understand the phenomena induced by state-of-the-art thermal management approaches upon the quality and integrity of features having different cross section thickness. This is of great importance, in order to define and develop suitable designs and thermal control solutions. A novel study was carried out on the effect of Rapid Heat Cycle Moulding (RHCM) on particle orientation and packing in green parts, achieved through microstructural analysis, density measurements, *in-situ* compressive tests and geometrical accuracy evaluations. Moreover, an investigation was carried out on the effect of the RHCM approach on mould-part adhesion during component demoulding, through measurements of ejection forces under the employment of different mould thermal control approaches.
- To design and demonstrate an innovative die-tool with a regional and optimised temperature control, to inject components having uneven wall thickness. The die-tool design was done by the introduction of heating and cooling elements, actively and independently run during all the stages of the injection moulding process, for the achievement of a localised control of mould temperature. A thermal model of the packing and cooling stages of the IM process was developed for the prediction of cooling rates and temperature distribution throughout the moulded component, arising during the process. Based on this, the temperature profiles of each heating and cooling element were op-



timised throughout the process, with the aim of minimising differences in cooling rates along the component, despite the presence of features having dissimilar thicknesses. The model was validated on the novel die-tool, using reference mouldings characterised by adjoined features having non-uniform wall thickness. The effects of the novel approach were evaluated through macro and micro-structural analysis of the studied reference components.

- To construct guidelines for applying and operating the novel proposed thermal management approach with generic complex components. For this purpose, the thermal control model and optimisation were applied to a case study ceramic core geometry, and a prototype mould for production applications is presented. The main challenges for the industrialisation of die-tools having the proposed novel thermal management system are presented, along with alternative modular design concepts.

# Chapter 2

## Literature Review

*The widespread use of injection moulding, in both plastic and ceramic applications, has motivated academic and industrial research efforts aimed at enhancing process understanding and capability. In this chapter, the conducted literature survey will be presented. First of all, as the majority of research in Injection Moulding (IM) has been carried out for plastic applications, an overview of the polymer moulding process will be given. Then, in order to achieve a profound understanding of Ceramic Injection Moulding (CIM) and the phenomena occurring during the process, a thorough analysis of the whole manufacturing chain will be reported, including all the steps of feedstock preparation, injection moulding, debinding and sintering, with a comprehensive review of the research work performed on the topic. This will be followed by an overview of injection moulding die-tools and state-of-the-art heating and cooling technologies and subsequently by a survey on the literature regarding quality outcomes from the ceramic injection moulding process as well as on the principal studies to enhance CIM capability. In the last part of the review, state-of-the-art research in thermal control approaches for injection moulding, with a particular focus on thermal control optimisation methods, will be reported. Based on the presented literature survey, the main research challenges that motivated the deployment of this*

*work will be highlighted at the end of this chapter.*

## 2.1 Injection moulding

Injection moulding (IM) is one of the principal processes to manufacture plastic products: it involves the melting of a polymer and its injection at high pressure into a mould with a cavity that has the shape of the part that needs to be produced. The plastic material (i.e. feedstock) can be a simple polymer or one containing fillers, which can be fibre reinforcements, ceramic or metal powder. In this section, a comprehensive review of the injection moulding process will be given, including the working details of IM machines, materials, main process stages and part design mouldability guidelines. Within the section, a theoretical framework will also be provided, to achieve a comprehensive understanding of the main physical mechanisms governing the IM materials behaviour and process conditions.

### 2.1.1 Injection moulding machines

To meet the requirements of a mass production process, including the manufacturing of high-quality standardised components at a high throughput, capital intensive machinery and tools are employed in the moulding industry. IM machines consist of four main assemblies: the power unit, the injection unit, the clamping unit and the control unit (Figure 2.1). The power unit consists of a hydraulic or electric motor, which drives the injection unit, whose role is to supply raw material (i.e. the feedstock) to the machine and to prepare it for injection by plasticising the melt. To do so, it comprises a hopper, which feeds the material to a heated barrel that, in turn, contains a rotating screw to plasticise and drive the material towards the clamping unit or a plunger that simply pushes the material to the clamping unit (Rosato, 2000). Depending on the injection compo-

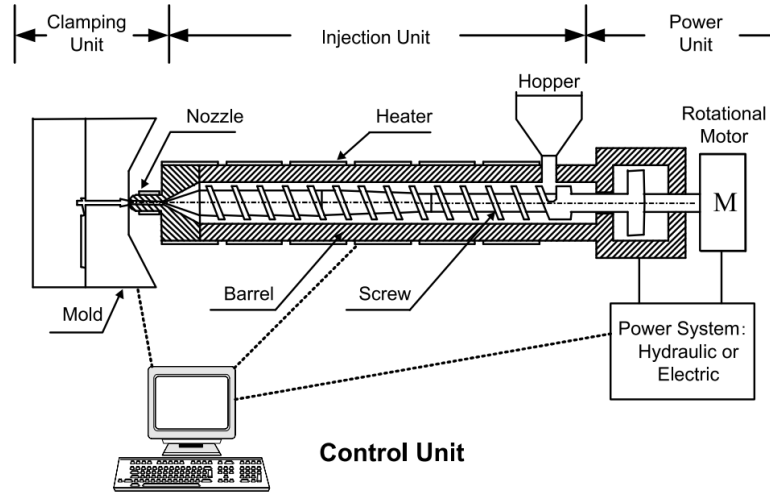


Figure 2.1: Schematics of a screw-type injection moulding machine (Chen, 2016).

ment, IM machines are classified as screw or plunger type. A nozzle links the injection to the clamping unit of the machine, and feeds the material to a mould, which consists of a stationary and a moving component and whose cavity is surrounded by cooling (and sometimes also heating) elements that ensure the achievement of a suitable temperature cycle during the IM process. The mould is held stationary through mechanical toggle or hydraulic cylinder systems, with a clamping direction that may be parallel or perpendicular to the injection direction. These systems are all connected to the control unit, which monitors and often regulates the aforementioned machine components as well as process parameters.

### 2.1.2 Injection moulding materials

IM feedstocks include a wide range of thermoplastic materials. In order to understand process requirements and challenges that can arise during injection, leading to specific part quality outcomes, it is necessary to have a good knowledge of the material properties that relate to the IM process. These properties are (Zhou, 2013):

- Morphology
- Rheological properties
- Pressure-Volume-Temperature (PVT) behaviour
- Thermal properties

In the following, these properties will be addressed and related to the IM process.

### **Morphology**

Feedstock morphology comprises a set of characteristics that influence molecular arrangement and which, in turn, affect other properties, such as shrinkage behaviour and viscosity.

Thermoplastic polymers can be classified based on their molecular morphology, into the three main categories of amorphous, semi-crystalline and liquid crystalline (LCPs) (Zheng 2011), as shown in Figure 2.2. Amorphous polymers are characterised by randomly arranged molecular chains in both solid (glassy) and liquid (rubbery) state: the passage between these states is associated to the so-called "glass transition temperature"  $T_g$ . In semi-crystalline thermoplastics, some of the molecules arrange in structured configurations (i.e. they crystallise) when cooled down from the molten state: depending on the percentage of crystalline and amorphous phase, these material can have different "degrees of crystallinity". LCPs are crystalline polymers which exhibit ordered molecular arrangements also in the molten state. As the present work is principally related to semi-crystalline materials, an understanding is needed of how the degree of crystallinity of a solidified polymer affects its properties and of how it is influenced by manufacturing conditions.

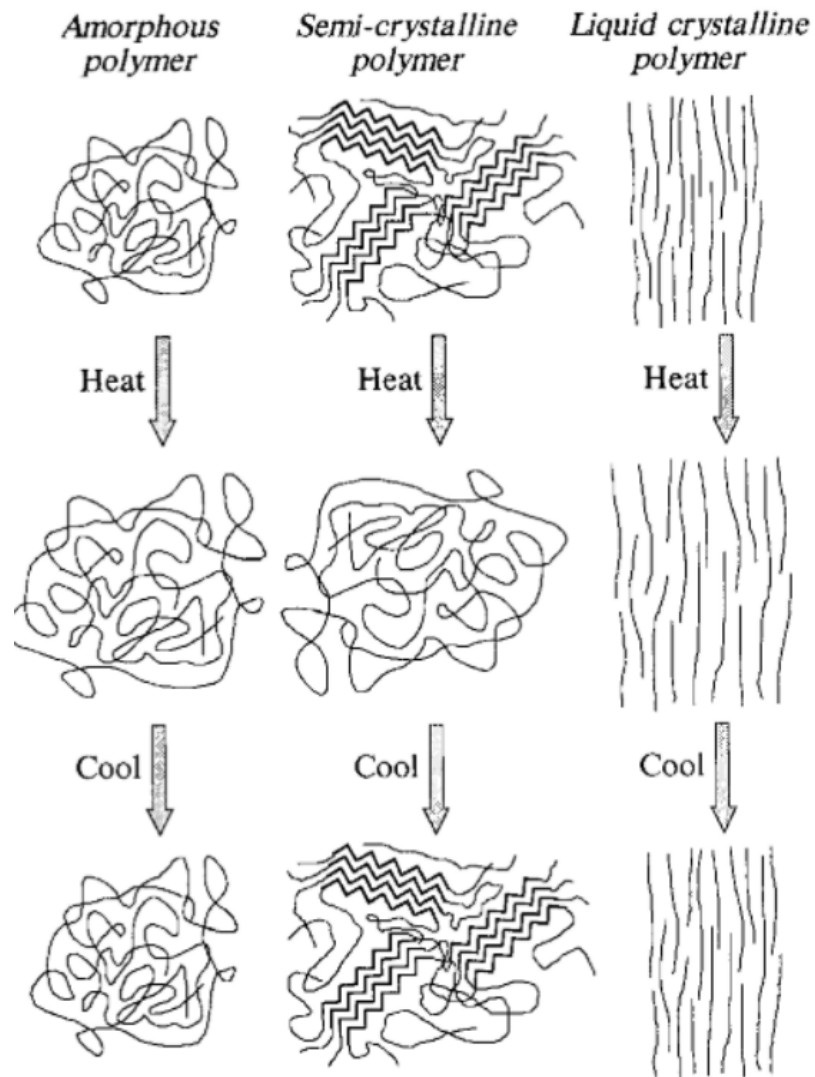


Figure 2.2: Molecular morphologies of thermoplastic materials (Malloy, 2010).

Considering a molten polymer (i.e. at a temperature above the melting point  $T_m$ ), the crystallisation process starts with nucleation and then follows the growth of crystalline regions around the created nuclei. These mechanisms occur upon cooling, at a temperature range lower than  $T_m$  but higher than  $T_g$  (called undercooling phase), when the amorphous regions become fully solid (Chen, 2016). Higher degrees of crystallinity promote polymer shrinkage, due to the ordered (and thus more "packable") structure of the material; moreover, due to the preferential alignment of molecules in the ordered regions, semi-crystalline polymers may present anisotropic mechanical properties and shrinkage, compared to amorphous plastics (Fischer, 2013).

Crystallisation kinetics are complex and depend on cooling rates, temperature gradients and applied shear rates and stresses on the material during cooling (Piorkowska, 2013). In particular, considering a polymer that cools at a constant rate, a faster cooling rate will cause, first of all, a shift of temperature window for crystallisation and a reduced degree of crystallinity, due to the lower time that crystal have available to grow and nuclei to form. Thermal gradients have, instead, a major role in determining the morphology and orientation of nucleated regions, as crystal growth is higher in areas that have been cooled more. As for shear flow, it not only causes a preferred orientation of molecules along the flow direction, but also increases the overall degree of crystallinity, which has been both experimentally observed and can be theoretically explained by a lengthening of undercooling due to an increase of  $T_m$  of the material (Piorkowska, 2013; Van Der Beek, 2006). Similar effects to the equilibrium melting point of polymers are attributable to pressure conditions, linked to changes in the specific volume of the material (Piorkowska, 2013).

Semi-crystalline polymers, upon heating from the solid state, exhibit a sharp

transition at the  $T_m$ , due to the melting of the crystals, while amorphous polymers (and the amorphous region of the semi-crystalline plastics), exhibit a gradual evolution from a glassy state (below  $T_g$ ) and a rubbery state (between  $T_g$  and  $T_m$ ).

### Rheological properties

Rheology studies the flow of matter under applied forces and rheological properties describe how a material deforms and flows when is subject to stresses. Considering a fluid flowing between two parallel plates, one stationary and one moving, a velocity gradient will develop at a normal direction to the flow, from the walls to the centre of the fluid (Figure 2.3).

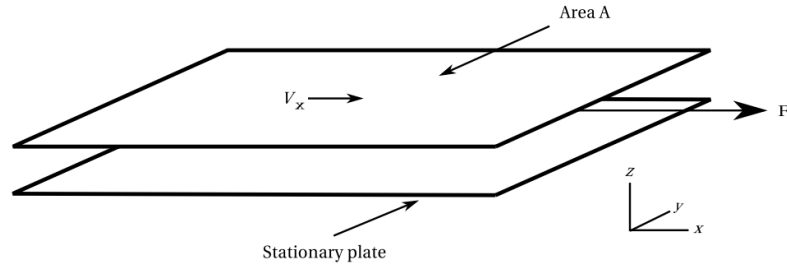


Figure 2.3: Schematic of simple shear flow (Kennedy, 2013).

The fluid will be therefore subjected to shear, with a shear stress  $\tau_{zx}$  on the top plate:

$$\tau_{zx} = \frac{F_x}{A} \quad (2.1)$$

where  $F_x$  is the force applied to the fluid and  $A$  is the plate area. The shear rate, being the velocity gradient along the orthogonal direction to the flow (in this case the thickness of the plate), can be defined as:

$$\dot{\gamma}_{zx} = \frac{dv_x}{dz} \quad (2.2)$$

The shear viscosity  $\mu$  parameter describes the resistance of a fluid to applied



shear forces (Gupta, 2012) and links the shear stress and shear rate through the following equation:

$$\tau_{zx} = \mu \frac{dv_x}{dz} = \mu \dot{\gamma}_{zx} \quad (2.3)$$

For several materials, viscosity changes according to processing conditions: non-Newtonian fluids, whose viscosity varies with the shear rate and fluid temperature, can be classified into Bingham plastics, pseudoplastic fluids and dilatant fluids. Bingham plastics are fluids that are characterised by remaining rigid when subject to shear stresses below a threshold level (i.e. yield stress) and exhibiting a quasi-Newtonian behaviour when subject to stresses higher than the yield. The two other categories are characterised by a viscosity that generally decreases or increases with the shear rate: these are defined as *shear thinning* (for pseudoplastic fluids) and *shear thickening* (for dilatant fluids) respectively. The majority of polymers exhibit a pseudoplastic fluid behaviour (Zheng, 2011), as shown in Figure 2.4: this is particularly relevant for materials employed in IM, as the opposite rheological behaviour would cause an increased resistance of the feedstock during mould filling.

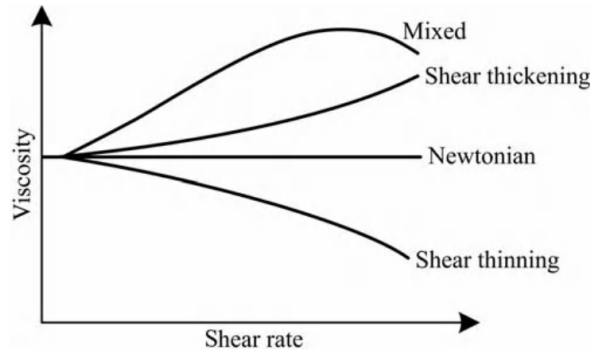


Figure 2.4: Types of pseudoplastic material flow as a function of shear rate (Zhou, 2013).

Considering a thermoplastic fluid, three main viscosity regions can be identified when the polymer is subject to shear (Figure 2.5): upper Newtonian region ( $\mu = \mu_0$ ) at low shear rates, shear thinning region at intermediate rates and lower Newtonian region ( $\mu = \mu_\infty$ ) at high rates. Several mathe-

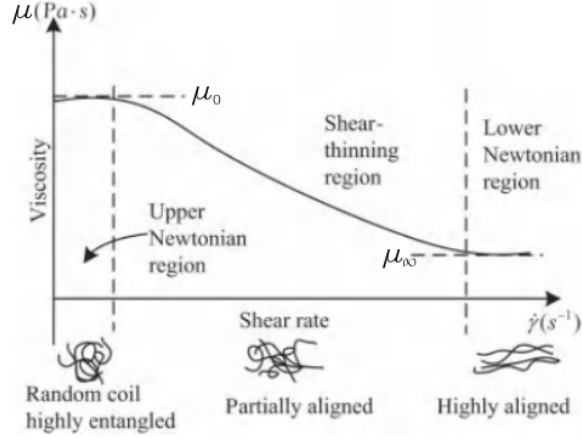


Figure 2.5: Viscosity behaviour of shear thinning polymeric fluids (Zhou, 2013).

matical models have been used to describe the rheology of polymers exhibiting a pseudoplastic behaviour and, in particular, how viscosity varies with temperature and shear rates. As some of these models will be employed to build numerical simulations of the IM process in the present work, it is worth to provide an insight on their main features and an understanding on how they define the viscosity behaviour of thermoplastic materials, depending on temperature and shear rates.

The simplest and most common mathematical model describing the shear thinning region of this characteristic curve is the Power Law model, developed by Waele and Ostwald (1925):

$$\mu = \mu_0 \dot{\gamma}^{n-1} \quad (2.4)$$

where the constant  $n$  is known as the power-law index, which has a value

between 0 and 1 (the equation describes a Newtonian fluid, when  $n = 1$ ).  $\mu_0$  (or zero-shear rate viscosity) describes the relationship between viscosity, temperature and pressure. This can be described using the exponential model:

$$\mu_0 = B \exp\left(\frac{T_b}{T} + DP\right) \quad (2.5)$$

where  $B$  is called consistency index and the constants  $T_b$  and  $D$  show the sensitivity of the material viscosity to the temperature  $T$  and the pressure  $P$  respectively. Another model, used in injection moulding applications, to describe  $\mu_0$  is the Willam-Landel-Ferry (WLF) one, written in the form:

$$\mu_0 = D_1 \exp\left(\frac{-A_1(T - T_c)}{A_2 + (T - T_c)}\right) \quad (2.6)$$

$$T_c = D_2 + D_3P \quad (2.7)$$

where  $D_1$ ,  $D_2$ ,  $A_1$  and  $A_2$  are constants. The WLF model, for the description of zero shear rate viscosity, presents the disadvantage of a higher complexity compared to the exponential one, but is one of the most used in injection moulding applications, as it better reflects the variation of viscosity with temperature and pressure (Zhou, 2013).

The Power-Law model approximates well the viscosity behaviour of plastics at high shear rate levels; however, it does not describe the upper-Newtonian region, which is relevant for injection moulding. To overcome this, more complex models have been developed to describe also the low-shear rate region of the pseudoplastic fluids viscosity curve, the Cross model (1965) being one of the most employed in literature regarding IM (Lee, 1997, Has-

san, 2010 and Chang, 2016):

$$\mu = \frac{\mu_0}{1 + \left(\frac{\mu_0 \dot{\gamma}}{\tau^*}\right)^{1-n}} \quad (2.8)$$

where  $\tau^*$  is the critical shear stress at the upper-Newtonian plateau region and  $n$  is the power-law index. To describe  $\mu_0$ , both the models described by Eq. 2.5 or Eq 2.6-2.7 can be used, thus referring to the whole model as Cross-Exp or Cross-WLF respectively.

### Pressure-Volume-Temperature (PVT) behaviour

Pressure-Volume-Temperature (PVT) behaviour describes compressibility, i.e. how the specific volume of a material (and hence density) varies with temperature and pressure. In general, specific volume will increase with lower applied pressure and higher temperatures; polymers exhibit higher density variations compared to other materials and, between different polymers, PVT behaviour changes significantly depending on the morphology of the plastic, being amorphous or semi-crystalline (Zhou, 2013). While both types of polymers present a linear increase of specific volume with temperature, for  $T > T_g$ , at  $T < T_g$ , the dependency remains linear for amorphous polymers, it becomes exponential for the semicrystalline ones (Figure 2.6). As already discussed, this is due to the more ordered structure of the molecules, which rearrange in a more ordered way during solidification, hence causing higher density variations. Moreover, as specific volume changes with temperature will depend also cooling rates for semicrystalline polymers, their characteristic PVT curves will vary according to the rates of temperature variation (Zuidema, 2001).

Also for this behaviour, mathematical models are used (and will be employed in the present work) to describe how specific volume varies with

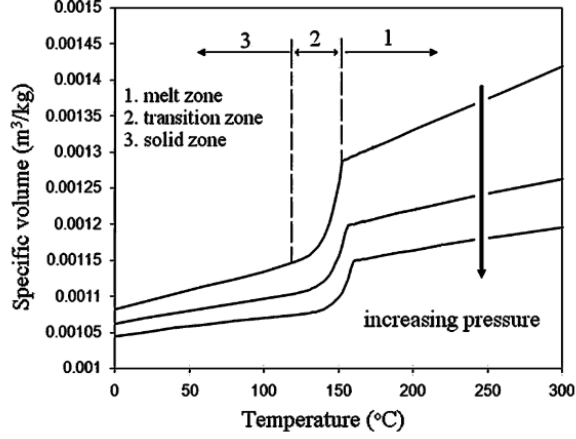


Figure 2.6: Example PVT diagram for a semicrystalline polymer (Zheng, 2011).

temperature and pressure. The most used of these models is the two-domain Tait equation (1888):

$$v = v_0 \left[ 1 - C \ln \left( 1 + \frac{P}{B} \right) \right] + v_t \quad (2.9)$$

where  $P$  is the pressure,  $C$  is the universal Tait constant valid for polymers (having value of 0.0894), and  $v_0$ ,  $B$  and  $v_t$  are piecewise functions for which different sub-functions apply depending on whether the feedstock temperature is above or below the material  $T_g$  and are described by the following equations:

$$v_0 = b_{1s} + b_{2s}T_b, \text{ if } T \leq T_t \quad (2.10)$$

$$v_0 = b_{1l} + b_{2l}T_b, \text{ if } T > T_t \quad (2.11)$$

$$B = b_{3s} \exp(-b_{4s}T_b), \text{ if } T \leq T_t \quad (2.12)$$

$$B = b_{3l} \exp(-b_{4l}T_b), \text{ if } T > T_t \quad (2.13)$$

$$v_t = b_7 \exp(b_8 T_b - b_9 P), \text{ if } T \leq T_t \quad (2.14)$$

$$v_t = 0, \text{ if } T > T_t \quad (2.15)$$

where  $T_b = T - b_5$  and  $T_t = b_5 + b_6 P$ , being  $b_5$  and  $b_6$  two constants.

### Thermal properties

Distinctive thermal properties of thermoplastic materials include melting point  $T_m$ , glass transition temperature  $T_g$ , thermal conductivity  $k$  and specific heat capacity  $c_p$ . As previously stated, crystalline phases in polymers exhibit a sharp melting point at  $T_m$ , in which molecules cease to be ordered, while amorphous phases melt more gradually, going from a rubbery state to a glassy state at  $T_g$ . Thermal conductivity and specific heat capacity are particularly relevant in injection moulding, as they will affect the solidification rates occurring during the process, as they respectively represent the capability of a polymer to conduct heat and the energy required to change the temperature of a unit of mass of material by 1  $K$ : together, they determine the material thermal diffusivity  $\alpha = k/(\rho c_p)$  (being  $\rho$  the density symbol), which is a parameter that indicates how well the material conducts heat rather than storing it. Thermal diffusivity is particularly relevant parameter as it varies less with temperature compared to thermal conductivity, density and specific heat (Zhou, 2013). Another relevant thermal property is the coefficient of thermal expansion of the polymer: however, this parameter is usually embedded in the PVT behaviour of polymers within IM applications, as it actually represents the variations in volume of a mass of material depending on temperature changes.

### 2.1.3 Injection moulding process stages

The injection moulding process includes four main steps: filling, packing, cooling and ejection. The process dynamics can be understood by looking at Figure 2.7, which shows the cavity pressure cycle (measured at the gate, i.e. the point where the molten material enters the part) during injection moulding, whose stages will be described in the following subsections.

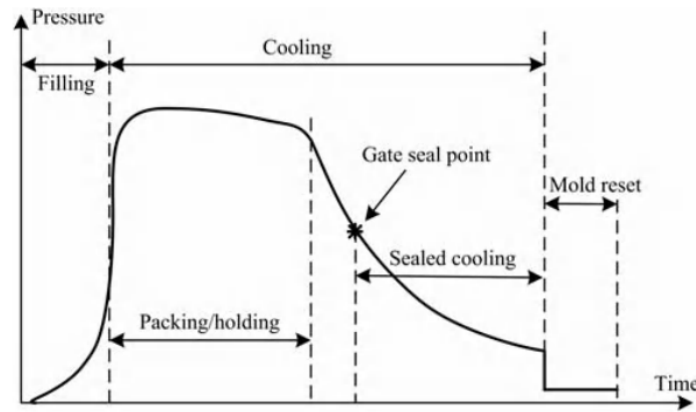


Figure 2.7: Cavity pressure profile at the nozzle during injection moulding (Zhou, 2013)

At the beginning of the process, the mould is closed and the pressure inside the cavity is at ambient level; in the filling phase, the material (i.e. the feedstock) is injected into the mould at a constant velocity and pressure increases as a function of feedstock viscosity, cavity geometry and processing conditions (melt and mould temperature). After this, in the packing (or holding) phase, the rest of injection is based on pressure control, with flow rates varying accordingly. This phase runs simultaneously to the cooling phase and ends with the solidification of the gate (i.e. seal point), after which, the part ends its cooling process and the pressure goes back to ambient levels at mould opening, when the part is ejected from the mould. These phases of the moulding process will be described in this section, with an insight on the main phenomena and the physical laws describing them, which are essential for the understanding and modelling of the IM process.

## **Filling**

As previously stated, the filling stage is a speed-controlled phase, in which the feedstock is injected at a fixed flow rate ( $Q_{Inj}$ ) into the cavity, until the pressure at the nozzle reaches a pre-determined "switch-over" level ( $P_{SO}$ ). In some cases, the switch-over point is based on a prescribed filled cavity volume (in percentage to the total), rather than achieved pressure level.

The filling phase is mainly dominated by shear forces and the feedstock behaves as a viscous fluid flowing in a cavity (Kennedy, 2013): in this stage, it is of uttermost importance to maintain temperature and shear rate levels which can ensure a sufficiently low viscosity to enable full cavity filling. This process window will depend on the selection of main IM parameters, in particular the volumetric flow rate, maximum pressure, mould and melt temperature, and their selection will depend, in turn, on the design of the part to be injected. Mould temperature is a particularly relevant parameter in the case of high surface-to-volume ratio geometries, especially in the IM of components containing micro-features (Lucchetta et al. 2014), to prevent premature feedstock solidification.

Analytical and numerical models have been used to simulate the filling stage since the early seventies (White, 1975) with the aim to predict filling patterns and eventual premature feedstock freezing: however, the joint occurrence of heat and mass transfer phenomena, the non-Newtonian and compressible behaviour of IM feedstocks and the complexity of cavity geometries make this process step extremely challenging to model analytically. For this reason, special-purpose software packages employing the Finite Volume Method (FVM) and Finite Element Method (FEM) are widely employed to simulate this stage of the process, especially in the case of



reference geometries characterised by uneven features, for which simplifications and assumptions of a 2-Dimensions (2D) process cannot be made: these approaches use the equations governing the flow of compressible viscous fluids under transient heat transfer conditions, which are based on the conservation laws of mass, momentum and energy.

The conservation of mass law is based on the fact that the mass  $m$  of a fluid contained in a volume  $V$  without any sources or sinks will not change; hence it will depend on the net flow rate of fluid in that volume. This can be expressed as the so called continuity equation:

$$\frac{\partial \rho}{\partial t} + \nabla \cdot (\rho \mathbf{v}) = 0 \quad (2.16)$$

being  $\rho$  the fluid density (and hence the mass per unit volume) and  $\mathbf{v}$  is the fluid velocity.

The conservation of momentum law states that the rate of change of fluid particle momentum in a volume  $V$  of fluid will equalise the sum of the external forces acting on it.

$$\frac{\partial \rho \mathbf{v}}{\partial t} = -\nabla p - \nabla \cdot \boldsymbol{\tau} + \rho \mathbf{g} \quad (2.17)$$

where  $p$  represents the external pressure,  $\boldsymbol{\tau}$  is the viscous stress tensor and  $\mathbf{g}$  is the gravitational acceleration.

The conservation of energy law describes that the total rate of change in internal energy per unit volume of a fluid equalises the sum of rate of internal energy per unit volume due to thermal energy by conduction, the work done

on the system and the viscous dissipation.

$$\rho c_p \left( \frac{\partial T}{\partial t} + \mathbf{v} \cdot \nabla T \right) = \nabla \cdot (k \nabla T) + \mu \dot{\gamma}^2 \quad (2.18)$$

where  $c_p$  is the specific heat capacity of the fluid,  $k$  is its thermal conductivity,  $\mu$  its viscosity and  $\dot{\gamma}$  is the shear rate.

The three conservation laws, coupled with appropriate pressure, flow rate and thermal boundary conditions constitute the governing equations for modelling the flow of viscous fluids with the main FEV-FEM simulation tools that will be used in the present work.

### Packing

The packing stage starts at the switch-over point, when the flow stops being controlled by an imposed flow rate, whilst a pressure ( $P_{Pack}$ ) is applied to ultimate the cavity filling and to compensate for part shrinkage. The switch-over point can be determined in different ways: in terms of percentage of cavity volume filled or of a maximum pressure level ( $P_{SO}$ ) reached at the sprue location; in the last case,  $P_{SO}$  may be generally higher, lower or equal to  $P_{Pack}$ .

The control of packing pressure is critical in injection moulding and several approaches have been investigated in literature (Greco, 1997; Gao, 1996), since this should be high enough to compress the feedstock and compensate for part shrinkage during solidification, but low enough to prevent overpacking, which determines residual stresses in the component, that eventually lead to warpage as well as issues during ejection, such as part sticking to the mould (Huang, 2007).

During these stages, due to the temperature difference between mould cavity surface and feedstock, the material cools down and starts solidifying, hence there is an overlapping between the packing and cooling phases of IM. Once the material in the gate (i.e. the melt entrance point to the mould) is solidified, the pressure in the cavity will drop and the part continues to cool down and shrink constrained only by the mould cavity geometry. The PVT (and hence the compressible) behaviour of the feedstock, together with the pressure and temperature profiles in the cavity during IM helps understand the effect of packing pressure (Figure 2.8).

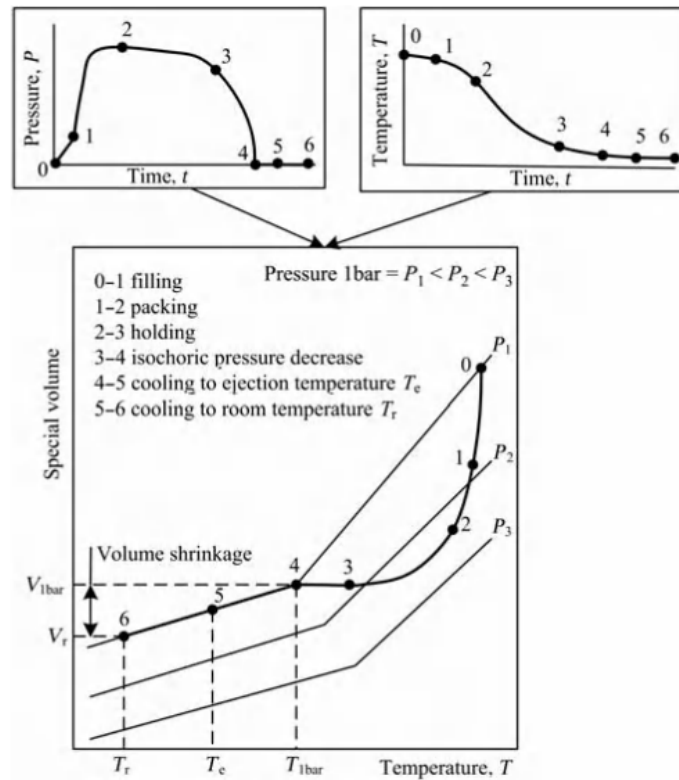


Figure 2.8: Volume shrinkage development during injection moulding (Zhou, 2013)

A premature solidification of the gate would cause Point 4 in Figure 2.8 to correspond to a higher temperature level, thus determining a higher volume shrinkage (difference in specific volume between points 4 and 6).

As with the filling stage, the packing phase has been object of several studies, aiming at modelling the pressure build-up in the cavity (Chung, 1985) and the last stage of mould filling: also in this case, the three conservation laws of mass, momentum and energy govern the heat and mass transfer phenomena occurring during the process and they will be taken as a reference within this work for modelling purposes.

### Cooling

The cooling stage, which, as previously stated, partially overlaps with the packing phase, highly affects the quality of injection moulded parts, and the productivity of the process (Bai, Yin, Fu, and Yang, 2006), being the longest portion of the total IM cycle time. The heat transfer phenomena occurring first of all during the packing and filling stages of the process and then during cooling, highly influence shrinkage and hence the geometrical accuracy of the moulded parts: for these reasons, a good understanding of the in-mould cooling process is vital to adopt solutions for thermal management and control in injection moulding that can be beneficial to the quality of moulded components.

During the cooling stage, heat is transferred from the feedstock to the mould and the part solidifies. Assuming absence of viscous flow and neglecting heat generated within the material, Equation 2.18 can be modified to get the law of heat transfer, used to describe the temperature distribution over time within the mould and the part during the cooling stage of IM:

$$\nabla^2 T = \frac{\rho c_p}{k} \frac{\partial T}{\partial t} \quad (2.19)$$

Heat transfer between the mould and part constitutes, instead, a convection

boundary condition for the system, which can be described by the equation:

$$\dot{q} = h_c(T_{mould} - T_{melt}) \quad (2.20)$$

where  $q$  is the heat flux density [ $\text{W}/\text{m}^{-2}$ ],  $h_c$  is the thermal conductance between the mould and the part, having values ranging between 1000 and 10000  $\text{W}/\text{m}^{-2}\text{K}$  depending on mould surface roughness, feedstock material and processing conditions (Somé et al., 2015),  $T_{mould}$  is the mould temperature at the cavity wall and  $T_{melt}$  is the molten part temperature. The estimation of the thermal contact resistance ( $1/h_c$ ) is one of the main challenges in modelling heat transfer between part and mould and several studies have been carried out to account for this parameter, especially in simulating the cooling of parts with high surface-to-volume ratios (Massé et al., 2004; Somé et al., 2015; Liu and Gehde, 2015): these studies investigate how thermal contact resistance is influenced by mould surface topography, variation of melt temperature and cavity pressure.

After the part has cooled down, it can be safely ejected from the mould: this last step of the process is crucial, as part chipping, breakage and distortion may occur as an effect of too high or unbalanced ejection forces as well as part adhering to the cavity surface.

## 2.2 Ceramic injection moulding

Ceramic injection moulding (CIM) is a particular Powder Injection Moulding (PIM) process to manufacture ceramic components: in this, ceramic powder is mixed with a plastic or wax binder to obtain a viscous blend that will be subjected injection moulding. Subsequently the as-moulded (or green) part undergoes the process steps of firing (or debinding), in which the polymeric binder is thermally or chemically removed, and sintering of the remaining powder, to reach the desired final density. In this section, an

overview of the process steps from feedstock preparation to sintering of the moulded parts will be given, with an insight of state-of-the-art research in the field.

### 2.2.1 Feedstock preparation

The first step in the CIM process chain is feedstock preparation: during this stage, a uniform blend of ceramic powder and polymeric or wax-based binder is created. Highly loaded slurries are usually prepared by milling, in order to guarantee a homogeneous mix of powder throughout the feedstock. Powders employed in CIM can range from submicron particles to large ones of the order of hundreds of microns, and their shape can be from spherical to plate-like, while solid loadings (e.g. amount of powder in the slurry) for injection moulding go from 50% to 75% of the total volume (Liu, 1997).

Although the selection of suitable feedstocks is out of the scope of this work, it is worth highlighting the relevance of this step for the subsequent process stages (Merz et al., 2002): in fact, as it will be explained in Section 2.4, the origin of some defects arising in CIM can be linked to powder morphology and to the rheological properties of the injected material. In particular, the selection of ceramic feedstocks with specific solid loadings (Hidalgo, 2012) and particles with suitable morphology and size have a fundamental role in determining the rheological properties of the feedstock, which are, in turn, of uttermost importance to select IM process parameters, as well as to understand and predict the moulding behaviour and microstructure of moulded parts (Sommer et al., 2014, Mannschatz et al. 2011, Janardhana Reddy, 2000).

Figure 2.9 shows a schematics of different solid loadings (and hence binder

content) levels in ceramic feedstocks which, in turn, influences their rheology and mouldability.

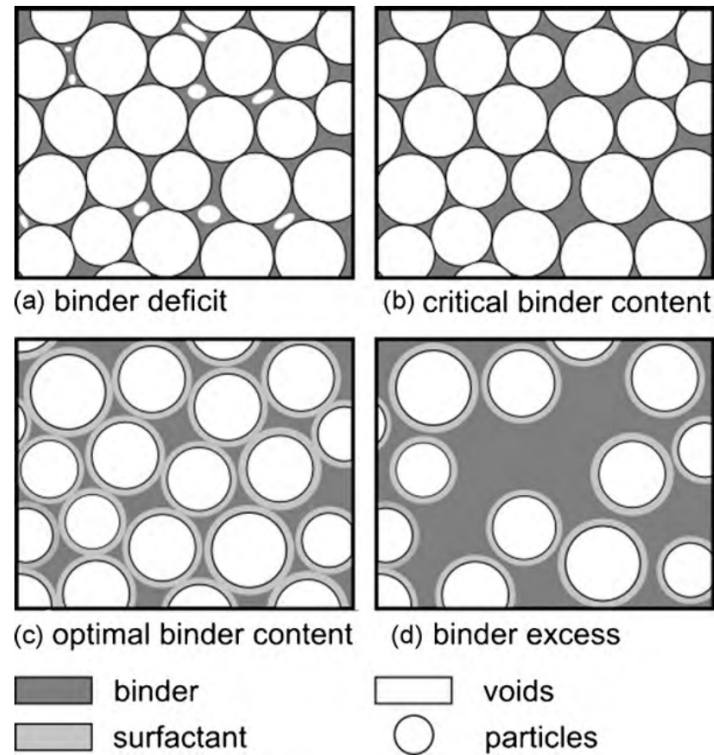


Figure 2.9: Binder content in CIM feedstocks (Mannschatz, 2010)

If the solid loading is too high (Figure 2.9-a), then voids will be formed among powder particles, since the binder will not be enough to fill these areas and particles movement will be hindered. Decreasing solid loading, a critical binder content (Figure 2.9-b) can be reached, where particles are touching each other and the binder content is enough just to fill the empty spaces between them. Also in this second case, the feedstock viscosity will be high, as particles will not be able to move relatively to each other. Slightly increasing binder content, optimal solid loadings can be achieved (Figure 2.9-c). In this case, the binder forms a lubrication coating that covers all the particles which do not touch each other and are, hence, free to slide one relative to the other. However, if the binder content is too high (Figure 2.9-d), powder particles are free to move and rotate, but

the excess in binder will lead to powder-binder separation issues (see Section 2.4.3) and post-debinding defects. It is therefore fundamental to design feedstocks with optimal solid loadings: these need to be enough to ensure green parts to sustain the firing process and, if wanted, achieve high sintered densities; however, critical loadings must not be exceeded to guarantee feedstock viscosities that are sustainable for the IM process.

### 2.2.2 Injection moulding

The injection moulding process step is analogue to that employed in plastic industries. It includes three main steps: filling, packing and cooling, as described in Section 2.1.3.

The presence of powder in the feedstock makes the CIM process more complex than traditional plastic IM, as feedstocks are generally more viscous and cause faster wearing of the mould. Moreover, CIM slurries are characterised by higher thermal conductivities than unfilled polymers, hence causing faster heat transfer and subsequent quicker part solidification, hence reducing feature replication capability. The presence of high and uneven shear rates, depending on the cavity geometry and processing conditions, also determine differential particle distribution in moulded ceramic parts, which, in turn, is the cause of several detrimental defects for these components, as will be explained in Section 2.4.

In order to decrease shear forces during the injection process, subsequently reducing internal residual stresses in green (pre-firing) components and to limit tool wear when using highly abrasive ceramics, lowering the injection pressure is an effective technique, for which the process variant "Low Pressure Ceramic Injection Moulding" (LPCIM) is employed (Loebbecke 2009,



Sardarian, 2017). While in the conventional CIM process pressures over 100 to 200 Bar are operated, these are reduced down to 5 to 50 Bar, together with melt temperatures, which are usually kept below 100°C in the LPCIM case. This choice of process parameters brings about the drawback that feature replication capability is reduced with respect to conventional CIM and, to cope with this, smarter mould temperature control approaches need to be operated, as will be discussed in Section 2.3.

### 2.2.3 Debinding and sintering

After IM, the green (i.e. as-moulded) part is ejected from the mould and is subjected to a debinding process to remove the polymeric binder by either thermal or chemical methods. Often, green parts are placed in a furnace where the temperature is increased up to degradation and then burnout point of the binder components, which is usually in the range between 250 °C and 500 °C (Oliveira, 2005). Thermal debinding is extremely critical in the formation of cracks on moulded ceramic parts a for multiple reasons: first, wrong heating rates may cause component failure when the vaporised binder does not have sufficient time to escape from the component through diffusion mechanisms. Moreover, IM outcomes, such as stresses and microstructural imperfections in the green parts will cause cracking during debinding due to residual stress relief and particle rearrangement occurring upon heating (Evans, 1997). After debinding, the component is either moved or remains in a furnace for the sintering process, in which diffusion mechanisms bring ceramic particles joined together through the formation of so-called "necks" between them (Carter, 2007), with sintering temperature corresponding usually to 80% of the material melting point. Final porosity of sintered ceramic parts can range from less than 1% to over 70%, depending on sintering temperature, particle size, particle content and the

use of sintering aids which can either form a liquid phase that helps neck formation, or decrease the eutectic point and hence the sintering temperature of the powder mixture. Upon sintering, ceramic parts can shrink up to 35% in volume and, as a consequence, also the sintering process can cause or further worsen cracking in moulded ceramic parts due to either temperature and pressure inhomogeneity or non-uniform powder distribution from the previous process steps (i.e. IM and debinding), causing "differential sintering" (and subsequent cracking due to uneven shrinkage) in the component (Oliveira, 2005, Krug, 2002a).

## 2.3 Tooling for injection moulding

Mould (or die) tools play a fundamental role in achieving high quality components in both plastic and ceramic injection moulding (Heaney, 2012) and an understanding of their main components, as well as the state-of-the-art heating and cooling technologies is hence fundamental to implement suitable tool design and thermal control choices, depending of the components to be moulded. In the following, an overview of the principal components and features of injection moulding die-tools will be provided and then a review of state-of-the-art thermal management solution technologies will be reported.

### 2.3.1 Injection moulding die-tools components

Die-tools for plastic and powder injection moulding are typically manufactured with high strength steel, hardened and coated on the surface, in order to improve wear resistance, needed because of the high shear the cavity is subjected to. Mould design is usually characterised by several components, and a schematic of a generic mould configuration is displayed in Figure 2.10. Simplest mould designs are usually constituted by two plates, which are

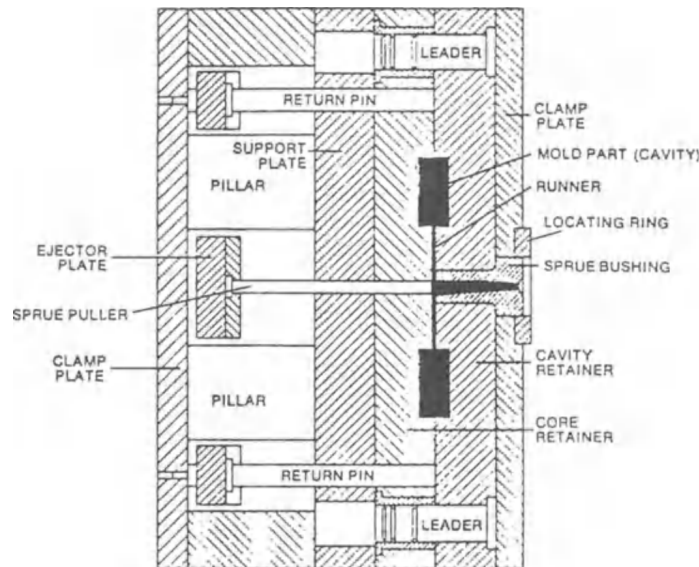


Figure 2.10: Generic mould configuration (Rosato, 2000)

accessed by the feedstock through a sprue; the molten material is then directed towards a runner system that leads it to one or multiple cavities having the negative shape to the geometry of the part to be moulded. The design of mould cavities have significant effects in the replication of part features (Zhang, 2015), as their geometry will determine shear rate levels and solidification rates occurring during the process and mould sprues are often equipped with pressure sensors for process monitoring purposes. Venting channels need also to be included in the mould cavity, to allow for air escape and hence avoiding defects such as air traps, as well as averting back-pressure, which is detrimental for cavity filling. Alternatively, vacuum can be applied to the mould, with appropriate sealing, to let air escape from the cavity. For the part removal from the mould, an ejection system is usually present in industrial die-tools, characterised ejector pins which push the part out of the cavity.

Upon part ejection, lines (or flash) can be present as injection moulding defects that occur when the feedstock enters the gap between the two mould tool halves. They are particular evident if the tool is worn out, which is

a common phenomenon for CIM, since the feedstock is abrasive because of the ceramic powder, or flash can also be formed due to improper alignment of mould tool plates. Although the removal of die lines in injection moulded components is a task that is usually performed after demoulding and in sintered ceramic parts, tooling technologies for flash prevention and in-mould removal exist. Niewels (2005) used active materials, such as piezoceramics, to apply a force against a mould core insert, thus preventing the flash formed between this and the rest of the mould. Hobson (2004) proposed an in-mould trimming system to cut off flash before part ejection. Hurst (1970) and Boenig (1995) presented a solution for in-mould removal of flash based on the use of interlocking systems through undercut features in the mould, to retain flash during part ejection.

Finally, mould tools are also usually equipped with a cooling channel system (water or air-based), in order to ensure rapid component solidification after injection; heating channels or elements can also be employed to raise mould temperature during the injection phase, to keep the feedstock viscosity low enough to ensure complete cavity filling. As the objective of the present work is on the development of novel thermal control techniques for injection moulding die-tools, in the next section, a more in-depth review of state-of-the-art mould heating and cooling technologies will be provided.

### 2.3.2 Mould heating and cooling technologies

The selection of suitable technologies for mould heating and cooling is fundamental in both plastic and ceramic injection moulding and its low pressure (LPCIM) variant. In particular, in components with uneven wall thicknesses, feature replication capability is reduced for thin-walled and micro features (Speranza, Liparoti, Tosello, and Titomanlio, 2017), as they expe-

rience conduction of heat along the thickness direction as a dominant effect over viscous heating and other concurring heat transfer phenomena, potentially causing premature freezing of the feedstock (Yao and Kim, 2004), as shown in Figure 2.11.

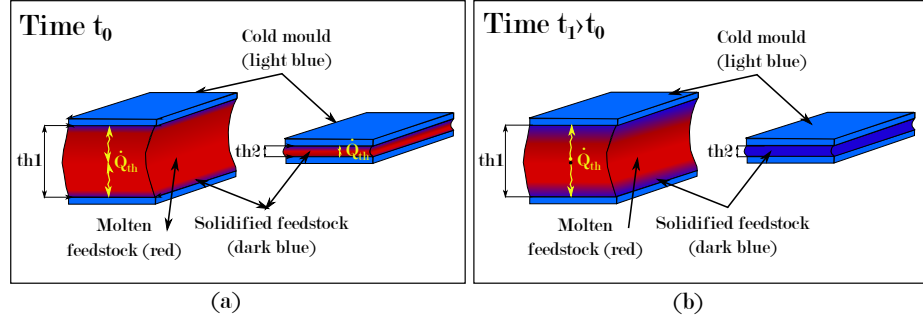


Figure 2.11: Feedstock solidification in cavities of different thickness  $th_1 > th_2$ : (a) instant  $t_0$  in which material enters the cavity; (b) instant  $t_1$ , end of filling

To overcome this problem, mould temperature can be increased above the feedstock glass transition temperature ( $T_g$ ) and then rapidly reduced to achieve part cooling within a required cycle time (Wang and Mao, 2009): a technique usually referred to as Rapid Heat Cycle Moulding (RHCM).

When this technique is employed to mould complex-shaped parts, straight-drilled cooling channels are often not capable to maintain an even mould cavity temperature during the process: therefore, conformal cooling channels to the component shape can be used (Shayfull et al., 2014). These require higher investments for mould manufacturing to guarantee a fast and uniform solidification of the injected components, quickly enough to achieve industry-standard cycle times.

Considering the complexity of both conformal cooling and RHCM approaches from design and control aspects, industrial and scientific efforts have been made to propose novel heating and cooling approaches, improve their per-

formances, and analyse the effects of different heating and cooling elements configurations on the efficiency and effectiveness of the mould thermal systems.

The numerous RHCM methods investigated in literature include both passive (Yao and Kim, 2002) and active approaches, the latter comprising flow of steam and water (Jeng, 2010; Wang, 2014a; 2010), electric (Zhao, 2011, Xiao, 2014a and Wang, 2010; 2013a) and induction (Nian, 2014; 2014; Menotti 2015) heating. An effective combination of conformal channels for steam heating and water cooling, achieved with the introduction of shaped baffles in order to enhance the cooling efficiency through the creation of a turbulent flow, (Figure 2.12), was proposed by Wang et al. (2014a), to be used within automotive applications.

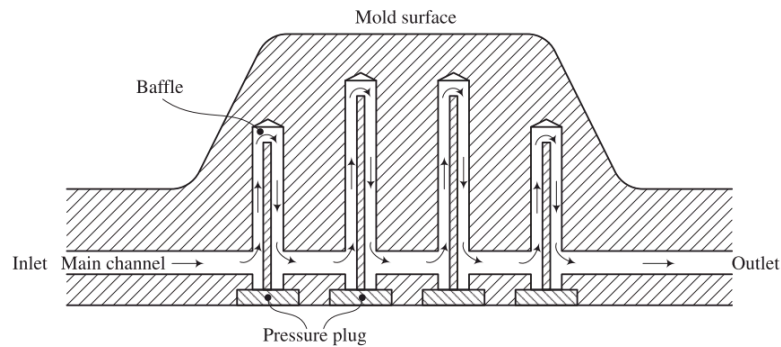


Figure 2.12: Shaped baffles for conformal cooling (Wang, 2014a)

The same researchers also developed a novel electric heating method based on cartridge heaters surrounded by annular gaps with flowing water (Wang, 2014b; 2018), demonstrating a higher energy efficiency of this design concept with respect to other conventionally used electric heating configurations. In another study, Collomb et al. (2017) compared the thermal performance of different geometries for oil circulation channels, to be used for the heating of moulds within composite moulding applications.

Although several studies have been carried out on RHCM for plastic injection moulding (Wang, 2014b, Zhao, 2011), and considerable enhancements in the microstructure and quality of plastic parts have been detected as a consequence (Wang, Zhao, Guan, and Hui, 2015), RHCM has not been studied in the research work regarding CIM.

## 2.4 Outcomes of ceramic injection moulding

The complexity of the phenomena occurring during the CIM process and the inter-dependance between the IM and the subsequent firing stages make the analysis of defect formation a challenging task. For this reason, a thorough understanding of the mechanisms determining different CIM process outcomes is essential to adopt suitable processing conditions and tooling technology to enable prevention of flaws. A review of injection moulding outcomes is then presented: the most critical defects addressed in the present work will be examined in detail, and conducted research for eliminating them will be reported; others will be defined and their causes will be briefly described.

Before going through the description of CIM process outcomes, it is worth reporting the main parameters of the IM stage that influence component quality and that will hence be referred to in the following sections.

### 1. Material parameters:

- Solid loading  $S_l$  [%vol]

### 2. Filling parameters:

- Flow rate  $Q$  [ $cm^3/s$ ]
- Maximum filling (or switch-over) pressure  $P_{SO}$  [Bar]

- Melt temperature  $T_{melt}$  [ $^{\circ}C$ ]
3. Packing parameters:
- Packing pressure  $P_{Pack}$  [Bar]
  - Holding time  $t_{Hold}$  [s]
4. Cooling parameters:
- Cooling time  $t_{Cool}$  [s]
5. Mould parameters:
- Mould temperature  $T_{mould}$ , which can be a temperature cycle  $T_{mould}(t)$  [ $^{\circ}C$ ]

### 2.4.1 Feature replication capability and lack-of-fill

Feature replication capability is a critical outcome from the IM process, as it represents the capacity to fill the mould cavity and hence to actually achieve component manufacturing. Lack-of-fill is therefore an injection moulding defect which consists of an incomplete filling of the cavity and can be due to premature feedstock solidification or excessive pressure drop. These two root causes are inherently linked to each other, as shown in the Hagen-Poiseuille equation, which describes the pressure drop of a Newtonian fluid flowing (in a laminar flow) within a length  $L$  of a duct having hydraulic diameter  $R$ :

$$\Delta P = \frac{8Q\mu L}{\pi R^4} \quad (2.21)$$

Although Equation 2.21 is valid for a Newtonian fluid with constant viscosity  $\mu$ , it is evident that, for a constant channel geometry, a more viscous feedstock will cause a proportionally higher pressure drop than a less viscous one. As, upon cooling, the feedstock viscosity increases, the required pressure to fill the whole channel will raise, hence causing lack-of-fill defects. For



this reason, RHCM is an effective technique to avert these kinds of flaws, by raising mould temperature and maintaining low feedstock viscosity during the filling phase.

### 2.4.2 Weld lines

Weld lines are injection moulding defects that occur when, during filling, two or multiple separate flow fronts merge due to obstacle geometries, such as bosses or holes, to multiple gates or because of articulate filling patterns. Weld lines usually appear as marks on the surface of moulded parts and are regions with reduced strength in the components, due to the merging of solidified flow fronts, usually causing a weaker bonding compared to portions of materials made of a single flow front. Moreover, a V-notch is usually created in correspondence to the merging region of the flow fronts, making weld lines also stress concentration regions, as shown in Figure 2.13.

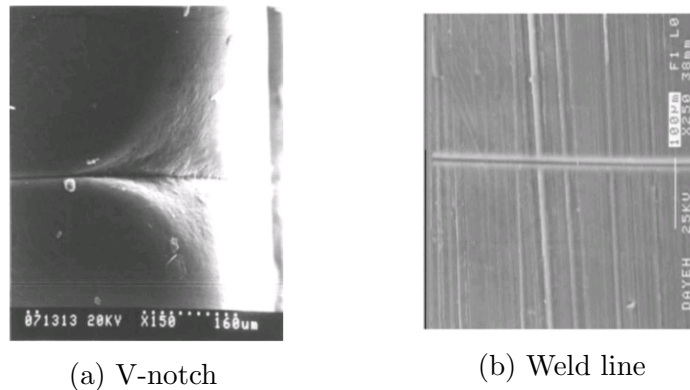


Figure 2.13: SEM micrographs of a V-notch (a) and weld line (b) in a polypropylene specimen (Wu, 2005)

Several studies have been carried out on how weld lines strength is affected by component geometries (Ozcelik, 2012; Xie, 2008; Wu, 2005) and injection moulding parameters (Turng and Kharbas, 2003; Selden, 1997) in the field of plastic injection moulding. Also in this case, mould temperature plays a fundamental role in determining feedstock viscosity and consequent

merging of different flow fronts (Wang, 2013b; Xie, 2009; Chung, 2001). The rapid heat cycle moulding (RHCM) technique has been demonstrated to be effective in the improvement of surface quality of injection moulded plastics and in particular in the reduction or even elimination of weld line marks (Wang et al. 2013a; 2014b; Chen, 2006), due to the high mould temperature kept during the filling stage, which allows the flow fronts to mix before solidification.

In CIM, weld lines may appear as marks on green parts, but their lower strength often leads to detrimental cracks in sintered components: therefore, more than a surface aesthetic issue, the achievement of good merging of multiple flow fronts becomes a structural issue when moulding ceramic parts. For this reason, RHCM has the potential to be an effective approach to enable the manufacture of ceramic components having intricate filling patterns and the lack of studies on its application to CIM calls for research efforts in developing smart mould heating and cooling technologies in this field.

### **2.4.3 Shrinkage-related defects**

Shrinkage naturally occurs in polymeric components during injection moulding upon solidification due to variations in specific volume at the different temperature and pressure conditions. Several defects can arise due to uncontrolled part shrinkage, including sink marks and voids, which are respectively surface depressions and holes inside moulded components and are caused by localised high shrinkage in the central portions of the part: if the outer portions are not fully solidified or stiff, sink marks occur, otherwise, as it happens in the case of large thick moulded parts (Krug, 2002a), voids will appear inside the component. Moreover, when the features of

a moulded part shrink non uniformly, distortion (or warpage) of the component arises. Differential shrinkage can be particularly detrimental for ceramic components, as not only warpage, but also cracks are likely to develop as a consequence of this.

To avert differential shrinkage, design-for-mouldability guidelines are usually followed. Chief among them is the requirement of a uniform cross section thickness for the moulded part, which allows to achieve good component replication and to prevent uneven part shrinkage (Fischer, 2013). Nevertheless, these design rules cannot always be fulfilled when components with fixed functional requirements have to be produced by CIM, as it happens for the manufacturing of ceramic cores to be used in turbine blades for investment casting (discussed in Chapter 1). Consequently, improved flexibility in the process would beneficially increase the types and complexity of parts producible via CIM.

In components having features of uneven thickness, differential shrinkage defects may appear in both as-moulded (green) parts, as well as in those in the final sintered state. These defects mainly arise due to the following two binder and powder related types of phenomena: (i) uneven binder shrinkage during injection moulding, with specific volume changes related to temperature and pressure conditions, as well as to polymer crystallinity and molecular orientation and (ii) non-homogeneous particle packing and orientation, which originate from the injection process and result in differential sintering (Mannschatz, 2011; Zhang, 1996; Wright, 1990). These two categories of phenomena will be discussed in the following.

### 2.4.3.1 Binder shrinkage and residual stresses

The phenomena related to binder shrinkage are analogous to those occurring in the polymer within plastic injection moulding, which have been widely addressed in scientific literature (Pantani, 2015; Zhang, 2015; Guevara-Morales, 2014) and have been discussed in Section 2.1.2. Although the study of these phenomena is outside the scope of this work, they must be taken into account in order to have a clear and broad understanding of shrinkage-related defects in moulded parts, and of how processing parameters, part and mould geometries affect these material properties.

If differential shrinkage is unconstrained, the moulded part will warp, causing errors in dimensional accuracy of the final component; however, during injection moulding, binder shrinkage is often constrained by both mould and (in CIM) by the presence of the ceramic powder, thus causing residual stress development. These can be flow- or thermally-induced, depending on the nature of shrinkage development, as shown in the schematic representations of residual stress formation displayed in Figures 2.14 and 2.15.

From studies on plastic injection moulded components, packing pressure has been found to be the parameter that mostly influences the development of residual stresses, due to the imposed compressive force on the material (Guevara-Morales, 2014): hence, the employment of low holding pressures (or of techniques like LPCIM) is beneficial to limit the development of residual stresses. However, low packing pressures increase part shrinkage, as specified in the previous sections, hence the other process parameters need to be adjusted to balance this effect.

Thermal conditions (i.e. mould and melt temperature) are also relevant

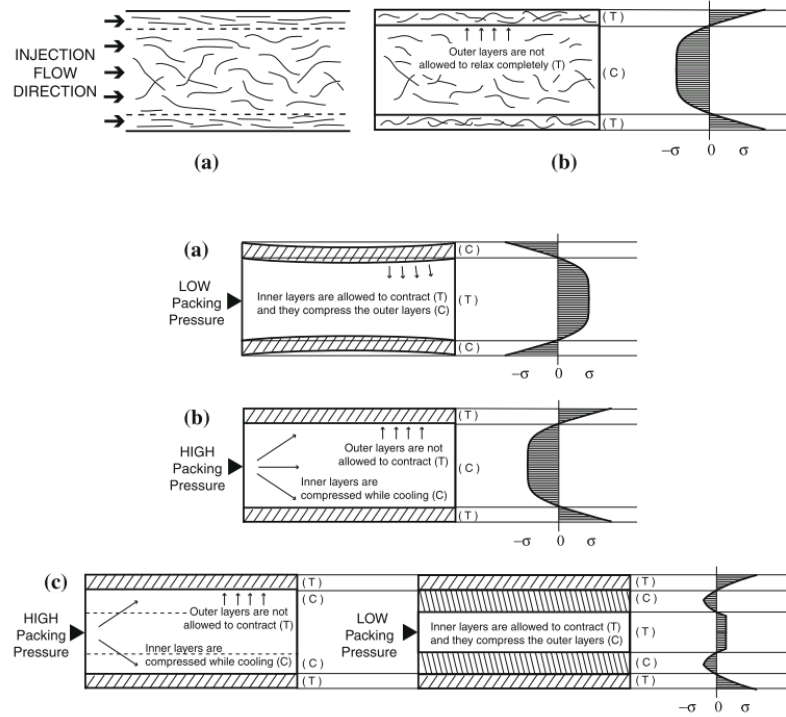


Figure 2.14: Formation of flow-induced residual stresses (Guevara-Morales, 2014)

factors in the formation of stresses, as shown in Figure 2.15, with higher temperatures reducing overall stresses in the polymer (Wang, 2005; Jansen, 1998). Also the effect of the RHCM technique has been analysed in literature of plastic injection moulding (Wang, Zhao, Guan, and Hui, 2015) showing its contribution to the reduction of residual stresses in polypropylene crystalline parts.

In the case of CIM, a few studies on these phenomena related to binder shrinkage and residual stress formation have been carried out. Krug and Evans (2001) studied the effects of moulding conditions on binder crystallinity and morphology using large ceramic blocks, mapping the temperature of different portions of their cross section, thus allowing to correlate results to different cooling rates during the injection moulding process. Results show that mould temperatures and, in particular, cooling rates highly affect the microstructure of green ceramic components: in accordance with

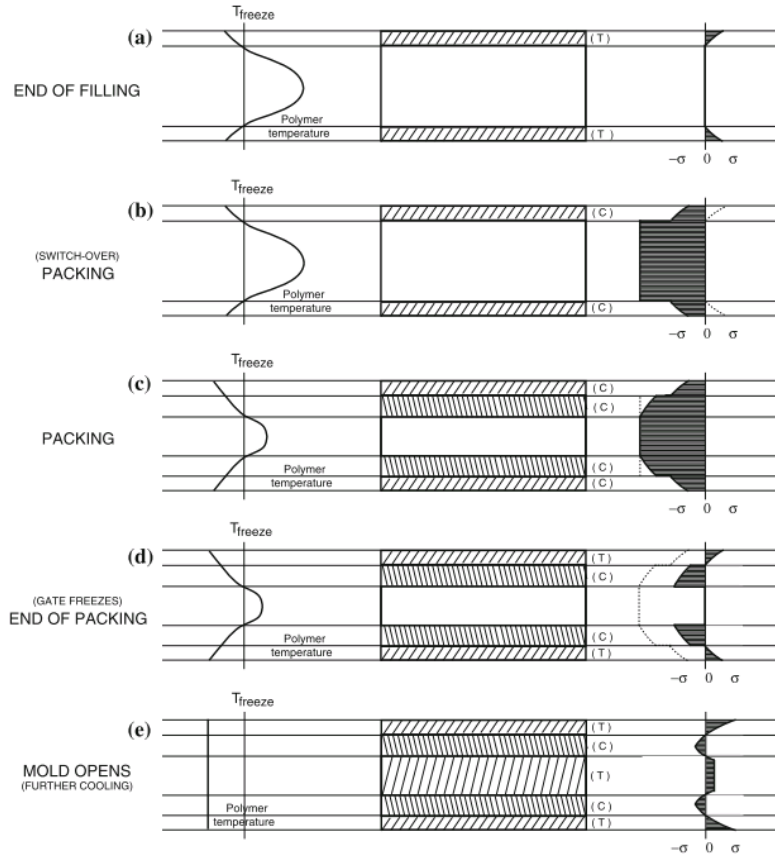


Figure 2.15: Formation of thermal residual stresses (Guevara-Morales, 2014). Left: Temperature profile across part thickness. Centre: Schematics of residual stress sign in across part thickness. Right: Schematics of stress magnitude across part thickness.

studies on polymer injection moulding, they found a skin-core morphology, with the skin layer having highly oriented polymer molecules, increasing at lower mould temperatures and higher cooling rates. The same effect of core layer reduction has been found in parts having thin cross section thicknesses (Giboz, 2007). Kostic et al. (1992) measured residual stresses in ceramic injection moulded components using the layer removal method and correlated stress levels in the component to the holding pressure applied during moulding, showing that, also in ceramic components, low holding pressures reduce stress formation in the centre of the parts.

Considering the influence of processing conditions, several studies focussing on the manufacturing of large ceramic blocks and bars ( $\sim 10-25$  mm thick) have shown that the use of different techniques to prolong sprue solidification time allows components to be injected with reduced shrinkage-related defects as a result of a lower residual stress level. This was achieved also thanks to a controlled particle orientation distribution (Krug, Evans, and Ter Maat, 2002a; Zhang, Evans, and Bevis, 1996; Krug, Evans, and Ter Maat, 2002b). Examples of these techniques include "open-ended" moulding (i.e. having material flowing back and forth between two gates), insulated sprue and low holding pressure moulding.

#### **2.4.3.2 Particle orientation and packing**

CIM feedstocks are highly loaded (usually more than 50% in volume) of ceramic particles, whose distribution, in terms of orientation and packing, is influenced by the injection moulding processing conditions. Elongated particles tend to orient parallel or perpendicular to flow direction depending on shear rate levels during the process. During the cooling phase of injection moulding, and during the debinding and sintering stages, areas of the parts characterised by highly oriented particles, tend to shrink more in

the orthogonal direction to the particles main axis, while randomly oriented regions shrink more uniformly. Moreover, particle content can vary across the component geometry due to shear stresses and rate levels which tend to "push" ceramic powder away from high shear rate level regions, towards areas having lower shear rates. In extreme cases, separation between powder and binder occurs during filling: this causes high shear rate regions, such as corners, to be usually characterised by a higher binder content while particle agglomerates migrate to lower shear zones (Figure 2.16).

Greiner and co-workers (2011) simulated and experimentally validated the

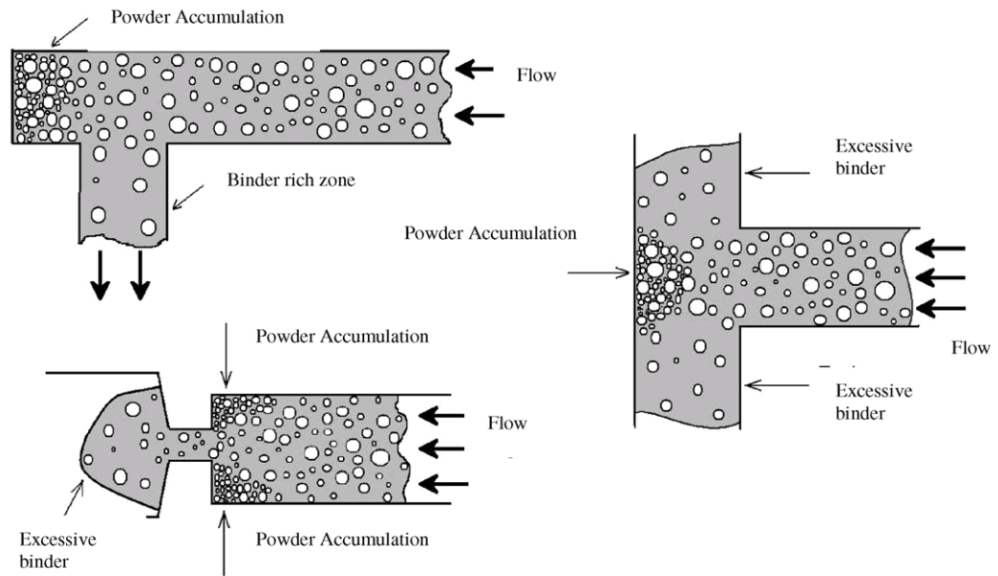


Figure 2.16: Powder-binder separation due to geometrical configurations (German, 1997; Karatas, 2008)

powder-binder segregation in parts with obstacle geometries and different corner convexities and showed that powder tends to concentrate at convex corners, where lower shear rates occur, as displayed in Figure 2.17.

Voids and erosion defects can therefore occur after binder removal in areas of high binder concentration, and differential shrinkage arises during sintering due to the regions with higher particle content shrinking less, resulting in



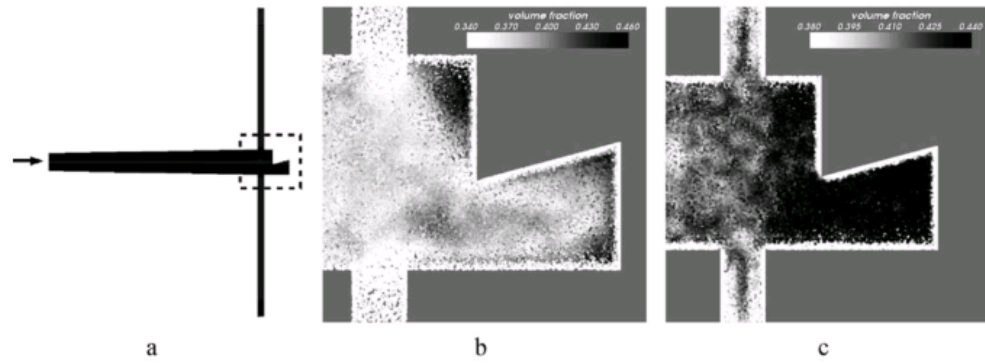


Figure 2.17: Powder distribution in a complex shape with convex and concave shapes (Greiner et al., 2011). (a) Schematics of the part. (b) Particle distribution at early stage of filling. (c) Particle distribution at a later stage of filling.

cracks and deformations in sintered components (Krug et al. 2002a). Therefore, the microstructural phenomena of particle packing and orientation are among the main causes of differential shrinkage in CIM and are outcomes of the injection moulding process stage. Consequently, several studies have been carried out to understand the governing phenomena and how material properties and processing conditions influence them. Powder-binder separation on a two-component gear wheel was observed and analysed by Mannschatz et al. (2010) using an innovative sample preparation technique based on ion beam polishing to perform microstructural analysis of green ceramic injection moulded samples. Oshaka (1995) analysed particle packing on green parts for a feedstock of alumina powder, using polarized light microscopy, focussing more on the method for analysing the part microstructure rather than on the effects of the moulding process on particle packing. Yang et al. (2013) carried out X-ray Computer Tomography (CT) on as-moulded parts to analyse powder-binder separation for feedstocks having different solid loadings. Nevertheless, these studies have been mainly focussed on the understanding of the influence of feedstock properties (e.g. solid loadings and powder morphology) on the microstructure of green parts

rather than exploring how the injection moulding parameters affect powder packing and orientation.

As for the effect of mould temperature and cooling rates on particle packing and orientation, Zhang et al. (1997), studied the alignment of binder molecules and ceramic particles developed during injection moulding of bars: their results show a stratified structure consisting of an outer layer with particles having an increasing degree of orientation (from the external surface to the centre) parallel to the flow and a core layer having preferred orientation perpendicular to the flow direction. Although this work takes into account moulding solidification during the injection moulding cooling phase, it does not consider how varying mould temperature affects parts microstructure.

Mannschatz et al. (2011) showed that anisotropic particles, having platelet shape, cause a non-uniform powder orientation and distribution in the part, which determines high porosity gradients, voids and cracks in the sintered parts.

They show an evolution of defects in ceramic parts occurring throughout the three process stages of injection moulding, debinding and sintering, as shown in Figure 2.18, and explained this evolution in a closed tube shaped moulding.

This worsening of defects has been caused by the orientation of powder particles which determines an anisotropic shrinkage of the part. During filling, as the molten material hits the cold mould, a frozen layer is created, in which ceramic particles in the fluid do not have time to change orientation, and they become, hence, randomly oriented. Inside the cavity, further from the mould wall, particles in the flow front are able to rotate and they orient themselves at a parallel direction to the flow. This differential particle ori-

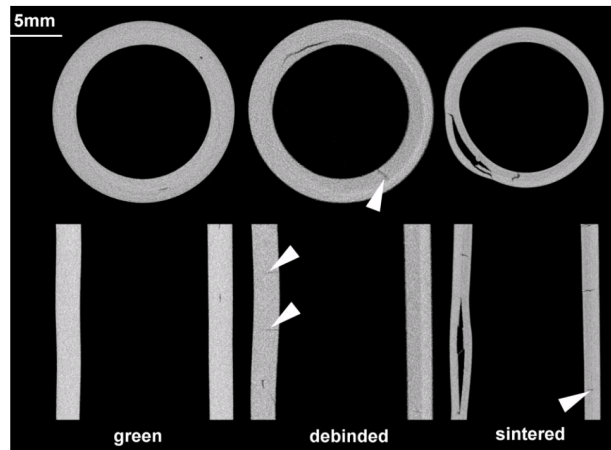


Figure 2.18: Evolution of cracks in ceramic moulded parts from green to sintered state (Mannschatz, 2011). Note: the arrows show cracks and voids observed in the injection moulded parts.

entation across the moulding also causes a higher packing and lower binder content at the mould wall than in the centre of the cavity (Figure 2.19).

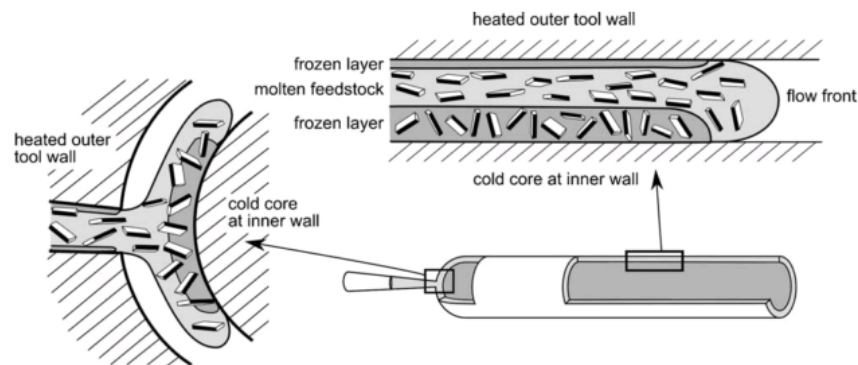


Figure 2.19: Particle orientation in feedstock during filling (Mannschatz, 2011)

This study offers a qualitative explanation of these mechanisms arising during the moulding process, relating flow patterns and non-uniform mould temperature, which cause differential sintering: during debinding, relaxation of residual stress occurs and ceramic particles react with rotation and displacement. The higher amount of binder and more ordered particle orientation of the central part of the mould causes a higher sintering shrinkage

in this area with respect to the mould wall. This phenomenon of *differential sintering* induces residual stresses in the part that degenerate into cracks. This phenomenon has been analysed by Evans (1997), Zhang (1997) and Krug (2002a) in large ceramic mouldings.

Although very interesting, this research scope was mainly focussed to understand how powder morphology affects components microstructure, while the mould temperature, which is an important factor in this process outcome, was not investigated. Moreover, this microstructural study was carried out only on sintered parts, whose structure could change from the green state (Uematsu, 1997).

From the literature it seems that, despite its relevance, mould temperature has not been fully analysed as a parameter affecting particle packing and orientation in components manufactured through CIM. This could be due to the fact that most studies focus on CIM of thick blocks, which can be injected at ambient mould temperature. However, in components with thin or uneven wall thicknesses, as seen before, the RHCM technique can be used to allow for complete cavity filling and, although considerable changes in the microstructure of plastic parts have been detected as a consequence (Wang, Zhao, Guan, and Hui, 2015) of this approach, it has not been studied in the research work regarding CIM.

Considering the current reviewed literature, it can be concluded that there is limited reporting on how different thermal management approaches for mould temperature control affect the microstructural phenomena of particle orientation and packing and subsequent part shrinkage. In particular, this research topic could be regarded as a key enabler for the implementation of RHCM in CIM of components with uneven wall thickness. This will

ultimately enhance the process flexibility and capability to injection mould ceramic parts of increasing complexity.

#### 2.4.4 Demoulding issues

Relevant issues in injection moulding occur during the demoulding stage of the process, as the green part has to be ejected from the mould without compromising its integrity: this is often a challenge, as part-mould interaction at the end of cooling can cause parts chipping or cracks during ejection.

The principal interactions causing demoulding issues are related to wear of mould ejection system components, or to adhesion between part and mould. The first cause is often solvable with proper selection and maintenance of mould components, and several mould design solutions have been adopted to solve demoulding issues. Michaeli and Gärtner (2006) proposed different ejection methods without movable pins or plates: demoulding with ultrasonics, with vacuum and cavity retreat (i.e. cavity opening with sliding inserts) and demonstrated that, among them, cavity retreat was the only successful solution for safe part ejection.

Adhesion between part and mould can be due to several mechanisms (De-laney, 2012b): thermodynamic or chemical affinity of part and mould materials, electrostatic adhesion, capillary attraction (related to moisture trapped into the surface micro-roughness), and mechanical interlocking (friction) between part and mould.

Thermodynamic, chemical and electrical affinity between part and mould should be in the first place avoided by choosing suitable mould materials and coatings, while some examples of solutions for reducing the capillary effects

are available in the literature. Wetttable coatings have been used by Worgull (2008), who performed demoulding experiments with and without a release agent and showed a decrease in static friction coefficient of about 30%. Neto et al. (2009) presented some preliminary results on the application of polycrystalline diamond coatings on steel mould inserts: they showed potential improvements on heat dissipation, but further studies are needed to demonstrate the employability of these coatings for reduce capillary effects factor between part and mould. Navabpour (2006) tested magnetron-sputtered coatings in moulds for LDPE. All the tried coatings resulted in reduced adhesion between part and mould.

Mechanical interlocking is a particularly challenging phenomenon to control, as it is not only related to mould roughness, but also to in-mould part shrinkage, (which can be constrained by cavity features, e.g. bosses for moulding holes, or protrusions in the cavity), and to processing conditions.

On this regard, studies have been conducted on the influence of injection moulding process parameters on ejection forces. Fu (2006) carried out research on micro-metal injection moulding of microstructures and showed that a critical material demoulding temperature existed, depending on the holding pressure, at which demoulding forces are set at minimum level. Worgull (2008) analysed the effects of moulding temperature and pressure on demoulding forces also in microstructure manufacturing, this time with plastic hot embossing. They found that a higher melt temperature cause an increment in demoulding forces and explained that the hotter and less viscous plastic fills the mould micro-roughness.

Considering the reviewed literature, it is clear that mould temperature plays a role in the easiness of part ejection, and hence mould-part adhesion needs

to be taken into account when developing novel thermal control systems for injection moulding die-tools. In CIM, as the green part strength is often lower than in conventional plastic moulded components, cracking during demoulding is a critical issue. Since limited work has been done on developing heating and cooling approaches for these applications, there is little understanding of how mould temperature and, in particular, the RHCM approach affects ejection forces in CIM.

## 2.5 Injection moulding process modelling

The IM process entails large financial investments for die-tools: predicting the outcomes of the IM process is therefore of uttermost importance in order to ensure the suitable design and development of both parts and moulds. For this reason, efforts in modelling the IM process and subsequent part quality outcomes have been made using different simulation methods and tools since the early seventies (Kamal and Kenig, 1972). Two-dimensional (2D) models, using a Hele-Shaw flow formulation, were developed and implemented (Holm and Langtangen, 1999), with the geometry related thin wall limitations brought by the approach. This cannot predict abrupt changes of part thickness and complex flow behaviours giving rise to weld line phenomena (Fernandes 2016). For the simulation of complex three-dimensional (3D) flows, and the subsequent prediction of outcomes, such as shrinkage and residual stresses, Finite Element and Finite Volume methods are normally used (Hassan, 2010, Zheng 1999, Pontes 2000). Special-purpose software packages (e.g. Autodesk Moldflow and Moldex3D) are based on these methods and are of widespread use for industrial and academic purposes to simulate the IM process of complex components, from the filling to the cooling stage (Ozcelik , 2009; Nikolic, 2014; Nian, 2015; Babenko, 2018), and have been validated to accurately simulate the IM process, as well as

its quality outcomes.

General-purpose Finite Element (FE) software packages, especially ABAQUS and ANSYS, have been instead widely used to simulate the cooling phase of the IM process for the prediction of part solidification and the efficiency of IM thermal systems (Park, 2010; Wang, 2011; Xiao, 2014b). In this respect, since the main objective of the present work is to develop a novel thermal control system for CIM, a more in-depth review of thermal control models and optimisation methods used for the performance assessment of IM die-tools is present in the following section.

### **2.5.1 Thermal control models and optimisation for injection moulding die-tools**

In the previous sections, a review of state-of-the-art mould heating and cooling technologies has been provided; moreover, a survey of the current literature on the effects of processing conditions and, in particular, of mould temperature and of the RHCM technique on the quality of ceramic moulded components has been presented. This collection of studies reported in Section 2.3.2 is focussed on evaluating, by experiments and often numerical simulations, the thermal response of different proposed systems, measuring their effectiveness based on their efficiency in heating and cooling within targeted cycle times and in ensuring temperature uniformity throughout the mould cavity. Some of these studies also take into account other performance parameters, in particular the residual stresses in the mould due to differential thermal expansion, and evidence of part quality improvement from the employment of the different RHCM techniques has been also provided, especially in terms of surface integrity (related to glossiness and visibility of weld lines) and hardness (Wang et al. 2013b; 2013a; 2013c).



However, the optimisation methods followed in these studies are generally based on trial-and-error-approaches, while more structured methods would be more flexible and robust in being applicable to a wider range of problems and component geometries. In this respect, work has been done to optimise heating/cooling elements configurations and subsequently mould temperatures, using different methods. Dang and Park (2011) proposed a mould with milled conformal cooling channels and presented an optimisation methodology for their design, in order to minimise non-uniformity in temperature throughout the mould cavity surface. Another algorithm for design automation of conformal cooling channels for moulding different complex geometries was presented by Wang et al. (2011).

A novel approach, based on a heat conduction inverse problem was proposed by Agazzi and co-workers (2013), who showed a method of thermal optimisation that firstly calculates the optimal mould temperature distribution for a given cavity geometry and, only after, optimises cooling channel geometries to provide a mould temperature distribution similar to the optimal. This method targets cycle time efficiency and cavity temperature homogeneity. Metaheuristics optimisation has also been used to optimise the design of heating and cooling channels: Wang (2011), Xiao (2014b) and co-workers optimised the layout of steam heating/cooling channels and electric heater locations respectively, using coupled Particle Swarm Optimisation (PSO) and Finite Element Method (FEM) to minimise cycle time with constraints on maximum temperature difference and Von Mises stresses in the moulded part. Global optimisation methods, such as PSO or Genetic Algorithms (GA), are particularly useful in such complex design problems, with unknown cost functions and with a large search space; moreover, compared to other approaches, such as the GA, PSO has been proven to converge more quickly to the optimal solution (Suresh, 2007; Wang, 2011; Xiao 2014b),

which is of high importance to allow for reasonable computation time when solving problems whose solution needs to be calculated through FEM.

Despite the relevance of these pieces of work in developing effective and efficient heating and cooling methods, the reviewed studies mainly focus on the injection moulding of plastic components following design-for-mouldability guidelines imposing constant wall thickness. On the other hand, looking at the injection of geometrically complex ceramic parts, having features of uneven thickness, and especially when employing the Low Pressure Ceramic Injection Moulding (LPCIM) variant, two main limitations can be found in the analysed literature.

The first aspect is linked to the fact that state-of-the art studies base the heating/cooling system optimisation on cavity temperature uniformity, which may not be a suitable approach in the case of components having features with different surface-to-volume ratios, and hence dissimilar solidification rates, for which tailored thermal control approaches need to be developed. Local mould heating and cooling methods has been proposed in previous research, firstly by Kim and Wadhwa (1987), who presented the idea of a novel low-thermal-inertia mould, containing thermoelectric modules to enable the local heating and cooling of the cavity: the study proved the use of Peltier technologies for the thermal control of injection moulds, but did not propose any temperature optimisation strategy. An approach based on regional temperature control, applied to polymer IM, has been presented by Nian et al. (2015): this method successfully reduces temperature-induced part warpage by taking into account how the component will deform at different cross sections, based on their neutral axis (Figure 2.20). However, the study does not present any specific algorithm for the determination of the optimal local temperatures and does not con-

sider a RHCM approach, which is necessary in order to achieve complete filling of components having thin features through LPCIM.

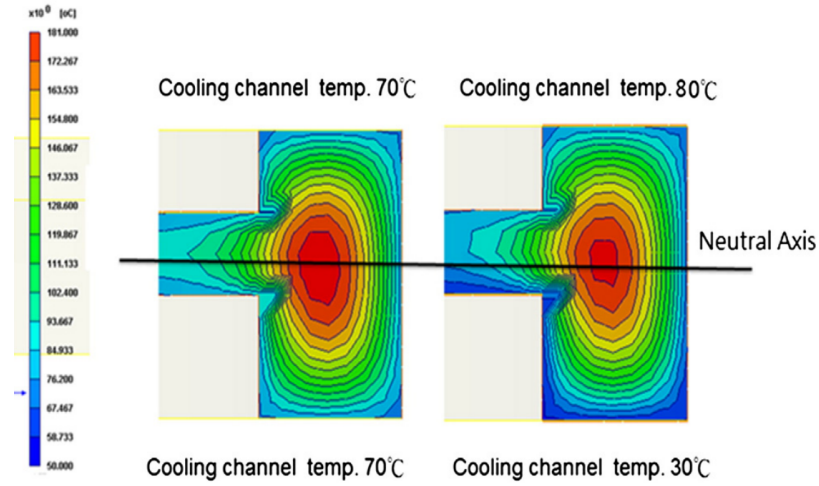


Figure 2.20: Temperature distribution in a cross section of a case study component, with two temperature profiles, with respect to the neutral axis of the part (Nian, 2015).

The second limitation relates to the analyses on the effects of the proposed systems on parts quality, as they have been mainly restricted to surface appearance and to macroscopic defects, such as sink marks and warpage (Wang, 2013c). Some microstructural analyses have been performed on both unfilled and fibre-filled polymers, to correlate the effect of RHCM on tensile and impact strength to weld line morphology and fibre orientation at merging flow-front locations (Wang et al. 2013b). On the other hand, as reported in the previous sections, when injecting ceramic feedstocks, complex microstructural phenomena such as particle packing and orientation, which are influenced by mould temperature (Bianchi et al., 2019), arise in addition to other mechanisms occurring in polymer moulding, such as process-induced residual stresses, complex crystallisation kinetics and differential binder molecular morphology: the combination of these phenomena cause defects and adverse microstructures in green parts, which often result in detrimental cracking after debinding and sintering. This brings about

further challenges when injecting components having uneven wall thickness with LPCIM. Despite the relevance of these phenomena, not only coupled conformal cooling and RHCM have not been employed in literature regarding CIM, but also no study accounted for the effects of optimised heating and cooling conditions on moulded ceramic components.

In light of this, it seems that current literature presents strong limitations in developing optimal heating and cooling systems for the injection moulding of components having uneven wall thickness, both because of the lack of optimisation strategies that take into account uneven cooling rates in the part and for restricted understanding on how different approaches affect components quality.

## **2.6 Summary of the literature**

A comprehensive review of the literature regarding the plastic and ceramic injection moulding processes, their quality outcomes, as well as of state-of-the-art thermal control systems and optimisation approaches has been presented. First, an introduction to the injection moulding process has been provided, with a description of industrial IM machines (Section 2.1.1), and an in-depth review of injection moulding material properties (Section 2.1.2) has been presented, together with a description of the main process stages and their physical governing equations (Section 2.1.3). Subsequently, the CIM process has been introduced, with a description of the feedstock preparation (Section 2.2.1), injection moulding (Section 2.2.2), debinding and sintering stages (Section 2.2.3). Having gained a theoretical understanding of IM and CIM, in Section 2.3 a description of injection moulding die-tools has been presented, with a preliminary focus on main die-tool components (Section 2.3.1) and then an in-depth review of state-of-the-art mould heat-

ing and cooling technologies (Section 2.3.2). Subsequently, in Section 2.4 a thorough description of the quality outcomes and their links to the injection moulding (and especially CIM) process have been provided, as well as an overview of how manufacturing conditions influence these quality issues and defects, with a special focus on mould temperature effects. The discussed outcomes include feature replication capability (Section 2.4.1), weld lines (Section 2.4.2), shrinkage-related defects (Section 2.4.3) and demoulding issues (Section 2.4.4). In this section, a comprehensive literature survey has been provided on the main studies performed to enhance the theoretical understanding of both the physical phenomena affecting the quality of plastic and ceramic parts manufactured by IM, and of the influence of processing conditions on the process outcomes. The focus has then been shifted to a survey of IM process modelling (Section 2.5), with particular attention to mould thermal control modelling and optimisation approaches for the management of the presented thermal systems (Section 2.5.1).

From the provided theoretical framework and literature survey, the complex nature of the CIM process has been highlighted, in terms of the strong inter-relationship among the different stages of IM, debinding and sintering, and of the feedstock behaviour, which not only presents the criticalities of semi-crystalline polymers, but also brings about challenges related to particle orientation and packing. These aspects make the CIM process difficult to analyse and to isolate the influence of the IM stage on final sintered component outcomes. A methodology that enables these kind of studies is hence strongly needed to allow for progress to be made on CIM process conditions and related tooling technologies. Moreover, considering state-of-the-art mould heating and cooling approaches, especially Rapid Heat Cycle Moulding (RHCM), studies have been mainly limited to their application to plastic IM: this means that there is a knowledge gap on how these tech-

niques affect the quality of ceramic moulded parts. This understanding is fundamental to operate these approaches to ceramic moulding and to ultimately develop novel thermal control systems for die-tools that can help to improve CIM process capability. On this regard, if relevant applications are taken into account, such as the manufacturing of investment casting cores, a need emerges for heating and cooling technologies that enhance the capability to inject components characterised by features having uneven wall thickness. In fact, in the plastic industry, part design is usually adapted to design-for-mouldability guidelines that include the need for a homogeneous thickness of the moulded parts: therefore, state-of-the-art heating and cooling technology designs and control models and optimisation strategies aim at achieving a uniform mould cavity temperature. This represents a strong limitation to the application of currently available thermal management approaches to the moulding of complex components having uneven feature thicknesses, such as ceramic cores. Consequently, this brings the need to develop thermal control systems and models for mould temperature optimisation, which can be fully tailored to components characterised by uneven wall thickness. Finally, unlike current design and control models, which are usually validated based on enhancements in feature replication capability and in macroscopic defects (e.g. sink marks and warpage), in the case of CIM, novel designs need to be verified based also on the microstructural integrity of injected components.

The present work aims to address the research challenges emerging from the summarised literature, for which a summary is provided in the following section, to give a starting point for the modelling and experimental work that will be described in the subsequent chapters of the present thesis.

## 2.7 Research challenges from Literature Review

Considering the reviewed literature, some crucial elements emerge which are worthy of consideration to extend the capability of manufacturing complex ceramic components through injection moulding. These can be identified by focussing, in particular, on the interconnected and complementary aspects of (i) the relationship between the injection moulding process and sintered parts quality, (ii) the effect of state-of-the art thermal control approaches on the quality and integrity of green injection moulded ceramic parts and (iii) novel tooling technologies and mould thermal control approaches and models. In light of this, the present work intends to address these aspects by facing the identified gaps in current literature that are presented in the following sections.

### 2.7.1 Research challenges – Methodology for the evaluation of thermal systems performances in CIM

The quality of sintered ceramic injection moulded parts depends on the outcomes from all the interdependent CIM process stages of injection moulding, debinding and sintering. In order to develop mould tooling technologies that enhance the quality of moulded components, the influence of the IM process stage on final quality outcomes needs to be therefore understood: this requires an analysis methodology that allows to isolate the effect of IM conditions on the CIM process outcomes.

- Temperatures and shear rates developing in the part during the injection moulding process cannot be experimentally measured and hence need to be numerically predicted. Therefore, a model of the injection moulding process that is capable of capturing the effects of different

thermal control approaches on the filling behaviour needs to be developed.

- The proposed methodology must directly relate quality outcomes on the moulded parts to the IM process. To achieve this, the quality of sintered components needs to be linked to moulding processing conditions, despite the firing and sintering stages highly affect the microstructure of moulded parts.

### **2.7.2 Research challenges – Effect of RHCM on outcomes of CIM**

Heat transfer phenomena strongly affect the injection moulding process, as temperature variations influence feedstock viscosity and cooling rates, which will ultimately affect final part quality. In order to pursue suitable thermal control strategies and develop effective novel die-tools for the injection moulding of complex ceramic components, a thorough understanding on how currently available thermal control approaches and subsequent heat transfer phenomena influence macro- and micro-structural properties of injection moulded parts is needed.

- The Rapid Heat Cycle Moulding (RHCM) approach has never been applied to CIM, despite its widespread success in plastic injection moulding and its high potential in ceramic applications, especially when using the Low Pressure Ceramic Injection Moulding (LPCIM) technique. A need, therefore, exists, of validating this thermal control approach to the manufacturing of ceramic components by injection moulding.
- Particle packing and orientation are two microstructural outcomes which derive from shear rates developing during injection moulding,



which are, in turn, influenced by heat transfer throughout the process. The phenomena of particle orientation and packing are key to final part quality, as they are among the main causes of differential sintering defects. However, the influence of mould temperature on them has not been fully addressed in current literature, especially regarding novel thermal control approaches, such as RHCM.

- Adhesion between mould and part is a critical issue and is highly affected by temperature cycles during injection moulding. However, as advanced thermal control techniques, such as RHCM, have not been applied to CIM, there is limited understanding on their effect on the demoulding process. It is therefore of uttermost importance to understand how RHCM affects adhesion during part ejection, to be able to adopt current and novel thermal control approaches and prevent issues during the demoulding of ceramic components.

### **2.7.3 Research challenges – Novel thermal system and control optimisation for CIM die-tools**

Thermal control approaches play a fundamental role to ensure the manufacturing of defect-free components through injection moulding, while keeping suitable process cycle times. For the manufacturing of complex components characterised by features having uneven wall thickness by CIM and, in particular, using the LPCIM variant, the development of tailored thermal control systems and model is required.

- State-of-the-art mould heating and cooling technologies are usually based on the RHCM technique and conformal cooling channels and hence involve the employment of tools having a system of heating elements and cooling channels, which quickly and uniformly heat and

cool mould cavity. These designs may not be suitable for components having non-uniform wall thickness, thus requiring local heating and cooling. Die-tools having independent and regionally controllable heating and cooling elements hence need to be designed and developed.

- While strong research efforts have been focussing on the development of novel thermal control models and optimisation methods for mould heating and cooling, these are mainly based on the achievement of a uniform cavity temperature. On the other hand, to manufacture components having features with different surface-to-volume-ratios via LPCIM, optimisation models that minimise differential cooling rates during part solidification are required.
- The validation of the effectiveness of novel thermal control approaches and optimisation methods requires the analysis of their effect on the quality of injection moulded parts, which has been usually only restricted to surface quality and part warpage. However, as optimisation methods for mould heating and cooling have not been employed in CIM applications, their effect on ceramic parts microstructure is yet to be investigated.

#### **2.7.4 Industrial challenges – Application of novel thermal control models and optimisation to generic complex ceramic components**

Once regional thermal control systems and optimisation methods are developed and validated for CIM, strong efforts need to be placed to bring these novel technologies and approaches from laboratory to industrial applications.

- Models and optimisation methods need to be adapted to generic complex geometries and, if necessary, further simplifications and assumptions have to be considered, without compromising the success in the employment of the developed techniques.
- The design of mould tools with regional heating and cooling to be used within industrial injection moulding machines brings about the need to consider and design further mould tool components, such as ejection and runner systems, which need to be integrated with the novel design solutions.
- Further complications in the development of industrial die-tools with novel thermal control approaches need to be considered. These are related to the need for design solutions that account for more challenging structural conditions (e.g. higher clamping forces and pressures with prolonged operations and thermal cycles) that the equipment needs to withstand.

# Chapter 3

## Methodology

*This chapter outlines and discusses the adopted methodology to develop the novel thermal control system for injection moulding die-tools. As the followed research approach relies on the employment of experimental equipment, including injection moulding test rigs, machines, materials and characterisation techniques, these will be introduced. Finally, the main modelling and simulation tools used in the present thesis will be described.*

### 3.1 Introduction

The development of a novel thermal control system for injection moulding die-tools requires a research methodology to be outlined and followed (Figure 3.1). From the gaps in the reviewed literature, a need emerges for developing, first of all, a strategy to relate the quality of sintered parts to the injection moulding process step: for the development of this strategy, the selection of injection moulding feedstock materials has been a fundamental step, and details of the employed materials will be firstly provided in the following section.

This will allow to develop an understanding of how thermal control ap-

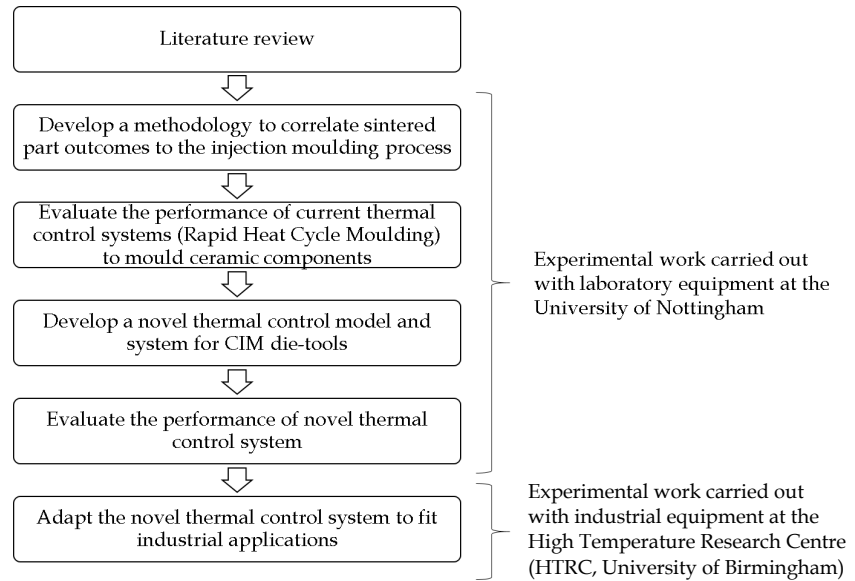


Figure 3.1: Flow diagram defining the main steps involved in the presented research.

proaches currently employed in plastic injection moulding (in particular, Rapid Heat Cycle Moulding) perform in ceramic applications. Then, the novel thermal system can be designed and validated as a proof of concept, and its performances can be evaluated for the injection moulding of ceramic components.

Then, the achievement of these goals calls for the realisation of several bespoke test moulds, whose design and development may be challenging and expensive for industrial injection moulding machines: this led to the decision of performing the main tests of the present work at the University of Nottingham, using an experimental apparatus which replicates a plunger-type injection moulding machine. The laboratory equipment employed in this project, including rig design, instrumentation and control tools, as well as the moulds used throughout the present work, will be described in Section 3.3.1.

Industrial equipment will instead be employed for the final step of this

work, for the adaptation of the developed system to fit industrial applications. This will be done through the validation of the performed models (Chapter 7) with a material used for the manufacturing of ceramic cores, and through the design and development of an industrial prototype of the developed system. The used injection moulding machine and die-tools used for this work will be presented in this chapter (Section 3.3.2), followed by a description of the analysis and characterisation techniques and equipment used throughout this study (Section 3.4). Finally, the modelling methods and tools employed in the present PhD work will be presented (Section 3.5).

## 3.2 Materials used in the study

The correlation between the quality of sintered ceramic moulded parts and the injection process is challenging, as the debinding and sintering steps affect components microstructure. For this reason, as it will be more thoroughly described in Chapter 4, preliminary tests were carried out with a wax feedstock, before the main trials and analyses were performed on the ceramic feedstock used in this study. The two materials used in the present work will be described in this section, with details of their relevant properties.

### 3.2.1 Wax feedstock

A readily commercially available investment casting wax feedstock (FR60, from Blayson Olefines Ltd), was used for the preliminary tests, consisting of a blend of paraffin and micro-crystalline wax ( $C_nH_{2n+2}$ ), and an approximately 30% volumetric content of cross-linked polystyrene ( $(C_8H_8)_n$ ) spherical fillers, having a 30 to 50  $\mu\text{m}$  diameter (Figure 3.2).

The melting point of the wax is 62 °C, its specific heat (at 25° C) is 4000

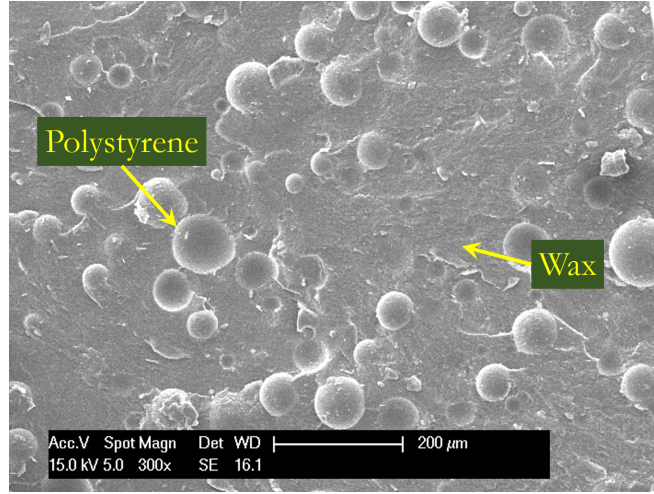


Figure 3.2: SEM micrograph of fracture surface for the wax feedstock.

$J/(Kg \cdot K)$  and its thermal conductivity  $0.17 W/(m \cdot K)$ . This feedstock exhibits a pseudoplastic behaviour, with a sharp reduction in viscosity at the melting point, due to its semi-crystalline nature, which also determines a large variation of specific volume corresponding to the glass transition temperature. An approximation of the viscosity and PVT behaviour of this material, based on suppliers data and on a wax reference feedstock from the standard material library of Moldex3D, is shown in Figure 3.3.

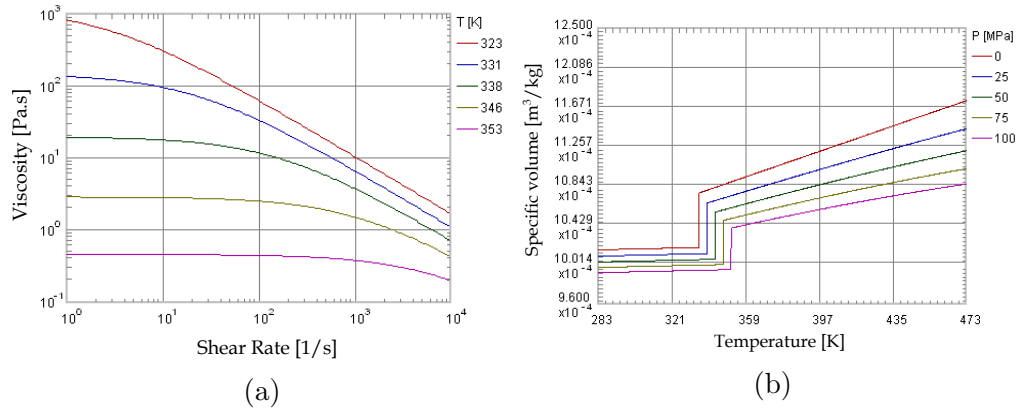


Figure 3.3: Material properties of the wax feedstock. (a) Viscosity behaviour. (b) PVT behaviour.

A Cross-Exp model was used to describe the wax viscosity as a function of

shear rate and temperature (Nikolic, Randelovic, and Milutinovic, 2014):

$$\mu = \frac{\mu_0}{1 + \left(\frac{\mu_0 \dot{\gamma}}{\tau^*}\right)^{1-n}} \quad (3.1)$$

$$\mu_0 = B \exp\left(\frac{T}{T_0}\right) \quad (3.2)$$

where  $\mu_0$  is the zero shear rate viscosity [Pa.s],  $\dot{\gamma}$  is the shear rate [1/sec],  $T$  is the temperature [K],  $T_0$  is a reference temperature [K],  $\tau^*$  is the critical shear stress at the Newtonian plateau [Pa] and  $n$  is the power-law index. To describe the PVT behaviour, a modified Tait model (1888) was instead used:

$$v = v_0 \left[1 - C \left(1 + \frac{P}{D}\right)\right] + v_t \quad (3.3)$$

$$v_0 = \begin{cases} b_{1S} + b_{2S}T^*, & \text{if } T \leq T_t \\ b_{1L} + b_{2L}T^*, & \text{if } T > T_t \end{cases}$$

$$D = \begin{cases} b_{3S} \exp(-b_{4S}T^*), & \text{if } T \leq T_t \\ b_{3L} \exp(-b_{4L}T^*), & \text{if } T > T_t \end{cases}$$

$$v_t = \begin{cases} b_7 \exp(b_8 T^* - b_9 P), & \text{if } T \leq T_t \\ 0, & \text{if } T > T_t \end{cases}$$

$$T_t = b_5 + b_6 P$$

$$T^* = T - b_5$$

where  $P$  is the pressure [Pa],  $v_0$ ,  $B$  and  $v_t$  are piecewise functions for which different sub-functions apply depending on whether the feedstock temper-



ature is above or below the material  $T_g$  (i.e. the  $b_5$  constant in the model) and  $C$  is the universal Tait constant.

### 3.2.2 Ceramic feedstocks

The main ceramic feedstock used in the present work consists of a mixture of silica ( $SiO_2$ ) and zircon ( $ZrSiO_4$ ), both having elongated particles and being 80% and 20% of the powder volume respectively, within an organic binder containing a blend of paraffin wax and ethylene-vinyl acetate (EVA). The binder composition (and subsequently its rheological, PVT and thermal properties) is very similar to the already described FR60 wax, and a micrograph representing the ceramic feedstock structure and composition is shown in Figure 3.4.

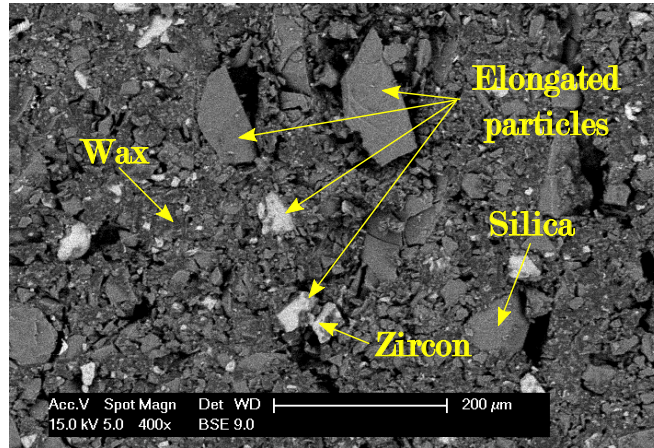


Figure 3.4: SEM micrograph of fracture surface for the ceramic feedstock.

The feedstock has a volumetric solid loading of 70% ( $\approx 85\%$  in weight), with ceramic platelets having a heterogeneous particle size distribution (Table 3.1) ranging from sub-micron particles, up to  $200\ \mu\text{m}$  in the long axis direction. The material has its glass transition temperature ( $T_g$ ) at  $45^\circ\text{C}$  and melting point at  $62.5^\circ\text{C}$ , while its specific heat and thermal conductivity (at  $25^\circ\text{C}$ ) are  $1200\ \text{J}/(\text{Kg}\cdot\text{K})$  and  $0.7\ \text{W}/(\text{m}\cdot\text{K})$ .

Despite the similarities between the binder of this feedstock and the FR60

Table 3.1: Particle size distribution for the analysed ceramic feedstock

Cumulated distribution [Volume%]	Particle size [ $\mu m$ ]
10	4.5
50	45.5
90	72

wax, the ceramic material is characterised by a lower heat capacity and higher thermal conductivity due to the presence of the ceramic powder; moreover, the material exhibits a higher viscosity and lower specific volume than the wax, as shown in Figure 3.5, obtained by fitting experimental data, provided by the supplier. Also for the ceramic feedstock the Cross-Exp model (Equation 3.2) and the modified Tait model (Equation 3.3) were used to describe material viscosity and PVT behaviour. It is worth noting that the spike present at the solid-liquid transition in the PVT curve (Figure 3.5b) is a discontinuity due to the use of a Tait model, characterised by a piecewise function (Wang et al. 2019).

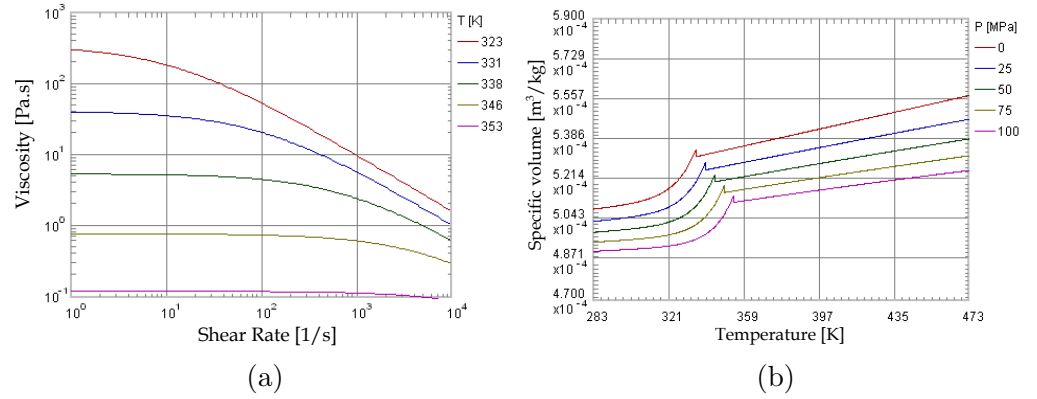


Figure 3.5: Material properties of the ceramic feedstock. (a) Viscosity behaviour. (b) PVT behaviour.

A second ceramic feedstock, employed in the production of industrial cores for aeroengine turbine blades, was used in the present work: this contains the same mix of powder of the just described ceramic formulation, but a

slightly different, more viscous binder. Detailed properties of the industrial feedstock cannot be provided in the present thesis due to confidentiality reasons.

### 3.3 Injection moulding equipment

In this section, the laboratory and industrial injection moulding equipment used in this work will be described. This include a test rig, used to replicate an actual machine in a laboratory environment and an industrial injection moulding machine; several mould tools were also employed for different investigations carried out throughout this PhD work. These will be briefly introduced in this section, while details on their design and characteristics will be provided in the following chapters, where the work related to them will be described and discussed.

#### 3.3.1 Laboratory equipment

As stated in Section 3.1, an experimental apparatus was built in order to achieve the step-wise validation of the novel developed thermal control system for CIM die-tools in a laboratory environment. This will be described in the following sections.

##### 3.3.1.1 Description of the injection moulding test rig

The test rig (Figure 6.4), which replicates a plunger-type injection moulding machine used in production environments for Low-Pressure Ceramic Injection Moulding (LPCIM), was originally supplied by the industrial partner Rolls-Royce plc.

From the original design, the metallic frame and the actuation system, which was a double acting pneumatic cylinder (SMC, 50 mm Bore, 80 mm Stroke,

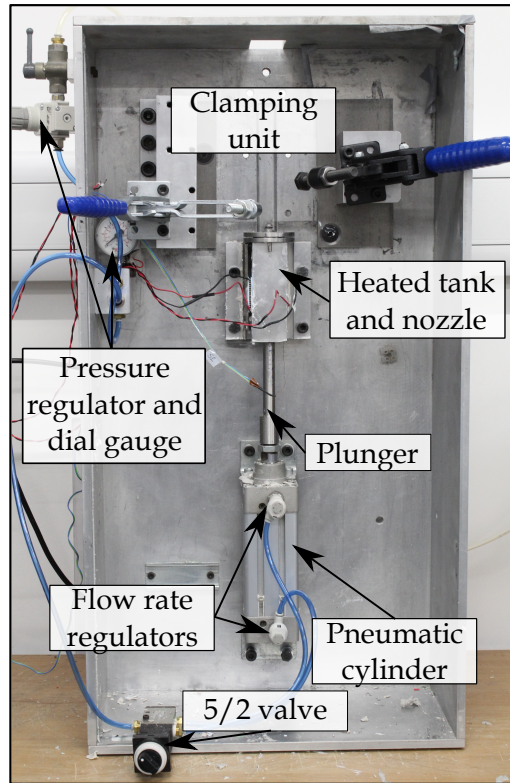


Figure 3.6: Test rig used for injection moulding experiments.

CP95 Series) were kept, while the rest was readapted to fit the needs of the work to be carried out during the PhD project.

The pneumatic cylinder, having a maximum operating pressure of 10 Bar, pushed the feedstock from an aluminium tank to the mould cavity through a nozzle. The aluminium tank (Figure 3.7) was heated up with two closed-loop controlled thermoelectric (Peltier) modules, whose working principle will be discussed in Section 3.3.1.2, to maintain a constant melt temperature.

The nozzle (Figure 3.8) was manufactured in stainless steel, in order to have a material that was more resistant to wear, due to higher shear rates occurring in this component. Housings for o-rings, designed following the BS ISO 3601-2:2016 Standard, were needed in order to prevent leakage of the molten feedstock during injection at high pressure. For the same reason,

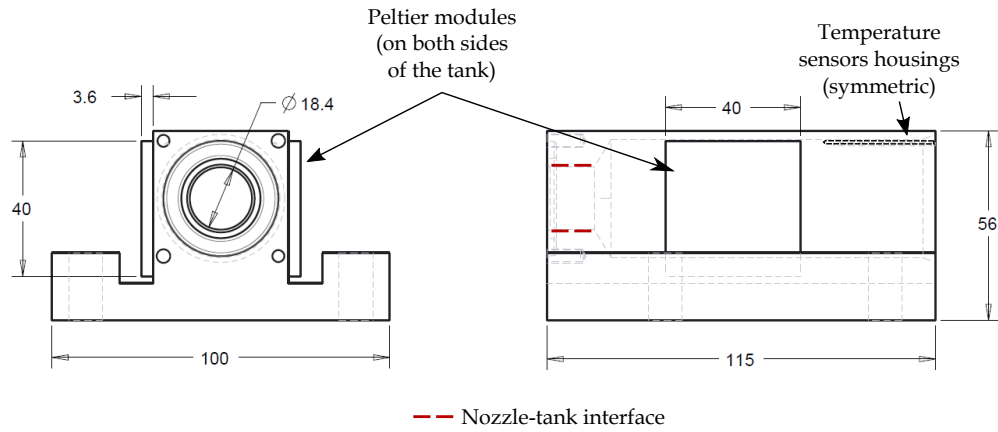


Figure 3.7: Heated aluminium tank: main dimensions and locations of Peltier modules and temperature sensors.

part of the nozzle was designed to fit into the front part of the heated tank, which is displayed in Figures 3.7-3.8 as "Nozzle-tank interface".

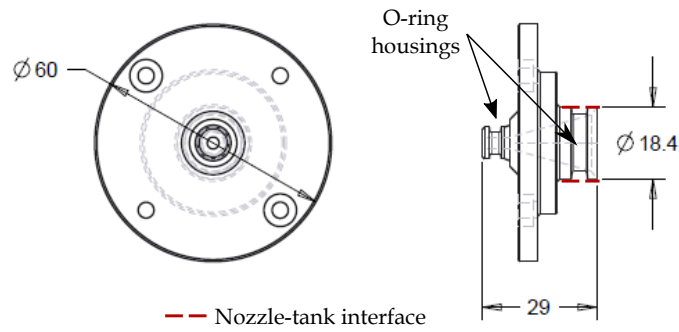


Figure 3.8: Nozzle: main dimensions and o-rings housings.

Flow rate was controlled by two regulators, while the injection pressure was measured and adjusted through a gauge and regulator (RS Pro 8327493); a 5/2 valve was instead used to actuate the cylinder for injection and retraction from the mould (the pneumatic system is illustrated in the schematic diagram in Figure 3.9). Toggle clamps, providing a total force of 11 kN, were used to hold the mould in place during injection, in order to prevent leakage and flash. The required clamping force was calculated from the surface area of the mould cavities to be used and from the maximum injection pressure of the pneumatic cylinder, using appropriate safety coefficients.

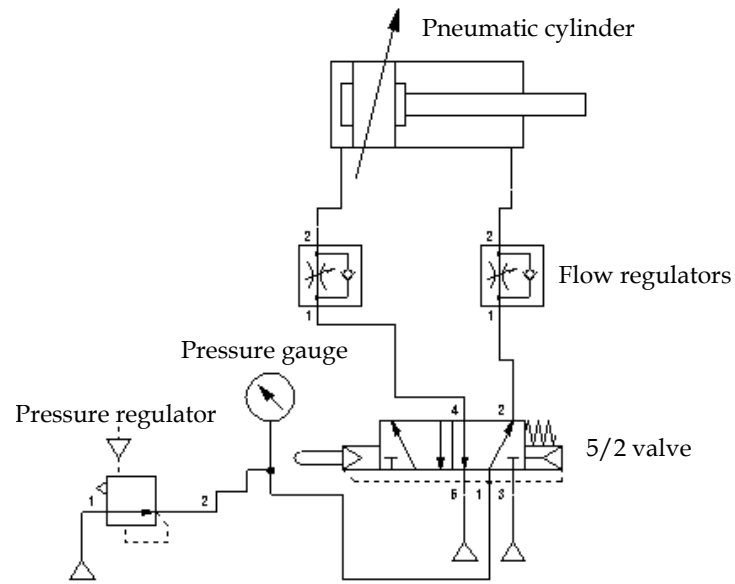


Figure 3.9: Schematic diagram of the pneumatic system employed in the laboratory rig.

While in this chapter a description was provided of the main components of the developed test rig, detailed drawings of the assembly and of its main components can be found in the Appendix of this thesis.

### 3.3.1.2 Description of temperature control equipment

All the heating and cooling performed for the moulds employed throughout this research work (which will be described later in this section), and for the feedstock heating inside the aluminium tank, were achieved by the use of thermoelectric (Peltier) modules (Figure 3.10).

These are solid-state elements that can be used for both heating or cooling and are constituted by a number of thermocouples, made by two different semiconductors (N- and P-type thermoelements), which are electrically connected in series and thermally in parallel, having two ceramic plates on their opposite sides. These thermocouples operate according to the Peltier

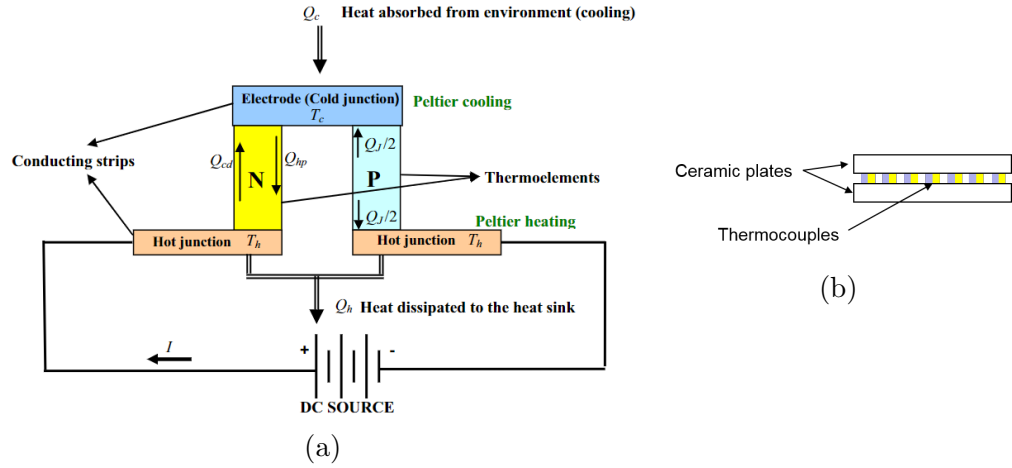


Figure 3.10: Schematics of thermoelectric modules. (a) Working principle of a single thermocouple (Enescu and Virjoghe, 2014). (b) Schematic representation of a whole thermoelectric module.

effect, by transferring heat from one side of their surface to the opposite (i.e. from one ceramic plate to the other) when a voltage is applied at their junction (Zhao and Tan, 2014). If voltage polarity is swapped, the direction of heat transfer is inverted accordingly: hence, thermoelectric modules have the advantage of being usable for heating or cooling without changing their physical configuration, and by only reversing the current direction. The cooling power of a Peltier module will depend on the thermoelectric properties of the thermocouples, on their number (which will be an indicator of the surface area of the module), on the electric current applied, on the temperature of the hot side and on the temperature difference between the hot and cold junctions. Heating power depends on the same parameters, but is usually higher than the cooling one, due to the resistive heating. Heat dissipation from the hot side of Peltier modules is fundamental in order to avoid overheating of the thermocouples, so, in the design of a thermoelectric assembly, the choice of appropriate heatsinks having suitable heat capacities is fundamental. When using the same module for both cooling and heating of a target, it is relevant to take into account that this will have the role of "heat source" during cooling and of heat sink during heating, hence

its thermal diffusivity ( $k/\rho c_p$ , where  $k$  is the thermal conductivity,  $\rho$  the density and  $c_p$  the specific heat) should be high enough to allow for heat dissipation, but sufficiently low to allow for the target to be heated with the available Peltier power.

For the heating of the aluminium tank, a TEC1-12706 Peltier module was used, with the following properties:

- Surface area: 40 mm x 40 mm
- Max. current 6.4 A
- Max. voltage 15.4 V
- Max. power 57 W
- Max. temperature difference between the two parallel faces 75° C
- Max. operating temperature 138° C

Details on the thermoelectric modules used for heating and cooling of the different moulds used throughout this work will be provided in the following chapters, together with the descriptions of the moulds.

### **3.3.1.3 Description of the developed moulds used with the laboratory rig**

Different moulds were used throughout the development and validation process of the novel thermal control system, which will be described in detail in the following chapters. In the following, a brief description of the different moulds used with the described test rig will be provided (summarised in Table 3.2), with an insight on the terminology that will be used in the present work to nominate them. For simplicity, illustrations of only the bottom



cavity plates and of the Peltier modules will be provided, while more details on the moulds designs will be given in the relevant chapters where the moulds are used. The followed methodology for which the different mould tools have been conceived and designed will be also explained in this section.

Table 3.2: Summary of the moulds designed for the laboratory rig throughout this PhD work.

<b>Mould name</b>	<b>Thermal control</b>	<b>Feedstock</b>	<b>Purpose of the mould</b>	<b>Related Chapter</b>
Cross-channels mould	No thermal control	Wax	Validate the filling model on wax.	Ch. 4
Parallel channels mould	Isothermal, RHCM	Wax; Ceramic	Validate the filling model on wax and ceramic feedstock. Analyse the effect of RHCM on particle orientation and packing.	Ch. 4-5
Adhesion test mould	Isothermal, RHCM	Ceramic	Understand the effect of RHCM on part-mould adhesion during ejection.	Ch. 5
Regional controlled mould	Isothermal, RHCM,  Regional	Ceramic	Validate the thermal control model and optimisation.  Assess the outcomes of the novel developed thermal control approach on the quality of injection moulded parts.	Ch. 6

The first mould (Figure 3.11) was employed in order to get a preliminary validation for a model of the injection moulding filling stage.

As will be explained in Chapter 4, this was performed using the wax feed-

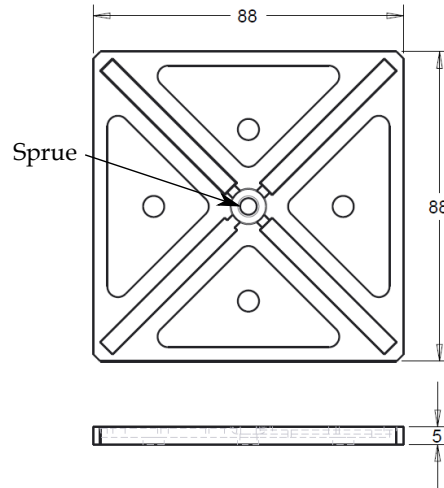


Figure 3.11: Cross-channels mould: main dimensions.

stock, on a test geometry consisting of four channels in a cross configuration. In order to obtain more complex flow patterns, a second mould (Figure 3.12) was designed and manufactured with four channels, having the same geometries of those of the first mould, but placed in a parallel configuration, next to each other.

In this way, it was possible to connect the channels through bridges, which could be blocked, if desired. Moreover, the mould could be equipped with a Peltier module and a thermocouple, to provide heating and cooling and hence to validate the filling simulation not only at ambient mould temperature, but also using the Rapid Heat Cycle Moulding (RHCM) approach. The same mould was also used to obtain test pieces for the analysis of the effect of RHCM on particle packing and orientation. In order to study how adhesion is influenced by the RHCM approach, a third mould was designed (Figure 3.13, assembly and main components drawings can be found in the Appendix), having a disc-shaped cavity and instrumented with a Peltier module, a thermistor and a load cell, in order to control mould temperature and measure ejection force (details on the methodology employed for these tests will be provided in Chapter 5).

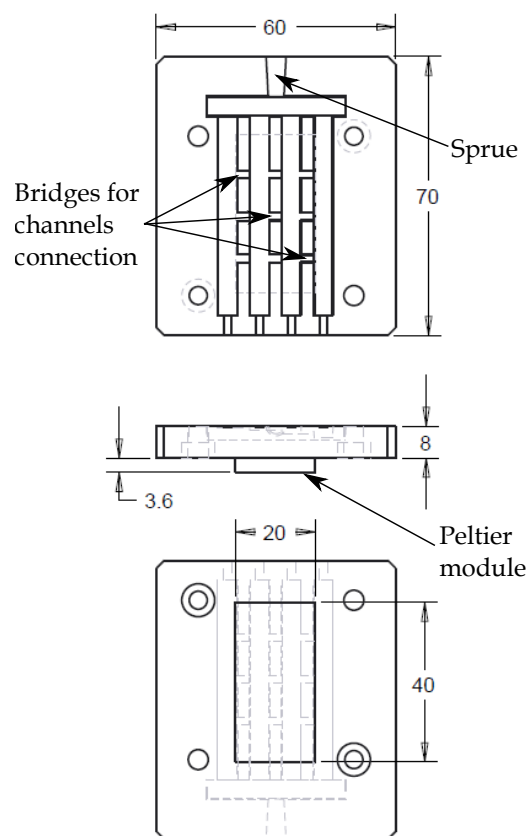


Figure 3.12: Parallel channels mould: main dimensions of mould and Peltier module.

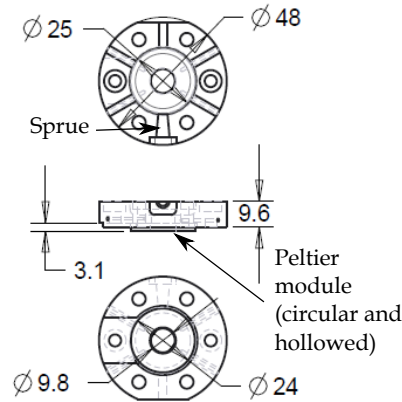


Figure 3.13: Adhesion tests mould: main dimensions of mould and Peltier module.

Having gained an understanding of the effect of RHCM on both the microstructure and adhesion behaviour of ceramic moulded parts, the final mould, with a regional thermal management system was designed (Figure 3.14, assembly and main components drawings can be found in the Appendix). This die-tool was instrumented with multiple Peltier modules and thermistors, in order to provide tailored temperature control to different features of the injected components, based on a developed thermal control model and temperature optimisation (Section 3.5.1).

The mould was then used to validate this model and to study the effect of the newly developed regional thermal control system upon the quality and integrity of ceramic moulded parts, in comparison to both an isothermal approach (i.e. using constant, ambient temperature) and RHCM.

#### 3.3.1.4 Injection moulding process parameters

As the present work focusses on the development of mould thermal control systems, the main parameter varied in the performed tests was die-tool temperature. The selection of the other parameter values was based either

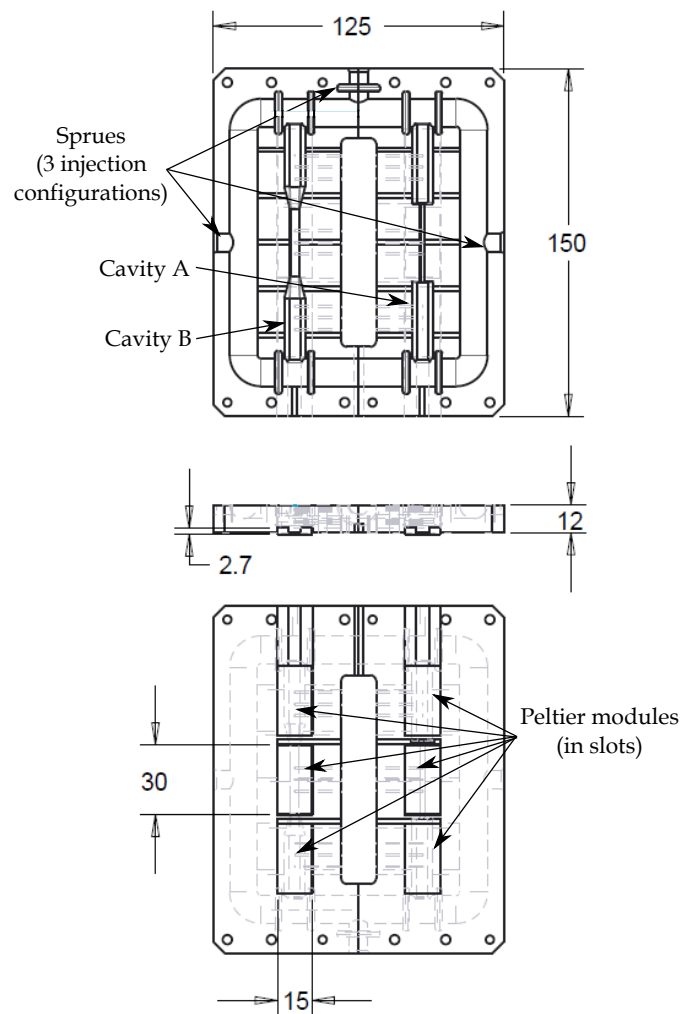


Figure 3.14: Regional controlled mould: main dimensions of mould and Peltier modules.

on feedstock suppliers recommendations or on preliminary tests.

- **Melt temperature** was selected based on feedstock supplier recommendations. For the wax feedstock, three different temperatures were used (65 °C, 70 °C and 75 °C) while it was kept constant at 75 °C for the ceramic one.
- **Flow rate and injection pressure.** Industrial injection moulding machines work with two distinct phases: the filling stage, in which the material is injected at a constant flow rate and an accordingly increasing pressure, and a packing phase, with a controlled pressure and a consequent variable flow rate level. Unlike these machine, the employed test rig was actuated by a pressure-controlled pneumatic cylinder: therefore, neglecting the initial piston acceleration, for the whole injection, the pressure level was fixed and the flow rate varied accordingly (based on the viscosity properties of the material and on the mould geometry). The employed pressure was set up based on short-shot preliminary tests with the different moulds: the objective of these tests was to select the minimum needed pressure to fill the cavity using ambient mould temperature. When changing mould temperature control approach, pressure levels were, generally, kept constant, unless excessive flash was created, in which case, the pressure level was reduced. In this way, it was possible to actually compare the feature replication capability obtained using each distinct mould thermal control approach. Although the pressure level was readable from the employed gauge in the rig, the actual pressure at the nozzle was lower, due to the drop caused by the material viscosity (Figure 3.15). To assess the entity of this pressure drop, this was estimated due to

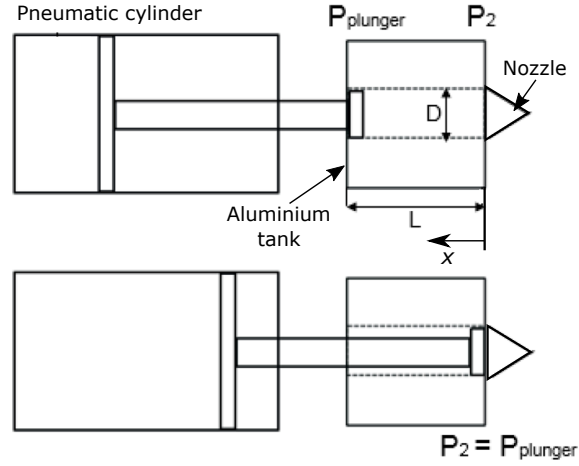


Figure 3.15: Schematic diagram of the effect of pneumatic cylinder movement on the pressure drop across the aluminium tank.

the Hagen-Poiseuille equation:

$$\Delta P(x) = P_{plunger} - P_2(x) = \frac{Q8\mu x}{\pi R^4} \quad (3.4)$$

where  $P_{plunger}$  is the pressure exerted by the pneumatic cylinder,  $P_2(x)$  is the pressure at the end of the aluminium block,  $R$  is the tank internal radius ( $D/2$ ),  $x$  — varying from  $L$  to  $0$  — is the distance from the plunger to the end of the aluminium tank and  $\mu$  is the wax viscosity.

The flow rate level was instead measured by filming the piston movement with a camera having a speed of 60 frames per second. The average piston speed was taken into account to calculate flow rate as  $Q = vA$ , where  $v$  is the linear speed of the plunger and the area  $A$  was calculated from the aluminium tank cross section.

- **Holding time.** A constant holding time was employed for all the tests with the same moulds. The holding time was calculated based on the required solidification time of the thickest features in the moulds, in order to guarantee that any lack of packing was due to premature

freezing of portions of the part closer to the gate, rather than for an insufficient packing time.

Details on the levels for the different parameters employed in each test will be specified within the relevant chapters.

### 3.3.2 Industrial equipment

Industrial injection moulding equipment was also employed, in order to validate the developed models with production materials, and taken as a case study to design an industrial prototype of the mould with novel thermal control system. In particular, an MPI SA56-25-24 injection moulding machine, usually employed for wax IM, located at the University of Birmingham High Temperature Research Centre (HTRC) was employed for the injection moulding experiments (Figure 3.16).



Figure 3.16: Picture of the injection moulding machine used in the conducted experiments.

The machine was used with a clamping force of 100 kN, filling-to-packing switchover point based on a threshold hydraulic pressure (calibrated to the nozzle pressure level), and the fixed process parameters (i.e. melt temperature, flow rate, packing pressure and clamping force) were monitored with



sensors embedded in the machine. Details on the processing conditions used in these tests will be provided in Chapter 7.

Two moulds were designed and manufactured to be employed with this injection moulding machine: the first one (Figure 3.17) was used to validate the developed models with a production material, and did not have any heating or cooling approach implemented, other than the water channels available in the bolster (i.e. the mould base)

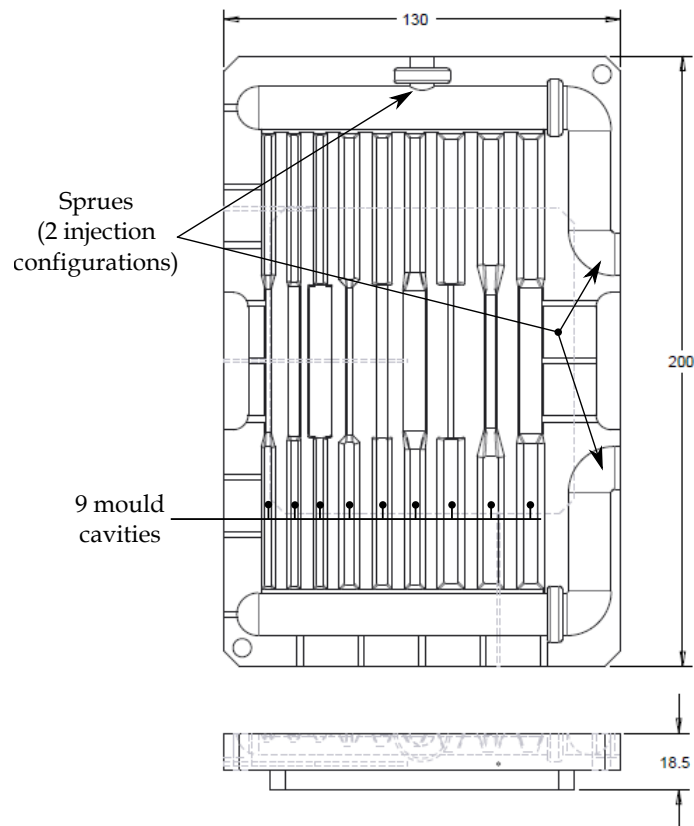


Figure 3.17: Regional controlled mould (industrial): main dimensions of mould and Peltier modules.

The second mould (Figure 3.18) was instead a larger version of the regional controlled mould (Figure 3.14) adapted to the industrial injection moulding machine, and hence was equipped with Peltier modules and thermistors, to achieve a regional, closed loop temperature control.

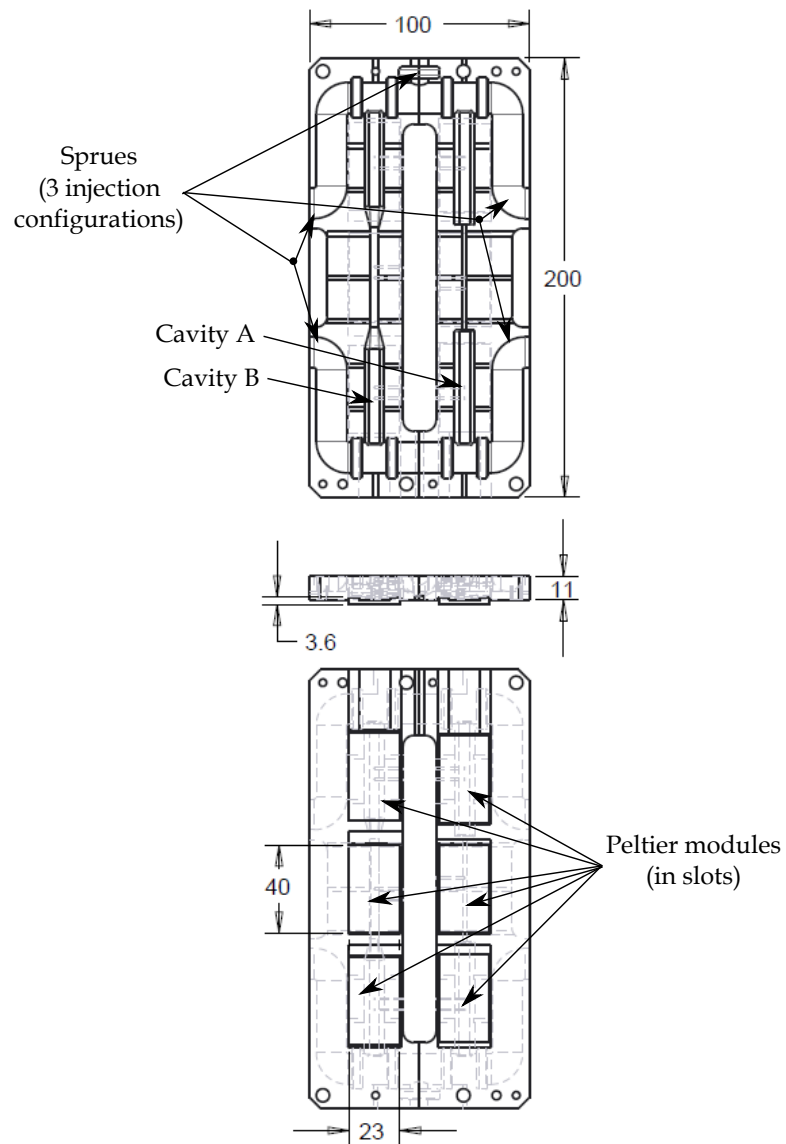


Figure 3.18: Regional controlled mould (industrial): main dimensions of mould and Peltier modules.

## 3.4 Materials analysis and characterisation techniques

The development of novel thermal control systems for ceramic injection moulding die-tools requires an understanding of the influence of both currently available and novel systems on the quality and integrity of ceramic injection moulded components, from both a macro and micro structural perspective. To achieve this, a number of experimental techniques for material analysis and geometrical accuracy assessment have been used in this work. The principal characterisation aspects are:

- Microstructural characterisation.
- Dimensional control and surface integrity characterisation.
- Density characterisation (to evaluate particle content and packing).

The experimental equipment employed to characterise these properties will be described in the following sections.

### 3.4.1 Microstructural characterisation

The analysis of parts microstructure is essential for the verification of ceramic moulded components quality and, in particular, particle (or fillers) packing and orientation can be visualised using microscopy techniques. Scanning Electron Microscope (SEM) analysis was used, with equipment available at the University of Nottingham Nanoscale and Microscale Research Centre (nmRC), in order to observe these microstructural properties and to analyse the morphology of the injected components, especially in correspondence to weld line formation.

SEM working principle for reproducing the image of an analysed sample is

based on the scansion of the sample surface with an electron beam. The interaction between the electrons and the sample surface produces different signals, which depend on the atoms and elements present in the sample. These signals provide information on the topography of the sample surface and chemical composition, and the acquired signal depends on the used SEM detector. The two main SEM detectors used in this work are the Secondary Electron (SE) and Back-Scattered Electron (BSE) detectors. In the former, signals sent from the secondary electrons of the sample atoms are detected, which are emitted from the proximity to the specimen surface: consequently, SE images provide a representation of the sample topography. On the other hand, the BSE detector acquires signals which are reflected depending on the elastic interaction between the electron beam and the specimen: BSE signals come from deeper regions and their intensity depends on the atomic number of the element the sample is made of. Therefore, the output images from this kind of analysis will give more information on the composition of the samples, rather than details on the surface morphology. To be analysed through SEM, samples usually need to have an electrically conductive surface, hence this kind of analysis requires a thin platinum, gold or carbon coating to be applied on the surface of non-conductive specimens. While usually SEM chambers are held in high vacuum, Environmental SEM (ESEM) have the option of being used in a low-vacuum mode, which provides the advantage of enabling the analysis non-conductive samples, despite loosing resolution at higher magnifications.

Two main SEMs were used in for the analysis of samples microstructure in this work, the Philips XL30 SEM and the FEI Quanta 650 Environmental SEM: the first is a conventional SEM with a tungsten filament gun and was used with a range of acceleration voltage between 15 kV and 20 kV; the second is an ESEM, which was used in low-vacuum mode at an

chamber pressure of 70 Pa and was used with lower acceleration voltage (10 kV to 15 kV), to reduce electron charging effects, present due to the non-conductivity of samples surface. After the acquisition of images from the microscopes, the software package ImageJ was employed to post-process SEM micrographs and quantify particle orientation detected by microscopical analysis.

The level of particle packing within green ceramic moulded samples was assessed with different direct and indirect methods. One of the latter approaches was by carrying out *in-situ* micro-mechanical testing, under an SEM. A Gatan Microtest 200VT tensile-compressive stage (Figure 3.19), equipped with a load cell having a maximum applicable load of 200 N, was employed to conduct these uniaxial compressive tests.

The stage was mounted within the FEI Quanta 650 Environmental SEM chamber to enable live visualisation of the specimens during the mechanical testing.

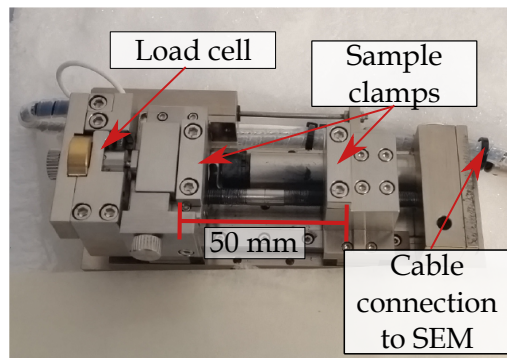


Figure 3.19: Picture of Gatan Microtest 200VT tensile-compressive stage.

The stage was used with the slowest speed, of 0.1 mm/min and data were acquired at a sampling frequency of 10 Hz, due to the brittleness of the analysed samples. This indirect technique to characterised particle packing

in green components was coupled with density measurements, which will be described in the following section.

### 3.4.2 Density characterisation

The assessment of powder content in ceramic moulded parts can be indirectly performed by measuring samples density and using the rule of mixture in order to calculate volumetric particle content:

$$\rho_T V_T = \rho_C V_C + \rho_B V_B \quad (3.5)$$

where  $\rho_T$  is the density of the mixture (in this case, the green part) (which can be measured),  $V_T$  is the volume of the mixture,  $\rho_C$  and  $V_C$  are the ceramic density and volume, and  $\rho_B$  and  $V_B$  are the binder density and volume respectively. Knowing both the powder and binder densities and being able to measure the component volume, it is possible to calculate the volumetric content of the ceramic.

Gas pycnometry was the employed method for measuring part volume, using an AccuPycTM 1330 helium pycnometer: this technique uses the gas displacement method to measure the volume of a sample, using helium as displacement medium. Gas pycnometers have two chambers, one which contains the sample and the other with a reference part having a known mass and volume. Three valves are present in the system: one is used to control the access of pressurised gas into the sample chamber, one to conduct the gas from this to the reference chamber, and one to vent the system from the second chamber. The inert gas firstly fills the first (sample) chamber, whose pressure ( $P_1$ ) is measured with a transducer; then, the gas expands also towards the second chamber, and the total gas pressure ( $P_2$ ) is measured again.

The sample volume  $V_s$  is calculated using the law:

$$V_s = V_{cal} + \frac{V_R}{1 - P_1/P_2} \quad (3.6)$$

where  $V_{cal}$  is the volume of the empty sample chamber (obtained during calibration) and  $V_R$  is the volume of the reference part.

### 3.4.3 Surface integrity and dimensional control

The study of the effects of the employed thermal control approaches on ceramic moulded parts was coupled with an analysis on how the employed temperature management systems affect dimensional control and surface integrity of the injected components.

Geometrical accuracy and dimensional control of the injected components had to be experimentally measured to assess the performance of the employed thermal control techniques, as heating and cooling rates, and subsequent levels of packing pressure influence shrinkage. This is especially relevant in the case of components having features with differential wall thickness, since diverse cooling rates develop during the injection moulding process and, hence, shrinkage-induced warpage will occur.

Surface integrity is also highly affected by thermal control approaches employed during the Injection Moulding (IM) process step, and aspects such as part surface roughness, weld lines morphology and other defects (e.g. sink marks) were analysed in this work.

A comprehensive characterisation of the employed moulds is also of utmost importance to analyse both aspect of dimensional control and surface integrity of the injected parts, as any geometrical inaccuracy or flaw in the

surface topography of the mould cavity will affect the components, independently on the effect of the IM process conditions. To evaluate all these aspects, a series of metrology instrumentations were employed, which will be described as follows.

A Mitutoyo Euro-C-A121210 Coordinate Measuring Machine (CMM), available at the University of Nottingham was used to measure the geometrical accuracy of the employed mould tools. CMMs use a probe to locate discrete points of an object in a 3-Dimensional Cartesian (or polar) coordinate system and the sensed data points can be used to assess the geometrical accuracy of the measured sample.

An Alicona InfiniteFocus G5 optical microscope (Figure 3.20), offered from the Metrology department of the University of Nottingham, and a Bruker ContourGT-I, working through white light interferometry, were used for assessment of both dimensional control and surface accuracy of mould cavities and injected parts.

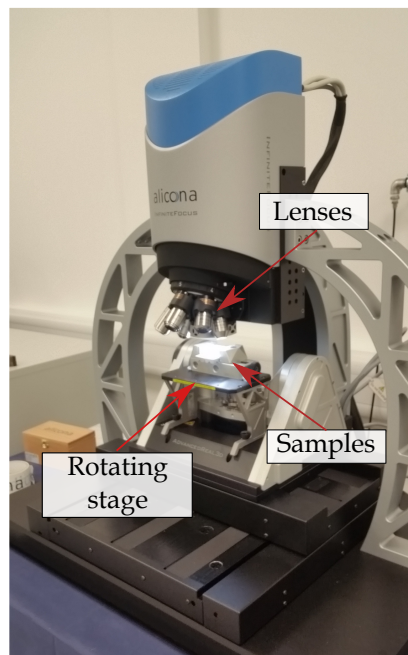


Figure 3.20: Picture of the Alicona InfiniteFocus G5.



These optical inspection systems vertically scan the sample surface and are able to stitch a series of 2D micrographs containing information of the measured object surface topography. The Alicona InfiniteFocus was employed with a 5x and 10x lenses (having respective working distance of 23.5 mm and 17.5 mm and vertical resolution of 410 nm and 100 nm) to assess geometrical accuracy, while the 10x, 20x and 50x lenses (the last two having working distances of 13 mm and 10.1 mm and vertical resolution of 50 nm and 20 nm) were used to measure surface topography and roughness of the injected parts and moulds. The MountainsMap software developed by Digital Surf was used to post-process surface data from both Alicona InfiniteFocus and Bruker.

The main advantage of using the Alicona system compared to the Bruker was the higher scanning speed and the higher ability to measure non-reflective and tilted surfaces. Moreover, the benefit of using these optical systems compared to a CMM for geometrical accuracy evaluation is that they offer the possibility of performing non-contact measurements, which is particularly helpful in the case of small, brittle parts, as green ceramic moulded components.

To obtain a comprehensive analysis of part surface integrity, these methods were coupled with SEM imaging of the surfaces of the injected components, to further verify results of the topography measurements obtained by these optical techniques.

## **3.5 Modelling and optimisation methods and equipment**

The novel developed thermal control system was based on a mould temperature optimisation which was developed alongside with a model of the the CIM process. Two main approaches were used to model CIM in the present work. The first models the filling and packing stages using the Finite Volume Method (FVM); the second is a thermal model of the cooling stage using the Finite Element Method (FEM). Coupled with the FE model of the cooling stage, mould temperature throughout the process was optimised using the Particle Swarm Optimisation (PSO) approach.

### **3.5.1 Modelling of the injection moulding process**

The two modelling approaches used to simulate the injection moulding process, FEM and FVM, are numerical methods used to compute approximate solutions of boundary value problems for partial differential equations. These techniques solve problems by subdividing the modelled physical structures into smaller parts (i.e. elements) to which simpler equations can be applied and then re-assembled into a system of equations. Variational methods are then used to find a solution to the given system of equations that minimises an associated error function. In the FVM, the single element is referred as to a "cell", which is the volume surrounding the mesh nodes. Volume integrals are converted to surface integrals by using the divergence theorem and they are treated as fluxes, which follow conservation laws. For these reasons, this method is widely used in Computational Fluid Dynamic (CFD) problems, which are based on the three constitutive conservation laws of mass, momentum and energy.

The filling stage of the moulding process was modelled using the special-purpose software Moldex3D, with the aim of predicting filling patterns as well as the related temperature and shear rate distribution along the part throughout the process, when using different thermal control approaches. A special-purpose software was chosen with the objective of accurately model the complex joint heat and mass transfer phenomena occurring during the injection moulding process, which are challenging to be replicated within a general-purpose package, where the scope of the present work was not to bring innovation in the modelling of this stage of the IM process. A schematic of the model setup and employed boundary conditions (BC) is shown in Figure 3.21.

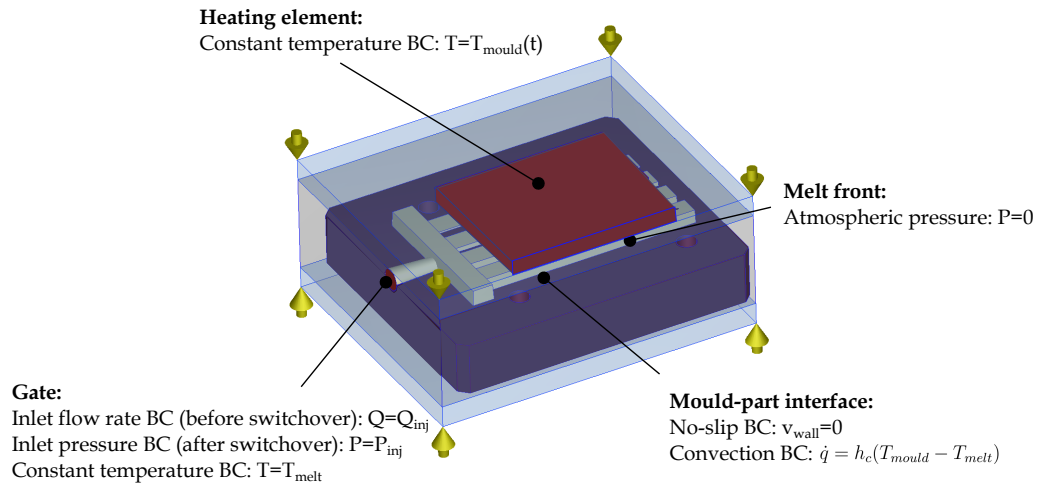


Figure 3.21: Schematics of filling model BCs.

The obtained data from this first model were instead helpful in the development of the novel temperature management system for two main reasons. First, as shear rates arising during mould filling throughout the part are difficult to be experimentally measured, their visualisation through a model supports the understanding of observations regarding the quality and microstructure of the injected components. Secondly, the model output of temperature distribution at the end of filling was used as an input for the

FE model of the cooling stage of the process, which was coupled with the mould temperature optimisation, carried out using the Particle Swarm Optimisation (PSO) method.

The model of the cooling stage was implemented as a transient heat transfer simulation within the FEM software package ABAQUS CAE, which has a built-in Python Application Program Interface (API) through which the simulation thermal boundary conditions could be parametrised and integrated with the temperature optimisation. A schematic of the model setup and BCs of the thermal model is shown in Figure 3.22.

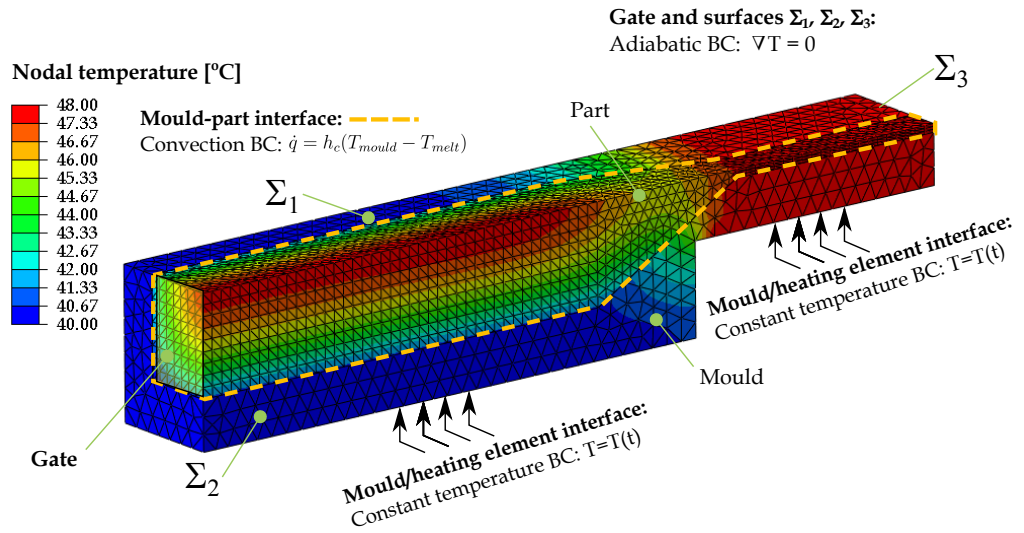


Figure 3.22: Schematics of thermal model BCs.

### 3.5.2 Mould temperature optimisation

As stated before, coupled to the cooling stage model, a mould temperature optimisation was performed with the Particle Swarm Optimisation (PSO) approach (Kennedy and Eberhart, 1995). PSO is a metaheuristic computational method that optimises a problem by minimising or maximising a given objective function  $f(\mathbf{x})$  across a number of iterations  $K$ , by looking for improvements of a candidate solution within a population of possible

candidate solutions.

The peculiarity of this approach stands in both the search method within the solution space and in the analogy of the said method with a nature-based phenomenon, which is the movement of a swarm of particles. Candidate solutions, or possible instances of the problem, are, in fact, corresponding to single particles in a swarm (i.e. the population of possible candidate solutions). Each  $i$ -th particle ( $i = 1, \dots, n$ ) at each iteration  $k$  ( $k = 1, \dots, K$ ) is characterised by a specific position  $\mathbf{x}_k^i$ , which is related to the values assumed by the problem variables for the specific particle in each  $k$ -th iteration. The cost function (i.e. the objective to be minimised or maximised) is computed for all the particles in the swarm, to assess the "performance" of the position of each particle. The whole swarm will tend to the optimal solution by "moving" the particles across the search space between iterations, with the new position  $\mathbf{x}_{k+1}^i$  at iteration  $k+1$  of a given particle  $i$  being computed and updated based on the best position assumed in the past by that particle and by the whole swarm, according to the formulas:

$$\mathbf{x}_{k+1}^i = \mathbf{x}_k^i + \mathbf{v}_{k+1}^i \quad (3.7)$$

$$\mathbf{v}_{k+1}^i = \mathbf{v}_k^i + c_1 r_1 (\mathbf{p}_k^i - \mathbf{x}_k^i) + c_2 r_2 (\mathbf{p}_k^g - \mathbf{x}_k^i) \quad (3.8)$$

where:

- $\mathbf{v}_k^i$  is the velocity of the  $i$ -th particle at the  $k$ -th iteration (particle velocities at the first iteration are initialised as 0).
- $c_1$  and  $c_2$  ( $c_1 + c_2 = 1$ ) are parameters respectively determine how much each particle moves across the search space based on its or the whole swarm's previous history.

- $r_1$  and  $r_2$  are random numbers between 0 and 1.
- $p_k^i$  is the best position of the  $i$ -th particle until the  $k$ -th iteration.
- $p_k^g$  is the best position of the whole swarm until the  $k$ -th iteration.

As the coupled FE-PSO thermal control model and optimisation required a FE simulation to be performed to compute the value of the cost function per each particle of the swarm in each iteration, this approach resulted highly computationally expensive. To handle this, the University of Nottingham *Augusta* High Performance Computer (HPC) was used as a remote workstation to perform the simulations needed to optimise the problem.

The employed modelling and optimisation methods will be further detailed in the following chapters, and related to their specific use within the present PhD work.

## Chapter 4

# Methodology for the evaluation of thermal systems performances in CIM

*This chapter reports the preliminary studies carried out in the present PhD work, with the objective of establishing a methodological framework to assess the performance of thermal control systems for CIM die-tools. To achieve this, the quality of ceramic moulded parts needs to be correlated to the Injection Moulding (IM) process stage and to the heat transfer phenomena occurring during this. In this perspective, a model of the IM filling stage has been developed and validated using both a wax and a ceramic feedstocks: the aim of this filling model is to predict temperature distribution in the part during the IM process, and its results can be used as a support to the performance analysis of thermal control systems, which is reported in the following chapters. After this, to establish a methodology for analysing the effect of IM thermal processing conditions on the quality of IM green and sintered parts, two investigations were carried out. The first is an analysis of green parts quality, carried out on a wax feedstock with cross-linked polystyrene fillers to have an understanding of the micro- and macro-structure of parts*

*having similar microstructure and properties to green ceramic components. The second is an analysis of a sintered ceramic block, with the aim of reconstructing the root cause of observed defects and univocally link them to the IM process stage. In both these studies, the developed filling simulation has been used as a support tool to correlate the observed defects, macro- and micro-structural properties to the IM process. This enabled the development of a robust methodology that can be used in the future work carried out for the present thesis, for the analysis and development of thermal control systems for CIM die tools.*

## 4.1 Introduction

The analysis of the reviewed scientific literature on CIM shows a clear gap regarding the employment of advanced thermal control approaches for the injection moulding of ceramic components and strong limitations exist in the general understanding of how IM thermal processing conditions affect the quality of ceramic parts. In order to develop novel thermal control systems for CIM, their performances need to be evaluated, in relation to how they affect components quality, for which a methodology has to be developed. Although this has been previously done in polymer IM, novel thermal control systems have not be developed for ceramic applications, and the development of such a methodology for CIM presents two main challenges, which is discussed in the following.

The first challenge regards the limitations in assessing thermal conditions of the components during IM, depending on the mould temperature management system employed. Cooling rates during filling are geometry dependant and highly affect flow patterns in CIM; moreover, the component temperature and consequential cooling rates during filling are difficult to



be experimentally measured inside the part, due to the short length of the filling process (usually  $< 1$  s), and because of the difficulty in accessing the components with sensors (e.g. thermocouples or thermistors).

The second challenge is linked to the fact that, as green moulded ceramic parts need to undergo the subsequent firing processes (debinding and sintering), sintered parts are usually investigated in order to assess ceramic components quality. The main limitation of this approach stands on the microstructural changes that ceramic parts undergo during the firing processes (i.e. debinding and sintering), which make it difficult to associate the presence of cracking or warpage defects to the injection moulding process univocally, without observing the microstructure development of ceramic moulded parts across the CIM process stages.

To overcome the said challenges and develop a methodology to evaluate the performance of thermal systems for CIM die-tools, a step-wise approach is hereby proposed (Figure 4.1).

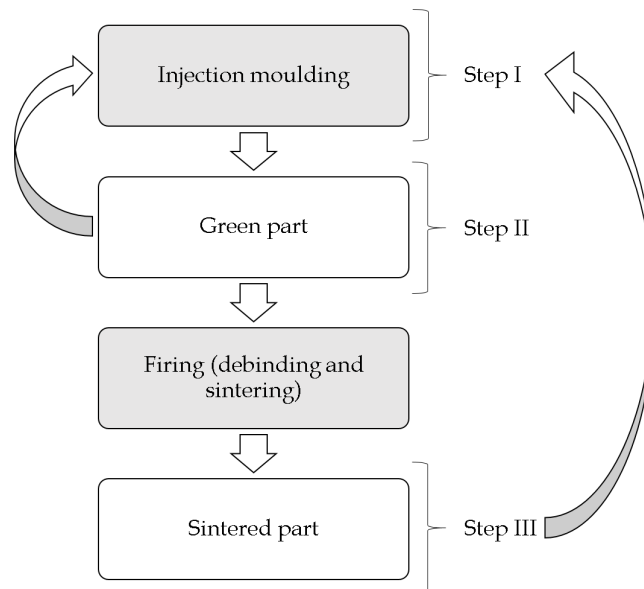


Figure 4.1: Flow-chart of the followed approach to develop a methodology for the evaluation of thermal systems performance for CIM die-tools.

- **Step I: Development of a filling simulation.** Heat and mass transfer phenomena during the filling phase of injection moulding are highly interconnected and dependant on the thermal control approaches employed during the process. In order to predict temperature distribution and cooling rates in complex parts during the filling stage of IM, a simulation needs to be developed, as these cannot be measured experimentally. This model needs to capture the effect of different thermal processing conditions on the filling behaviour for simple and more complex components and was used as a support to the understanding of how observed quality outcomes (e.g. feature replication capability, surface integrity and dimensional control) relate to thermal conditions occurring during the IM filling process. The simulation was validated based on predicted filling patterns firstly in simple and then more complex cavity geometries.
- **Step II: Analysis of IM outcomes from green components.** The study of green ceramic components is necessary in order to understand the influence of thermal conditions during the IM process on quality outcomes. To evaluate the main challenges and effects from different thermal approaches on the quality of green components, a study was carried out on parts moulded using a wax feedstock with spherical cross-linked polystyrene fillers, having similar thermodynamic and rheological properties to the binder of the reference ceramic feedstock. These preliminary tests were performed on this material, due to its lower filler content compared to a ceramic feedstock, which allowed to have an easier understanding of fillers packing through microscopy observations. Moreover, the cross-linked polystyrene fillers presents the advantage of being spherical, thus allowing to initially neglect the complexity related to particle orientation. The filling sim-

ulation was used as a support to correlate the performed analyses to the heat transfer phenomena occurring during the IM process.

- **Step III: Analysis of IM outcomes from sintered components.**

The univocal correlation between defects in sintered ceramic parts and heat transfer phenomena occurring during the IM process stage is challenging due to microstructural changes arising during the firing processes, which may affect the quality of components independently from IM. In order to have a deeper understanding of this challenge, and to evaluate the possibility of directly correlating sintered parts quality to the IM process, a study was performed on a fired ceramic block. The component was debound and sintered with pre-optimised conditions, and the observed defects were correlated to the injection moulding process, with the support of the developed filling simulation. The study was carried out on a large (210 mm x 120 mm x 40 mm) ceramic block injected at ambient mould temperature, in order to capture, within a single geometry, different defects, which can be related to thermal conditions arising in the component during IM.

## 4.2 Reference geometries for model development and analysis of IM outcomes

As previously stated, in order to develop a methodological framework for the performance evaluation of thermal control systems for CIM die-tools, a step-wise approach was followed, including both modelling and experimental work.

The first two steps of this study require the design of reference geometries, which are challenging to manufacture with conventional "cooling-

only” mould temperature control systems, due to diverse cooling rates developing during the IM process. Therefore, two sample parts were designed: *Cross-channels* geometry (Figure 4.2) and *Parallel-channels* geometry (Figure 4.3), both characterised by features of dissimilar wall thickness.

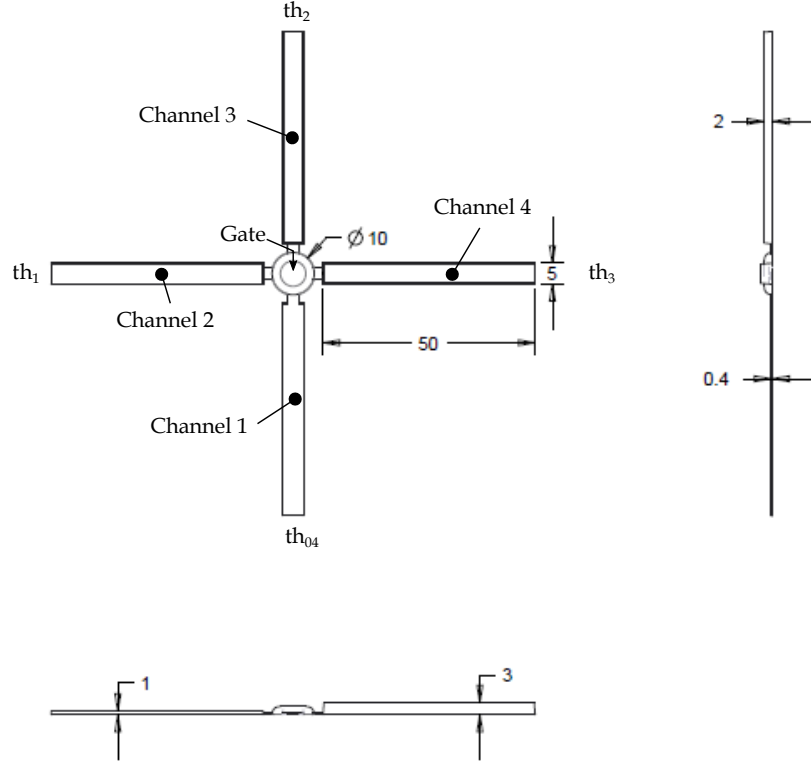


Figure 4.2: *Cross-channels* reference component

The two reference components were designed with four rectangular channels having the same length  $l$  and width  $w$  (50 mm and 5 mm respectively) and four different thicknesses  $th$  (0.4 mm, 1 mm, 2 mm and 3 mm in the first; 0.4 mm, 2 mm, 4 mm and 6 mm in the second), with the aim of achieving geometries with dissimilar aspect ratios, defined as  $w/th$ . For consistency, the moulds designed to inject the two components and that are described in Section 4.3.2, are called Cross-channels mould and Parallel-channels mould. The dimensions for the two reference geometries have been chosen based on standard feature size of turbine blade cores, in order to replicate the heat transfer phenomena occurring while injecting actual industrial components, which are challenging to be manufactured through CIM.

In this study, for simplicity, the reference components were designed with *disjoined* features, in order to enable the isolation of different heat transfer phenomena occurring in parts having dissimilar wall thicknesses. However, in order to replicate more complex flow patterns, and to analyse the effect of different thermal conditions on weld line morphology (Section 4.4), the Parallel-channels geometry was also designed in a configuration having channels connected through bridges (Figure 4.3b). Moreover, it is worth noticing that the Cross-channels reference component has only been used for a preliminary model calibration and that the main studies reported in Section 4.4 and in Chapter 5 have been carried out using only the Parallel channels geometry.

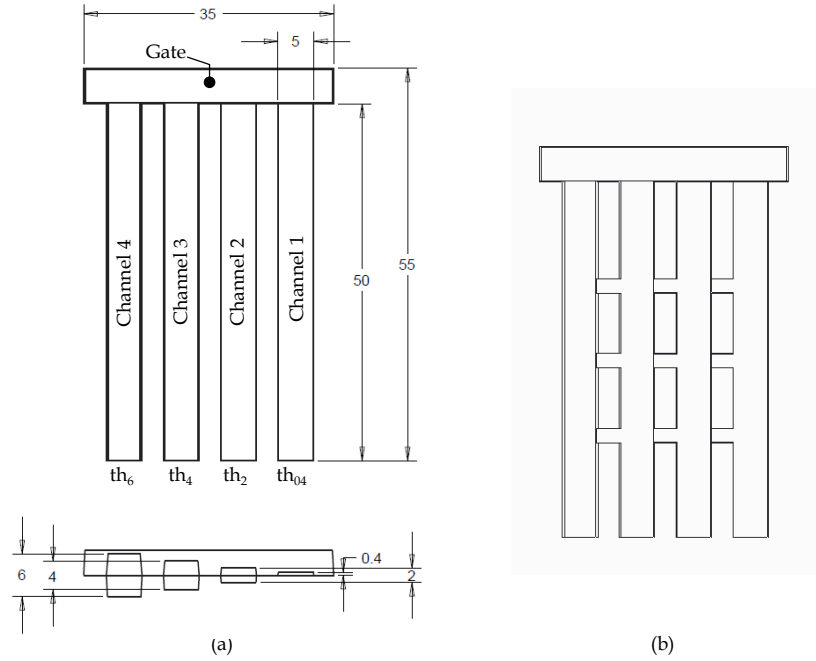


Figure 4.3: *Parallel-channels* reference component. (a) Main dimensions for the component in the "disconnected channels" configuration. (b) Component in the "connected channels" configuration.

In the following sections, the main findings of the three stages of this study are reported and discussed.

## 4.3 Step I: Development of a filling simulation

To develop a methodology for the performance evaluation of thermal control systems for CIM, a numerical simulation for the filling stage of the IM process was carried out using the software package Moldex3D. The model enables the prediction of temperature and shear rates within the moulded parts, which cannot be easily measured during IM experiments. The results of this model have been used in Steps II and III to understand the cause of the observed green and sintered part defects and microstructure in relation to the heat transfer phenomena occurring during mould filling. Moreover, this simulation was the first step of the thermal control model used for the novel developed regional control system, which is described in Chapter 6.

Both the FR60 investment casting wax and the silica-zircon ceramic feedstock (described in Chapter 3) were used in order to setup and validate the simulation and the injection moulding validation experiments were carried out using the laboratory rig already described in Chapter 3. The filling simulation models the injection of the reference geometries (Section 4.2) and takes into account the thermal properties of the moulds used to inject them, as well as the employed mould heating and cooling methods, by thermoelectric modules: this is discussed in detail within the model validation description (Section 4.3.2).

In the following sections, the setup and validation of the developed simulation are presented and discussed.

### 4.3.1 Model setup

The simulation of the IM filling stage, developed in Moldex3D, consisted of a coupled heat and mass transfer model and was set up according to the following steps:

1. Definition of the modelled components
2. Construction of a mesh
3. Definition of material properties for the modelled components
4. Definition of Boundary Conditions (BCs) and Initial Conditions (ICs)

These steps are described in detail, with a particular insight on the differences in the model development for the two geometries injected in this work.

The main components were modelled for the two mould assemblies (Figure 4.4), which included:

- Mould cavity (i.e. the part).
- Mould *envelope*, consisting of the main cavity plates (which were made of brass for the Cross-channels mould and in aluminium for the Parallel-channels mould, as explained in detail in Section 4.3.2).
- Mould *inserts*: as the top and bottom plates of the die-tools were of different materials, the top plates were modelled as separated inserts of the mould.
- Heating element (heat source and sink): the Parallel-channels mould had a Peltier module in contact with the aluminium plate, to provide heating and cooling. This face of the Peltier was modelled as a rectangular plate, part of the assembly. The other face of the Peltier and the components on the opposite side of the thermoelectric module (which

is described in Section 4.3.2) were not modelled, as the two faces were thermally isolated (i.e. adiabatic BC).

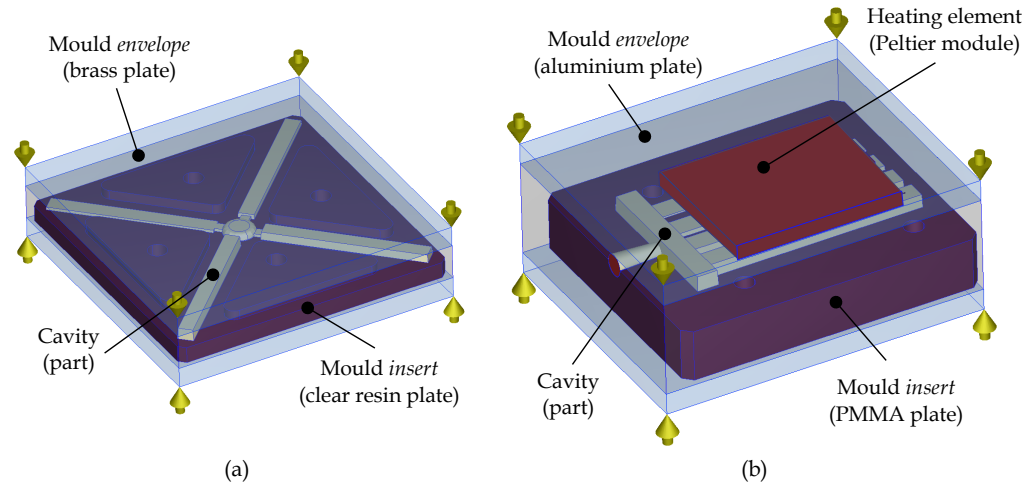


Figure 4.4: Modelled assemblies for the filling simulation. (a) Cross-channels mould. (b) Parallel-channels mould.

After defining the modelled assembly, a tetragonal mesh was generated, with a minimum seed of 0.1 mm, in order to guarantee a sufficient number of elements over the thinnest channels thickness (0.4 mm), according to common practices in IM process modelling (Ab, 2003, Ling, 2006).

All the components, apart from the Peltier module, were assigned their specific material properties: in particular, the mould plates were modelled with their mechanical and thermal properties to account for differences in heat transfer due to the employment of different materials for the top and bottom plates (Table 4.1). As for the feedstock material properties, viscos-

Table 4.1: Material properties used for mould plates in the filling model

Parameter	Brass plate	Aluminium plate	Mould inserts
Density [Kg/m <sup>2</sup> ]	8409	2800	1150
Thermal conductivity [W/mK]	116	154	0.21
Heat capacity [J/Kg.K]	380	880	2440

ity behaviour, as a function of shear rate and temperature, was described



through a Cross-Exp model (Nikolic, 2014):

$$\mu = \frac{\mu_0}{1 + \left(\frac{\mu_0 \dot{\gamma}}{\tau^*}\right)^{1-n}} \quad (4.1)$$

$$\mu_0 = B \exp\left(\frac{T}{T_0}\right) \quad (4.2)$$

where  $\mu_0$  is the zero shear rate viscosity [Pa.s],  $\dot{\gamma}$  is the shear rate [1/sec],  $T$  is the temperature [K],  $T_0$  is a reference temperature [K],  $\tau^*$  is the critical shear stress at the Newtonian plateau [Pa] and  $n$  is the power-law index (relevant values for the constants displayed in Table 4.2).

Table 4.2: Cross-Exp model parameters for wax and ceramic feedstocks

Parameter	Wax	Ceramic
B [Pa.s]	$1 \times 10^{-38}$	$6 \times 10^{-39}$
$T_0$ [K]	30000	30338
$\tau^*$ [Pa]	3321	4300
$n$	0.2	0.2

A modified Tait model (1888) was used to simulate PVT behaviour of the feedstocks:

$$v = v_0 \left[1 - C \left(1 + \frac{P}{D}\right)\right] + v_t \quad (4.3)$$

$$v_0 = \begin{cases} b_{1S} + b_{2S}T^*, & \text{if } T \leq T_t \\ b_{1L} + b_{2L}T^*, & \text{if } T > T_t \end{cases}$$

$$D = \begin{cases} b_{3S} \exp(-b_{4S}T^*), & \text{if } T \leq T_t \\ b_{3L} \exp(-b_{4L}T^*), & \text{if } T > T_t \end{cases}$$

$$v_t = \begin{cases} b_7 \exp(b_8 T^* - b_9 P), & \text{if } T \leq T_t \\ 0, & \text{if } T > T_t \end{cases}$$

$$T_t = b_5 + b_6 P$$

$$T^* = T - b_5$$

where  $P$  is the pressure [Pa] and  $v_0$ ,  $B$  and  $v_t$  are piecewise functions for which different sub-functions apply depending on whether the feedstock temperature is above or below the material melting point (i.e. the  $b_5$  constant in the model).  $C$  is a universal constant of 0.0894, while the other values of the employed Tait model parameters for the two feedstock materials, taken from standard software library are shown in Table 4.3.

Table 4.3: Tait model parameters for wax and ceramic feedstocks

Parameter	Wax	Ceramic
$b_{1L}$ [m <sup>3</sup> /Kg]	0.001077	0.00053
$b_{2L}$ [m <sup>3</sup> /KgK]	7x10 <sup>-7</sup>	1.9x10 <sup>-7</sup>
$b_{3L}$ [Pa]	1.7x10 <sup>8</sup>	1.7x10 <sup>8</sup>
$b_{4L}$ [1/K]	0.0058	0.0031
$b_{1S}$ [m <sup>3</sup> /Kg]	0.001	0.00051
$b_{2S}$ [m <sup>3</sup> /KgK]	4.8x10 <sup>-8</sup>	9.3x10 <sup>-8</sup>
$b_{3S}$ [Pa]	3.33x10 <sup>8</sup>	1.76x10 <sup>8</sup>
$b_{4S}$ [1/K]	1.74x10 <sup>-7</sup>	0.0033
$b_5 = T_g$ [K]	335.15	335.15
$b_6$ [K/Pa]	1.675x10 <sup>-7</sup>	1.89x10 <sup>-7</sup>
$b_7$ [m <sup>3</sup> /Kg]	0	2.12x10 <sup>-5</sup>
$b_8$ [1/K]	0.1	0.1
$b_9$ [1/Pa]	2.510 <sup>-9</sup>	1.89x10 <sup>-8</sup>

The initial values for the parameters of both the viscosity and PVT models were taken from data of a wax and a CIM feedstock, from a pre-defined library available on Moldex3D. Then, the viscosity model parameters  $B$  and  $T_0$  were calibrated respectively in order to predict the correct level of “zero shear rate viscosity” and viscosity-temperature dependence of the material, available from experimental data measured by the supplier of the ceramic feedstock.

Heat capacity and thermal conductivity data were defined as a function of temperature in a tabular format, based on data of a wax feedstock similar to FR60, taken from the literature (Gebelin et al., 2004) and from experimental data, provided by the supplier for the CIM material (not reported here due to confidentiality reasons).

As for the BCs and ICs definition, the simulation software reproduces the behaviour of an injection moulding machine, by modelling the filling stage with an inlet flow rate BC, the packing phase with an inlet pressure BC and defining the transition between the two (i.e. the filling-to-packing switch-over point) based on either a nozzle pressure level or cavity filling status (calculated as a percentage of the total cavity volume). On the other hand, the employed and modelled laboratory rig was based on a set inlet pressure throughout the whole process, due to the pneumatic cylinder action. To account for this, the filling-to-packing switch-over point of the simulation was set when the nozzle pressure reached the input values used in the experiments, and the value of flow rate employed during the model filling phase was experimentally calibrated. As for thermal BCs, in the Parallel-channels mould case, the Peltier element was modelled as a rectangular plate having an imposed temperature throughout the process, according to the thermal profiles employed during the conducted experiments. The feedstock inlet temperature was also set based on the different melt temperatures used in the tests (all the experimental values for the process parameters are specified in Section 4.3.2). A thermal conductance BC was instead established between the mould and the part, with a value of  $1500 \text{ W/m}^2\text{K}$  (Somé et al., 2015).

### 4.3.2 Model validation

The two moulds used to inject the reference components needed to be designed in a way that could enable the model validation, whose aim is to predict temperature and shear rates within the part during filling, which cannot be experimentally measured. This brings the challenge of how to validate the model. Temperature distribution and cavity geometry affect feedstock viscosity which, in turn, influences its flowability: therefore, the followed strategy was to validate the model based on comparing the predicted filling patterns to the actual flow in the mould. To do this, the moulds were designed with transparent top plates, which would enable the live visualisation and recording of the filling process from the top of the moulds. As previously stated in Section 4.3.1, the properties of the clear mould plates were considered in the model in order to account for the presence of mould plates having different thermal diffusivities.

Considering the chosen reference geometries, two moulds were designed and manufactured: the *Cross-channels* mould (Figure 4.5) and the *Parallel-channels* one (Figure 4.6).

The first, *Cross-channels* mould, which was only designed for the model flow rate calibration, was manufactured in brass through a hybrid 3D-printing and casting processes. The material choice was due to the fact that part ejection was easily achievable with a brass mould, because it exhibited lower adhesion with the FR60 wax, compared to other plastic materials and 3D-printed aluminium, respectively due to the lower compatibility between tool and feedstock materials and to the lower surface roughness achieved on the mould cavity (which was  $3.6\text{ }\mu\text{m Ra}$ , measured with the Bruker ContourGT-I optical microscope). The mould cover was also 3D-printed with Stere-

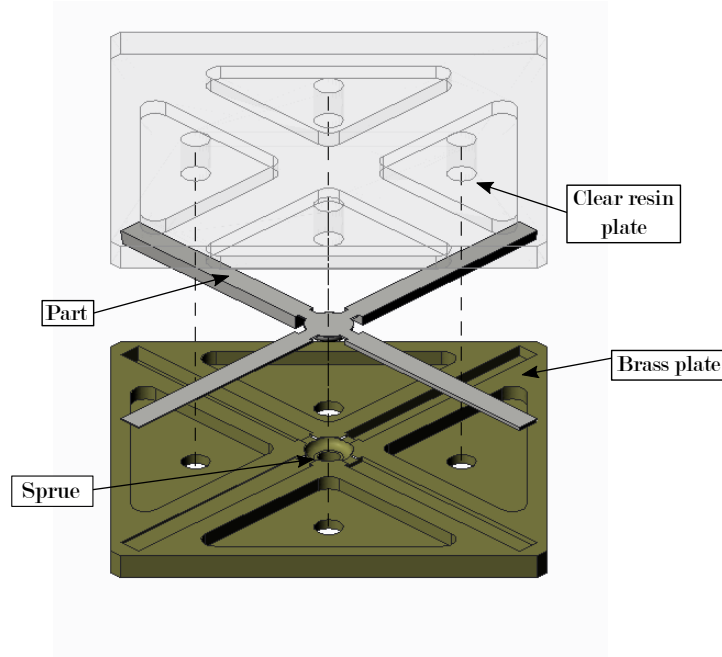


Figure 4.5: Exploded view of the *Cross-channels* mould.

olithography (SLA) technology using a clear acrylate resin.

The second, *Parallel-channels*, mould (Figure 4.6) was, instead, made by a bottom plate (1) machined in aluminium (2400 T651 grade) in order to have a low surface roughness (this was  $0.8 \mu\text{m Ra}$ ) compared to those obtainable through 3D-printing and a higher thermal conductivity than brass. Also this mould was designed with a transparent cover (2), which was machined in clear Poly-Methyl-Methacrylate (PMMA). A thermoelectric (Peltier) module (3) placed on a heatsink (4) with integrated fan (5), to allow for heat dissipation, was used to heat and cool the mould using a closed-loop control, implemented through a thermistor placed on the bottom face of the aluminium plate (Figure 4.6a). To let air escape from the mould during injection and avoid air entrapment, venting channels (0.1 mm deep) were machined at the end of the channels (Figure 4.6b).

Small bridges were machined on the mould cavity to connect the four channels: this was done to create more complex filling patterns and hence to

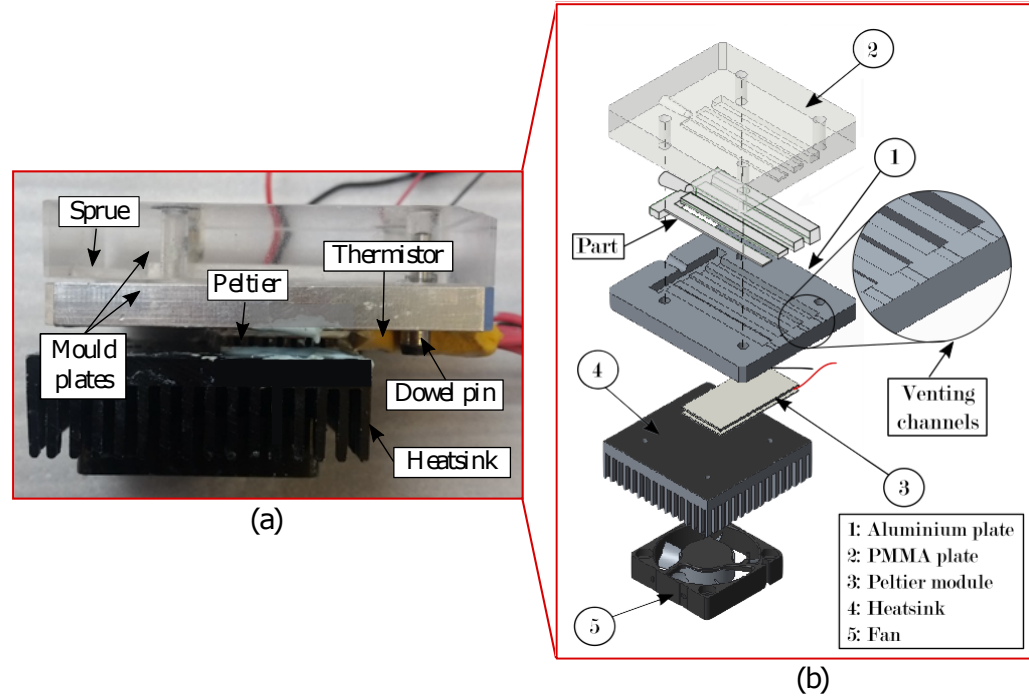


Figure 4.6: *Parallel-channels* mould. (a) Picture of the assembly. (b) Exploded view.

have a more complete validation of the model. These bridging channels could also be blocked with a cured high-temperature resin to enable the injection of the disjointed four features.

Using these moulds, the model validation was carried out in three subsequent steps:

1. Flow rate calibration: Cross-channels mould, wax feedstock.
2. Validation for wax feedstock: Parallel-channels mould, in the two configurations of disconnected channels and channels connected through bridges.
3. Validation for ceramic feedstock: Parallel-channels mould, in the configuration with disconnected channels.

Since the model needs to predict temperature and shear rates at different thermal conditions, this was validated with multiple temperature settings.

Two ways were followed for varying the thermal conditions: changing melt temperature ( $T_{melt}$ ) and mould temperature ( $T_{mould}$ ). Melt temperature was varied in the first two validation steps (with wax), which were carried out at ambient mould temperature ( $T_{mould} = 30\text{ }^{\circ}\text{C}$ ), while mould temperature was changed in the final validation step (with ceramics), which was, instead, performed at a constant melt temperature ( $T_{melt} = 75\text{ }^{\circ}\text{C}$ ). For this last validation step, two mould thermal control approaches were employed: first using a constant ambient mould temperature ( $30\text{ }^{\circ}\text{C}$ ), and then using the Rapid Heat Cycle Moulding (RHCM) approach, following a temperature profile consisting of a first stage of mould heating, up to approximately  $65\text{ }^{\circ}\text{C}$  (higher than the feedstock  $T_g$ ), holding of this temperature during injection, and finally cooling down to  $40\text{ }^{\circ}\text{C}$  (Figure 4.7). The same mould temperature profiles were used for the study which is described in Chapter 5.

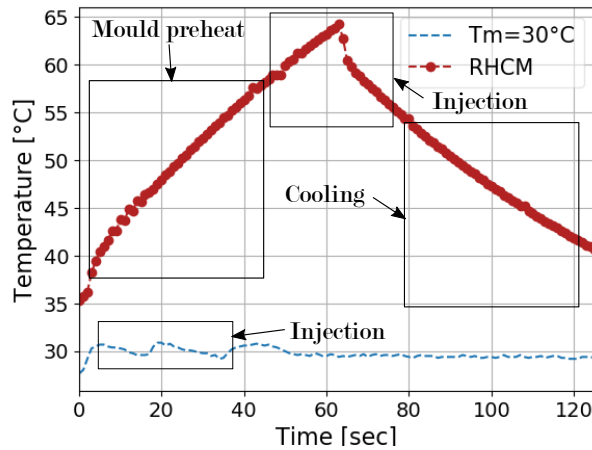


Figure 4.7: Mould temperature profiles during ambient temperature and RHCM trials, controlled through the Peltier element

Five repetitions were carried out for all the trials used to validate the model, for which results are shown in the following sections.

#### 4.3.2.1 Flow rate calibration

The model required calibration of the flow rate parameter, which was carried out based on the comparison of the experimental and simulated filling behaviour for the four channels of the Cross-channels mould, obtained at two melt temperatures (65 °C and 70 °C). For the calibration, the injection pressure of the pneumatic cylinder was set at 3.5 Bar: this coincided with the packing pressure BC and with the switch-over point of the simulation. The flow rate can be calibrated using two different approaches. First, by experimental measurements: this consisted of measuring the pneumatic cylinder speed during injection and computing its average value. Second, by calculating a flow rate value: this consisted on fitting a speed to the initial linear profile of the experimentally obtained curve showing flow length increase over time in the four channels.

In the case of injection with a melt temperature of 65 °C (Figure 4.8), the calibration shows a better correspondence between experimental and simulation results when the measured value (first approach) was used, due to the fact that the fitting accounted only for the first part of the injection process.

When raising melt temperature up to 70 °C, the measured and calculated flow rate values coincided, and were higher than that of the 65 °C case, due to the lower material viscosity. The experimentally measured flow length over time was compared with the simulation results obtained with the measured flow rates at both the 70 °C and 65 °C melt temperature cases, showing that the model better predicts the channel filling with the measured flow rate level (Figure 4.9). This is, again, due to the fact that, when increasing melt temperature, a reduction in feedstock viscosity occurs: therefore, for a constant inlet pressure, a lower flow rate is needed to fill the same geome-



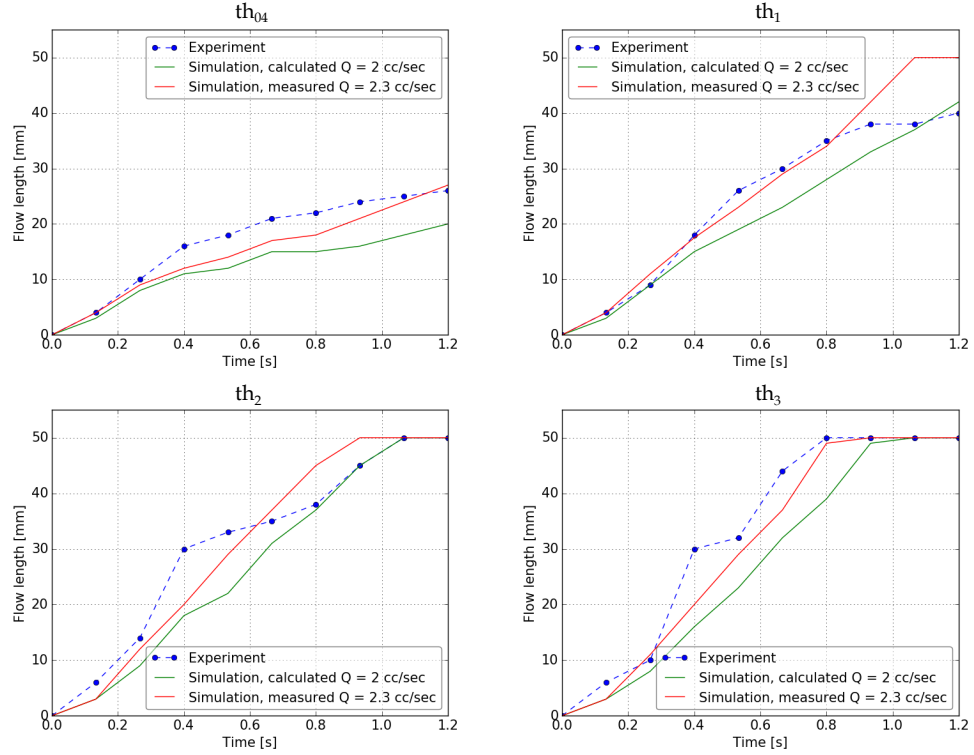


Figure 4.8: Flow rate calibration,  $T_{melt}=65\text{ }^{\circ}\text{C}$ : Experiment versus simulated flow length over time for different channel thicknesses of the Cross-channels mould.

try. This implies that a fixed flow rate cannot be used to model injection at different pressures and its value needs to be measured whenever experimental conditions (both in terms of injected geometry and process parameters) vary.

#### 4.3.2.2 Validation for wax feedstock

Once the model was calibrated, the Parallel-channels mould was used to perform the model validation, first with the wax and then with the ceramic feedstock. As previously stated, during model validation for the wax feedstock, melt temperature was varied in order to validate the model with different thermal conditions. Experimental data, compared to simulation results for different melt temperatures ( $65\text{ }^{\circ}\text{C}$  and  $75\text{ }^{\circ}\text{C}$ ) are displayed in Figures 4.10 and 4.11, for which the injection pressure was set at 3.5 Bar

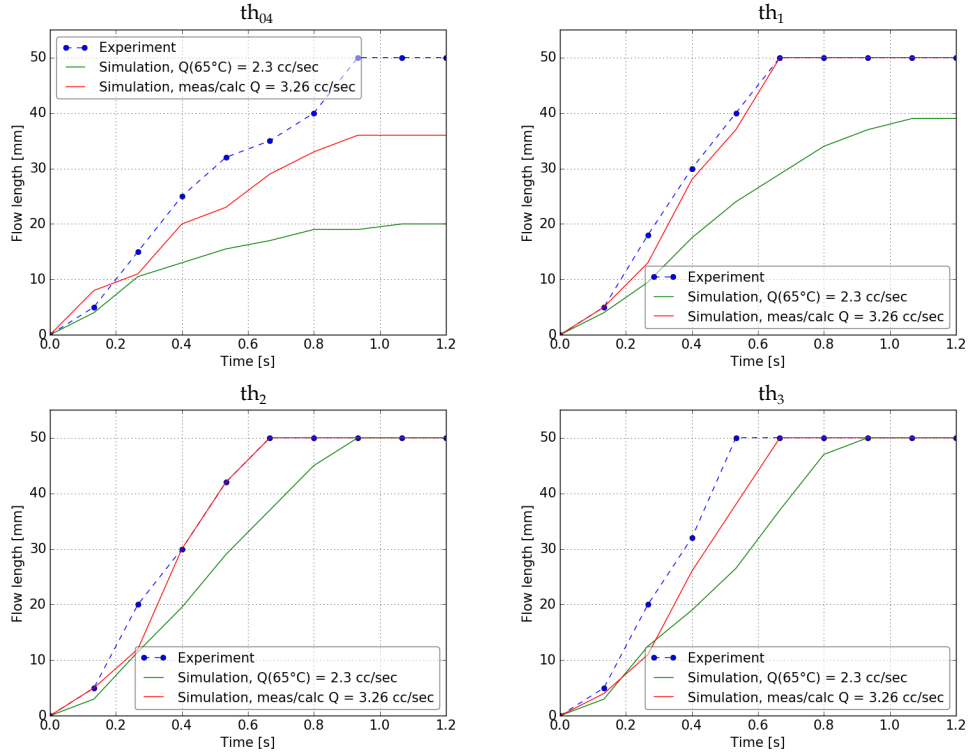


Figure 4.9: Flow rate calibration,  $T_{melt}=70\text{ }^{\circ}\text{C}$ : Experiment versus simulated flow length over time for different channel thicknesses of the Cross-channels mould.

and the flow rate was measured to be  $3.25\text{ cm}^3/\text{s}$  and  $5.4\text{ cm}^3/\text{s}$  respectively. As evident from the error bars shown in Figure 4.10, experimental results showed low repeatability, especially in the first case ( $T_{melt} = 65\text{ }^{\circ}\text{C}$ ). This was due to the fact that, since the employed feedstock has a semi-crystalline behaviour, it does exhibit a sharp transition of viscosity corresponding its melting point ( $T_m = 62\text{ }^{\circ}\text{C}$ ): therefore, the closer to this temperature the experiments are carried out, the larger the variations in viscosity (and hence in flowability) will be for small melt temperature fluctuations during the experiments. Moreover, at lower melt temperatures, and hence at higher feedstock viscosity levels, the pneumatic cylinder exhibited a highly inertial behaviour, showing higher variations of flow rate throughout the filling process, in contrast with the modelled constant speed. The errors between simulated and experimental results show that the model over-estimates flow length, which may be due to the fact that the cavity is assumed to be totally

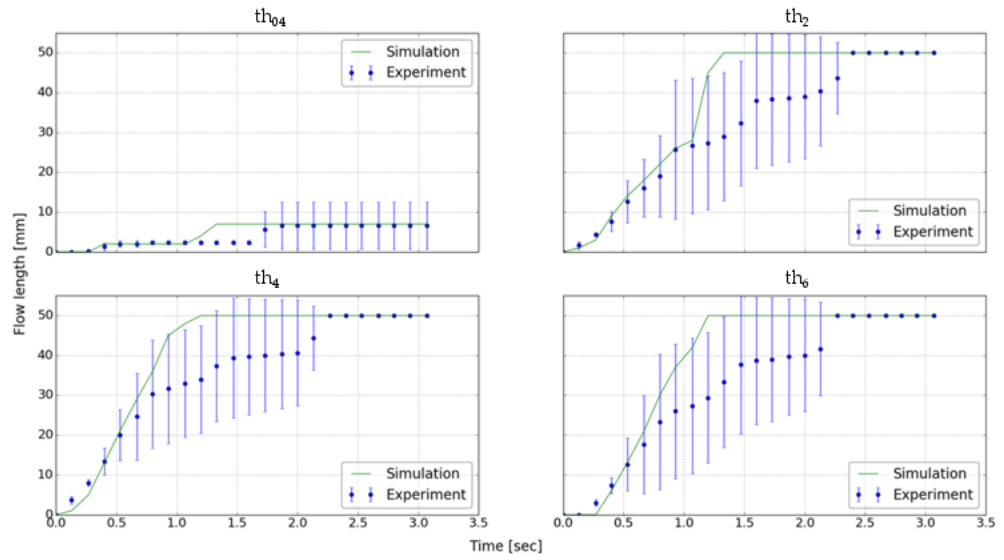


Figure 4.10: Filling model validation, wax feedstock,  $T_{melt} = 65\text{ }^{\circ}\text{C}$ . Experiment versus simulated flow length over time for different channel thicknesses of the Parallel-channels mould in disconnected channels configuration. The error bars represent the standard deviation over the five experimental measurements.

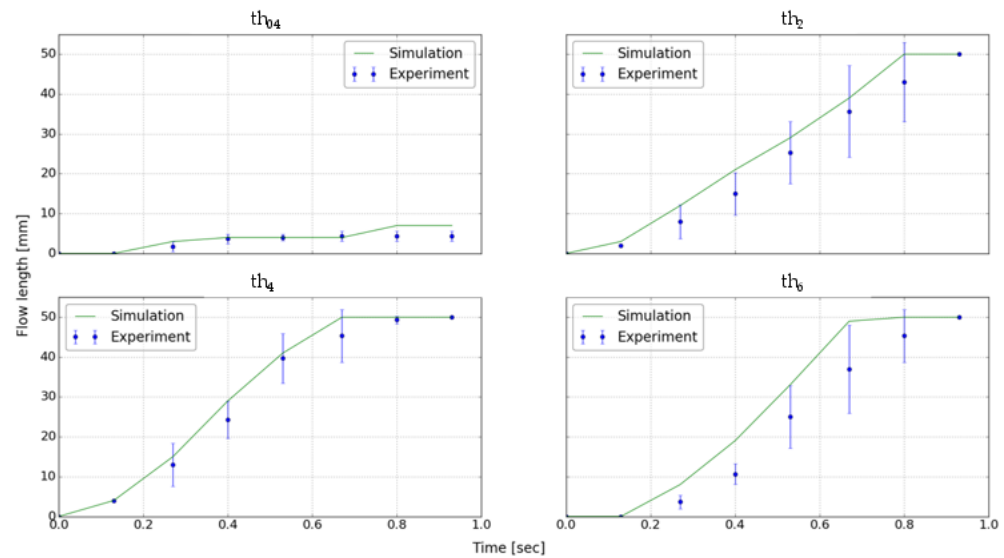


Figure 4.11: Filling model validation, wax feedstock,  $T_{melt} = 75\text{ }^{\circ}\text{C}$ . Experiment versus simulated flow length over time for different channel thicknesses of the Parallel-channels mould in disconnected channels configuration. The error bars represent the standard deviation over the five experimental measurements.

vented. Moreover, these deviations are likely to be due to errors in viscosity prediction as a function of temperature for the wax feedstock. These assumptions and deviations in viscosity modelling will cause higher errors in simulating the flow of thin channels, where the material temperature drops faster than in the other features and the flow is more sensitive to changes in back-pressure, due to lack of cavity venting. However, comparing the average flow lengths, the model and experimental observations follow similar trends, especially in the more repeatable  $T_{melt} = 75\text{ }^{\circ}\text{C}$  case.

Considering the more complex flow obtained by connecting the channels of this mould, a back-to-back visual comparison of the results for the filling simulation and the experimental trials is shown in Figures 4.12, 4.14 and 4.16 (with respective plotted results displayed in Figures 4.13, 4.15 and 4.17) for three different melt temperatures (65 °C, 70 °C and 75 °C). These tests were carried out at a pressure of 2.8 Bar and the measured flow rates were 3.2 cm<sup>3</sup>/s for the 65 °C, 70 °C melt temperature cases and 4.5 cm<sup>3</sup>/s for the 75 °C one.

Deviations in flow length over time between numerical model and experimental trials, show that the simulation predicts a quicker cavity filling than the actual, with delays of approximately 0.1 s. Similarly to the validation carried out in straight channel geometries, the model over-estimates flow length, especially in the thinnest ( $th_{04}$ ) channel. Other errors in flow prediction can be also attributed to inaccuracies of viscosity modelling, as discussed earlier, and to the assumption of perfect cavity venting. Despite these errors, flow patterns and weld line locations are correctly predicted, and the model is able to foresee lack of fill in the 65°C case, thus showing the simulation achieves good flow predictions at different thermal conditions, also for more complex geometries.

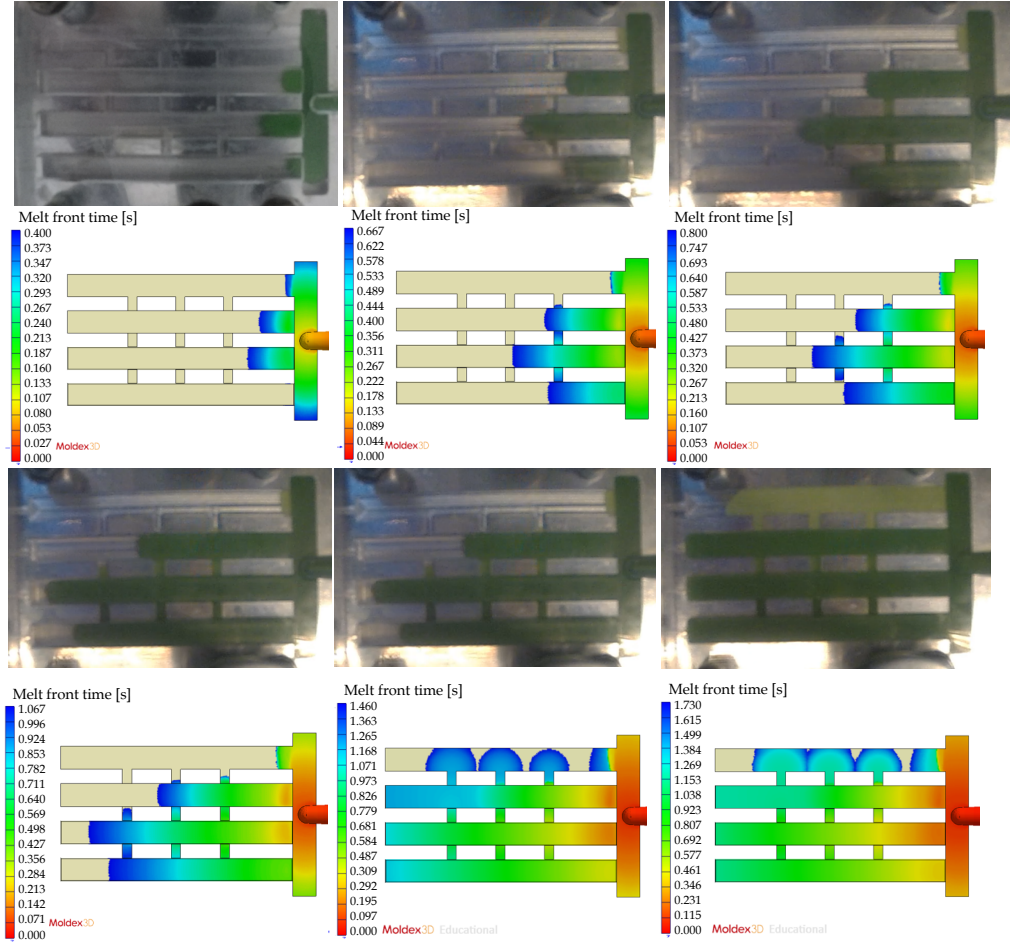


Figure 4.12: Filling model validation,  $T_{melt} = 65\text{ }^{\circ}\text{C}$ . Experiment versus simulated flow length over time for different channel thicknesses of the Parallel-channels mould in connected channels configuration - Visual comparison.

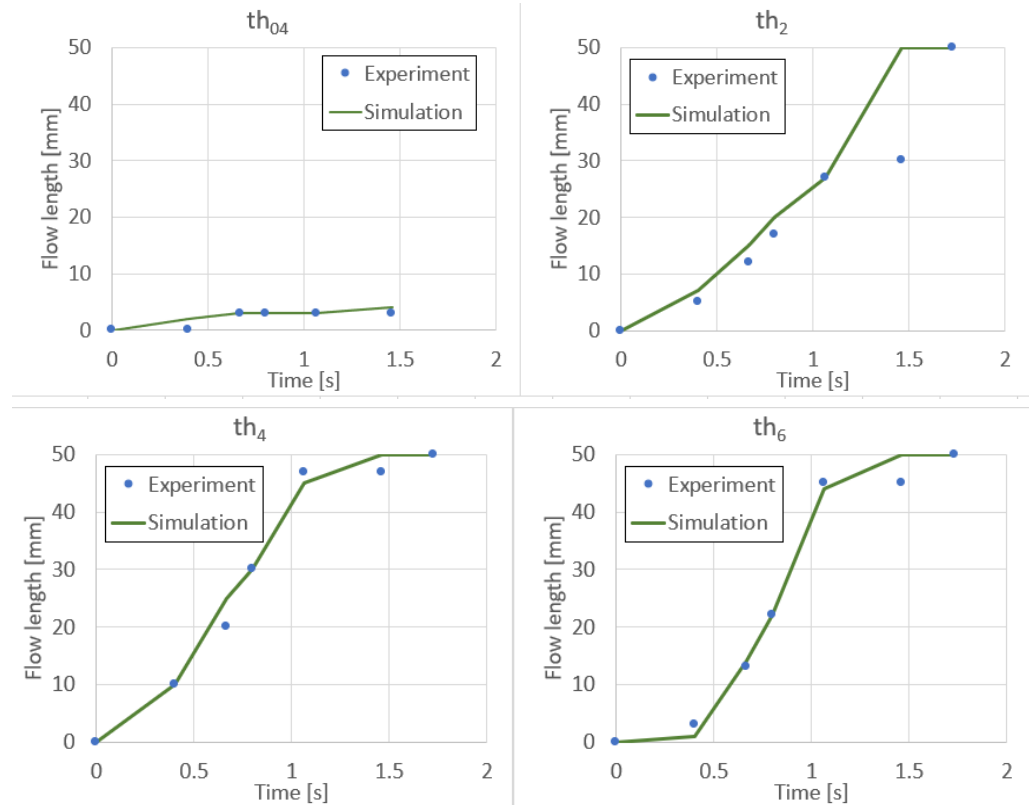


Figure 4.13: Filling model validation, wax feedstock,  $T_{melt} = 65\text{ }^{\circ}\text{C}$ . Experiment versus simulated flow length over time for different channel thicknesses of the Parallel-channels mould in connected channels configuration. Note: results for the  $th_{04}$  channel are plotted only for the first part of the process, as the feature is eventually filled from the largest channels through the machined passages.

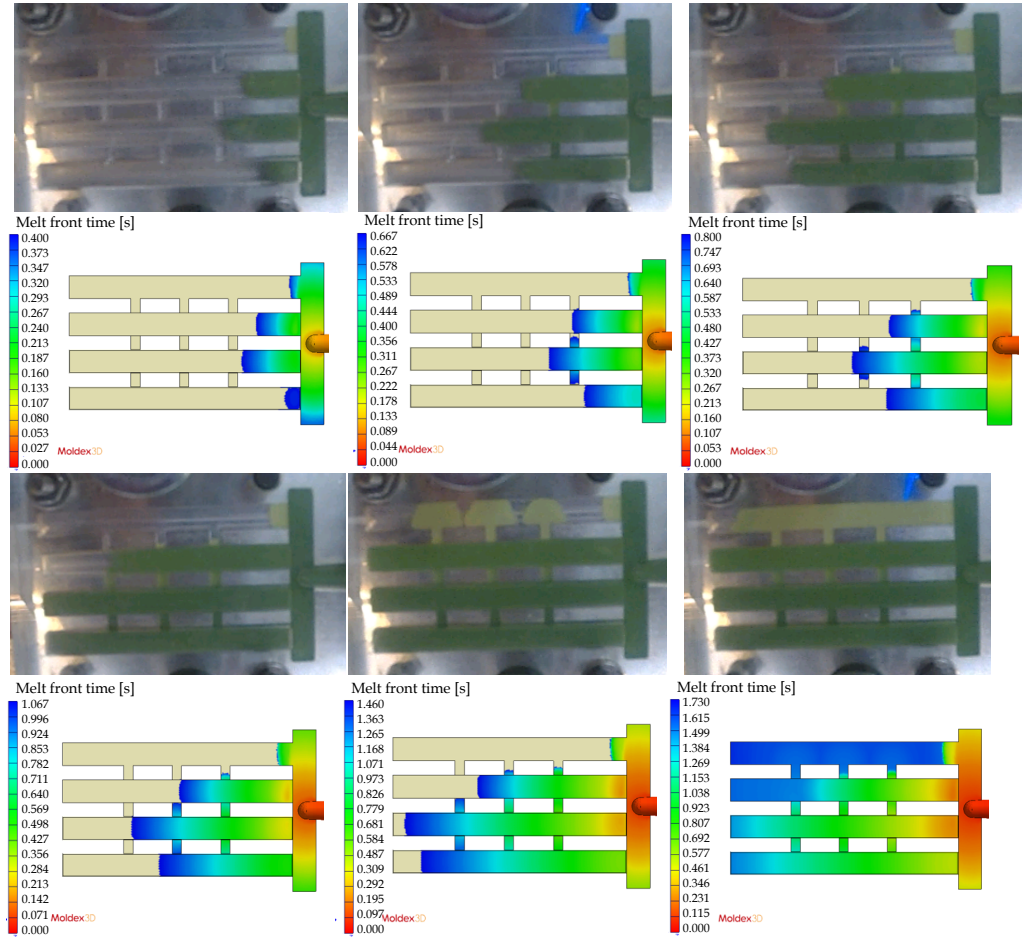


Figure 4.14: Filling model validation,  $T_{melt} = 70\text{ }^{\circ}\text{C}$ . Experiment versus simulated flow length over time for different channel thicknesses of the Parallel-channels mould in connected channels configuration - Visual comparison.

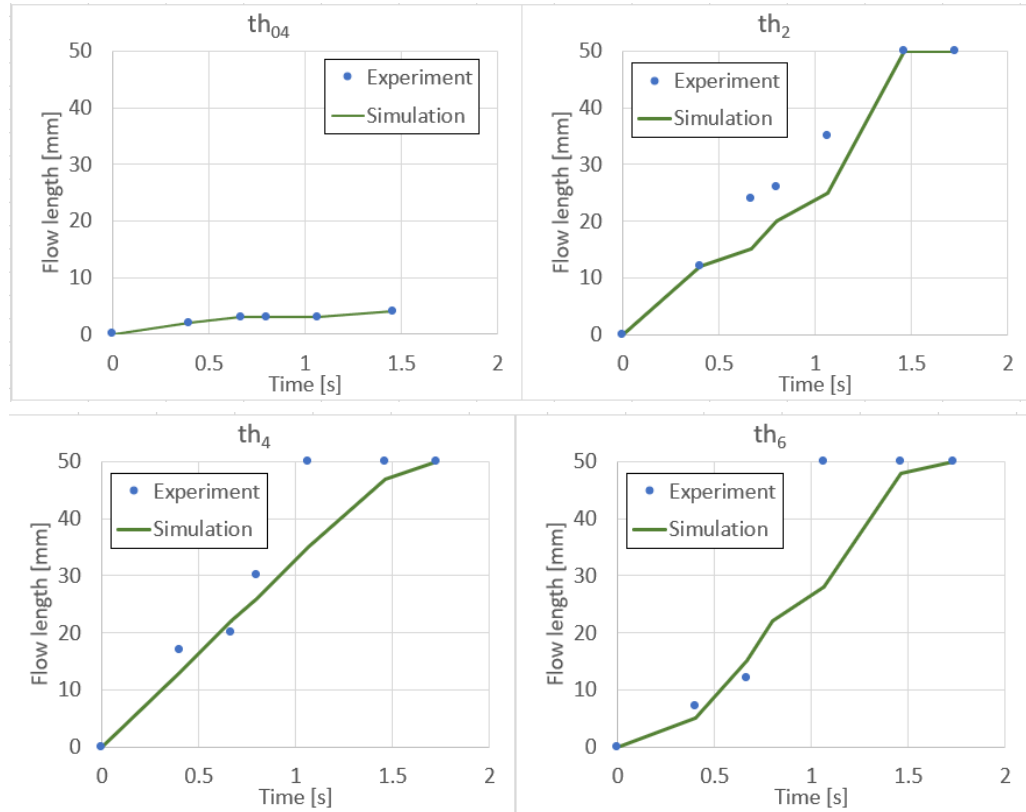


Figure 4.15: Filling model validation, wax feedstock,  $T_{melt} = 70\text{ }^{\circ}\text{C}$ . Experiment versus simulated flow length over time for different channel thicknesses of the Parallel-channels mould in connected channels configuration. Note: results for the  $th_{04}$  channel are plotted only for the first part of the process, as the feature is eventually filled from the largest channels through the machined passages.



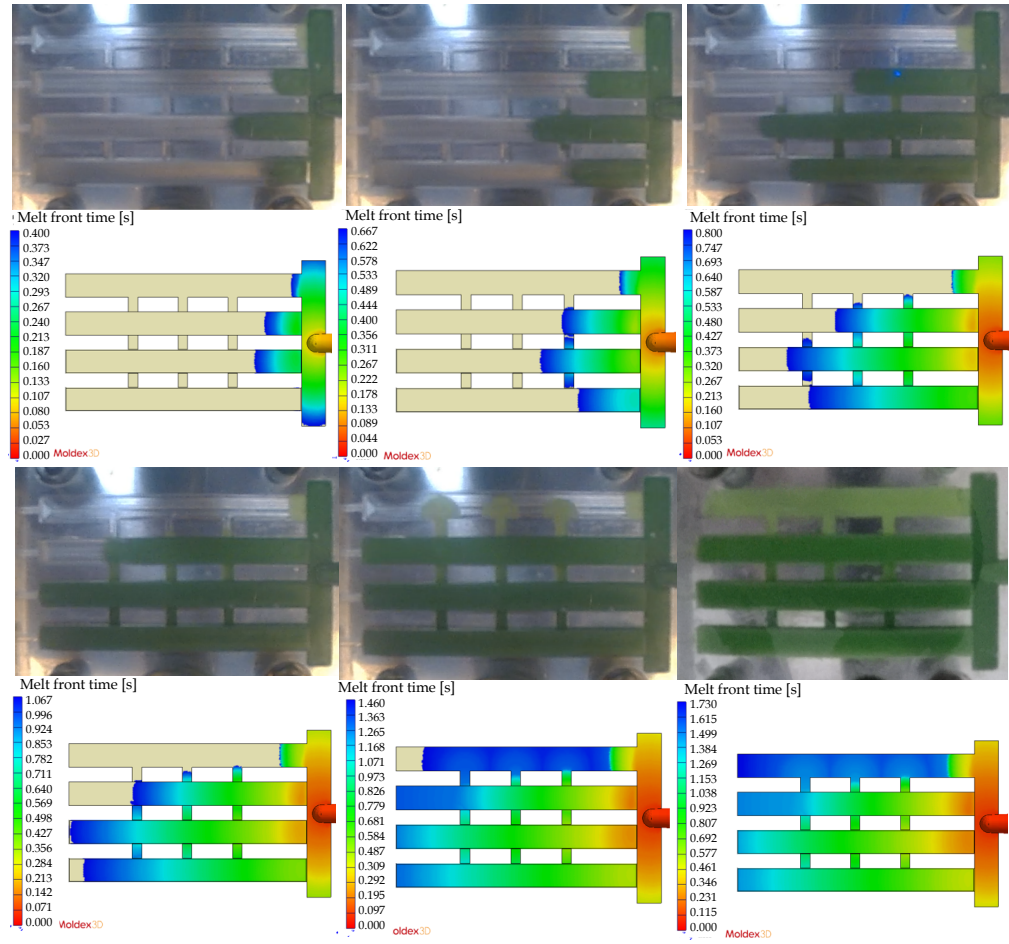


Figure 4.16: Filling model validation,  $T_{melt} = 75\text{ }^{\circ}\text{C}$ . Experiment versus simulated flow length over time for different channel thicknesses of the Parallel-channels mould in connected channels configuration - Visual comparison.

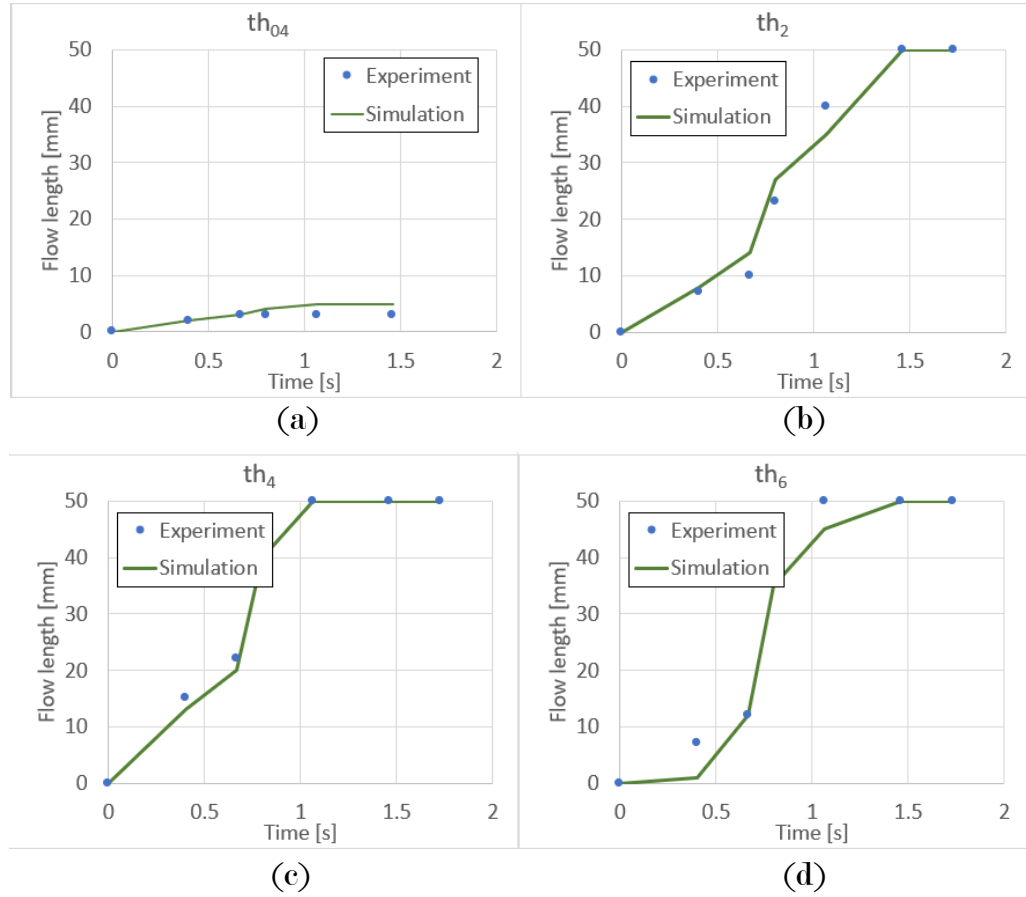


Figure 4.17: Filling model validation, wax feedstock,  $T_{melt} = 75\text{ }^{\circ}\text{C}$ . Experiment versus simulated flow length over time for different channel thicknesses of the Parallel-channels mould in connected channels configuration. Note: results for the  $th_{04}$  channel are plotted only for the first part of the process, as the feature is eventually filled from the largest channels through the machined passages.

#### 4.3.2.3 Validation for ceramic feedstock

The developed filling simulation was finally validated with the ceramic feedstock (using the model material, rather than the Rolls-Royce plc proprietary formulation), in the Parallel-channels mould with the disconnected channels configuration. In this case,  $T_{melt}$  was kept constant at 75 °C, due to the higher obtainable repeatability (being a higher value than the material  $T_m$ ) and higher feedstock viscosity, while mould temperature ( $T_{mould}$ ) was instead varied to validate the model capability to capture the effect of different thermal conditions on the filling behaviour. As previously specified,  $T_{mould}$  was initially kept constant at 30 °C (Figures 4.18-4.19) and then the RHCM approach was followed (Figures 4.20-4.21), by increasing mould temperature during mould filling and then cooling it at a rate of approximately 1 °C/s (Figure 4.7).

For both cases, injection pressure was kept at 4 Bar, and the flow rate was measured to be 12 cm<sup>3</sup>/s for the ambient mould temperature case and 4 cm<sup>3</sup>/s for the RHCM injections. The value of flow rates used in the ambient mould temperature case is higher compared to the equivalent injections in the Parallel-channels mould in the disconnected configuration using the wax feedstock as, due to the higher thermal conductivity of the ceramic material, the maximum injection speed of the pneumatic cylinder needed to be increased in order to achieve cavity filling at ambient mould temperature, before feedstock solidification. However, when increasing mould temperature during filling using the RHCM approach, such a high flow rate caused jetting in the cavity: therefore, the pneumatic cylinder speed was re-adjusted to a lower level.

In both cases, the model successfully predicts the filling behaviour for the

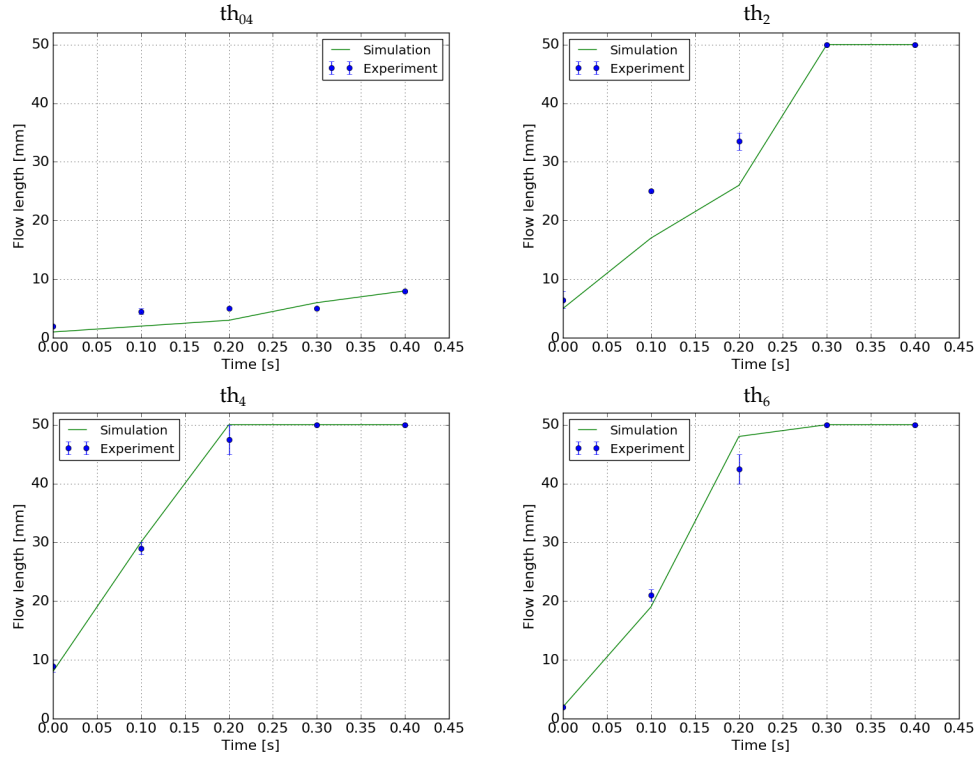


Figure 4.18: Filling model validation, ceramic feedstock,  $T_{mould} = 30\text{ °C}$ . Experiment versus simulated flow length over time for different channel thicknesses of the Parallel-channels mould in disconnected channels configuration. The error bars represent the standard deviation over the five experimental measurements.

four features. For the thinnest channels ( $th_{04}$  and  $th_2$ ), the simulation predicts a lower filling than the measured one, in contrast with what was previously observed with the validation using the wax feedstock: this may be due to the fact that, for thinner features, the channel thickness becomes comparable to the size of the largest particles, hence causing a higher increase of viscosity than the one accounted by the Cross-Exp model, which only considers the effect of temperature and shear rates.

Considering all the analysed cases, the main discrepancies between numerical simulations and experimental results are due to the following reasons:

- The software Moldex3D simulates an actual injection moulding machine, in which the filling is performed at a constant flow rate, while

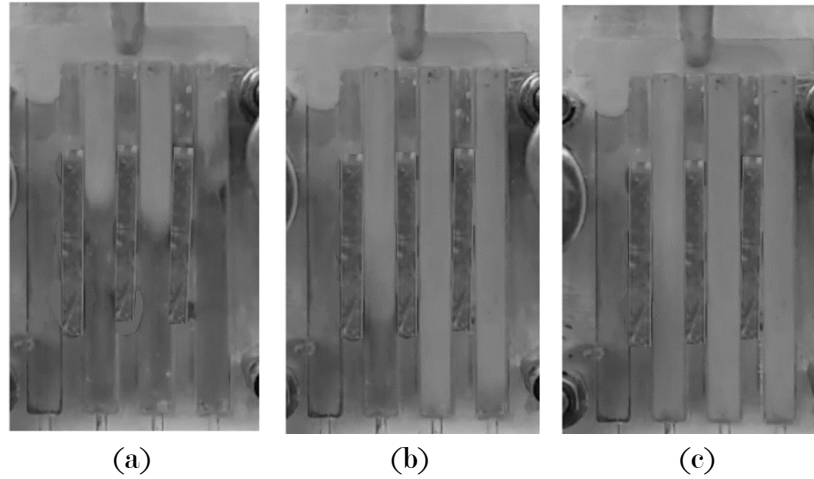


Figure 4.19: Pictures of mould filling, ceramic feedstock,  $T_{mould} = 30\text{ }^{\circ}\text{C}$ , at different time steps. (a)  $t = 0.1\text{ s}$ . (b)  $t = 0.2\text{ s}$ . (c) End of filling.

the pressure is accordingly adjusted automatically; on the contrary, the employed experimental rig works at a pre-set inlet pressure BC.

- Some model assumptions (e.g. cavity venting, viscosity model and part-mould heat transfer coefficient) become more relevant when simulating the filling in thin features, causing an over or under estimate of the actual cavity filling level.
- Inaccuracies in viscosity prediction can be also due to the fact this was modelled based on experimental data which accounted only for a limited range of shear rate levels.

In conclusion, since the trends in simulated and tested filling behaviours are similar for different thermal conditions, and since the sources of variation causing discrepancies between filling model and experimental observations have been identified, the developed simulation can be employed in the subsequent analyses. As previously stated, this was used to enable the visualisation of shear and cooling rates within mould filling, which is necessary to understand the effect of different thermal control approaches on the quality of injected components.

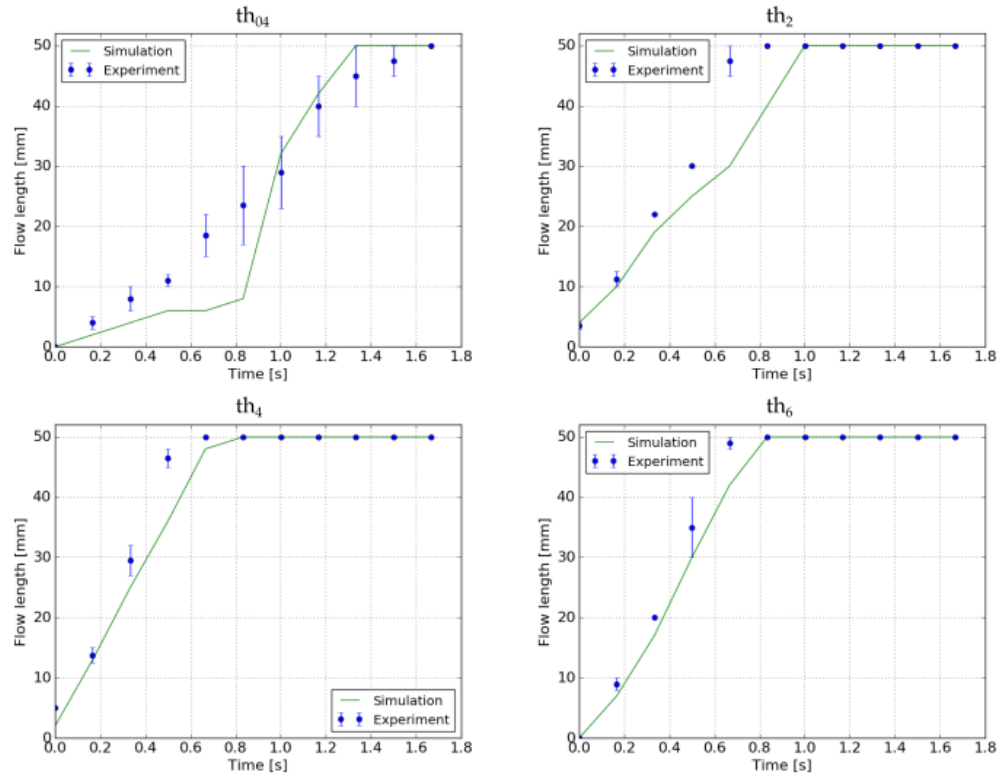


Figure 4.20: Filling model validation, ceramic feedstock, RHCM. Experiment versus simulated flow length over time for different channel thicknesses of the Parallel-channels mould in disconnected channels configuration. The error bars represent the standard deviation over the five experimental measurements.

## 4.4 Step II: Analysis of IM outcomes from green components

Once the filling model was developed and validated, the main challenges in using different thermal conditions during the filling stage of injection moulding were analysed, with the support of the simulation results, using the wax feedstock as a reference material. Likewise for the filling model validation, the Parallel-channels mould was used for this study, in both the connected and disconnected channels configurations, and all the injection moulding tests were carried out using the laboratory rig, described in Chapter 3. These investigations on green parts were performed at ambient mould temperature ( $T_{mould} = 30\text{ }^{\circ}\text{C}$ ), without employing any advanced

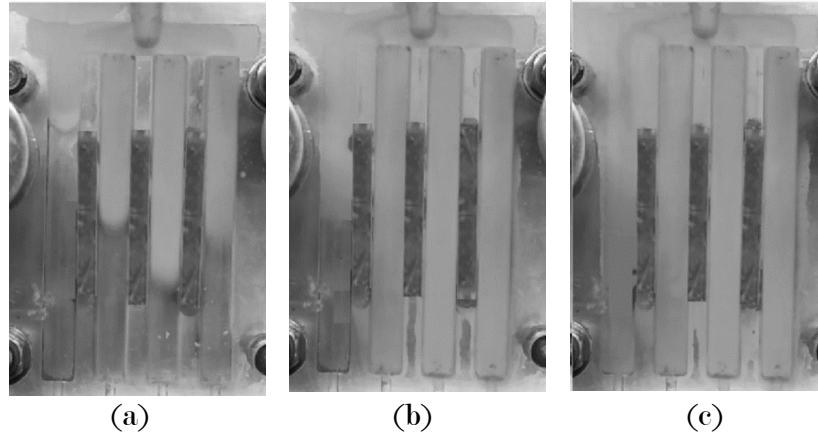


Figure 4.21: Pictures of mould filling, ceramic feedstock, RHCM, at different time steps. (a)  $t = 0.4$  s. (b)  $t = 0.8$  s. (c) End of filling.

thermal control approach, while three melt temperatures ( $T_{melt} = 65$  °C, 70 °C and 75 °C) were used to test the effect of different thermal conditions on as-moulded parts quality. In fact, as the analysed geometry of the Parallel-channels mould contained features having different thicknesses, differential cooling rates and hence a non-uniform temperature distribution were present throughout the part and could be the object of the analysis.

Both macro- and micro-structural properties were analysed, including feature replication capability, surface integrity, weld lines morphology (in the injection configuration with interconnected channels) and filler packing (i.e. distribution within the part).

Feature replication capability was highly affected by the used melt temperature: at  $T_{melt} = 65$  °C the thinnest feature (0.4 mm) could not be entirely filled, even in the mould configuration with connected channels, in which the material could flow from the thicker to the thinner features. When increasing melt temperature, the thinnest feature could be only filled up to approximately 15% of the total flow length in the disconnected channels configuration, but the whole cavity could be filled in the connected channels

one, with the bridges allowing the material to flow from the thicker features to the thinner ones. The inability to fill the thinnest feature despite the increased melt temperature can be attributed to the fast heat transfer towards the cold mould, which causes material solidification before the 0.4 mm thick channels can be filled: this is one of the reasons why increasing mould rather than melt temperature is a more effective strategy to enhance feature replication capability for components having thin wall thickness. Despite the enhanced flowability, with a higher melt temperature, sink marks could be observed on the surface at the end of the thickest bars ( $th_6$  and  $th_4$ ), caused by higher shrinkage occurring in areas farther from the gate, hence solidifying at lower levels packing pressure (Figure 4.22).

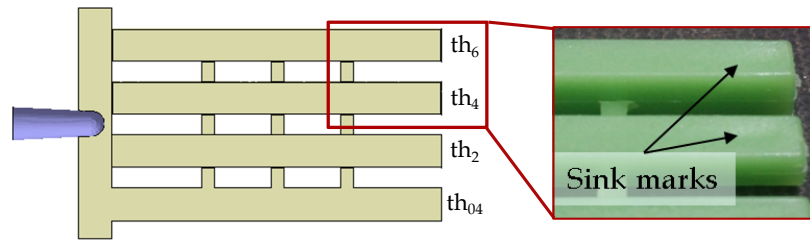


Figure 4.22: Sink marks at the end of the thickest channels,  $T_{melt} = 70\text{ }^{\circ}\text{C}$

Moreover, parts breakage and chipping, due to components sticking to the mould, were experienced when injecting at the highest melt temperature, because of a higher adhesion of the component to the die-tool surface.

Surface and weld lines morphology, as well as filler packing were studied through SEM analysis for the samples moulded with the three different melt temperature configurations, and correlated to simulation results. Considering surface morphology, a clear difference could be observed comparing the surfaces of samples injected at different melt temperatures (Figure 4.23): at lower melt temperatures (Figure 4.23d-e), in fact, the cross-linked polystyrene fillers are observable on the parts surface, while a



smoother top surface is present at increasing temperatures (Figure 4.23f).

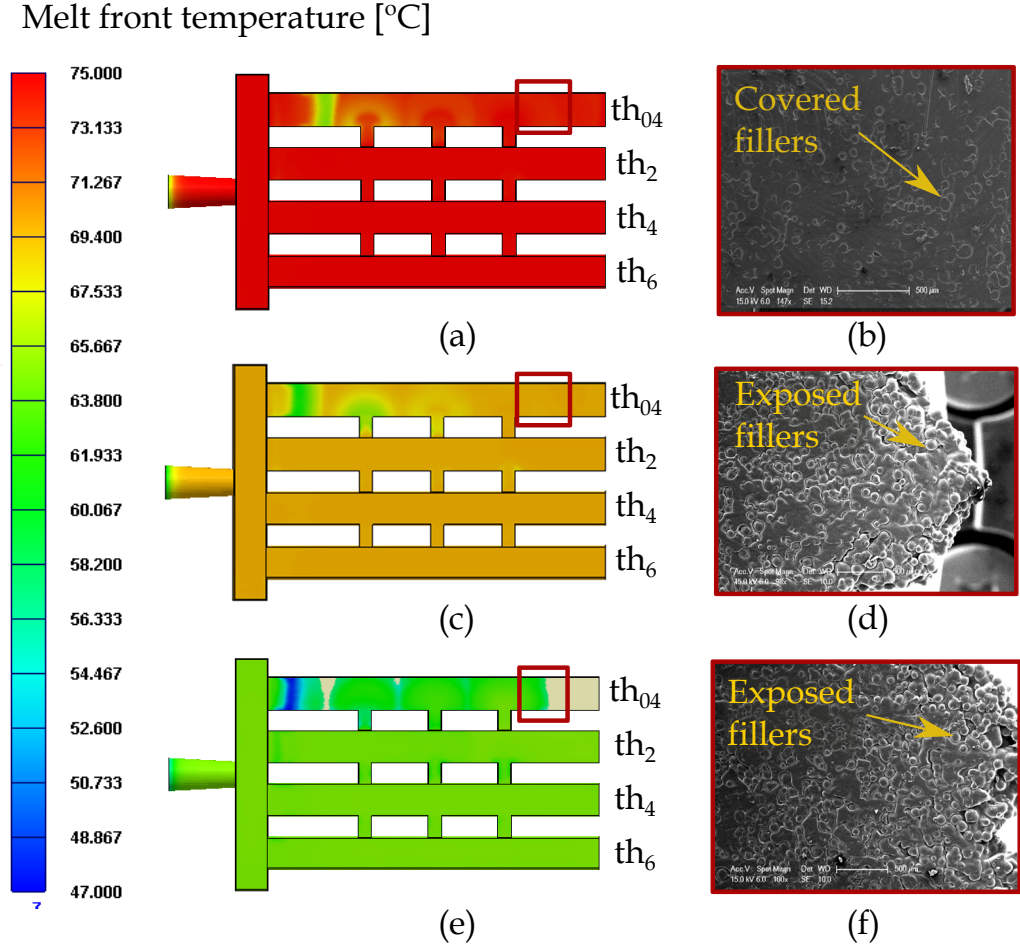


Figure 4.23: Filler exposure. (a) Simulation results for melt front temperature,  $T_{melt} = 75$  °C. (b) SEM micrograph of the top surface of the  $th_{04}$  channel, showing exposed fillers,  $T_{melt} = 75$  °C. (c) Simulation results for melt front temperature,  $T_{melt} = 70$  °C. (d) SEM micrograph of the top surface of the  $th_{04}$  channel, showing exposed fillers,  $T_{melt} = 70$  °C. (e) Simulation results for melt front temperature,  $T_{melt} = 65$  °C. (f) SEM micrograph of the top surface of the  $th_{04}$  channel, showing covered fillers,  $T_{melt} = 65$  °C.

These observations can be related to the melt front temperature (i.e. the temperature of the feedstock during cavity filling), visualised from the filling simulation results (Figures 4.23a, 4.23c and 4.23e), showing a 10 °C variation among the analysed surfaces of the parts injected at the three different temperatures. These changes in temperature cause variations of binder surface tension, which decreases when the feedstock is warmer, thus

increasing its capacity to wet the fillers. In other words, the wax binder will better surround polystyrene fillers and hence result into a smoother surface (Wang, Zhao, and Wang, 2013a). This outcome of surface integrity is therefore related to variations of binder surface tension, showing that keeping the feedstock at higher temperature during mould filling enhances surface finish, which is one of the favourable effects from mould thermal control techniques such as Rapid Heat Cycle Moulding (RHCM).

Analysing the top surfaces of the components moulded with the interconnected channels configuration at weld lines locations, a clear difference in their morphology can be observed because of dissimilar bonding of the flow fronts in different areas of the part (Figure 4.24).

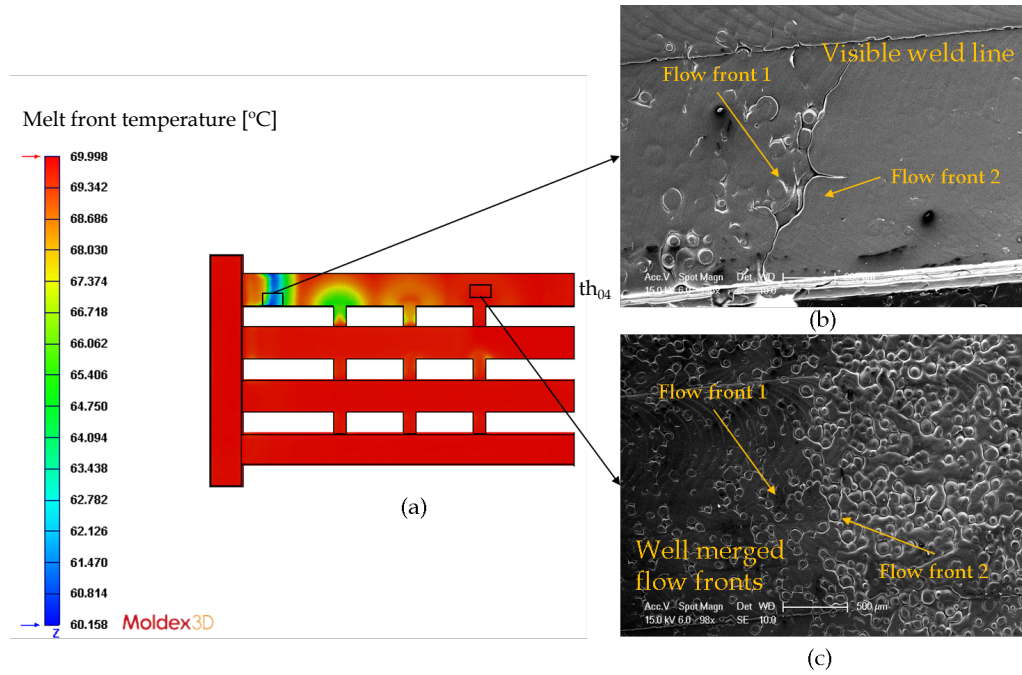


Figure 4.24: Weld lines morphology. (a) Simulation results for melt front temperature,  $T_{melt} = 70$  °C. (b) SEM micrograph of the top surface of the  $th_{04}$  channel, showing a visible weld line  $T_{melt} = 70$  °C. (c) SEM micrograph of the top surface of the  $th_{04}$  channel, showing a well merged weld line  $T_{melt} = 70$  °C.

In all of the analysed areas, good merging of the flow fronts was reached, apart from a visible weld line created on the thinnest ( $th_{04}$ ) channel (Fig-

ure 4.24b). Also this observation can be related to the flow front temperatures during merging, from the filling simulation results (Figure 4.24a), showing that the visible, poorly bonded weld line is, in fact, formed at a temperature (approximately 60 °C) lower than the binder  $T_m$  (62 °C).

The microstructural aspect of fillers packing, which was also studied through SEM analysis, is of particular interest, as this can be assimilated to particle packing in CIM. From the analysis of the surfaces of samples injected at different melt temperatures, variation in fillers content is visible (Figure 4.25) between the portion of the part on the passage connecting the two thinnest channels ( $th_{04}$  and  $th_2$ ) and that of the channel immediately "after" the passage (thus on the material flowed from the passage, as shown in Figure 4.25b).

As an uneven exposure of the fillers was also observed on the parts surface, due to the melt front temperature (Figure 4.23), a further analysis of the cross sections of the two portions of the component showing differential filler content on the surface was also carried out (Figure 4.26). This was performed to assess whether there was actually an uneven filler content, or if this observation was only an effect of differential fillers exposure on the surface.

From this, a clear difference in filler content can be observed, not only on the surface, but throughout the whole analysed cross sections, with a significantly higher packing on the channel (Figure 4.26c), compared to that in the passage (Figure 4.26b). The reason for this variation of fillers packing can also be linked to the simulation results and, in particular, to shear rate levels during mould filling in the analysed areas (Figure 4.25b). A high variation in shear rate is, in fact, measurable in these areas of the compo-

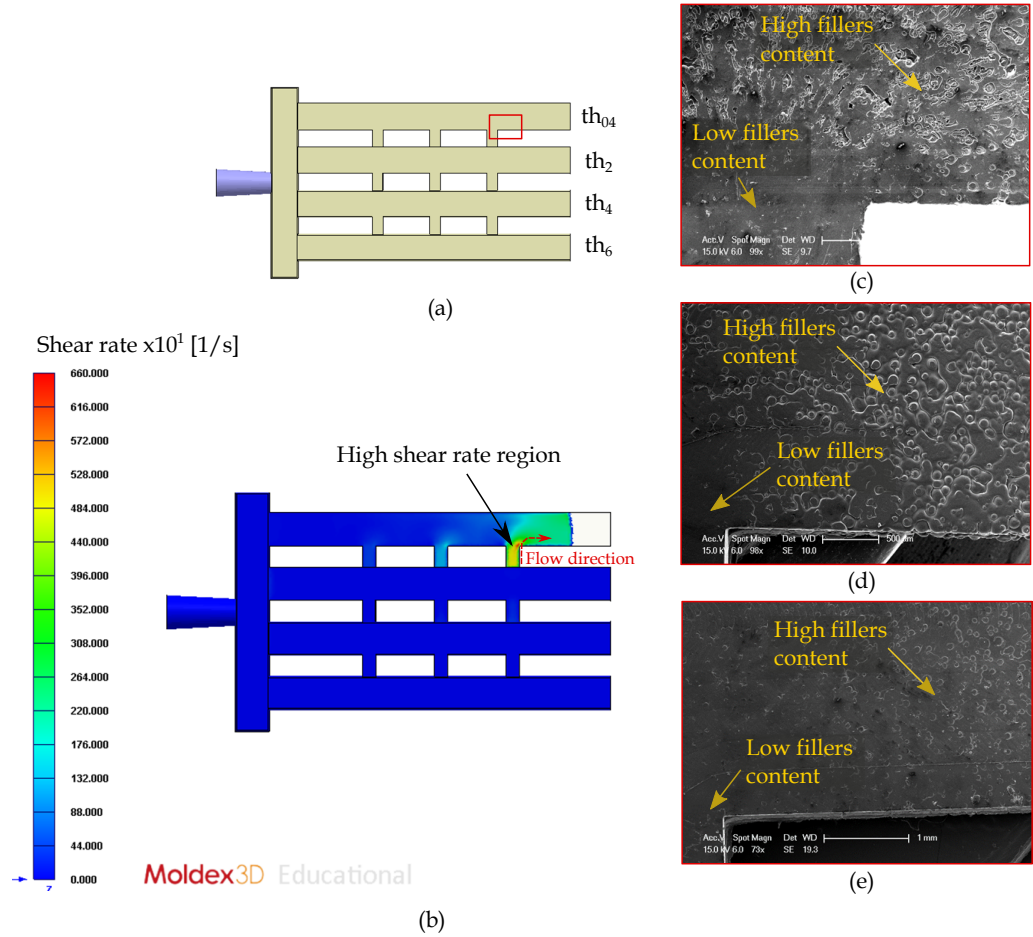


Figure 4.25: Fillers packing. (a) Schematics of samples location in the component. (b) Simulation results for shear rates,  $T_{melt} = 70$  °C. (c) SEM micrograph of the top surface of the  $th_{04}$  channel at bridge location,  $T_{melt} = 65$  °C. (d) SEM micrograph of the top surface of the  $th_{04}$  channel at bridge location,  $T_{melt} = 70$  °C. (e) SEM micrograph of the top surface of the  $th_{04}$  channel at bridge location,  $T_{melt} = 75$  °C.

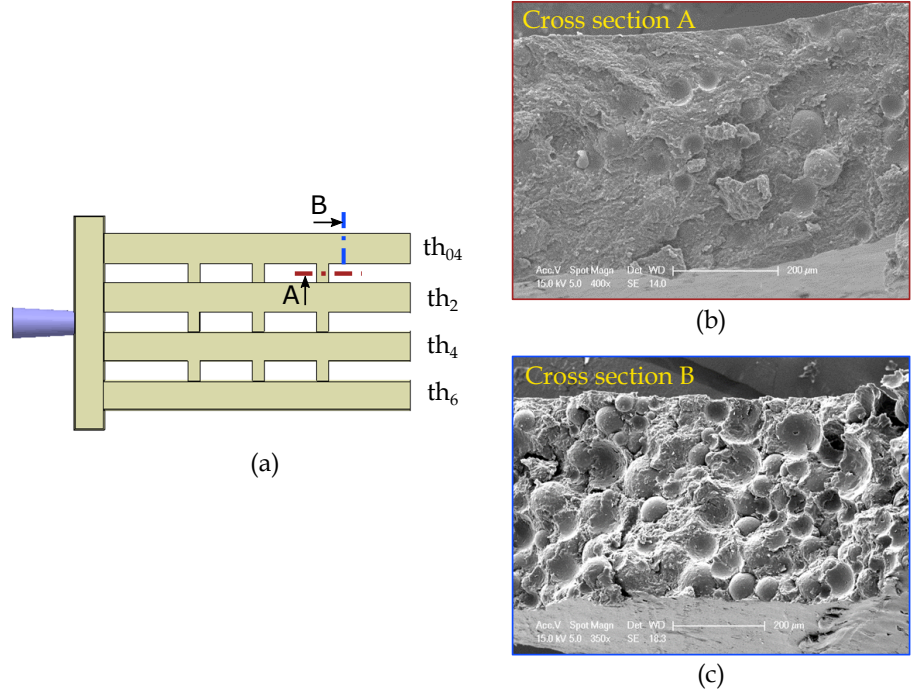


Figure 4.26: Fillers packing. (a) Schematics of samples location in the component. (b) SEM micrograph of the cross section of the bridge between the  $th_{04}$  and  $th_2$  channels,  $T_{melt} = 75$  °C. (c) SEM micrograph of the cross section of the  $th_{04}$  channel,  $T_{melt} = 75$  °C.

nent, with a shear rate on the passage approximately double than on the channel, which has a higher fillers content. The cross-linked polystyrene is therefore separated from the binder due to the high shear rate level on the channel and "pushed" towards the lower shear area on the channel. It is worth noticing that this phenomenon does not change for the three different analysed melt temperature cases. This is due to the fact that shear rate is geometry dependant and, in this area of differential shear rates, the melt front temperature is above the melting point of the material in all the three  $T_{melt}$  cases (Figures 4.23a, 4.23c and 4.23e), due to the low thermal conductivity of the wax feedstock. This means that the actual filled geometry and consequential shear rate variations are the same in the three temperature scenarios. However, when considering a solidifying flow front, the actual cavity geometry changes, due to the material not flowing any more between the cavity plates, but between the solidified flow front, in

contact with the mould. This behaviour is particularly relevant for highly thermal conductive feedstocks (e.g. those employed in CIM), and relates thermal conditions during the process with shear rate levels and consequential fillers packing, hence, this needs to be further investigated. Moreover, the analysed wax feedstock contains spherical fillers, while, when analysing materials with elongated particles, differences in shear rates also play a role in their orientation, which is needed to be analysed for CIM applications.

From this study (Step II) the main effects and challenges related to the presence of different thermal conditions during the filling process on the quality of as-moulded (equivalent to green) parts have been highlighted, with the aid of the results from the developed filling simulation. The following conclusions can be drawn:

- Feature replication capability is highly influenced by thermal conditions during the process, due to changes in feedstock viscosity. However, an approach based on a uniform increase of temperature (e.g. using a higher  $T_{melt}$ ) brings about the drawback of localised higher shrinkage at portions of the part farther from the gate, and hence solidifying at lower packing pressures, as demonstrated by the observed sink marks on the thickest channels.
- Adhesion between part and mould was observed at higher melt temperatures, thus raising the need of investigating the capability of guaranteeing part ejection, when evaluating the performance of thermal control systems.
- Enhanced surface quality, was promoted at higher melt temperature, due to a higher feedstock temperature maintained during mould filling, which could be visualized from the simulation. This, caused by a lower wax surface tension which, in turn, increased fillers wettability.

- Weld lines morphology is highly related to the flow fronts temperature during merging, which could be visualised through the filling simulation results and showing that, good flow bonding is enabled when injection is carried out at higher temperatures.
- Differential fillers packing was observed, due to their migration towards areas of lower shear rates, which could be visualised from the filling simulation. This behaviour was independent on the used melt temperature due to the low thermal conductivity of the wax feedstock, which did not solidify prematurely, hence not causing variations of actual filled geometry.

## 4.5 Step III: Analysis of IM outcomes from sintered components

Once the study of as-moulded parts was carried out with the wax feedstock (Step II), the main research challenge to address is on whether a sintered ceramic part can be analysed to univocally relate its quality outcomes to the IM process. To achieve this, the last step in the development of a methodological framework for the evaluation of thermal system performances for CIM was the microstructural analysis of a large sintered ceramic block (210 mm x 120 mm x 40 mm) moulded and supplied by Rolls-Royce plc (Figure 4.27).

The ceramic block was injected, and then fired with pre-optimised processing conditions by Rolls-Royce plc using a silica-zircon material having rheological and thermodynamic properties (which cannot be disclosed for confidentiality reasons) similar to the ceramic feedstock modelled in Step I. The block was then cut to obtain samples from different areas of the component

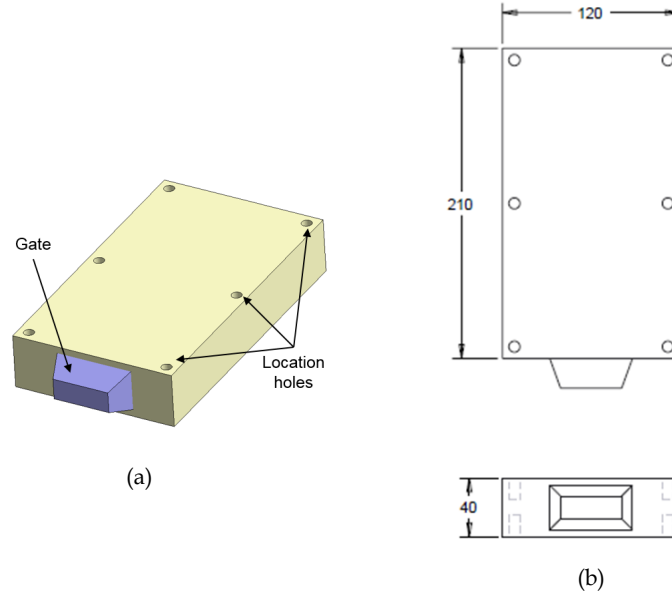


Figure 4.27: Ceramic block used for the study (Step III). (a) 3D view. (b) Main dimensions.

(Figure 4.28a). From each portion of the block (S1 to S6), three samples were cut in orthogonal directions (Figure 4.28b) and analysed through SEM.

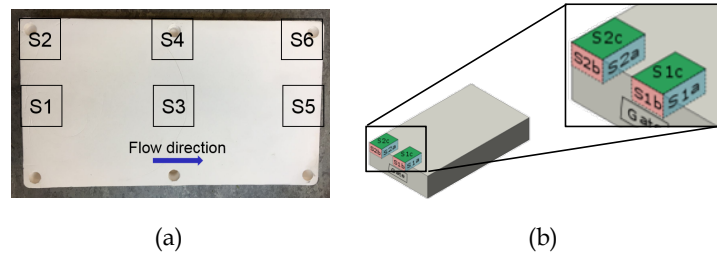


Figure 4.28: Sample location in the ceramic block. (a) Sample mapping in the block. (b) Example of samples location at the beginning of the block.

Defects were detected and related to the injection moulding process using the developed filling simulation, which was set-up using the process parameters displayed in Table 4.4. Since the block was moulded with a similar production material to the ceramic feedstock used in Step I of this study, the same properties were used to model the filling behaviour. From the mapping of the sintered block, the following detected defects were related to the injection moulding process through the support of filling simulation



results.

Parameter	Value
Injection pressure (max) [Bar]	14
Holding time [s]	500
Melt temperature [°C]	80
Mould temperature [°C]	30
Flow rate [cm <sup>3</sup> /s]	350

Table 4.4: Process parameters for ceramic block injection moulding

- **Beginning of the block (Figure 4.29).** Under the gate (S1b) voids were observed (Figure 4.29b), which could be linked to air entrapped in the corners and in the bottom of the block, as indicated from the simulation results (Figure 4.29c). Cracks, due to weld lines, which were correctly predicted by the simulation, were also found in S2b, around a location hole (Figure 4.29d-e).

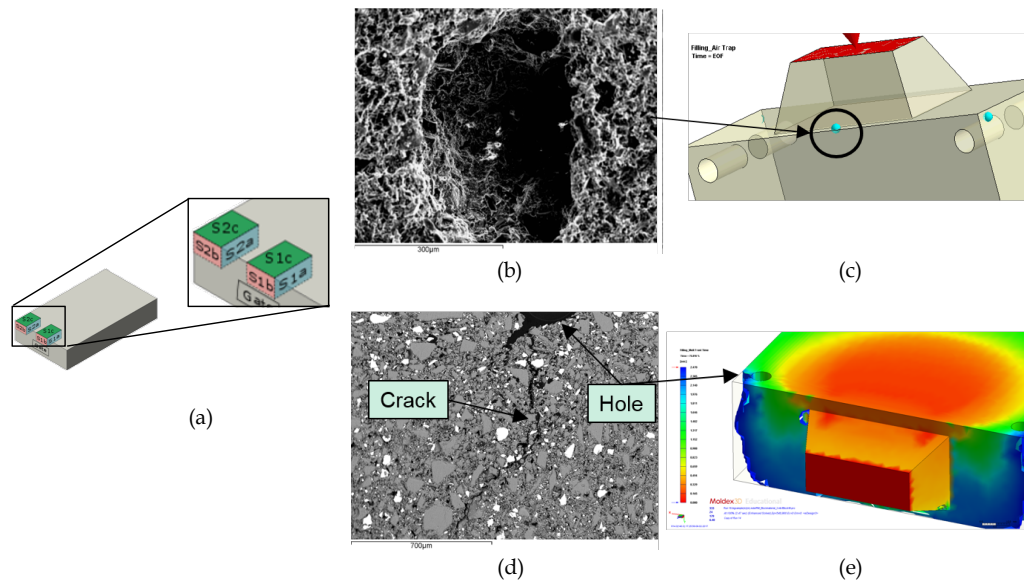


Figure 4.29: Defects at the beginning of the block. (a) Sample location legend. (b) S1b: SEM micrograph of a voids. (c) Simulation results for air trapped. (d) S2b: SEM micrograph of a crack around location hole. (e) Simulation showing mould filling and weld line creation around the location hole.

- **Centre of the block (Figures 4.30-4.31).** A large flow line was

observed along the bottom surface of the block. The cause of this flow line can be understood by looking at the flow-front behaviour in the filling simulation: this shows a fountain flow (Figure 4.30c) with the material depositing with hesitation in front of a solidified layer, created due to the premature solidification of the feedstock during injection, while in contact to the cold mould cavity. The frozen material deposits on the surface and causes a flow line with a similar mechanism to weld lines formation, but with a single flow front instead of two.

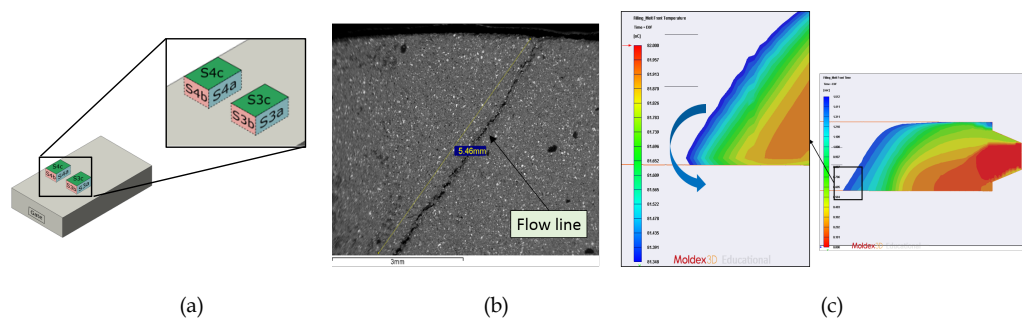


Figure 4.30: Defects at the centre of the block. (a) Sample location legend. (b) S4c: SEM micrograph of a flow line at the bottom surface of the block. (c) Simulation results showing melt front temperature and subsequent flow line creation.

Another defect occurring in the centre of the block is a separation line along the internal section of the block, a few millimetres from the top surface (Figure 4.31a).

This line separates a skin layer from the rest of the block and was detected only at the top half. An explanation to this can be given considering melt front temperature results (i.e. the temperature at which the flow front reaches each point of the block). Because of the high block thickness, gravity plays an important role in cavity filling, by causing the bottom part of the block to be filled first, hence at a higher flow front temperature. This causes a higher melt front temperature gradient at the bottom half of the block compared to the

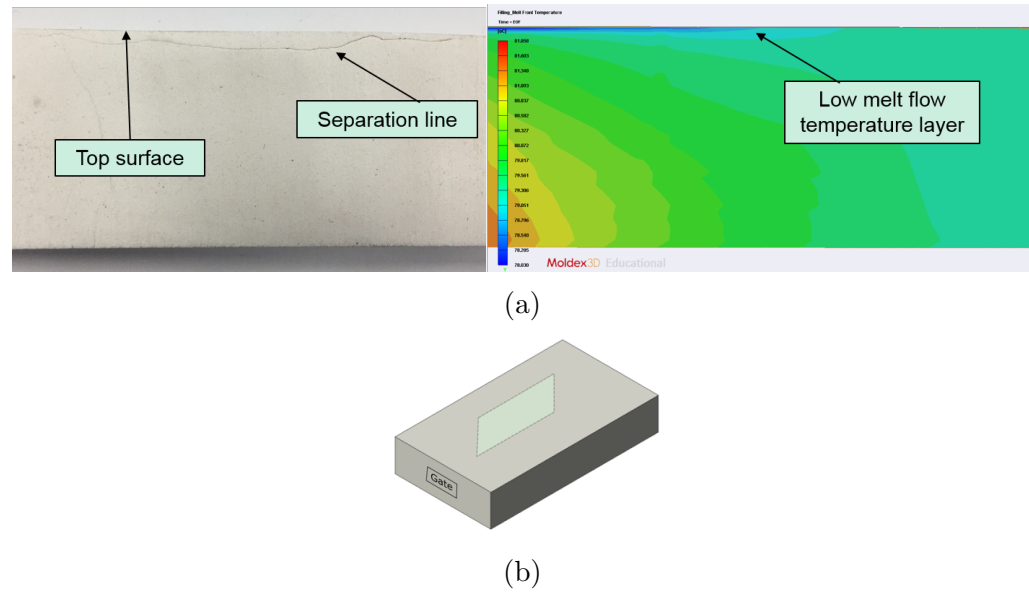


Figure 4.31: Defects at the centre of the block (II). (a) Separation line close to the top surface of the block; (b) Sample location legend.

top, which may have caused a non-uniform, layered microstructure in the green part.

Considering the firing processes, once the green component is placed inside a furnace and the binder starts to degrade and evaporate at high temperature, two main simultaneous phenomena occur: relaxation of residual stresses from the injection moulding process and variations in specific volume within the part, due to the expansion of gas generated in the process and to the shrinkage from binder removal. Alongside with these phenomena, ceramic particles may need to rearrange to accompany binder movements: when inter-particle space is non-uniform across the component, these movements may give rise to warpage and cracking. Once the binder removal is completed, the sintering process starts, in which the remaining ceramic particles merge together through diffusion. Particles closer to each other will have higher energy to diffuse compared to others farther apart and total shrinkage will be inversely proportional to inter-particle space. When a compo-

ment has an uneven packing of particles, different areas will shrink unevenly, hence causing differential sintering shrinkage (or simply, differential sintering), with the development of warpage and, often, cracks. However, similar defects can also arise due to debinding and sintering issues, for example, fast debinding rates, poor supporting of the component, or thermal shocks during cooling down after sintering.

Although differential sintering mechanisms are likely to have caused this crack, no differences in particle orientation or packing could be observed by SEM analysis, probably due to particle rearrangement and diffusion during the firing process. Therefore, it is not possible to have an experimental evidence that allows to univocally link this defect to non uniform particle packing or orientation to the IM process. When evaluating thermal control system performances for CIM, it is hence fundamental to analyse green parts microstructure to assess if the thermal approaches under analysis promote suitable packing and orientation of particles for the subsequent firing processes.

- **End of the block (Figure 4.32).** Voids were observed at the end of the block (Figure 4.32b): unlike those found near the gate, these voids could not be associated to air trapped results from the simulation. However, considering the flow pattern showed by the filling model in this area (Figure 4.32c), voids can be explained by flow disruptions due to the material hitting the end wall of the block and flowing backwards. This may have caused air to be trapped in this part of the block and thus generating the voids detected through SEM analysis.

Considering the performed analysis, cracks due to weld lines, flow lines and voids were detected and successfully univocally related to the IM process through the aid of the filling model results. However, some cracking defects,

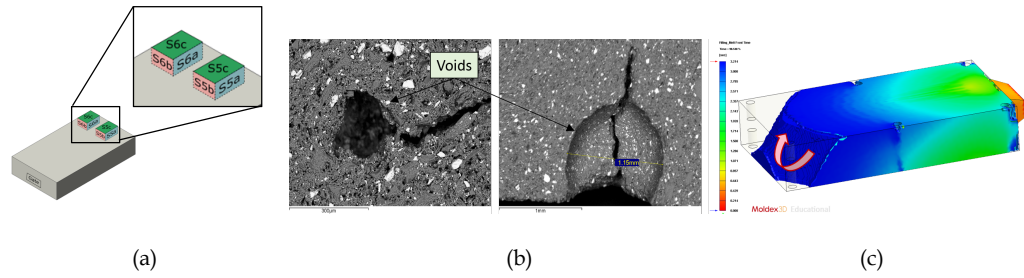


Figure 4.32: Defects at the beginning of the block. (a) Sample location legend. (b) S5a: SEM micrographs of voids. (c) Simulation results showing turbulences in flow.

which are thought to be attributable to microstructural outcomes from the IM process could not be proven through the analysis of the sintered component, probably due to microstructural changes from the firing processes. For this reason, in order to achieve a full understanding of the influence of different thermal conditions on injection moulded parts quality, and evaluate the performance of thermal control systems, in the present work, green parts were analysed and their microstructure was associated to final sintered part quality, based on results of studies available from the reviewed literature.

## 4.6 Conclusions

A methodological framework for the performance evaluation of thermal control systems for injection moulding die-tools has been introduced and developed using a step-wise approach. This study leads to the following conclusive remarks:

- A simulation of the IM filling stage was developed and validated for a wax and for a ceramic feedstock. The model enables the prediction of temperature distribution during IM. This provides the capability of using the model as a support tool to correlate the quality of moulded components to the thermal phenomena occurring during IM and, thus, to help evaluate the performance of thermal control systems.

- The effect of different thermal conditions (obtained by varying melt temperature) has been explored on the quality of as-moulded parts using a wax feedstock having similar properties to the binder of the CIM feedstock used within the present work, and containing spherical fillers. Higher temperatures during the filling process enhance feature replication capability, weld line morphology and surface quality, but promote shrinkage-related defects and increase mould-part adhesion, which can challenge the components ejection. Moreover, although differential fillers packing was observed, due to shear rate variations within the part, it was not possible to relate this phenomenon to cooling rate differences within the part, due to the slow solidification rates of the wax feedstock. The developed filling model was successfully employed to support the understanding of the observed green part microstructure, which is fundamental to evaluate the performance of thermal control systems in CIM applications.
- The microstructural analysis of a sintered ceramic block allowed the successful tracking of some defects which arise from the injection moulding process (e.g. weld lines and voids). However, variations in the component microstructure during debinding and sintering does not allow to univocally correlate some of the cracking defects to the IM process. For this reason, green ceramic components were analysed for the performance evaluation of current and newly developed thermal systems for CIM die-tools.

## Chapter 5

# Application of rapid thermal cycling to CIM

*Rapid Heat Cycle Moulding (RHCM) is a widely used thermal control approach, consisting of an increase of mould temperature during the filling stage of Injection Moulding (IM) and then a fast cool down of the die-tool, in order to achieve quick part solidification. This technique is effective in increasing feature replication capability and surface quality of injected parts and, therefore, has a great potential in being applied to Ceramic Injection Moulding (CIM), when components having fine features need to be manufactured. However, as RHCM has not been employed in CIM applications, an analysis of its performances needs to be carried out. In this study, two main aspects are going to be considered: the effect of RHCM on particle orientation and packing, which are fundamental microstructural outcomes affecting the quality of sintered parts, and on the adhesion behaviour between part and mould, which can cause components chipping and cracking during part ejection. This will provide an overview of the performance of this state-of-the-art mould thermal control approach, which will enable the development of a novel thermal control system that will be described in the following chapter.*

## 5.1 Introduction

In polymers applications, usually, components are designed according to mouldability guidelines imposing uniform wall thickness. This cannot often be done in CIM, when some components, such as the already introduced case of ceramic cores for the investment casting of turbine blades and vanes, present strict design requirements, imposing geometries having uneven wall thickness. The injection moulding of such ceramic components presents several challenges, related to feature replication capability, dimensional control and structural integrity throughout the three process steps of IM, debinding and sintering. While increasing injection pressure would help enhance feature replication capability, it also brings about the drawback of raising shear rates and stresses occurring during the process, which causes quick wear of die-tools, when using feedstock highly loaded with abrasive particles. Therefore, as explained in Chapter 2, the Low Pressure Ceramic Injection Moulding (LPCIM) approach is often employed for the injection of complex components, such as ceramic cores, consisting of moulding parts at low pressures and melt temperatures. This reduction of pressure parameters further increases the challenges in feature replication capability, which advanced die-tools thermal control approaches can contribute to solve.

RHCM is a widespread mould temperature technique in polymers application, which enhances the capability of injection moulding components having fine features, due to an increase of die-tool temperature during filling, while maintaining low cycle times through a rapid temperature decrease during the cooling phase (Wang and Mao, 2009). As concluded from the revision of state-of-the-art literature (Chapter 2), despite the potential of this approach, it has not been employed in CIM (and, especially, LPCIM) applications and, therefore, there is a need to evaluate the effect of RHCM on



the quality of ceramic moulded parts, in order to assess its suitability as an approach to enhance the capability of moulding ceramic components having uneven wall thickness. Some aspects of CIM outcomes are in common with conventional polymers applications and have been already addressed in the literature regarding RHCM, such as feature replication capability (Wang, Zhao, and Wang, 2014b) and weld lines morphology (Wang, Zhao, and Wang, 2013a; Wang, Zhao, and Wang, 2014b; Chen, Jong, and Chang, 2006).

However, as also discussed in Chapter 4, the integrity of ceramic moulded parts is highly affected by the microstructure developing during the IM process, which then evolves throughout the subsequent stages of debinding and sintering. Although, from the current literature, it is possible to achieve an understanding of how defects evolve throughout the CIM process stages (Mannschatz, Müller, and Moritz, 2011; Zhang, Blackburn, and Bridgwater, 1996; Wright, Edirisinghe, Zhang, and Evans, 1990), there is the need of investigating part quality in the green state. As no studies on performance evaluation of the RHCM approach in CIM has been performed, its effect on green part microstructure is yet to be investigated. In particular, the phenomena of particle packing and orientation are of interest, as they are one of the main causes of differential sintering in CIM.

Moreover, considering the main findings discussed in Chapter 4, variations in mould-part adhesion behaviour have been observed under different thermal conditions, and this had also been reported in previous studies on ejection forces in hot embossing (Worgull, Héту, Kabanemi, and Hecke, 2008). This aspect highly affects the ejection process, as strong adhesion between the moulded component and the die-tool can be detrimental for ceramic components during demoulding (i.e. part ejection), due to the brittle na-

ture of green parts. Despite this, probably due to the higher mechanical strength of polymer components, in the performance evaluation of rapid thermal cycling approaches, the aspect of ensuring integral part ejection has been neglected. With this in mind, there is a need to assess how RHCM affects part-mould adhesion behaviour and consequential ejection forces, in order to fully assess the suitability of this approach for CIM, and develop novel thermal control systems which account also for component demoulding.

Therefore, in the present chapter, the performance of RHCM for ceramic applications will be studied, by carrying out two investigations. The first (Section 5.2) studies the effect of rapid thermal cycling on particle orientation and packing. The study will be carried out following the methodological framework for the evaluation of thermal control systems for CIM die-tools, developed and discussed in Chapter 4: therefore, the developed filling simulation will be employed as a support tool to understand how observed microstructural outcomes originate from the heat transfer phenomena occurring due to the employed thermal control approach. The second investigation (Section 5.3) studies the effect of RHCM upon the adhesion between part and mould in CIM: this will be done by experimental measurements of demoulding forces, carried out using a bespoke test rig and with the aid of microstructural investigations.

## **5.2 Effect of RHCM on ceramic particle orientation and packing**

In the present section, the study on the effect of rapid thermal cycling on the particle orientation and packing in CIM is described and discussed. First,

the experimental methodology followed in this study is explained, and then the main findings of the work is presented and discussed.

### 5.2.1 Experimental methodology

To address the shortcomings in current knowledge around the influence of RHCM on particle packing and orientation in CIM, an experimental process has been undertaken, which is described in the following. The Parallel-channels reference part (Figure 5.1), already used in Chapter 4 was employed, in order to enable the visualisation of particle orientation and packing in a component having features with different wall thickness, when moulded at ambient mould temperature and using the RHCM approach.

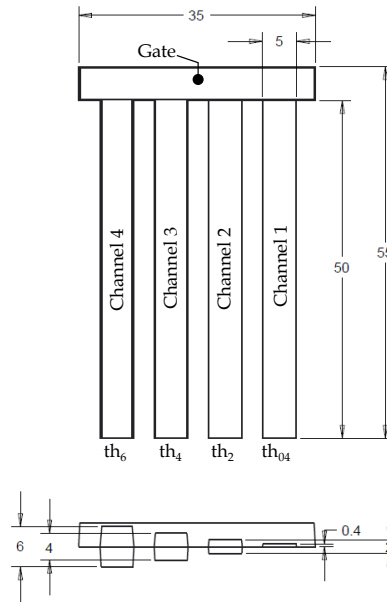


Figure 5.1: *Parallel-channels* reference component.

The component was injected using the Parallel-channels mould which was, as already described in Chapter 4, equipped with a Peltier module, used in order to heat and cool the die-tool. Low-Pressure Ceramic Injection Moulding (LPCIM) tests were carried out with the laboratory rig described in Chapter 3, with five repetitions per trial and using the same process parameters described in the model validation within Chapter 4 (Section

4.3.2.3). The silica-zircon ceramic feedstock, used for the filling model validation, was used for this study, as it contains elongated particles, which can exhibit a preferential orientation (Figure 5.2). As the model was validated for this feedstock, it could be used as a support to understand how the observed packing and orientation of particles correlate to the heat transfer phenomena occurring during mould filling in the present study.

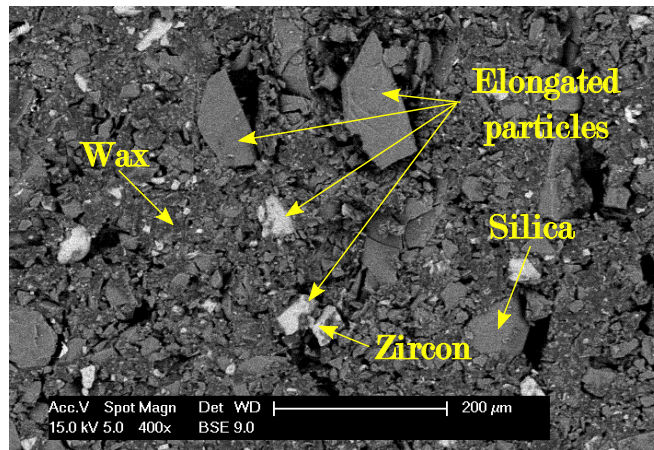


Figure 5.2: SEM micrograph of fracture surface for the ceramic feedstock, showing the presence of elongated particles.

Particle orientation and packing in injected ceramic parts were characterised by direct and indirect methods: the former consist of microstructural analysis through scanning electron microscopy, while the latter include density measurements, shrinkage evaluation and *in-situ* micro-mechanical testing.

For the microstructural analysis, samples were sliced from the channels to be analysed at locations shown in Figure 5.3: in order to preserve the microstructure of the analysed surface, a brittle cut was performed, with an incision on the external face in contact with the clear PMMA plate for the three thicker bars. The top half of the sample was not, hence, analysed, as part of the surface may have been smeared by the initial incision. The samples were then carbon-coated to better visualise different feedstock com-

ponents through the Scanning Electron Microscope (SEM) Back Scattering Electron (BSE) detector. The Philips XL30 SEM and a FEI Quanta 650 Environmental SEM were both used to analyse moulded parts microstructure, in order to assess particle packing and orientation.

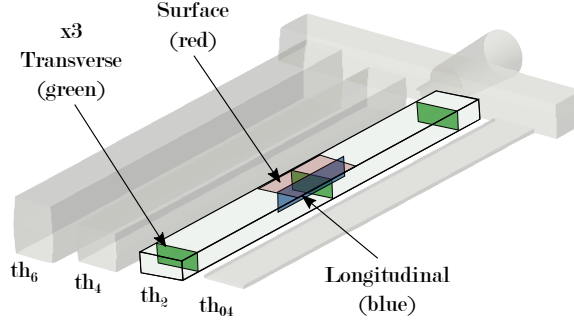


Figure 5.3: Schematics of samples cut for microstructural analysis to investigate particle orientation and packing

SEM micrographs were finally post-processed with the software ImageJ to determine particle orientation in ceramic samples: as all the micrographs were taken with the vertical axis parallel to flow direction, the Feret angle (i.e. the angle between the horizontal axis of the picture and the longest Feret diameter) was used to quantify the degree of orientation. Feret diameter is defined as the maximum distance between two parallel tangents on opposite sides that do not intersect the particle (Allen, 1981). Since the samples contained a broad particle size distribution, with largest Feret diameters being as large as  $200\text{ }\mu\text{m}$ , micrographs at low magnification (up to approximately 400x) had to be analysed: therefore only particles larger than  $50\text{ }\mu\text{m}$  were taken into account, as they could be clearly detected in the image post-processing. Moreover, to avoid bias from circular particles, thus without a preferred orientation, only platelets with a circularity lower than 0.7 were considered, as per the categories reported by Powers (1953). A qualitative evaluation of powder packing, in particular related to particle size distribution, was also performed through analysis of SEM micrographs.

Considering the indirect evaluation methods, particle content was inferred by density measurements of samples taken from the centre of the bars and having a volume ranging from 0.1 to 0.3 cm<sup>3</sup>, performed through an Accu-Pyc<sup>TM</sup> 1330 gas pycnometer: knowing that the powder density is higher than the binder one (approximately 2400 and 970 Kg/m<sup>3</sup> respectively), particle content will be proportional to the feedstock density. The solid loading could be directly calculated from the measured density of samples by the rule of mixtures (Demers, Turenne, and Scalzo, 2015); however, this method is not applicable to this case, due to the higher density of zircon compared to silica, hence causing a variable powder density, depending on the amount of each component (silica and zircon) present in each sample, which cannot be measured.

A shrinkage analysis was also performed by gauging parts after injection moulding and, to allow a cross-reference between part shrinkage and mould dimensions, the cavity was measured using a Mitutoyo Euro-C-A121210 coordinate measuring machine (CMM). The purpose of evaluating part shrinkage is to correlate it to different packing and orientation microstructures (due to various thermal control approaches) that would lead to diverse shrinkage rates in the injected parts.

A Gatan Microtest 200VT tensile-compressive stage was then employed to conduct uniaxial compression tests on the green ceramic injected samples, subject to the same preparation methodology as for the SEM analyses, and mounted within the FEI Quanta 650 Environmental SEM chamber to enable live visualisation of the specimens during the mechanical testing. Figure 5.4 shows the employed setup (from a top view), for which ceramic samples were fixed through epoxy resin into pockets machined at the two opposite sides

of two mild steel bars, in order to reach the required length to be fit within the clamping jaws of the compressive stage. For this analysis, the SEM was used in low-vacuum mode, with a chamber pressure of 70 Pa, to allow the observation of the non-conductive samples during cracking.

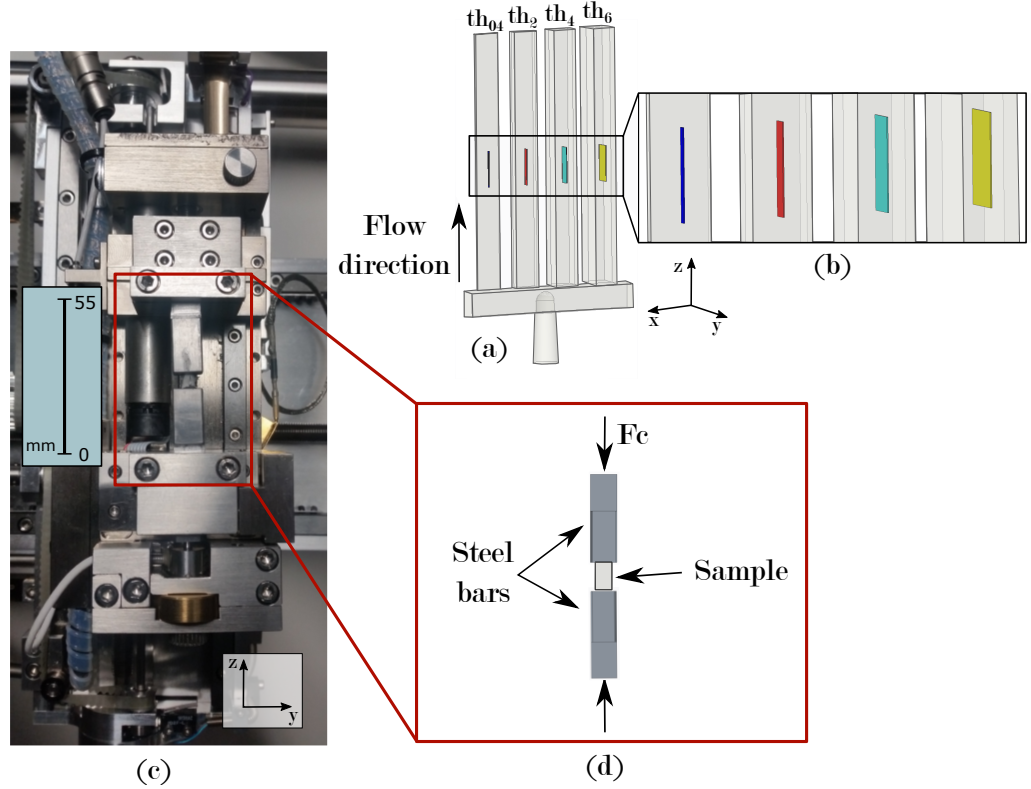


Figure 5.4: Setup for uniaxial micro-compression tests under SEM - Part thickness in the  $y$ -axis of the reference coordinate system. (a) Moulded part. (b) Samples location. (c) Stage mounted within the SEM (top view). (d) Specimen.

While mechanical tests have been used in literature to study the strength of die-pressed green components (Özkan and Briscoe, 1997; Amorós, Cantavella, Jarque, and Feliú, 2008), the approach in the present work presents a novel aspect, as compression tests were not used as a direct method to measure part strength, but as an indirect approach to detect particle orientation and packing in green ceramic samples. This was enabled by performing the tests inside a SEM chamber, to visualise cracking at a micro-scale level and relate it to packing and orientation of particles. In particular, this method

helps in the detection of particle packing and orientation in two ways: first, the cracking initiation locations under compression depends on the local mechanical strength of the material, which, in turn, is influenced by the level of packing and orientation in different regions of the specimen; second, from a quantitative point of view, differences in material stiffness between different samples is determined by the overall level of packing and orientation of the analysed parts. These interdependencies are discussed more in detail in the following section, together with results from the analysis.

### 5.2.2 Main findings of the study

In this section, experimental results are discussed with a focus on particle packing and orientation development in ceramic feedstocks during IM, using both the conventional process (i.e. constant temperature) and RHCM. The experimental observations are presented along with the numerical simulation results, in order to support the analysis of the phenomena in relation to temperature and shear rates occurring within the moulded part during the injection process.

Components injected at constant mould temperature (30 °C) presented short-shots at the thinnest feature ( $th_{04}$ , 0.4 mm thick), which could be filled only for approximately 16% of the total channel volume (8 mm length), shown as  $L_f$  in Figure 5.5a.

This can be explained as follows: during the injection phase, the material tends to flow in the thicker channels first, where the lowest pressure drop is needed to fill the features. When the thicker channels are filled, pressure in the mould rises and the feedstock starts flowing in the thinnest ones, as confirmed by simulation results (Figure 5.5b-d). By keeping mould tem-



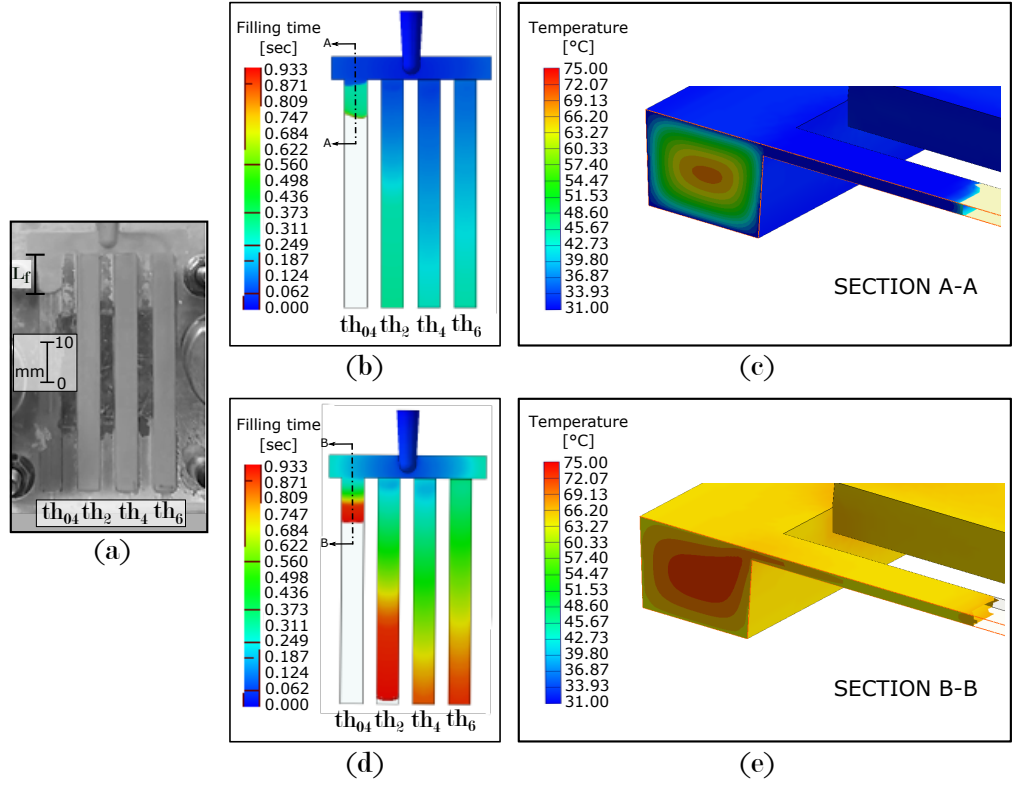


Figure 5.5: Example of cavity filling and temperature distribution (0.933 sec after the beginning of injection) for conventional and RHCM approaches. (a) Injection moulded part,  $T_{mould} = 30^\circ \text{C}$ . (b) Melt front time,  $T_{mould} = 30^\circ \text{C}$ . (c) Temperature distribution inside the thinnest (0.4 mm) channel,  $T_{mould} = 30^\circ \text{C}$ . (d) Melt front time, RHCM. (e) Temperature distribution inside the thinnest (0.4 mm) channel, RHCM.

perature below the glass transition point ( $T_g$ ) of the feedstock and close to ambient temperature, the feedstock has time to solidify whilst the thicker channels are being filled, hence causing a failure in replicating the thinnest feature. This temperature drop in the thinnest channel is evident from Figure 5.5c, where, in the longitudinal cross section of the 0.4 mm thick feature, temperature is evidently below the melting point and the  $T_g$  of the feedstock. On the other hand, by increasing mould temperature above  $T_g$ , the thinnest bar could be completely filled, being the feedstock still molten towards the end of the filling stage, as shown in Figure 5.5e.

### **Particle orientation and packing: direct characterisation methods**

As the scope of this work is to study the effect of RHCM on particle orientation in ceramic moulded parts, SEM micrographs of samples injected at ambient and mould temperature using rapid thermal cycling were analysed and compared. Figures 5.6 and 5.7 depict a schematic of particle orientation along the channel thickness (Figures 5.6a and 5.7a) and examples of alignment distribution for the four analysed bar thicknesses in the ambient mould temperature (Figures 5.6d to 5.6g) and the RHCM case (Figures 5.7d to 5.7g) respectively. As previously specified in Section 5.2.1, the SEM micrographs of the studied samples were postprocessed and the particles Feret angle was analysed across part thickness in order to assess the degree of orientation.

In all of the samples, a stratified microstructure, consisting of layers having different particle orientations, is visible (Figures 5.6d-g and 5.7d-g). Considering parts moulded at ambient temperature, the three thickest bars (6 mm, 4 mm and 2 mm), as shown in Figures 5.6e, 5.6f and 5.6g, present: (i) an external frozen layer, with randomly aligned particles; (ii) an intermediate shear layer with platelets oriented along the flow direction and (iii) a wider

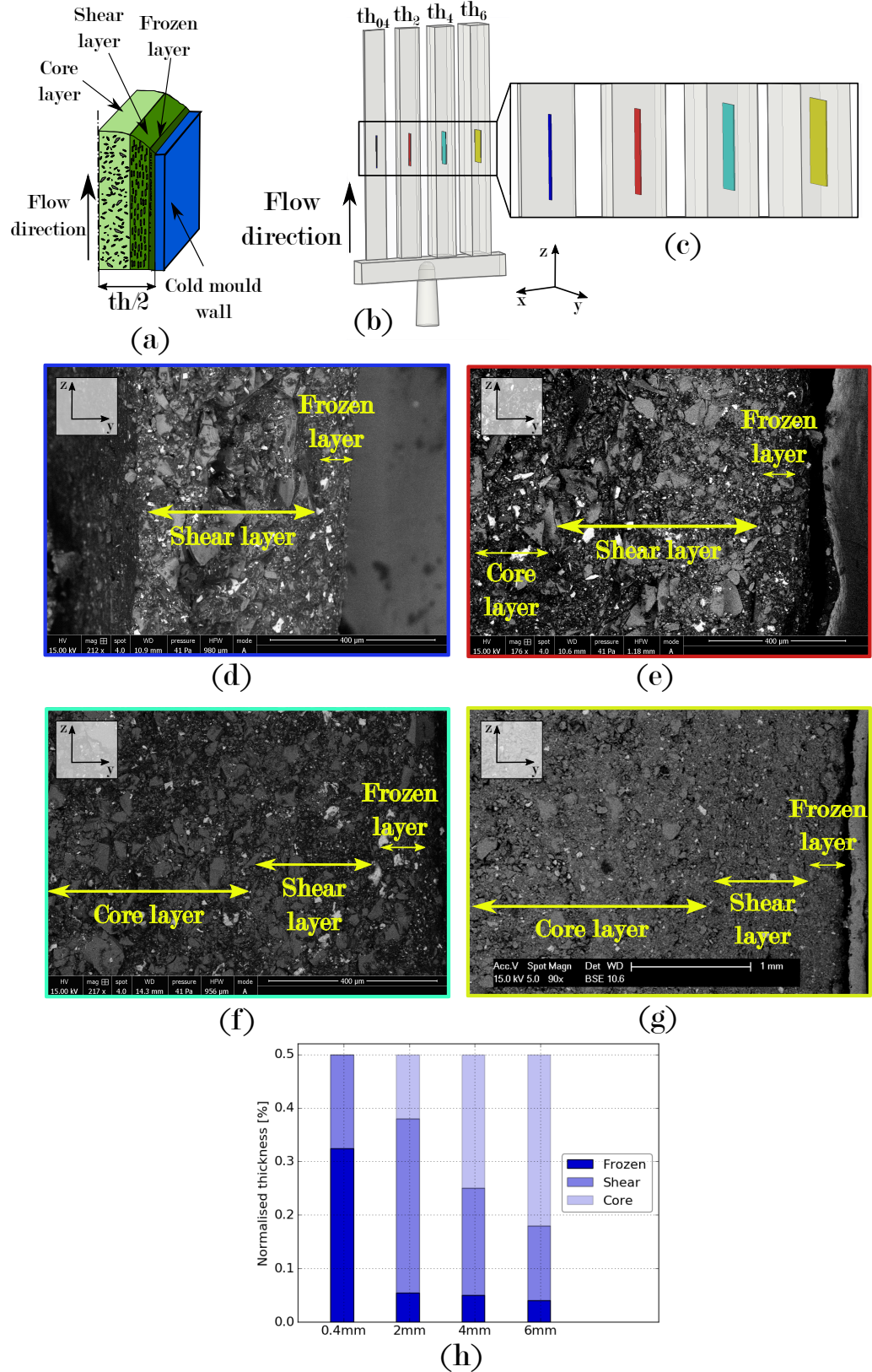


Figure 5.6: Examples of orientation distribution in ceramic injection moulded green samples, ambient temperature - Part thickness in the y-axis of the reference coordinate system. (a) Schematics of the microstructure. (b) Moulded part. (c) Samples location. (d) 0.4 mm channel. (e) 2 mm channel. (f) 4 mm channel. (g) 6 mm channel. Note: Various magnifications have been used to represent different scales of phenomena. (h) Chart summarising layers distribution.

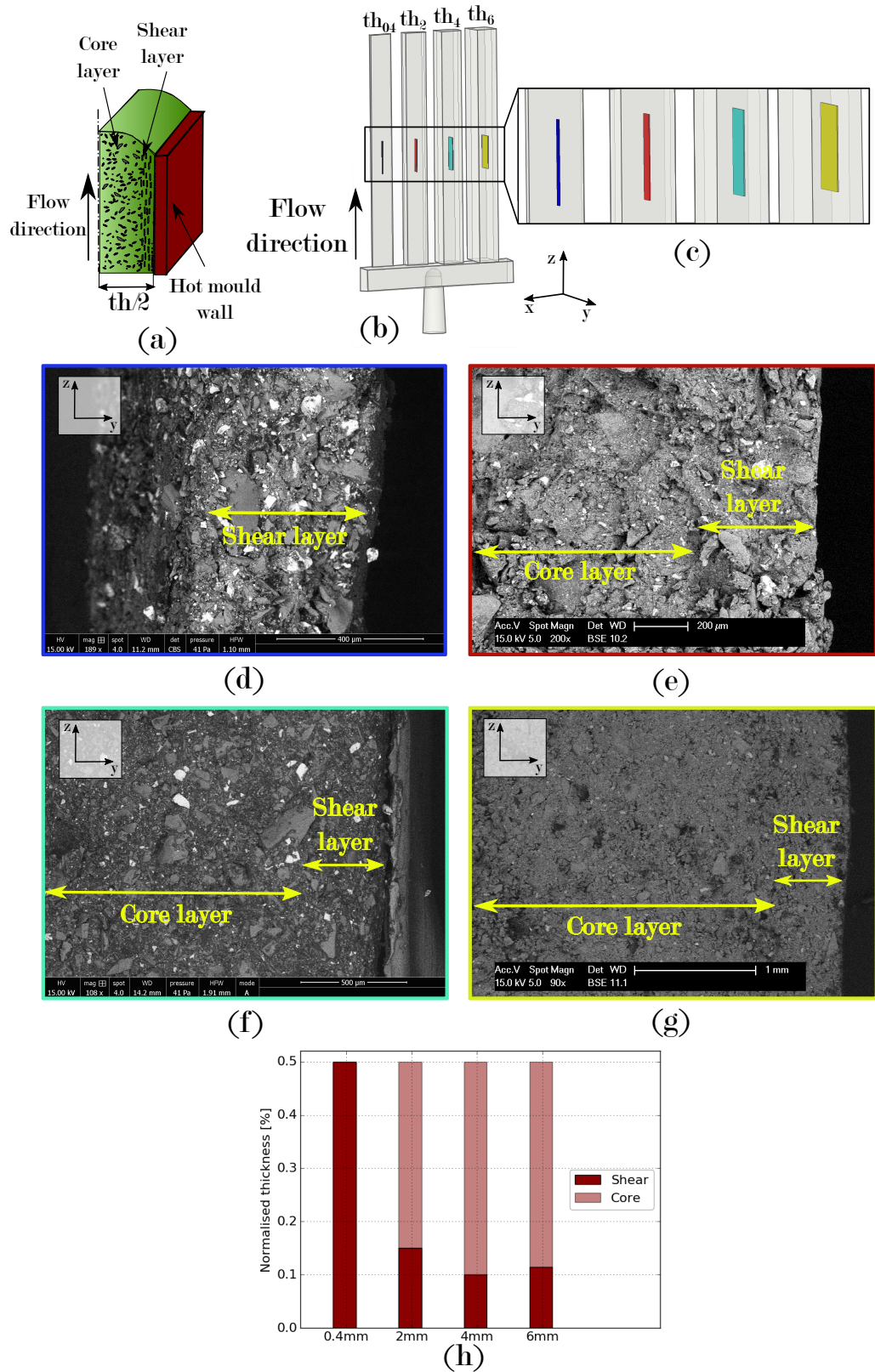


Figure 5.7: Examples of orientation distribution in ceramic injection moulded green samples, RHCM - Part thickness in the y-axis of the reference coordinate system. (a) Schematics of the microstructure. (b) Moulded part. (c) Samples location. (d) 0.4 mm channel. (e) 2 mm channel. (f) 4 mm channel. (g) 6 mm channel. Note: Various magnifications have been used to represent different scales of phenomena. (h) Chart summarising layers distribution.

core layer containing larger, randomly oriented particles. With decreasing channel thickness, the shear layer becomes wider than the core one: thus, in the thinnest bar (0.4 mm), the core layer is no longer visible and particles orient along the flow direction throughout the whole channel thickness, as depicted in Figure 5.6d.

Using RHCM, an overall lower degree of particle orientation is observed for the three thickest bars (Figures 5.7e, 5.7f and 5.7g) compared to their equivalent samples produced at ambient temperature conditions. Despite a banded microstructure still being present, the outer frozen layer disappears and the inner core layer constitutes a larger portion of the bar section, with an increased percentage over whole channel thickness from approximately 70% to 80% in the 6mm thick bar and from approximately 50% to 80% in the 4mm one. A high degree of orientation, with the shear layer extending throughout the whole bar thickness is, however, still present in the thinnest 0.4 mm channel, as shown in Figure 5.7d. By post-processing the micrographs taken at low magnifications (such as those displayed in Figures 5.6 and 5.7), a 15% reduction of average particle Feret angle is detected for the thickest bars in the RHCM case, compared to ambient temperature injection moulding.

In the case of injection at ambient temperature, the characteristic layered structure is due to the fact that, during injection, molten material enters the cavity and touches the cold mould surface, and undergoes fast cooling and solidification. This forms the outer frozen layer, characterised by a random orientation, since particles do not have time to align along the flow direction. This solidified layer, whose thickness corresponds to that shown in the simulations results (Figure 5.8b), causes a reduction in the channel wall thickness, which, in turn, increases shear rate levels at inner feedstock

layers that slide on the solidified outer ones.

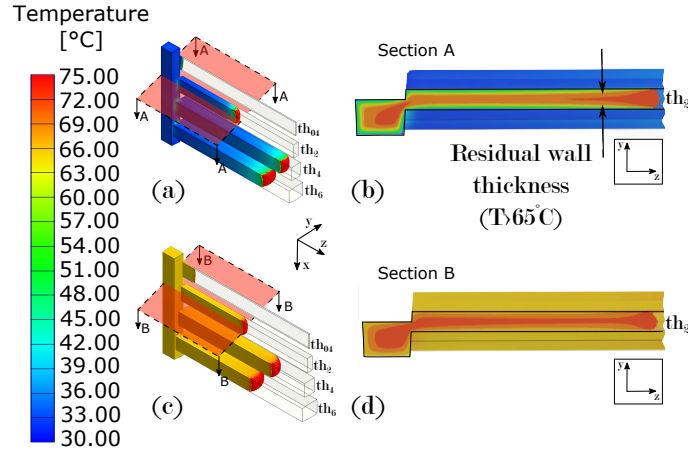


Figure 5.8: Temperature along channel thickness during mould filling from Moldex3D simulation - Part thickness in the y-axis of the reference coordinate system. (a) Part isometric view of part for  $T_{mould} = 30^\circ \text{C}$ . (b) Section of 2 mm channel for  $T_{mould} = 30^\circ \text{C}$ . (c) Part isometric view of part for RHCM. (d) Section of 2 mm channel for RHCM.

When elongated particles flow at high shear rates, they tend to orient along the flow direction, where they are subjected to minimum torque, thus forming the observed shear layer. At the centre of the part, the feedstock is subjected to lower shear rates and flows at higher velocity, hence determining the formation of a further (core) layer, characterised by randomly oriented particles. This non-uniform microstructure is in accordance to findings from previous work with injections at ambient mould temperature (Zhang, 1997) and implies differential shrinkage as the layers will shrink dissimilarly during the debinding and sintering processes, thus leading to post-sintering defects, as observed by Zhang (1996) and Mannschatz (2011).

By contrast, in RHCM, isothermal filling occurs (as shown in Figure 5.8d) and shear rates are reduced along part thickness. This prevents the formation of the frozen skin layer and implies an enlargement of the core zone, where a more random orientation is present. This more uniform and randomly oriented microstructure reduces particle anisotropy and subsequently



allows for a more homogeneous shrinkage during firing and sintering.

These phenomena can be compared with the shear rate profiles obtained from the numerical model (Figure 5.9), which are qualitatively similar to profiles previously obtained in literature (Thornagel, 2012): from this, it can be firstly visualised that the maximum shear rate during the filling process (across part thickness) decreases with feature  $th$ . Moreover, considering a normalised channel thickness ( $th_N$ ), being 0 at the mould wall and 0.5 at the centre of the channel, shear rates during filling present highest values at  $th_N = 0.1 - 0.25$ , which corresponds to the observed microstructural shear layer within the samples. This is also reflected by different shear rate profiles within the same channels when moulded with different thermal approaches, as the peaks are shifted more to the left (i.e. towards  $th_N = 0$ ) in the RHCM case. This confirms that variations of shear rates cause different particle orientation distributions in conventional moulding and RHCM. Further analyses, carried out using micrographs at higher magnifications,

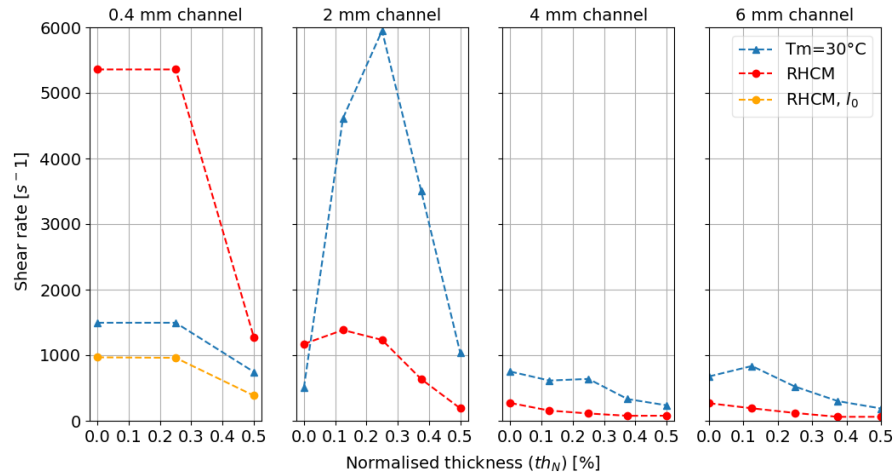


Figure 5.9: Maximum shear rate along channel thickness from mould wall to the centre during mould filling from Moldex3D simulation. In the case of the thinnest bar (0.4 mm), two RHCM shear rate profiles are depicted in Figure (a): the maximum shear rate at the filling stage corresponding to the maximum filled length at ambient mould temperature  $l_0$  (yellow) and the maximum shear rate at the end of filling (red).

show orientation effects even more evidently, as seen in Figure 5.10.

Comparing micrographs of regions at approximately  $950\text{ }\mu\text{m}$  from the mould wall, for green parts injected at ambient mould temperature and with RHCM the distribution is clearly different: while in the former case (Figure 5.10a) the analysed area is part of the shear layer, in the latter (Figure 5.10c) it belongs to the core layer. This is reflected in the histograms of Feret angle distribution over whole analysed areas: they depict a positively skewed distribution in the ambient temperature case (Figure 5.10e) and a more uniform one in the RHCM condition (Figure 5.10f).

Differential powder packing within and between the channels moulded at ambient temperature and RHCM was detected from SEM analyses, from which differential packing within thick features (6 mm and 4 mm) can be observed. A migration of larger particles towards the centre of the channel in thicker bars moulded at ambient temperature can be observed from SEM micrographs (Figure 5.11a), which is in accordance with results of theoretical and experimental studies on powder migration distribution in non-colloidal suspensions subject to shear flows in simple straight channels (Koh, Hookham, and Leal, 1994; Morris and Boulay, 1999).

This phenomenon, which is due to shear rate gradients along the part thickness, will promote differential shrinkage during sintering within features due to the uneven particle, and hence binder, distribution. Moreover, a higher powder content in the centre of the channel will also further hinder particle rotation in the core layer, thus promoting a less oriented microstructure. For the same features, moulded with the RHCM approach, the distribution of larger particles is more uniform throughout the whole channel thickness, which can be linked to lower shear rate variations during filling.



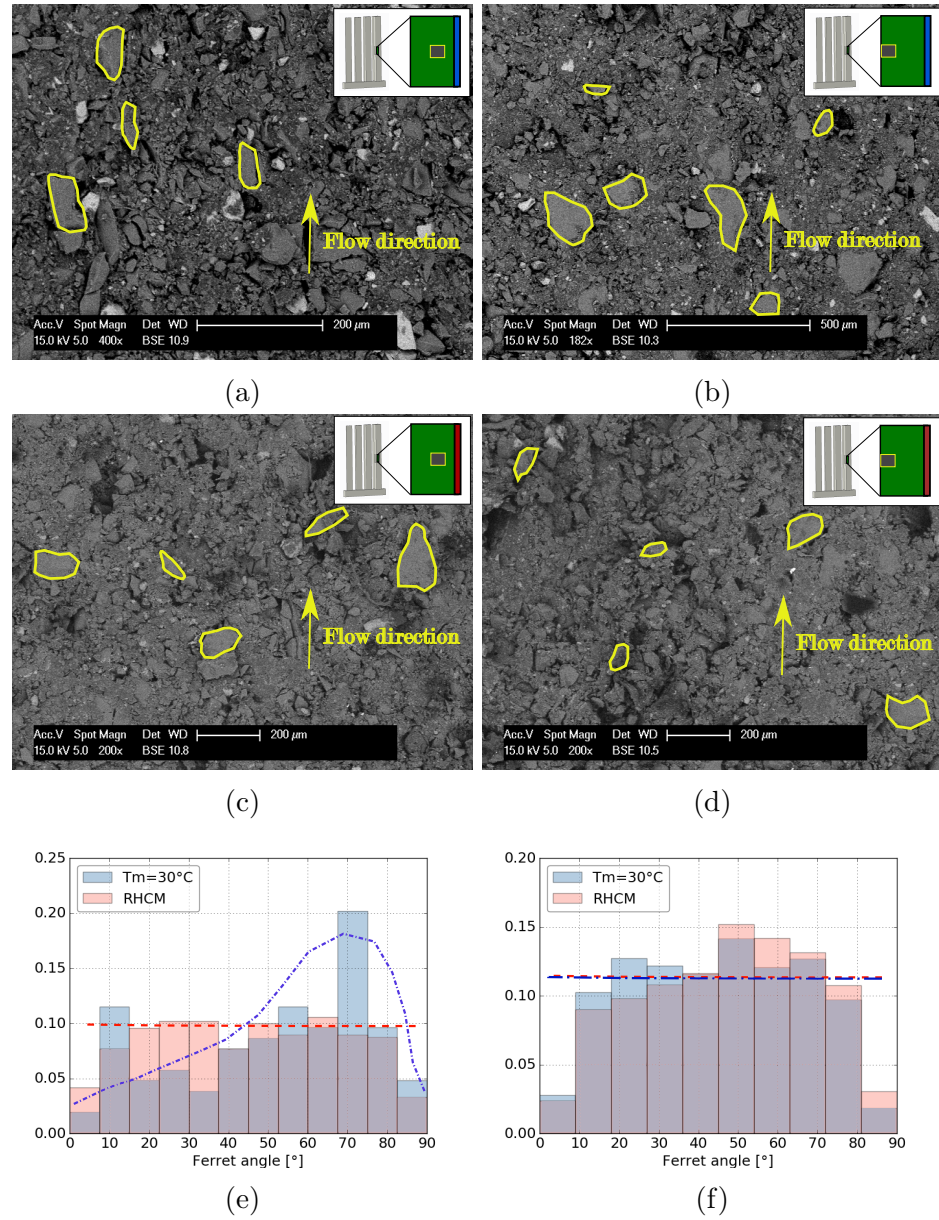


Figure 5.10: Examples of particle orientation in a 6 mm thick bar. (a)  $T_{mould} = 30^\circ\text{C}$ , 950  $\mu\text{m}$  from mould surface, micrograph taken at a higher magnification than the others because of lower particle size in this analysed area. (b)  $T_{mould} = 30^\circ\text{C}$ , centre of the moulding. (c) RHCM, 950  $\mu\text{m}$  from mould surface. (d) RHCM, centre of the moulding. (e) Ferret angle distribution, 950  $\mu\text{m}$  from mould surface. (f) Ferret angle distribution, centre of the moulding. Note: at least 70 platelets was  $^\circ$  in the samples.

### Particle orientation and packing: indirect characterisation methods

Particle packing was indirectly assessed through density measurements, for which two kinds of phenomena can be observed (Figure 5.12): (i) differential packing between features of different thickness and (ii) differential packing between same features moulded at different temperature conditions.

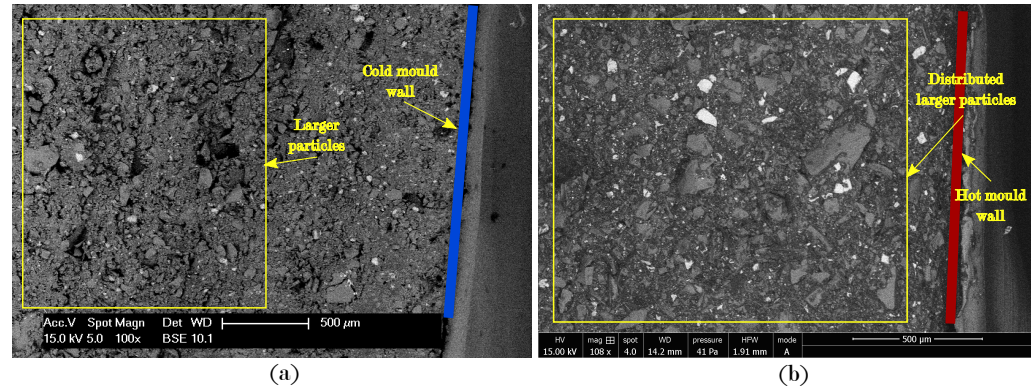


Figure 5.11: Example of particle size distribution in a  $th_4$  bar. (a)  $T_{mould}=30\text{ }^{\circ}\text{C}$ . (b) RHCM.

Considering the first observed phenomenon (i.e differential packing between features of different thickness), results from pycnometry measurements imply an increased particle content in thicker bars, with the decrease in powder fraction at finer features.

This is caused by high shear rates developing at the transition between the runner (5 mm thick) and the channels; additionally, in the thinnest (0.4 mm) bar, feature size starts to be comparable to particle dimensions, which causes increased particle-to-particle interactions and higher resistance against flow. It can be noted from Figure 5.12 that all the measured density values are below the nominal green density: this may be due to either an error in this latter value (which has been provided by the supplier), or it could also be a sign to a lower powder content in the channels, due to a

higher amount of particles in the runner.

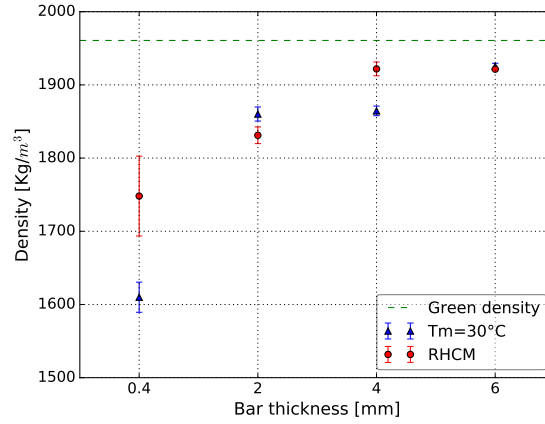


Figure 5.12: Average density of ceramic samples moulded at ambient temperature and RHCM. The error bars represent standard deviation calculated for five samples.

As for the second phenomenon, related to the influence of mould temperature, the three thickest features (2 mm, 4 mm and 6 mm) present a comparable particle content when moulded at ambient and high mould temperature, while the thinnest (0.4 mm) one has a significantly higher average particle content when injection moulded using RHCM. As already discussed, by injecting the thinner features at a mould temperature higher than the material  $T_g$  not only is filling capability enhanced, but also shear rates along the channel are reduced, due to the absence of a frozen layer which decreases the actual feature thickness. This drop of shear rates by increasing mould temperature is also evident from simulation results, as shown in Figure 5.13.

Moreover, the large standard deviations in the measurements of the density for the 0.4 mm channels produced by RHCM (Figure 5.12) can be attributed to differential powder packing along the channel length. When moulded using RHCM, the majority of the thinnest channel is filled towards the end of the process, when highest shear rates occur: this implies that shear rate

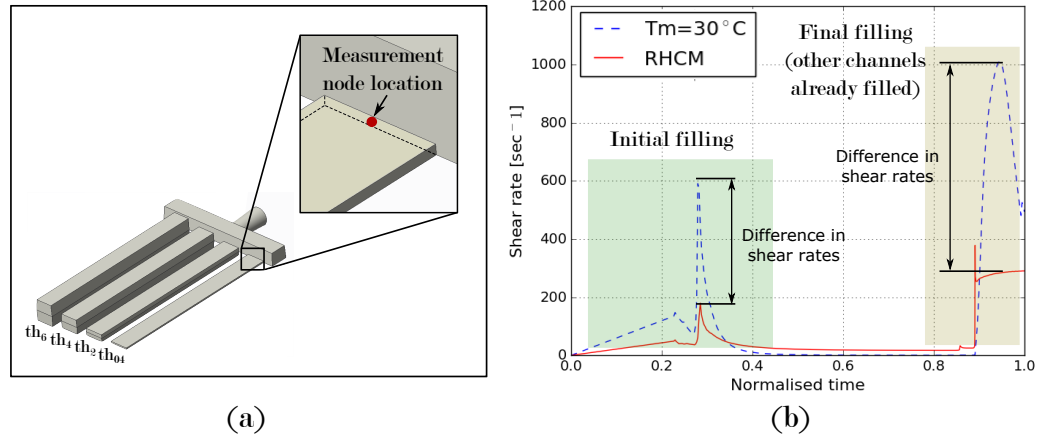


Figure 5.13: Simulation results for shear rates at the gate of the thinnest (0.4 mm) channel from the beginning of injection time to the completion of the filling stage. (a) Location of the measurement mesh node. (b) Shear rate over normalised time, where  $t=0$  is the beginning of injection and  $t=1$  the time at which the three thicker channels are completely filled.

gradients, and hence particle packing, will vary along the channel length. Hence, as samples analysed with the gas pycnometer were taken from the centre of the bar, the measured particle content varied considerably depending on the exact measurement location (i.e. slightly more towards the beginning or the end of the channel).

After injection, shrinkage ( $S\%$ ) was measured along the width and thickness directions of green ceramic parts, moulded both at ambient temperature and RHCM, and was calculated using the equation  $S\% = 100 \cdot (L_m - L_p)/L_m$ , where  $L_m$  is a specific mould length (thickness or width) and  $L_p$  is the same length measured on the part.

As shown in Table 5.1, higher shrinkage was observed in parts injected with RHCM, as expected as a consequence to the feedstock PVT behaviour, since the holding time was unvaried compared to the ambient temperature case, hence causing the feedstock to solidify under lower pressure. However, no subsequential cracking or warpage defect that could be related to particle

packing and orientation was detected from the performed measurements on green parts. This can be attributed to the presence of the solidified binder, which hinders particle movement.

Table 5.1: Average shrinkage measured in the green ceramic bars

Average Shrinkage [%]		
<b>Orientation effect</b>	Width direction	3.1
	Thickness direction	2.7
<b>Temperature effect</b>	$T_{mould} = 30^\circ \text{ C}$	2.2
	RHCM	3.6
<b>Channel thickness effect</b>	$th_2$	3.6
	$th_4$	2.4
	$th_6$	2.8

Effects of differential shrinkage between and within features arise, instead, subsequently to debinding and sintering processes, when stress relaxation occurs. This is in line with several other studies on particle morphology effects on moulding part quality (Mannschatz et al. 2011; Krug et al. 2002a), in which a worsening of defects is observed only after the debinding and sintering process. Moreover, considering the channel thickness effect, larger features do not shrink more than thinner ones, as they are not subjected to lower packing pressure during solidification.

Particle orientation and packing within the injected samples have also been studied through compressive tests under the SEM. As previously discussed in Section 5.2.1, two main outcomes from this characterisation technique were taken as a reference for the particle packing and orientation study: crack initiation locations and the stiffness modulus. The latter has been chosen as a reference parameter instead of the peak stress or the point of the stress-strain diagram corresponding to the visualised crack initiation, as it is independent on uncontrollable local microstructural imperfections that can be present in the samples and could trigger crack initiation, hence

influencing the peak stress value. The tested cases represent the situations of high (2 mm channel, moulded at ambient temperature) and low (6 mm channel, moulded with RHCM) particle orientation, as well as a benchmark case, to highlight only the temperature effect (6 mm channel, moulded at ambient temperature). Three repetitions were performed for these tests and representative stress-strain curves and micrographs are respectively shown in Figures 5.14 and 5.15.

Considering the failure locations outcome, under compressive loads, all the

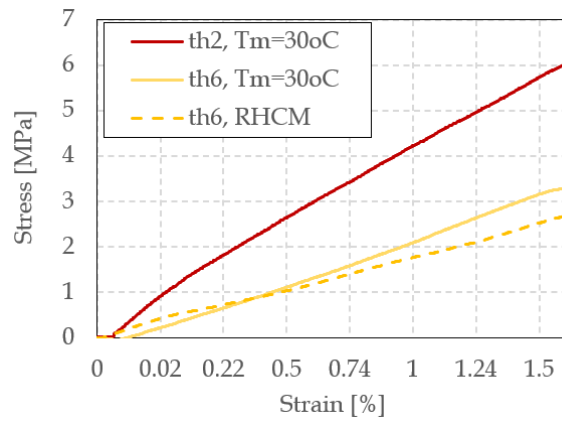


Figure 5.14: Examples stress-strain curves before sample failure for the three reference cases: 2 mm channel,  $T_{mould}=30^{\circ}\text{C}$ ; 6 mm channel, RHCM and 6 mm channel,  $T_{mould}=30^{\circ}\text{C}$

analysed green ceramic samples break with longitudinal cracks appearing parallel to the direction of the applied load and channel length (i.e. flow direction), as highlighted on the micrographs taken during the tests (Figure 5.15). This cracking behaviour of green moulded parts is in accordance to that observable in uniaxial compressive tests for concrete, when material fails as a consequence of local particle-matrix separation, which gives rise to cracks that propagate due to tensile stresses (Shi, 2009).

Comparing the locations of cracks (Figure 5.15) and orientation layers (Figures 5.6 and 5.7) with respect to feature thickness for the analysed channels ( $th_2$  moulded at ambient temperature and  $th_6$  injected with both ambient



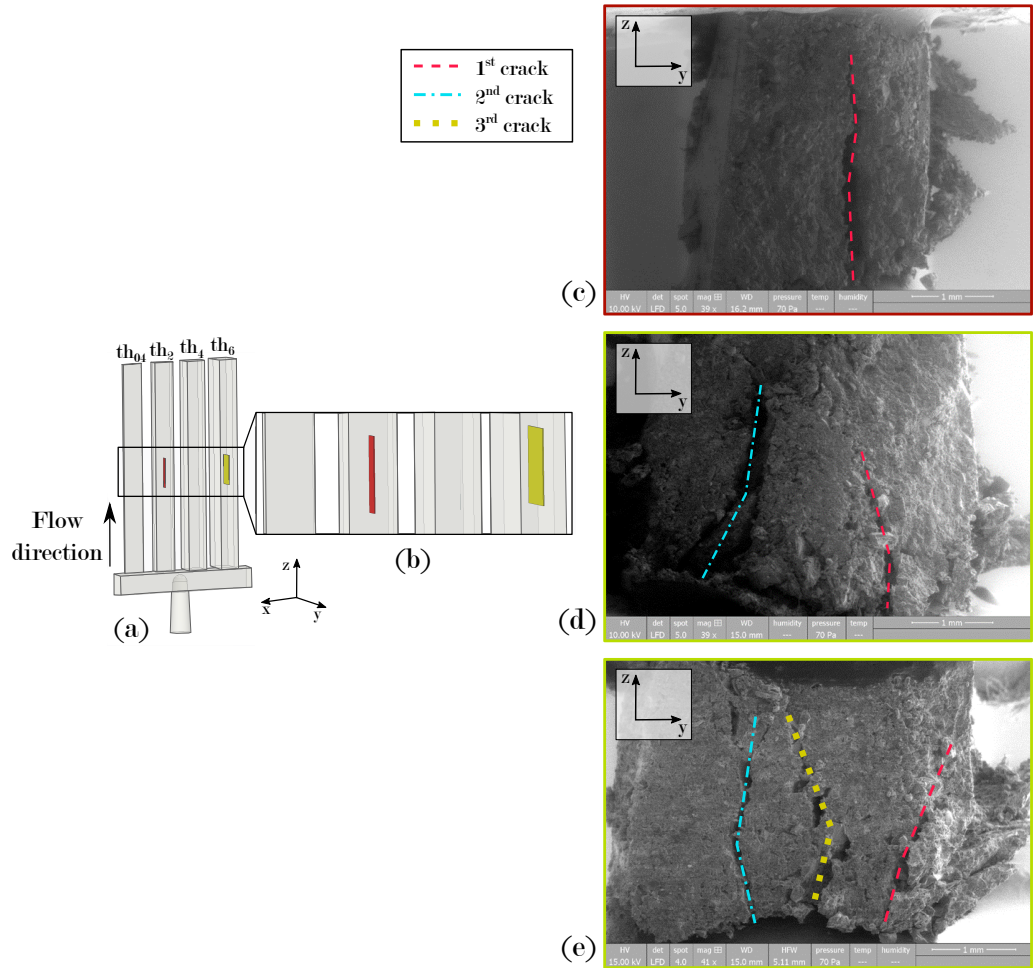


Figure 5.15: Examples of cracked samples under uniaxial compression - Part thickness in the  $y$ -axis of the reference coordinate system. (a) Moulded part. (b) Samples location. (c) 2 mm channel,  $T_{mould}=30^{\circ}$  C. (d) 6 mm channel, RHCM. (e) 6 mm channel,  $T_{mould}=30^{\circ}$  C.

temperature and RHCM approaches), it can be observed that the first crack consistently initiates and develops along the interface between the shear and core layers, followed by a preferential fracture of the core layer, where subsequent cracks appear. This can indicate a lower stiffness of this internal layer compared to the more external ones, which could be attributed to both a more random particle orientation (Figure 5.10) and to a higher particle content (Figure 5.11). The latter will imply a lower volume percentage in binder, which is the portion of material resisting to the load.

A more quantitative analysis that allows the study of particle packing and orientation not only within the same feature, but between different channels, can be drawn by considering the stress-strain behaviour of the samples during compression. In particular, the stiffness modulus of the material can be compared for channels of different thicknesses and moulded with ambient mould temperature and RHCM. Results, summarised in Table 5.2, show that thinner features present a higher modulus than thicker ones, while taking into account channels with the same cross section thickness, those moulded at ambient mould temperature are stiffer.

In particular, for the channels analysed in Figure 5.15, the 2 mm channel moulded at ambient temperature presents a stiffness modulus approximately 35% higher than that of the 6 mm feature moulded with the same temperature control approach, which, in turn, exhibits a modulus approximately 25% higher than that of the same feature moulded using RHCM.

The observed correlation between particle content and material stiffness is in accordance with results from mechanical testing used in literature to study the strength of die-pressed green components (Özkan and Briscoe, 1997). This can be, again, linked to both the levels of particle orientation



Table 5.2: Stiffness modulus values for main analysed cases. Calculated standard deviations for the moduli are of the order of 20 MPa.

Bar thickness	Temperature approach	Stiffness Modulus [MPa]
$th_2$	$T_{mould} = 30^\circ \text{ C}$	360
$th_6$	$T_{mould} = 30^\circ \text{ C}$	220
$th_6$	RHCM	170

and packing induced by different feature thicknesses and mould temperature approaches: a higher particle fraction is present in thicker features, which will result in a lower binder content and hence a lower resistance to strain. The reduced stiffness of parts moulded using RHCM can actually be an indicator of a less oriented microstructure compared to those injected at ambient mould temperature.

### 5.2.3 Conclusions

The phenomena of particle orientation and packing are critical for the CIM process, as they originate from cooling and shear rate variations arising during the filling phase, and are one of the main causes of differential shrinkage defects in both green as well as sintered ceramic parts. To fill the knowledge gap in the current literature on the effect of mould temperature and, in particular, of the RHCM approach on particle packing and orientation in CIM, a study was carried out using green silica-zircon ceramic injection moulded parts.

Results show that RHCM is not only an effective technique to allow higher feature replication capability, but it promotes a favourable microstructure, characterised by a more uniform particle orientation and packing in green parts, which is likely to reduce differential sintering defects at thicker sections. Considering the performed analyses, the following conclusions can be drawn:

- A banded microstructure, characterised by different layers of particle orientation (frozen, shear and core) was identified in ceramic bars, moulded at constant mould temperature and using RHCM. Results from the numerical model of the CIM process show a correlation between degree of particle orientation along part thickness and maximum shear rates which, in turn, depend on temperature gradients developing during the mould filling stage of the process.
- The RHCM approach determines a lower degree of particle orientation along the part thickness, as it causes an enlargement of the core layer. Furthermore, RHCM determines a considerable reduction of the shear layer and the disappearance of the outer frozen layer.
- For thicker features, RHCM can be an effective technique to prevent non-uniform green part microstructure in terms of both particle packing and orientation. This is due to lower shear rate gradients developing during the filling process.
- Using a RHCM approach also improves particle packing homogeneity between features having different thickness. However, differential particle content could still appear within thinnest features: this can be attributed to high shear rate gradients developing during filling.
- Differential shrinkage effects were not detected in green components. This is due to the presence of the binder hinders particle movements and to residual stresses which are not released in green parts. Moreover, in the reference Parallel-channels component, thick features were as close to the gate as thinner ones, and hence did not solidify under a lower packing pressure.
- A novel methodology has been proposed for the analysis of particle packing and orientation, based on *in-situ* compression tests under

SEM. Observations from these tests are in good agreement with microstructural analyses and density measurements and show difference in part stiffness modulus up to 60%, which could be attributed to different particle packing and orientation among the samples moulded with different thermal control approaches.

### **5.3 Effect of RHCM on the part-mould adhesion behaviour**

In the previous sections, a study has been presented on how the state-of-the-art tooling technology of Rapid Heat Cycle Moulding (RHCM) affects particle packing and orientation in CIM. Through this, it has been shown that this technique can be beneficial, not only for enhancing feature replication capability and surface quality, but also to guarantee a more uniform microstructure within the components, which helps obtain defect-free ceramic parts after the subsequent processes of debinding and sintering. However, in order to fully evaluate the performance of RHCM for CIM applications, an investigation on how this approach affects mould-part adhesion behaviour and consequential ejection forces has been carried out. In the following, this study is presented, first with a description of the experimental setup employed to measure demoulding forces as a function of the used thermal control approach, and then with a presentation and discussion of the main findings of the present work.

#### **5.3.1 Experimental setup**

In order to understand the effect of mould temperature on the adhesion behaviour between mould and part in CIM, a bespoke test rig has been developed (Figure 5.16), to inject a disc (25 mm diameter x 5 mm height)

and measure ejection forces under different mould temperature conditions.

For this study, the same ceramic model material employed for the influence of mould temperature on particle packing and orientation has been used. The choice of a sample part with a cylinder shape has been made to remove any effect on ejection forces coming from the component shrinking around mould cavity features (which causes a variation of demoulding forces). This, hence, allows to isolate adhesion as a main cause of ejection forces variation. Mould temperature was varied using two (a top and a bottom) Peltier modules, placed 3 mm below and above the cavity, and closed-loop controlled through thermistors, which were placed in two housings (Figure 5.16c): one 1 mm from each cavity surface and one 1 mm from each Peltier module. Round hollowed thermoelectric modules have been used, in order to allow for the placement of an ejector pin in the centre of the cavity, to de-mould the disc through a lever, actuated by a toggle clamp. To allow for heat dissipation from the Peltier faces opposite to the mould, two aluminium heatsinks were modified to be adapted to the rig design and placed on the two (top and bottom) extremities of the mould. Between the lever used for ejection force transmission, and screwed to the bottom side of the ejector pin, a load cell was placed, which measured forces up to 200 N (Figure 5.16d). In this way, after each moulding cycle, it was possible to eject the part and measure demoulding forces with the sensor. The mould cavity surface (which was made of aluminium) and the top of the ejector pin (in mild steel) were ground down to a roughness of 0.8 Ra, in order to provide similar interface conditions to industrial injection moulding die-tools.

The mould was designed to be used with the injection rig employed for the previously described tests; however, the main experiments were performed

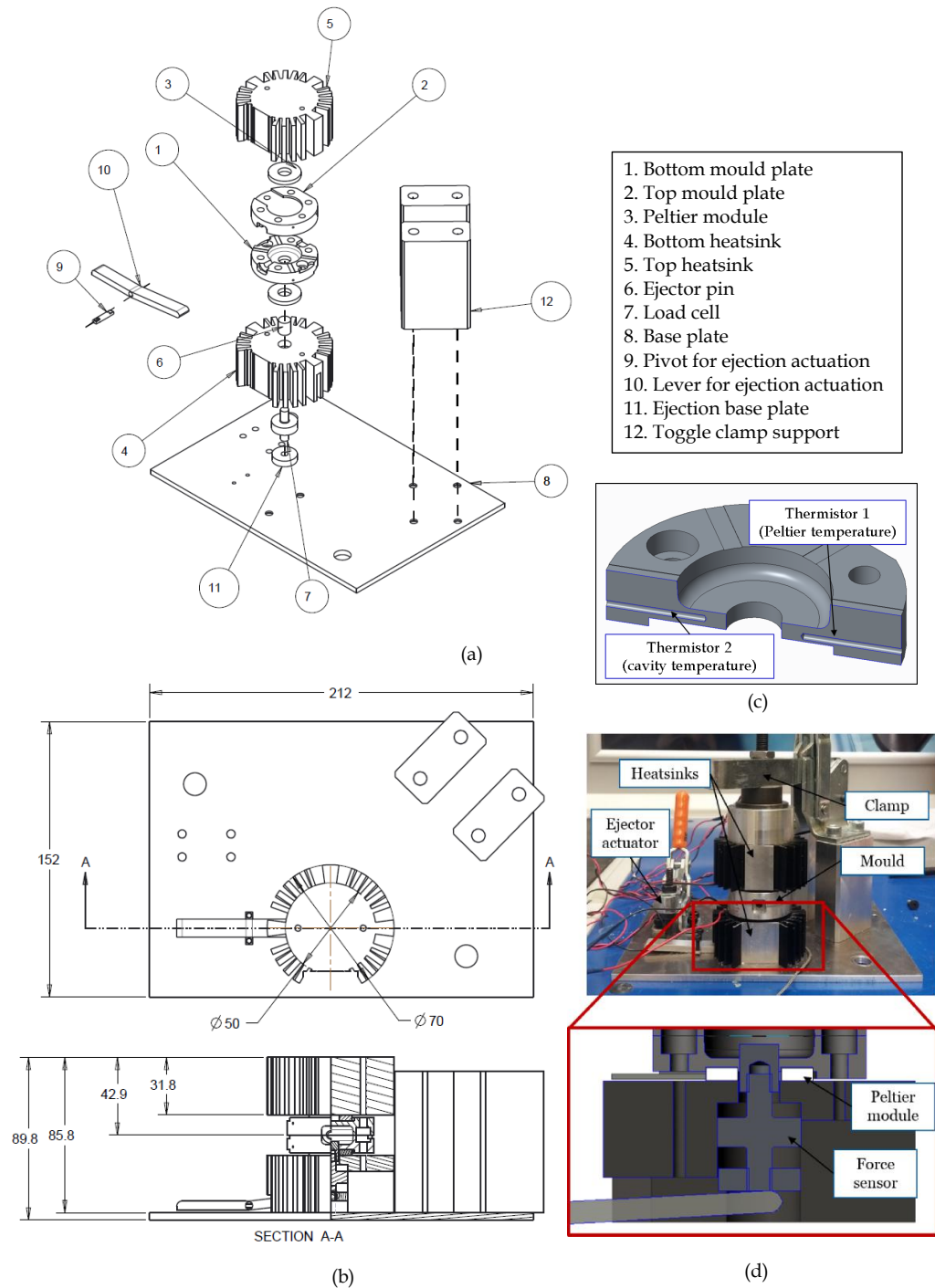


Figure 5.16: Setup for the adhesion tests. (a) Exploded view. (b) Drawing and main dimensions. (c) Picture of the setup.

by pouring molten material (at a controlled  $T_{melt}$  of 75 °C) onto the bottom side of the mould. This choice was due to the time needed to unclamp and open the two halves of the mould cavity, which could cause delays in ejecting the part, while the aim was to achieve demoulding at specific instants and at controlled mould temperatures. Moreover, as both the top and bottom mould plates were heated and cooled, any adhesion to the top plate may have caused a reduction in the measured ejection forces, due to the part being pulled out from the bottom cavity during die-tool opening. Pouring the molten material, instead of injecting, was also possible due to the fact that this study does not consider any effect of part shrinkage on demoulding forces, and hence, variations in ejection behaviour due to different injection or packing pressure conditions can be neglected.

### 5.3.2 Results and discussion

To study the effect of RHCM on the adhesion behaviour between part and mould, ejection force was measured using two temperature profiles: the first, with a constant, ambient mould temperature ( $T_{mould}=35$  °C, Figure 5.17a) and the second using the RHCM approach (Figure 5.17b), and ejection was performed, in both cases, when mould temperature was as 35 °C ( $T_{ej} = 35$  °C). Three tests were conducted for each temperature profile, showing ejection forces five times higher when using the RHCM approach, compared to the ambient mould temperature one, from approximately 35 N to 170 N.

In order to carry out a more complete study, and better understand if the variation in the measured forces was due to the injection temperature, demoulding tests were also performed using a third thermal profile (Figure 5.18).

This was an alternative RHCM approach, consisting of: injection at a tem-

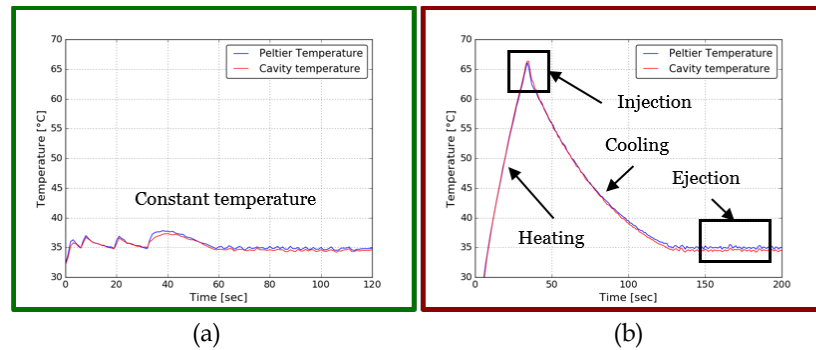


Figure 5.17: Main temperature profiles used for the adhesion tests. The graph show the temperature measured by the two used thermistors, which were respectively 1 mm distant from the Peltier module (Peltier Temperature) and 1 mm distant from the mould cavity surface (Cavity Temperature). (a) Profile 1: Constant mould temperature ( $T_{mould}=35^{\circ}\text{C}$ ). (b) Profile 2: RHCM.

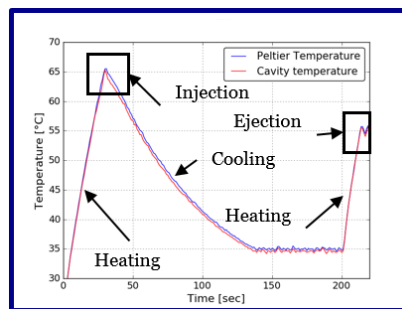


Figure 5.18: Third temperature profile, of "alternative RHCM" used for the adhesion tests. The graph show the temperature measured by the two used thermistors, which were respectively 1 mm distant from the Peltier module (Peltier Temperature) and 1 mm distant from the mould cavity surface (Cavity Temperature)

perature higher than the feedstock  $T_g$ , cool down to ambient mould temperature, and a fast increase of mould temperature up to the feedstock  $T_g$  for part ejection.

Results from demoulding forces using the three profiles (Figure 5.19) show that, while the “conventional” RHCM approach causes an increase in forces, the “alternative” RHCM profile, with mould reheating at ejection is characterized by similar demoulding forces to the ambient temperature case.

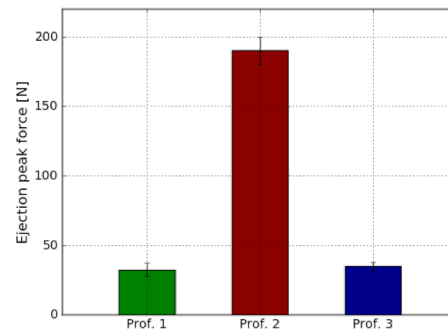


Figure 5.19: Absolute value of ejection force for the three temperature profiles. Prof. 1:  $T_{mould}=35\text{ }^{\circ}\text{C}$ ; Prof. 2: RHCM; Prof. 3: Alternative RHCM. The error bars represent the standard deviation over three carried out measurements.

In order to have a deeper understanding on the phenomena causing these changes in demoulding forces, the surfaces of both the part and the mould were observed through SEM (using the Philips XL30 SEM) after ejection, for the three studied mould temperature profiles (Figure 5.20).

Considering the part, in the ambient temperature case (Profile 1), an uneven surface was observed (Figure 5.20a), while in the other two cases, a flat surface was visualised, with signs replicating mould surface roughness (Figure 5.20c and 5.20e). This can be correlated to the fact that, in Profile 2 and 3, the feedstock is injected at a temperature above its  $T_g$  (Figure 5.21d



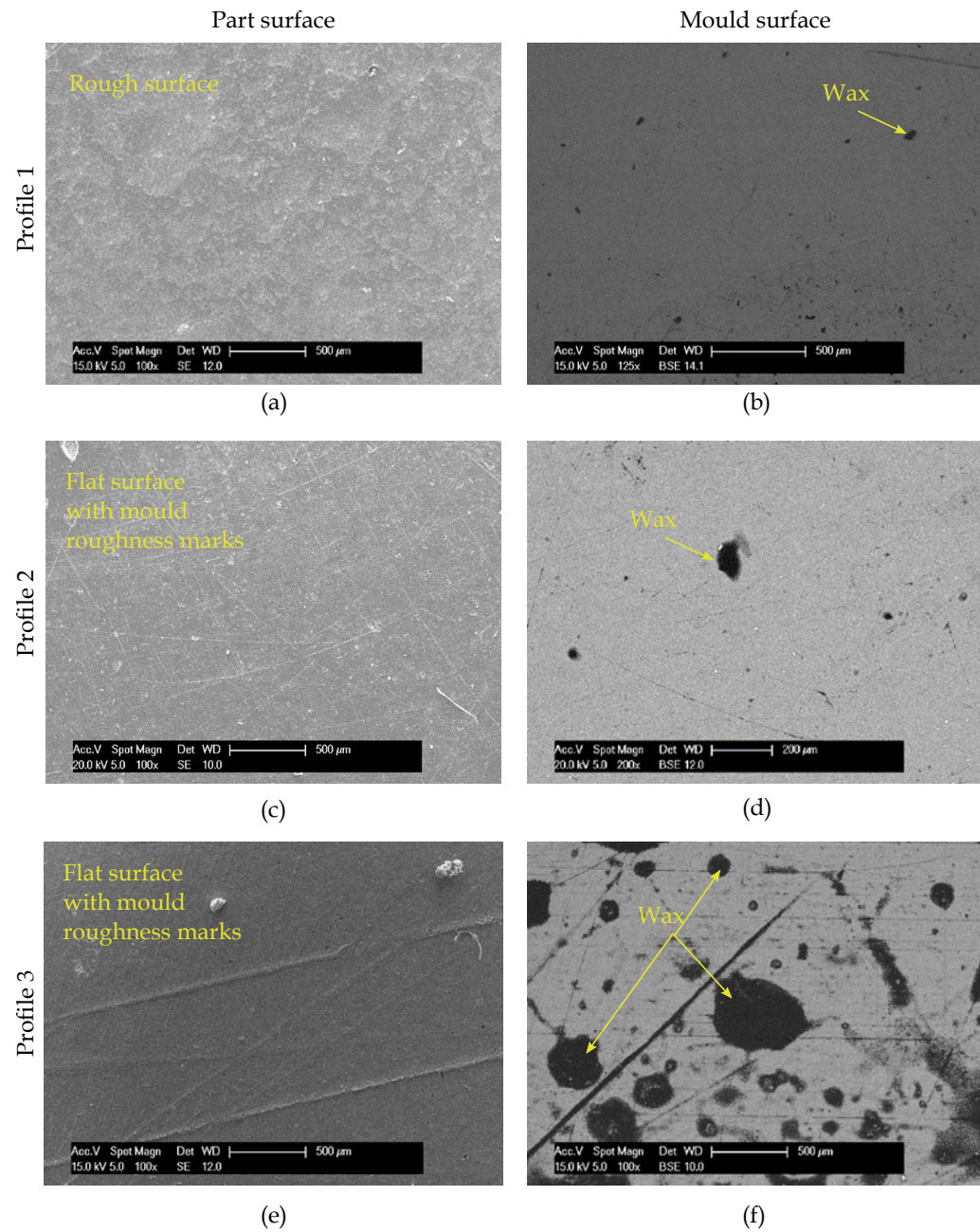


Figure 5.20: SEM micrographs of part and mould cavity surfaces after component ejection. (a) Part surface, Profile 1. (b) Mould surface, Profile 1. (c) Part surface, Profile 2. (d) Mould surface, Profile 2. (e) Part surface, Profile 3. (f) Mould surface, Profile 3.

and 5.21g): this causes a drop in the binder surface tension, which, in turn, allows the material to wet the mould cavity substrate, hence replicating the fine feature of the roughness from the die-tool. On the other hand, in Profile 1, the material quickly solidifies once in contact with the cold mould (Figure 5.21a-b), before spreading onto the cavity surface, hence causing an uneven profile compared to the other two cases. Comparing part-mould interface in Profile 1 and 2, the interfacial contact surface in the RHCM case (Figure 5.21f) is much higher than in the ambient temperature one (Figure 5.21c), due to the feedstock filling the micro-cavities of the surface roughness, causing higher mechanical interlocking.

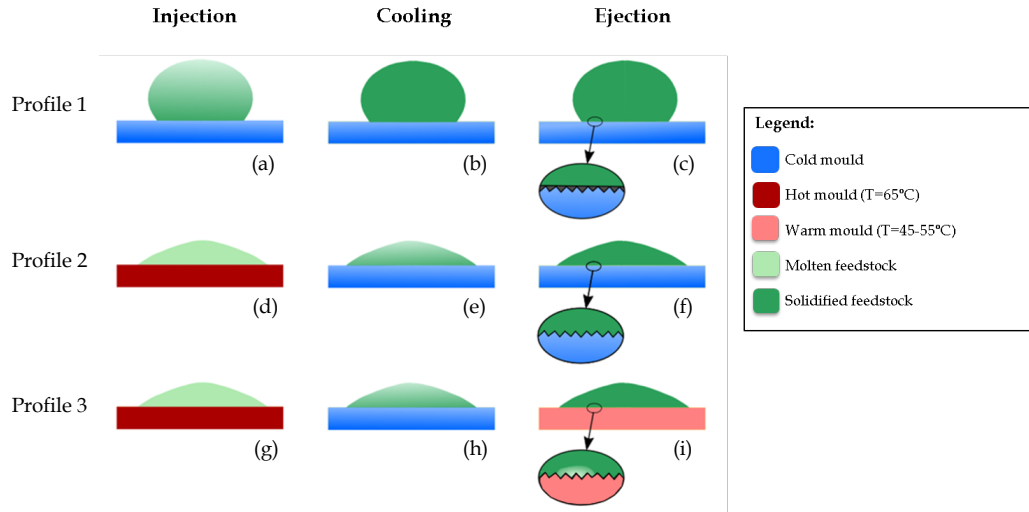


Figure 5.21: Schematics of part-mould adhesion behaviour at different stages of the IM process for the three analysed mould temperature profiles.

Looking at the mould surface, instead, Profile 1 and 2 (Figure 5.20b-d) show small residues of feedstock (maximum size  $< 200 \mu\text{m}$ ) stuck onto the mould cavity. However, analysing the mould cavity surface from Profile 3, these residues are significantly larger (up to  $500 \mu\text{m}$  diameter) and spread throughout the cavity. This is due to the fact that, while in the first two cases ejection is performed at ambient mould temperature, in Profile 3, ejection temperature occurs at approximately the feedstock  $T_g$ . Hence, cohesive

forces within the solidified feedstock drop at local areas of the part, probably due to amorphous portions of the binder which transit to the rubbery state in contact with the mould surface (Figure 5.21i). This phenomenon would explain the decrease in demoulding forces observed from the adhesion tests, and the larger feedstock residuals observed on the mould cavity, after ejection using Profile 3.

In order to confirm this deduction, demoulding tests were carried out using Profile 3, but varying mould temperature at ejection (i.e. ejection temperature). The output demoulding force was compared against the characteristic curve of normalised heat flow, obtained from Differential Scanning Calorimetry (DSC) measurements at a heating rate of 5 °C/min, showing the glass transition temperature of the ceramic feedstock. From this, it could be verified that a drop in ejection force was measured when ejection temperature was raised up to approximately the material  $T_g$  (Figure 5.22), hence confirming the previously discussed analysis of the phenomenon.

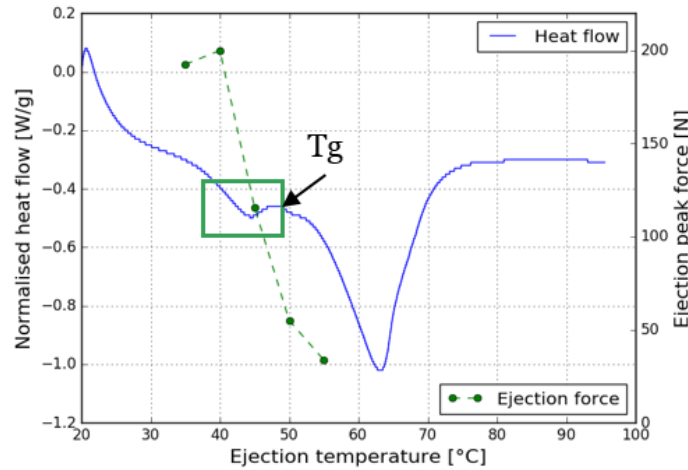


Figure 5.22: Ejection temperature versus the characteristic DSC output curve of normalised heat flow rate for the green ceramic feedstock and versus peak force during ejection. The graph shows correlation between the glass transition temperature ( $T_g$ ) of the binder, corresponding to the flex in the blue curve, and the drop in ejection force when the part is de-moulded at a mould temperature  $\geq T_g$ .

Relating the results from this study with the analysis of RHCM performance in CIM, it is evident that preservation of part integrity during ejection is one of the main drawbacks of this approach. Therefore, in order for RHCM to be applied to CIM, smarter temperature control methods need to be developed, which have to account for an increase of mould temperature, to allow for easy part ejection. This approach presents the challenge of controlling cavity surface temperature, in order to avert any excessive melting of the part, which may cause warpage or cracking during demoulding.

### 5.3.3 Conclusions

In this chapter, the performances of rapid thermal cycling in CIM applications have been studied, in terms of both its effect on particle orientation and packing, and on adhesion behaviour between part and mould, which affects ejection forces. From this study, the following conclusions can be drawn:

- Following the methodological framework developed in Chapter 4, the performances of the RHCM approach have been analysed, using the developed filling simulation as a support to understand how this technique influences particle packing and orientation in CIM.
- The RHCM technique is a more effective thermal control approach to enhance thin feature replication capability compared to increasing melt temperature, as it averts feedstock solidification during filling, when conduction is the main heat transfer mechanism between mould and part.
- The RHCM approach promotes a more uniform microstructure in thicker features, due to an enlargement of the inner core layer, characterised by randomly oriented particles. Moreover, for both thinner and thicker features, the RHCM determines the disappearance of the

outer frozen layer, which further helps achieve a less stratified microstructure, thus contributing to avert differential sintering.

- Homogeneity in particle packing between features having different wall thickness is also improved by the employment of RHCM, although not fully overcome.
- The effects of RHCM on green part shrinkage could not be fully analysed, but needs to be considered when designing novel thermal control system for CIM die-tools. In particular, the effect of RHCM on shrinkage in features with different wall thickness could not be observed and studied, due to the fact that the analysed reference geometry was made of disjointed features, which did not solidify at different packing pressures.
- The employment of RHCM causes a significant increase of ejection forces, due to the higher contact area between the part and mould cavity. Therefore, effective temperature control approaches for CIM needs to be designed novel thermal cycles, which account for lowering adhesion between part and mould and ensuring components integrity after ejection.

Based on this study, in the following chapter, the development of a novel thermal control system for die-tools is reported, in order to enable the manufacturing of components having adjoined features of different wall thickness through CIM. The performances of the developed system were analysed using the deployed methodological framework and compared to ambient mould temperature and RHCM approaches.

## Chapter 6

# Novel thermal control system for CIM die-tools

*The manufacturing of components having features of uneven wall thickness through Ceramic Injection Moulding (CIM) is challenging, due to differential heat and mass transfer phenomena occurring at areas of different thicknesses. The technique of RHCM has been studied in the present work and it has been shown to enhance replication capability of fine features, as well as to promote favourable green part microstructure, in terms of ceramic particle orientation and packing. However, when moulding ceramic components having adjoined features of uneven wall thickness, any thermal control approach based on the achievement of a uniform cavity temperature will cause uneven cooling rates in the parts, due to thinner features solidifying before thicker ones. Although using RHCM can help prevent lack-of-fill defects, the differential solidification rates upon cooling may cause uneven part shrinkage, which can result into warpage and cracking in green and sintered ceramic parts. Moreover, rapid thermal cycling, as seen in Chapter 5, has the disadvantage of increasing adhesion between part and mould, causing high demoulding forces and subsequent breakage of the green part during ejection. To overcome these issues, a novel regional thermal control*

*system is developed for CIM die-tools, based on a mould temperature optimisation with the objective of minimising cooling rate differences within the injected part. To demonstrate the developed system, a mould is designed and equipped with multiple Peltier modules, in order to achieve a local control, tailored to each cavity feature having different thickness. The proposed control approach also considers temperature profiles that reduce part-mould adhesion and subsequent ejection forces. Finally, the outcomes from injection moulding, obtained by employing the novel mould and thermal control approach are compared with those obtained by using constant ambient mould temperature and RHCM.*

## 6.1 Introduction

As discussed in the review of current literature (Chapter 2), state-of-the-art approaches for mould thermal control, such as Rapid Heat Cycle Moulding (RHCM), aim at achieving a uniform mould cavity temperature, which is usually suitable for components with constant wall thickness. Moreover, the performances of these approaches and systems are usually evaluated based on productivity criteria, and on macroscopic quality outcomes on the moulded parts (e.g. surface glossiness, sink marks and warpage).

However, when manufacturing ceramic components with uneven wall thickness using the Low-Pressure Ceramic Injection Moulding (LPCIM) process, mould thermal systems are needed with a tailored temperature control for features having different surface-to-volume ratios. This should be translated into both designs with heating and cooling elements that are regionally and independently controllable, and into effective control strategies which can minimise the effect of uneven cooling rates throughout the part. Furthermore, the thermal systems performances need to be evaluated based not

only on macroscopic quality outcomes, but also on the microstructure of green ceramic components. Finally, these systems need to ensure successful part ejection, by accounting for the adhesion behaviour between part and mould cavity surface.

In light of this, in the present chapter, a novel thermal control system for LPCIM is developed and demonstrated, consisting of regional heating and cooling of the mould cavity, with an optimised temperature control based on the minimisation of cooling rates within the moulded part throughout the IM process. The novel mould tool with regionally controlled temperature was designed and manufactured using thermoelectric (Peltier) elements to heat and cool the mould, and their temperatures were independently controlled based on the results from a coupled Finite Element (FE)- Particle Swarm Optimisation (PSO). The findings on part-mould adhesion behaviour from Chapter 5 are also considered in the optimisation, to guarantee successful part ejection using the developed system and control approach. The effectiveness of the approach is not only proven in terms of efficiency with respect to industry-standard cycle times, but also compared to the conventional constant ambient mould temperature and RHCM approaches in terms of effect on part quality, both at the macrostructural and microstructural levels.

## **6.2 Novel mould and temperature control concepts**

As previously stated, this work includes the joint development of a mould tool, locally heated and cooled, and of its control approach, which is based on an optimisation, with the objective to minimise cooling rate gradients



throughout the moulded parts, despite having differential wall thickness. In this section, the mould and the control approach concepts are described and discussed.

The mould design can be introduced by taking into account a generic component with features having different thicknesses (Figure 6.1a), and, for simplicity, symmetric along the separation plane of the mould (i.e. the interface between top and bottom mould plates). The die-tool with local temperature control is equipped with thermoelectric (i.e. Peltier) modules located at a fixed distance from the cavity surface, one per each feature (Figure 6.1b). Peltier elements have a uniform temperature throughout their face and can be used to locally heat and cool each cavity feature.

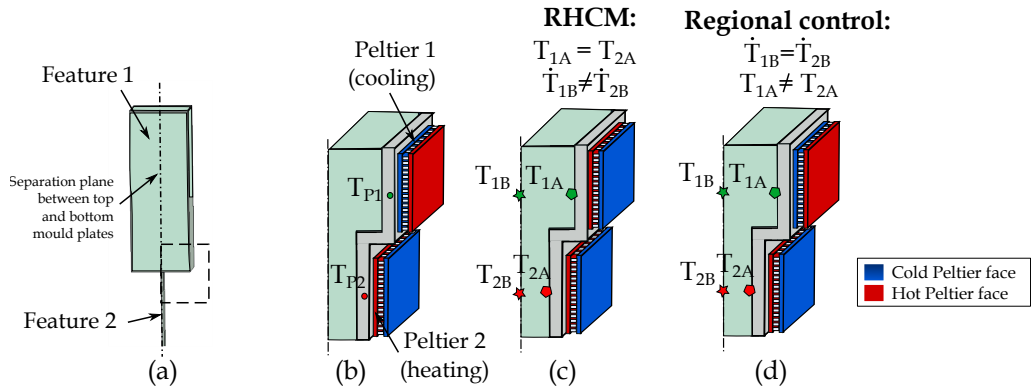


Figure 6.1: Concept of the novel thermal control system. (a) Generic component, isometric view. (b) Schematics of Peltier configuration and positioning, showing the independent control for the two features and the location of temperature sensors for closed-loop control of the thermoelectric modules. (c) Schematics of the control approach for RHCM. (d) Schematics of the novel regional control approach. Note: Whole Peltier modules are larger than those displayed, as they occupy the whole feature thickness.

One or more temperature sensors are placed between the Peltier surface and the mould cavity (measuring  $T_{P1}$  and  $T_{P2}$  shown in Figure 6.1b), in order to implement an independent temperature control for each thermoelectric element.

While, in the RHCM approach, temperature control is based on achieving a uniform mould cavity surface temperature (Figure 6.1c), the novel thermal control approach, as previously stated, is based on minimising thermal gradients within the parts (Figure 6.1d). Therefore, because of the component geometry symmetry, it is based on achieving a uniform temperature in the centre of the part. In order to fulfill this objective, since features of different thicknesses will cool at diverse rates, the temperature of each Peltier will need to be adjusted throughout the IM process. This can be explained by analysing an example cycle (Figure 6.2) in which, considering a component with two features of different size, and two Peltier modules placed in the cavity, one corresponding to each feature, the two modules are controlled in a different way, throughout the process stages of filling, packing, cooling and ejection.

Considering, once again, a generic component with features having different thicknesses, which is injected in a way that the feedstock has to flow from a thin (Feature 2) to a thick feature (Feature 1), each Peltier has an imposed temperature profile throughout the process. As previously stated in Chapter 3, one of the main advantages in employing Peltier modules is to enable local heating and cooling, without the need of changing physical configuration, as the face in contact with the mould can be inverted from heating to cooling, just by swapping the direction of the electric current passing through the element. In this way, the temperature of each Peltier can be independently controlled throughout the process, in order to achieve uniform cooling rates in the part.

The role of the implemented thermal model and optimisation is therefore to compute cooling rates inside the part for different combinations of Peltier temperature profiles, through a transient thermal FE model. Based on this,

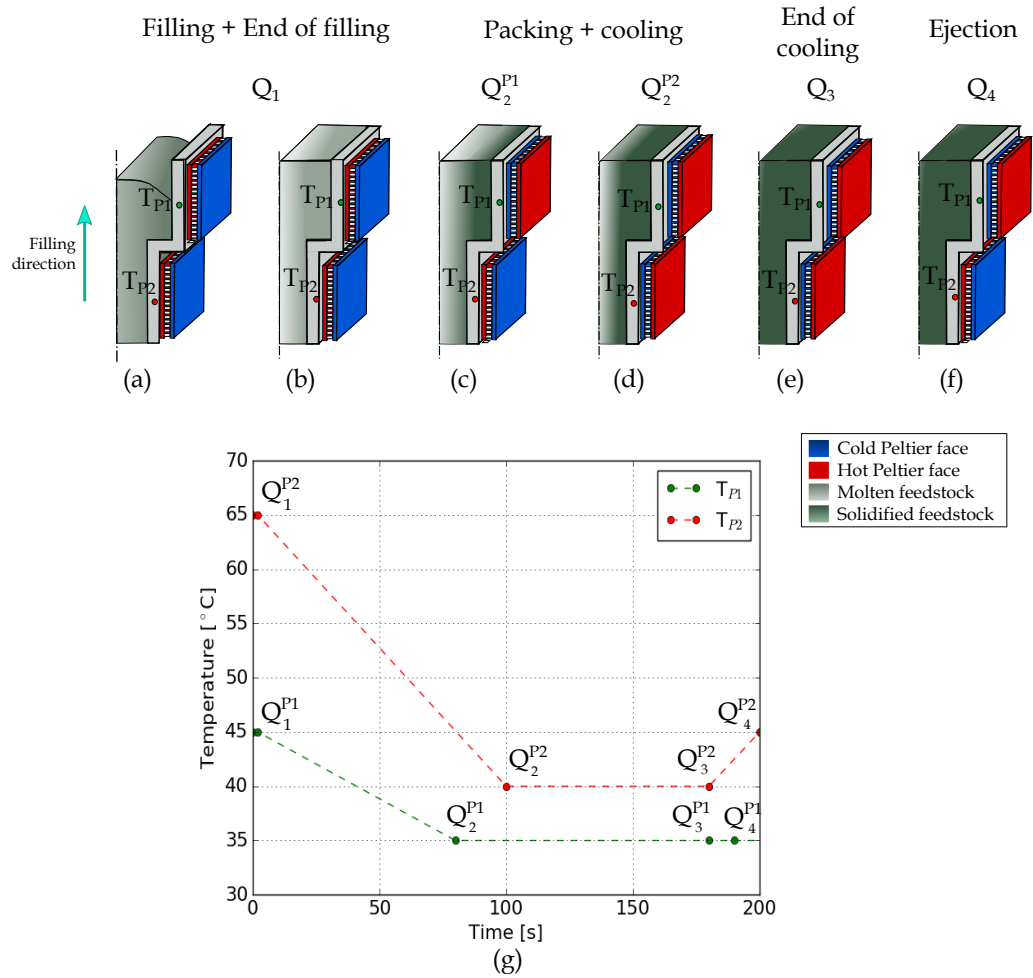


Figure 6.2: Example temperature cycle using the novel approach. (a) Filling stage. (b) End of filling. (c) Packing phase, Peltier 1 switches from heating to cooling. (d) Packing phase, Peltier 2 switches from heating to cooling. (e) End of cooling phase. (f) Ejection phase, Peltier 2 swaps to heating again to facilitate part ejection. (g) Thermal profile of the two Peltier modules shown in the schematics. Note: the graph shows hypothetical temperatures, which do not correspond to any specific thermal cycle.

for each thermoelectric element, the optimal profile were computed with the objective of minimising heating and cooling rate gradients throughout the part, during the whole IM process. Moreover, to account for the findings on the adhesion behaviour between part and mould (Chapter 5), the optimisation takes into account that, whenever mould filling for a feature (and hence for a Peltier) is performed at a temperature higher than the glass transition point ( $T_g$ ) of the binder, a re-heat up to approximately  $T_g$  is needed for that feature, in order to achieve part ejection (Point  $Q_5$  for Peltier 2 in Figure 6.2).

In the following sections, the experimental methodology followed for this study, including a detailed description of the reference geometries and of the employed mould and characterisation methods, is described. Then, the developed thermal control model and optimisation are presented and discussed.

### 6.3 Materials and methods

The development and validation of the regional mould thermal control system based on cooling rate optimisation requires an experimental methodology to be specified and adopted. The silica-zircon feedstock, previously used in Chapters 4 and 5, was employed for this study, and the novel mould with regional temperature control was designed in order to be adapted to the laboratory rig, actuated by a pneumatic cylinder, described in Chapter 3.

In the following sections, the reference geometries used in this study, as well as the designed mould tool, experimental setup and procedure employed for the injection moulding trials of this work are shown and discussed; finally,

the methodology for characterising the effect of the novel system on the macro- and micro-structure of the components is presented.

### 6.3.1 Novel die-tool: reference geometries and mould design

For the present study, the selection of sample parts with distinct surface-to-volume ratios is essential, as components geometry highly affects cooling rates in injection moulding; on the other hand, simplicity of the parts is needed for successfully isolating the root cause of any defect that may be detected in injected parts. To achieve that, two components characterised by straight channels having different cross sections were designed (Figure 6.3) and specifically conceived to have the following geometrical and process-related properties:

- Uneven wall thickness: sample parts are made of distinct channels having constant wall cross sections with dissimilar surface-to-volume (S/V) ratios (the thin features have approximately 10 times higher S/V ratio than the thick ones).
- Filling patterns going *from-thick-to-thin* and *from-thin-to-thick* features.

Two different draft angles between the Feature 1 (thick) and Feature 2 (thin) were designed also to account for gradual to abrupt transitions, causing possible powder-binder segregation.

In order to demonstrate the proposed thermal control model and system, the sample geometries were injection moulded using an experimental setup, comprising the following macro ensembles: injection unit, mould unit and control unit.

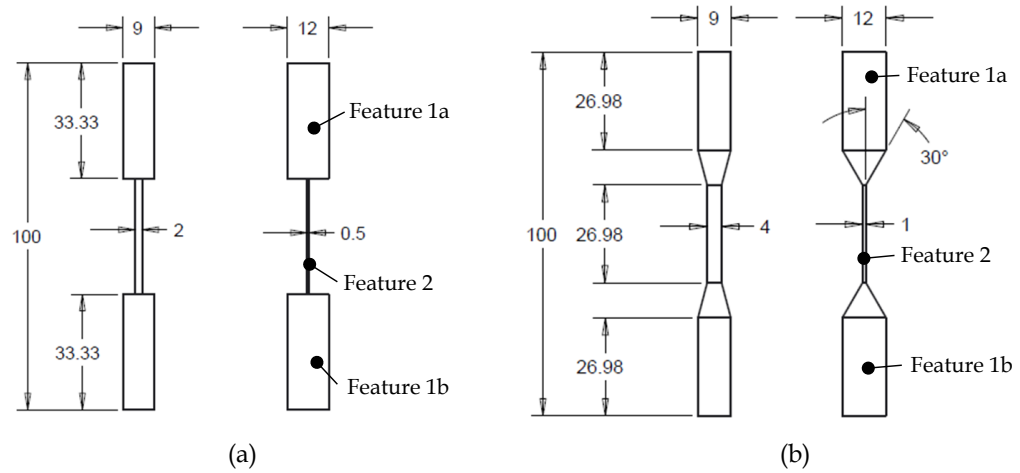


Figure 6.3: Sample components. (a) Component A. (b) Component B.

The injection unit, as previously stated, comprises the laboratory rig, actuated by a double action pneumatic cylinder, used to replicate a plunger-type injection moulding machine used in industrial environments for LPCIM.

The mould unit consists of the novel die-tool (Figure 6.4a), designed with four aluminium (Al 7075-T651) mould plates (1), having two bottom and two top plates for each cavity (i.e. two per each sample geometry); 12 thermoelectric modules (2) with an active surface area of 30 mm x 15 mm, were placed below or above (for bottom and top plates respectively) each feature, with 3 mm distance between the Peltier face and cavity surface (Figure 6.4d).

Separate mould plates (two bottom and two top) were designed for the two cavities, in order to allow for the drilling of temperature sensor housings between the features and the thermoelectric modules (Figure 6.4d). In particular, thermistors having a 0.5 mm probe diameter and a 10 k $\Omega$  resistance at 20 °C were employed, to ensure a fast enough response time ( $< 1$  s) over the desired temperature window (ambient temperature, up to 100 °C). To

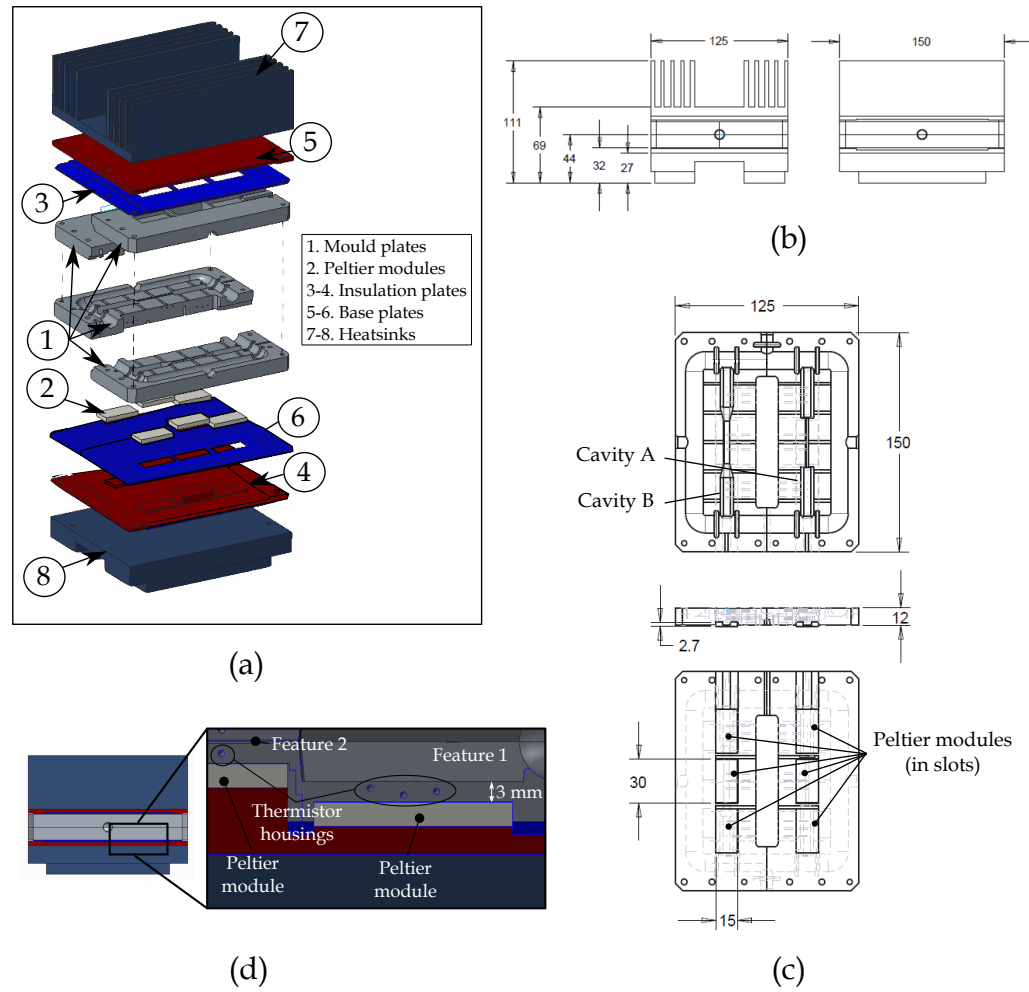


Figure 6.4: Prototype of the novel mould tool. (a) Exploded view of the assembly. (b) Main dimensions. (c) Mould cavity, main dimensions. (d) Cross section of the mould, showing Peltier modules and thermistor housings locations.

insulate the mould from the heatsink side and enhance Peltier efficiency, two glass-fibre filled resin sheets (3-4) were placed between the mould and base plates (5-6), where the faces of the Peltier modules opposite to the mould were situated. Two large heatsinks (7-8) were located at the two extreme top and bottom sides to allow for heat dissipation.

Housings for cylindrical inserts to block and deviate the material flow were machined to allow for four different injection configurations (Figure 6.5): filling of Cavity A with Single Sprue (SS), filling of Cavity B with SS, filling of Cavity A with Double Sprue (DS), filling of Cavity B with DS.

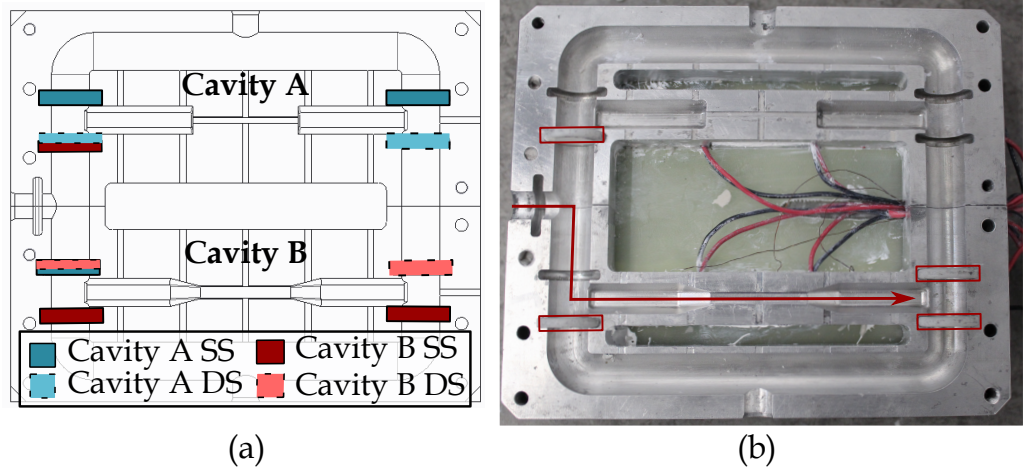


Figure 6.5: Mould unit, injection configurations. (a) Schematics of possible configurations (b) Example configuration for Cavity B SS.

The control unit was designed to independently regulate the Peltier modules temperatures, through a proportional control implemented in an Arduino. This was, in turn, connected to three driver shields with H-bridges, used to deliver the appropriate power to the thermoelectric elements with a pulsed-width-modulation (PWM) signal, depending on the temperature read by the thermistors. The melt temperature on the feedstock reservoir was controlled in a similar way with a separate Arduino, driver shield and sensors, and a thermistor inside the tank. Thermistors were also placed within the cavity to measure temperature inside the part and validate the thermal model.

In order to evaluate the novel proposed approach, three sets of injection moulding experiments were carried out, each corresponding to a specific thermal control method, with different temperature profiles per each feature (thin or thick), as shown in the example of Figure 6.6: isothermal (ambient mould temperature), RHCM and regional control (optimal case).

For each set of trials, three repetitions were carried out for every cavity



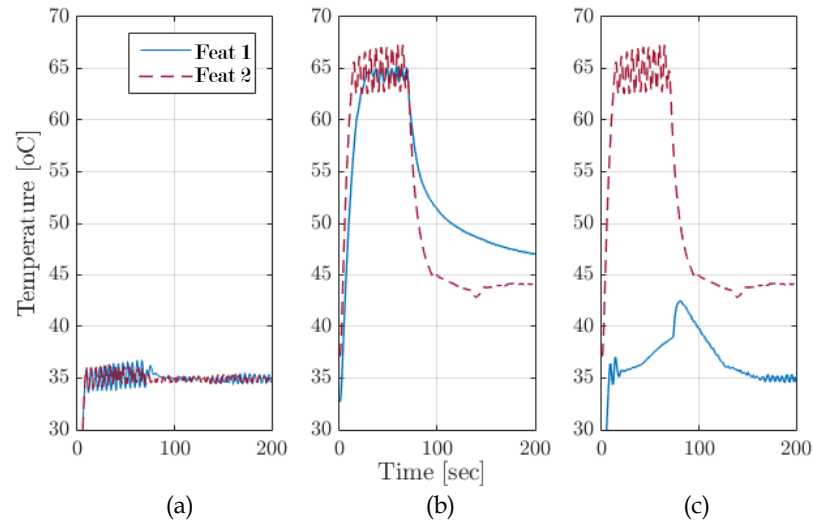


Figure 6.6: Example temperature profiles for the three employed thermal control approaches, showing the Peltier temperatures corresponding to the thin and thick features of the mould. (a) Ambient mould temperature. (b) RHCM. (c) Regional control approach.

and injection configuration (with a total number of 36 injections). Injection pressure and flow rate levels were selected to allow for maximum cavity filling without material flashing out of the mould, given the available clamping force (10.5 kN): based on this, injection pressure was set at 5 Bar and the maximum flow rate was 12 cm<sup>3</sup>/s, while melt temperature was kept constant at 75° C.

### 6.3.2 Characterisation methods

To assess the performances of the proposed novel thermal control system, and to compare them with the constant ambient mould temperature and RHCM approaches, parts injected using the three methods were analysed in terms of macro- and micro-structural quality outcomes, which were related to the heat transfer phenomena occurring during the IM process. First, feature replication capability was visually assessed, and the samples were then scanned with an Alicona InfiniteFocus optical microscope to evaluate differences in shrinkage among parts moulded with the different methods. A fixture was used to align the samples to a reference ground plane and

the top surfaces of the specimens were scanned to compare their relative heights. Alicona InfiniteFocus was also used jointly with the FEI Quanta 650 Environmental Scanning Electron Microscope (SEM) in low vacuum mode (at a chamber pressure of 70 Bar) to analyse the parts surface and evaluate the effect of the different thermal control approaches on weld lines morphology and powder-binder separation at components surface.

In order to enhance the understanding of the origin of the analysed phenomena, in relation to the employed thermal control approaches, results from macro- and micro-structural characterisations of the components are analysed and discussed relatively to the temperature and cooling rate profiles obtained through the thermal control model and measured within the injection experiments. This is reviewed in detail in Section 6.5, while, in the following one, the thermal control model and optimisation is described and discussed.

## 6.4 Thermal control model and optimisation

The development and demonstration of the mould with regional temperatures was supported by a thermal control model and optimisation, used to determine optimal temperature profiles for the Peltier modules (and hence for the mould cavity at different feature locations) throughout the moulding cycle. This was implemented using a coupled Finite Element - Particle Swarm Optimisation (FE-PSO) method (Figure 6.7).

The PSO optimises the temperature profile of each Peltier in the regionally controlled mould, to minimise thermal gradients in the centre of the part throughout the IM process. A FE transient heat transfer model of the packing and cooling phases of the IM process was implemented in ABAQUS, in

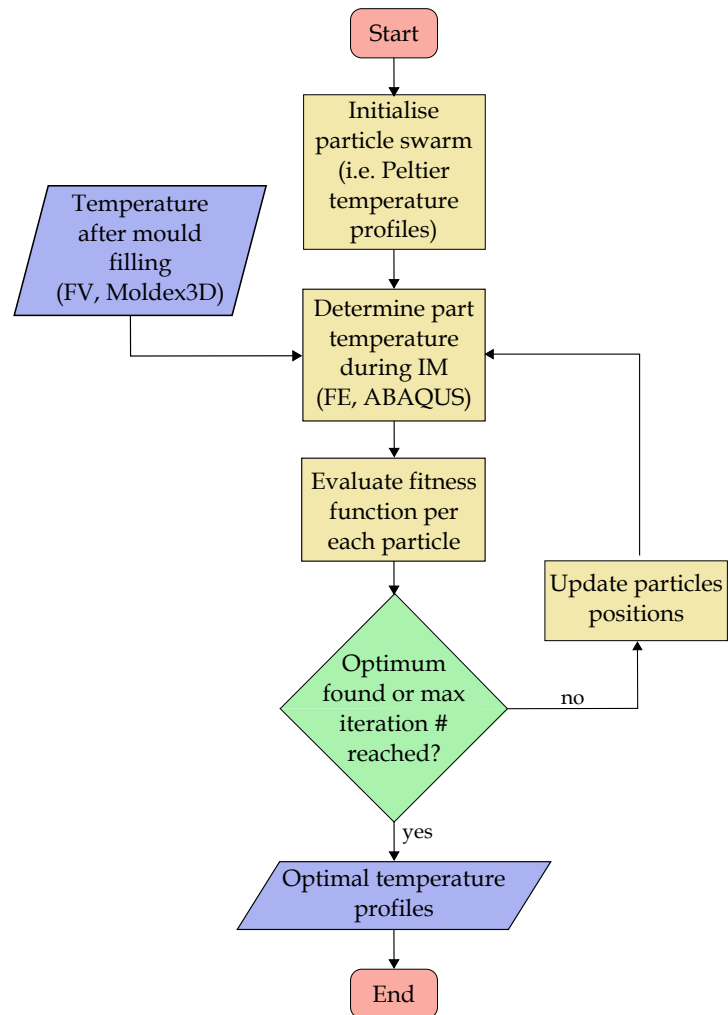


Figure 6.7: Flow chart of the thermal control model.

order to predict the temperature distribution and cooling rates inside the part, needed to compute the objective function of the PSO. Moreover, the heat and mass transfer simulation of the filling process, implemented in Moldex3D and previously validated (Chapter 4), was used in order to predict temperature distribution in the part at the end of the IM filling stage that was employed as initial condition to the thermal model in ABAQUS.

It is worth mentioning that the optimisation was run for the two reference geometries (Section 6.3.1) only injected with Double Sprue (DS) configuration. This was done because, in the case of Cavity A (i.e. the one without draft angle), mould filling with a Single Sprue (SS) configuration could not be achieved, even when the die-tool was heated up, as discussed in Section 6.5.2. As for Cavity B, entire cavity filling in SS configuration could only be achieved when the mould temperature under the thin feature (Feature 2) was above the glass transition temperature ( $T_g$ ) of the feedstock. In this case, temperature distribution throughout the part after mould filling is similar to that in the DS case, because of the large size of Feature 1 (12 mm x 9 mm) and the short filling time, not giving enough time to the feature to cool down. Therefore, optimisation results for DS configuration could also be considered as the optimal temperature profiles when injecting Cavity B in SS configuration.

In the following sections, the optimisation is firstly described, including the main variables, optimisation functions, constraints and PSO parameters. Then, the setup of both the filling and the "packing-cooling" models (in Moldex3D and ABAQUS respectively) are shown and discussed.

### 6.4.1 Optimisation of mould temperatures

As previously stated, the objective of the implemented optimisation is to find the temperature profiles over time  $T(t)$  per each region of the mould (i.e. per each Peltier module) which minimise thermal gradients in the part throughout all the IM process stages. Therefore, the definition of the optimisation variables is based on a subdivision of the whole process window. Considering a generic point  $Q$  with coordinates  $(t, T)$ , corresponding to a temperature  $T$  at an instant of time  $t$  during IM, the process window can be divided into three phases (Figure 6.8), going from points  $Q_1 - Q_2$ ,  $Q_2 - Q_3$  and  $Q_3 - Q_4$  of the graph respectively.

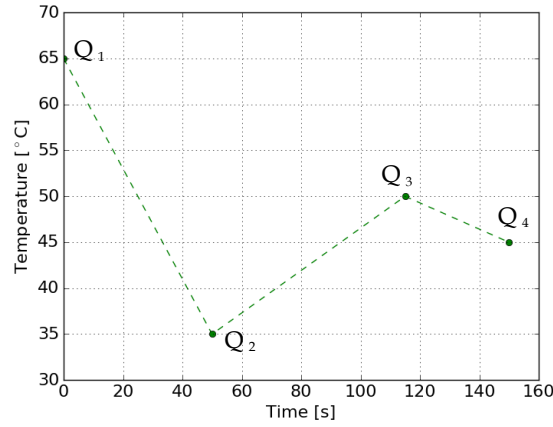


Figure 6.8: Example process window used for FE-PSO variable definition, for a single Peltier (P1). Note: a different set of parameters is valid per each Peltier.

The optimisation variables are then defined as the coordinates (i.e. time and temperature) of each control point: the temperature profile between each couple of control points  $Q_i - Q_{i+1}$  is assumed to be linear. Moreover, a different profile needs to be accounted simultaneously for each Peltier in the mould, leading to a total maximum of  $8P$  variables, where 8 accounts for the two coordinates for each of the four control points, and  $P$  is the number of Peltier modules (or regions) in the mould.

The use of this approach for constructing the optimisation enables a wide problem exploration, however, it implies the use of a high number of variables, which increases the computational time: this is not desirable, especially when a FE simulation has to be solved to compute the fitness function. Therefore, to simplify the problem, both the number and the domain of the optimisation variables have been selected based on the following:

- The initial time, corresponding to the end of injection and the beginning of the packing and cooling phases is the start of the analysis:  $t(Q_1) = 0$ .
- The initial mould temperature could only assume two values (RHCM or ambient):  $T(Q_1) = T_{low} \vee T(Q_1) = T_{high}$ .
- The final cooling temperature must be lower than the glass transition point of the material binder and was fixed to a value:  $T(Q_3) = T_{low}$ .
- All the temperature values were bonded to lower and upper limits coincident to the two possible values assumed at the beginning of the analysis:  $T(Q_i) = [T_{low}, T_{high}], \forall i$ .

To account for further process requirements, the following constraints were implemented:

1. The part must be solid at ejection:  $T(Q_4) \leq T_{sol}$ .
2. Mould-part adhesion: when the initial temperature of a Peltier is higher than the feedstock  $T_g$ , its temperature at ejection must be equal to  $T_g$ .  $T(Q_1) \geq T_g \Rightarrow T(Q_4) = T_g$ .
3. Each phase should end after its beginning:  $t(Q_i) \leq t(Q_j), \forall i, \forall j = i + 1$ .
4. Mould temperature at the thin feature needs to be higher than the feedstock  $T_g$  to allow for mould filling:  $T(Q_1) \geq T_g$ .

Moreover, the swarm initialisation includes the choice of the following parameters:

- Swarm size  $n$ : the number of particles within the swarm, where each particle corresponds to an instance of the optimisation variables.
- Maximum number of iterations  $K$ .
- PSO coefficients  $(\omega, c_1, c_2)$  which determine the method of movement within the search space (i.e. how, given the results from all previous iterations, the algorithm updates the values/position assumed by the particles in the swarm).

All the values used for the reference parameters, upper and lower bounds of the variables and PSO coefficients are displayed in Table 6.1.

The fitness function  $f_c$ , to be minimised with the PSO method, was defined as:

$$f_c = \alpha(\Delta\dot{T}_{max} + \Delta\dot{T}_{ave}) + \beta T_{bool} + \gamma t_{step} \quad (6.1)$$

where  $\Delta\dot{T}_{max}$  and  $\Delta\dot{T}_{ave}$  are respectively the maximum and the average differences in cooling rates in the centre of the thin and thick features of the channels, throughout the packing and cooling phases;  $T_{bool}$  is a boolean variable used to satisfy constraint number 1;  $t_{step}$  is the total packing and

Table 6.1: PSO parameters

Parameter	Value
$T_{low}$ [ $^{\circ}\text{C}$ ]	35
$T_{high}$ [ $^{\circ}\text{C}$ ]	65
$T_{sol}$ [ $^{\circ}\text{C}$ ]	47
$n$	50
$K$	100
$\omega$	0.5
$c_1$	0.5
$c_2$	0.5

cooling time, corresponding to the cycle time of the process;  $\alpha$ ,  $\beta$  and  $\gamma$  are weighting coefficients. Both  $\Delta\dot{T}_{max}$  and  $\Delta\dot{T}_{ave}$  were optimised to account for peaks in cooling rates as well as mean shifts. An example of fitness function values over iteration number is displayed in Figure 6.9.

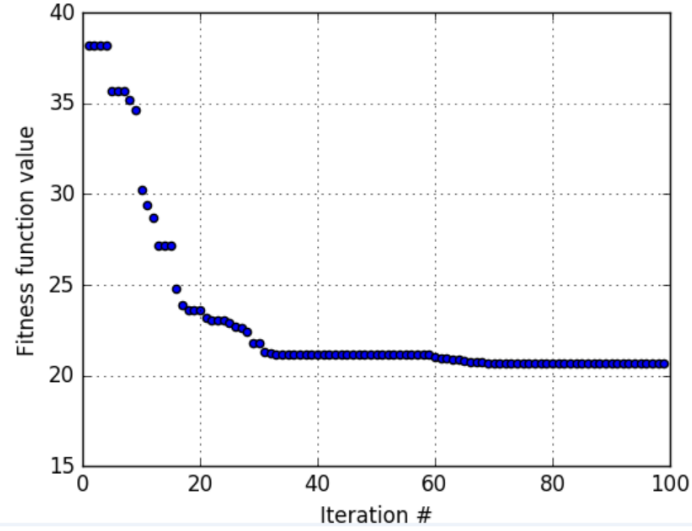


Figure 6.9: Example of solution convergence over iteration number.

At each PSO iteration, the fitness function value is calculated per each particle: to do this, values for cooling rates were determined using two numerical simulations of the IM process, which are described in the following section.

### 6.4.2 Numerical modelling of the IM process

The first developed model is a mould filling simulation, carried out using the injection moulding FEM-FVM software Moldex3D, from which the temperature distribution throughout the part at the end of filling was mapped and used as an initial boundary condition for the second model, used to simulate the packing and cooling phases, which was performed as a FE transient heat transfer analysis in ABAQUS.

For the implementation of both the filling and the packing-cooling models,



the following steps were followed:

1. Definition of the modelled components
2. Construction of a mesh
3. Definition of material properties for the modelled components
4. Definition of Boundary Conditions (BCs) and Initial Conditions (ICs)

For the first simulation, the modelled assembly (Figure 6.10) included the part (i.e. the reference geometries shown in Section 6.3.1), the mould envelope (i.e. the aluminium plates) and the Peltier modules, modelled as solid rectangular plates having an imposed temperature.

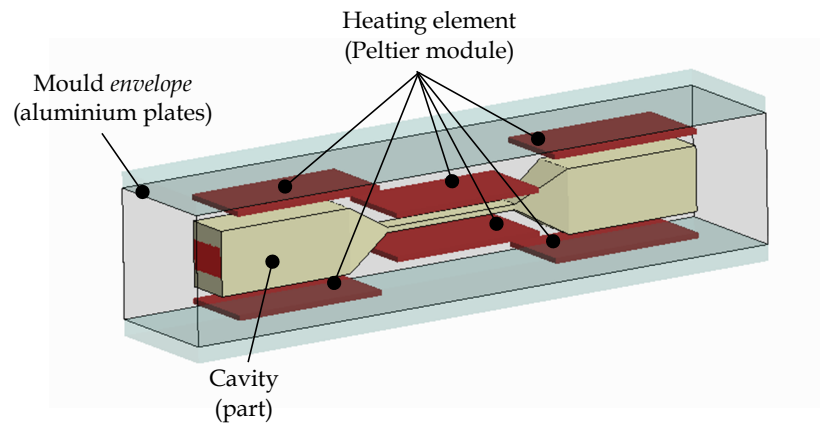


Figure 6.10: Assembly modelled in Moldex3D filling simulation.

The heatsinks were not modelled and thermal effects from the face of the thermoelectric cooler in contact with them were neglected, as the two Peltier faces (i.e. the one in contact with the mould and the one in contact with the heatsink) were thermally isolated. The assembly was meshed with tetragonal elements, having minimum seed size of approximately 0.1 mm to ensure a properly refined mesh of the thinnest features (0.5 mm thick). The material properties that were taken into account to simulate the filling process are the same used for the filling model developed in Chapter 4, and include

the feedstock viscosity behaviour as a function of shear rate and temperature, modelled with a Cross-Exp law (Nikolic, Randelovic, and Milutinovic, 2014), heat capacity and thermal conductivity, defined as a function of temperature, and PVT behaviour, modelled using a modified Tait model (Zheng, Tanner, and Fan, 2011). The mould envelope was modelled with Aluminium 7075-T651 density and thermal properties. As for the employed BCs and ICs, the flow rate and injection pressure values reported in Section 6.3.1 were respectively used as inlet BC and maximum pressure level during mould filling, and the pre-set pressure filling-to-packing switch-over condition was set at the point when nozzle pressure equalised the maximum injection pressure. The feedstock inlet temperature was set based on the melt temperature used in the IM experiments, while the Peltier temperatures were imposed according to two different modelled scenarios:

- All Peltier modules at 65 °C
- Peltier 2 (i.e. the one under the thin cavity) at 65 °C while Peltier 1a and Peltier 1b at 35 °C

For the second simulation (i.e. the FE model of the cooling stage implemented in ABAQUS), symmetry in load and geometry were used, and hence only one eighth of the assembly (because of the DS injection configuration). The assembly included only the moulded part and mould cavity, while the Peltier modules were instead modelled as temperature BCs on the mould bottom (and hence top, for symmetry) surfaces (Figure 6.3).

A tetragonal quadratic mesh with minimum seed of 0.1 mm was also constructed for this model, in order to ensure a sufficient number of elements along the thinner features of the mould and cavity. As the simulation is a transient heat transfer model, only the density, thermal conductivity and heat capacity of the ceramic feedstock and of the Aluminium 7075-T651

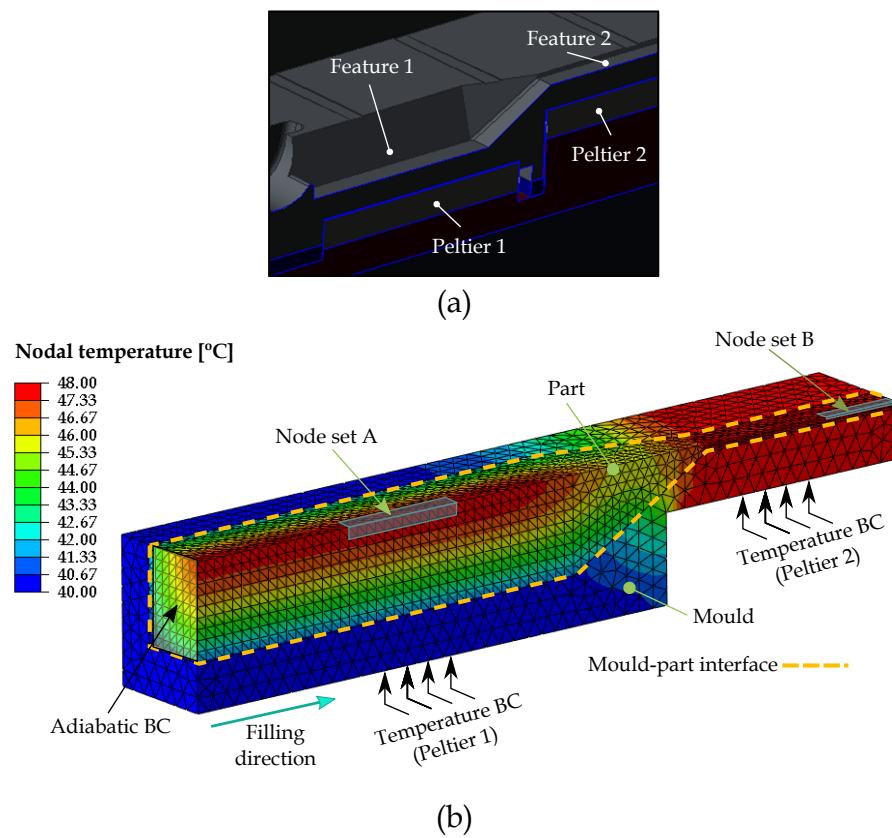


Figure 6.11: Example of ABAQUS-modelled assembly (Cavity B) (a) CAD model of the assembly. (b) Schematics of the model setup, showing the used mesh and temperature distribution.

mould were modelled. An adiabatic BC was imposed at surfaces corresponding to gate locations: this condition was considered under the assumption of simultaneous solidification of the runner features close to the gate location. A thermal conductance BC was employed between the mould and the part, with a value of  $1500 \text{ W/m}^2\text{K}$ , of the same order of magnitude with respect to values found in literature (Somé et al., 2015). As only the portion of the mould containing the cavity and the Peltier modules was modelled, preliminary thermal simulations were performed, in order to verify negligible heat losses within the whole mould (and also to validate the designed mould before manufacturing). This assumption of negligible heat losses was also made possible as thermoelectric module temperatures were closed-loop controlled, hence a temperature rather than a heat flux BC was imposed at Peltier-mould interface.

A workflow was implemented in order to automatically feed into the FE simulation both the temperature BCs corresponding to the Peltier thermal profiles (Figure 6.8) from the PSO algorithm, and the mapped temperature distribution throughout the part and mould at the end of filling, from the Moldex3D simulation results.

Through these numerical models, part temperature distribution during the whole IM process was determined, and the cooling rates  $\Delta\dot{T}_{max}$  and  $\Delta\dot{T}_{ave}$  were calculated as time derivative of the average temperature profiles within two node regions in the centre of the part features (Node sets A and B in Figure 6.11). Finally, these cooling rates were fed-back to the PSO simulation to compute the optimisation fitness function, also in this case by a developed workflow.

## 6.5 Results and discussion

In this section, the results of the performed modelling and experimental work is presented and discussed, as anticipated in Section 6.3. First the results of the PSO is presented, along with an analysis of the heat transfer phenomena occurring using the novel developed system and optimised control. In particular, an insight is given on how the novel and optimised system affect cooling rates and temperature distribution in the part. Moreover, the throughput and thermal efficiency of the designed system is discussed. Finally, the performance of the novel thermal control system is evaluated by analysing its effect on the macro- and micro-structural properties of injection moulded green parts.

### 6.5.1 Optimisation results and thermal analysis

As previously discussed, the development of a novel thermal control approach for ceramic components with uneven wall thickness needs to promote uniform cooling rates inside the part, despite the differences in the sizes of components features. To consider this, starting from the results of the thermal control model and optimisation, the cooling rates and solidification time of the reference component features have been primarily analysed. Moreover, system performance, in terms of heating and cooling efficiencies, have been accounted for and is presented at the end of this section.

The optimised Peltier temperature profiles, resulting from the PSO, include the employment of a different control for the thin and thick features for both reference geometries: Cavity A (Figure 6.12a) and Cavity B (Figure 6.12b).

In both cases, the Peltier profiles are a constant ambient temperature for the Peltier under the thick feature (Peltier 1) and a localised-RHCM ap-

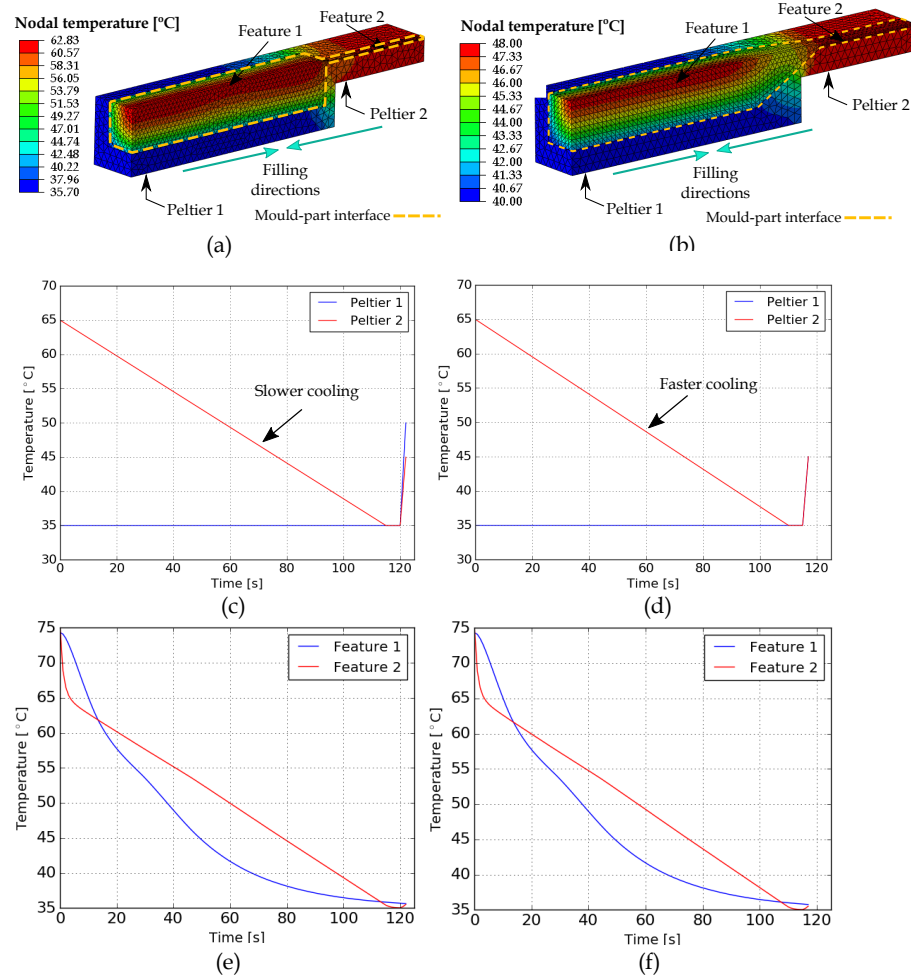


Figure 6.12: Results from the thermal control model and optimisation. (a) 3D mesh, Cavity A. (b) 3D mesh, Cavity B. (c) Optimal Peltier temperature profiles, Cavity A. (d) Optimal Peltier temperature profiles, Cavity B. (e) Optimal temperature profiles in the centre of Feature 1 and Feature 2, Cavity A. (f) Optimal temperature profiles in the centre of Feature 1 and Feature 2, Cavity B.

proach for the Peltier under the thick feature (Peltier 2). At the end of the process, to ensure successful part ejection, a rise of temperature is also included for both Peltier modules, up to the feedstock  $T_g$ .

The only difference in the two temperature profiles is the rate of cooling of Peltier 2 of the two geometries: Peltier 2 in Cavity A has a slower rate than Peltier 2 of Cavity B. This can be explained by the fact that the rate of mould cavity surface cooling (i.e. the Peltier thermal profile) is optimised in a way that the temperature difference in the centre of Feature 1 and 2 is minimised. Therefore, to match the slow cooling rate of Feature 1, as Feature 2 of Cavity A is thinner than Feature 2 of Cavity B, the rate of cooling for its corresponding Peltier needs to be lower. This is confirmed by the equal temperature distributions in the centre of the features for the two cavities (Figure 6.13d-e). The same applies to the difference in ejection peak temperature for Peltier 1 in Cavity B, compared to Peltier 1 in Cavity A: in order to maintain similar internal temperatures to Feature 2, the Peltier of Cavity B needs to be heated up to a higher temperature. However, this last result does not take into account that a too high local cavity temperature causes warpage and damage to the part, hence the increase of temperature during ejection is limited to the feedstock  $T_g$  (i.e. 45 °C) during the injection experiments.

Considering the packing and cooling phases of the process (i.e. neglecting part ejection), it is possible to compare the effects on the cooling rates within the part of the optimised regional controlled approach (Figure 6.13a and Figure 6.13c) to what happens in RHCM (Figure 6.13b and Figure 6.13d). First of all, a clear distinction between the two thermal control approaches can be noticed in terms of temperature profiles inside the parts. In the RHCM case (Figure 6.13e), the material in the thin feature (Feature 2)

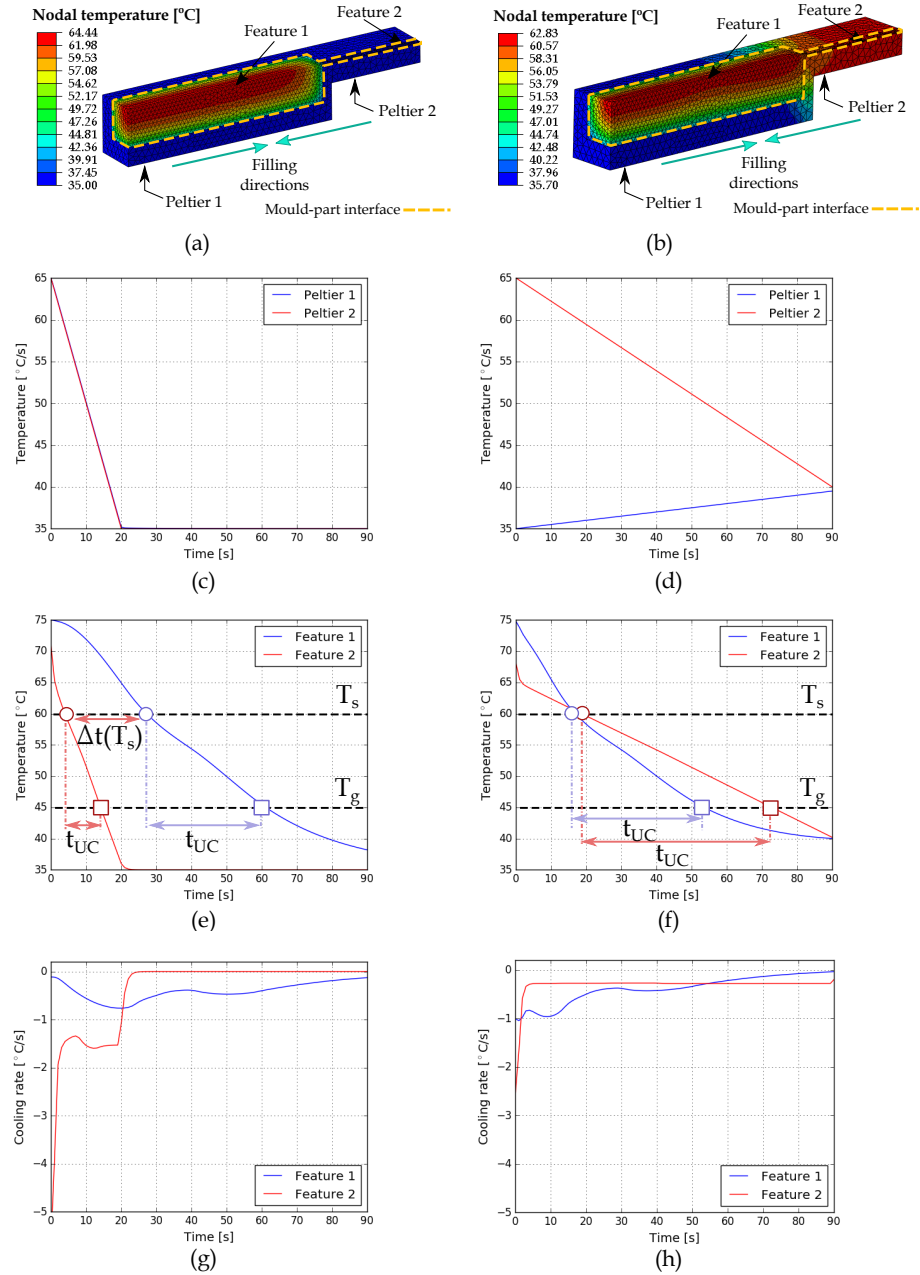


Figure 6.13: Results from the thermal control model: example for Cavity A in DS configuration. (a) 3D mesh, RHCM. (b) 3D mesh, optimised regional. (c) Peltier temperature profile, RHCM. (d) Peltier temperature profile, optimised regional. (e) Feature cooling rate profile (node sets A and B), RHCM. (f) Feature cooling rate profile (node sets A and B), optimised regional. (g) Feature temperature profile (node sets A and B), RHCM. (h) Feature temperature profile (node sets A and B), optimised regional.



solidifies faster than the feedstock in the thick feature (with a difference in solidification time  $\Delta t(T_s)$  of approximately 20 seconds); on the other hand, in the optimal case (Figure 6.13f), joint freezing occurs between the two features. In the case of single sprue (SS) injection configuration, if the thin feature solidifies faster, the thick feature farther from the gate will not be packed properly during the holding stage (Figure 6.14).

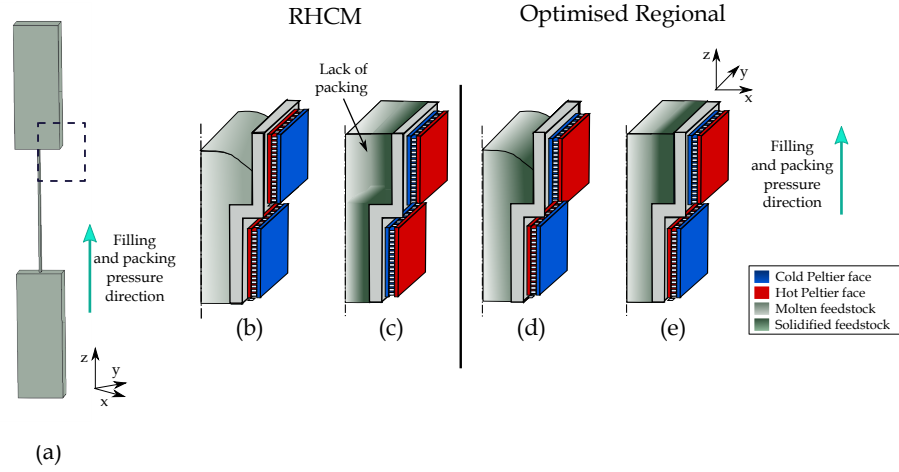


Figure 6.14: Schematics of lack of packing during single sprue moulding with RHCM approach compared to the optimal case. (a) Schematics of the analysed sample and detailed view of the magnified area. (b) Filling stage, RHCM. (c) Packing stage, RHCM. (d) Filling stage, optimised regional. (e) Packing stage, optimised regional.

Therefore, even more importantly than in the DS case, the simultaneous solidification of the features despite their differential thickness, promoted by the optimised solution, enables a more uniform shrinkage compensation within the part, as discussed more in depth in Section 6.5.2.

Moreover, upon cooling, the glass transition temperature of the material in the thin feature (Feature 2) is reached considerably faster than in the thick one, using the RHCM approach. Hence, the material within the component undergoes different undercooling times ( $T_{UC}$  in Figure 6.13e-f): this leads to a dissimilar development of the binder crystalline microstructure, which plays a fundamental role in shrinkage behaviour (Fischer, 2013), as seen in

## Section 6.5.2.

This difference in temperature profiles can be translated into the cooling rate difference between the two approaches. In the optimised case, the average difference in cooling rates between the thin and thick features is approximately two times lower than in the RHCM case during the first 10 seconds after mould filling, and 50% lower during the rest of the process (Figure 6.13g-h).

The thermal model was validated through injection moulding experiments performed with the setup and materials described in Section 6.3. The temperature at the centre of Feature 2 of Cavity B, injected in SS configuration, was measured by inserting a sacrificial 10 k $\Omega$  thermistor having 0.5 mm diameter (with a 1% error, leading to a  $\pm 0.5$  °C accuracy), inside the mould cavity (Figure 6.15a). and a comparison between model and experimental results for the temperature profile inside the cavity at Feature 2 are presented in Figure 6.15b and c for the RHCM and optimal cases respectively. It is worth mentioning that, due to the fact that the mould was adapted to the employed test rig, higher limitations in heat dissipation on the heatsink side emerge, compared to an industrial die-tool with water-based cooling channels. This caused a lower efficiency of the system compared to the initially simulated one, implying that a slightly different heating and cooling profile had to be used for the trials compared to the optimisation results. This explains the difference in temperature profiles comparing the results shown in Figure 6.13 and 6.15, and especially in Figure 6.13e and 6.15b. However, this did not constitute a limitation for the validation of the model and concept, as it implied a narrowing of the binding ranges for the time and temperature variables at the control points shown in Figure 6.8, while similar cooling rates were achieved between thin and thick features in the

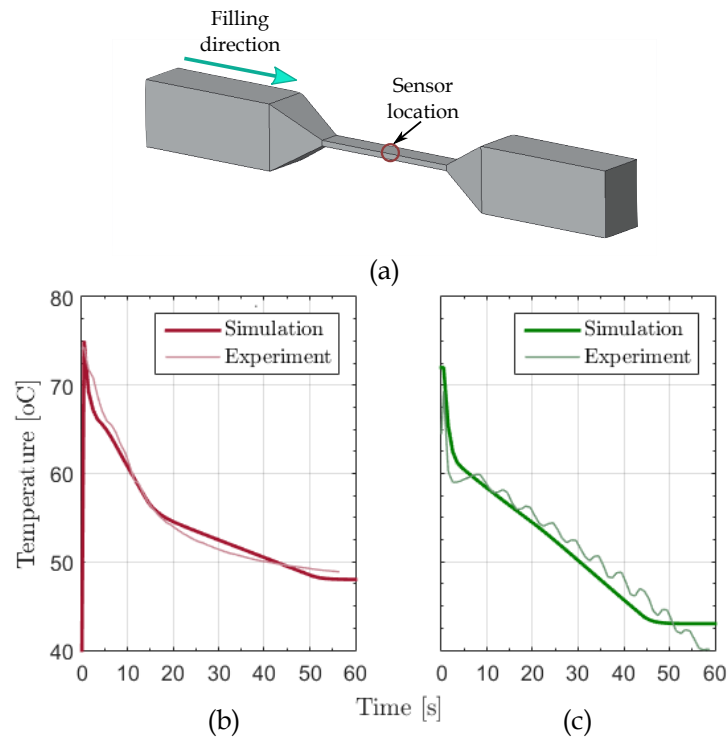


Figure 6.15: Validation of the thermal control model: example for Cavity B in SS configuration. (a) Schematics of the component and location of the sensor in the cavity. (b) Validation, RHCM. (c) Validation, optimised regional control.

optimal case, as shown in Figure 6.16. The oscillations in Figure 6.15c and Figure 6.16 are instead due to the proportional control: the instability is, however, limited to oscillation of  $\pm 2^\circ\text{C}$ , which is negligible compared to temperature variations that would induce changes in part quality and integrity at macro and microstructural levels. This is because, during filling, mould temperature is kept  $5^\circ\text{C}$  higher than the feedstock melting point, and the observed temperature range where the fluctuations occur is above the material  $T_g$ .

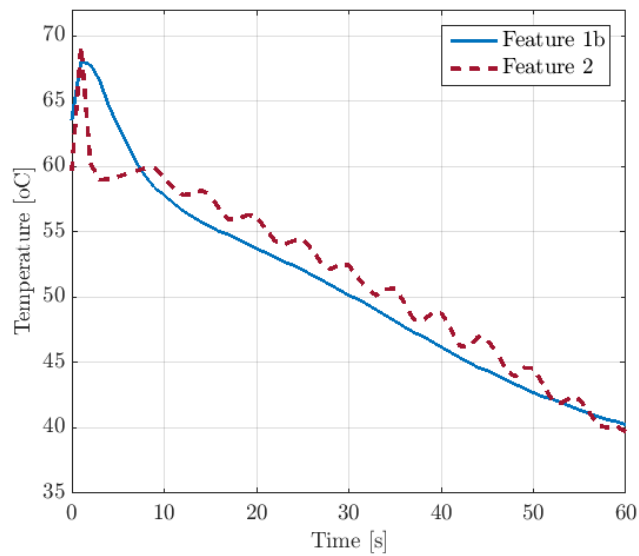


Figure 6.16: Measured temperature inside Feature 1b and in the centre of Feature 2 for Cavity B injected in DS configuration, using the regional optimised temperature approach. Note: the exact location of the thermistor inside Feature 1b could not be determined, but the figure show that similar cooling rates occur in the two features using the optimised control.

As for cycle time considerations, no substantial difference can be detected between the regional control approach and RHCM. This is due to the fact that, although maintaining some cavity features at ambient temperatures should decrease the required cooling time, the differential control of the thermoelectric coolers causes heat transfer from warmer to colder areas of the cavity to occur, which prolongs cooling time. However, an enhanced

insulation between mould features and an increased heat dissipation of the bolster side of the mould can be better achieved with simple straight cooling channels.

### **6.5.2 Performance evaluation of the novel thermal control approach: effects on injection moulded parts**

As previously stated in Section 6.3, to validate the performance of the proposed mould temperature control approach, the already described thermal analysis is coupled with an investigation of macrostructural and microstructural properties of the components injected in this study. This analysis is divided into three parts: the first discusses feature replication capability, followed by an analysis of dimensional control for the injected parts and concluding with a study of surface quality and weld lines.

#### **6.7.2.1 Feature replication capability**

A sharp enhancement in feature replication capability was observed by increasing mould temperature below the thin channel (Feature 2) in the cavities (Figure 6.17), showing that the local heating of the finest features is enough to ensure the complete injection of the components, without increasing the temperature of the whole mould.

In both the RHCM and regionally controlled cases, more than 100% flow length increase is observed with respect to the ambient temperature approach, leading to the achievement of complete filling of Cavity A (Figure 6.17b-c) when injected with double sprue configuration and of Cavity B (Figure 6.17d-e) when injected in both single and double sprue configurations. The thinnest (0.5 mm) channel of Cavity A could not be fully filled with SS configuration, even using the RHCM approach, due to the

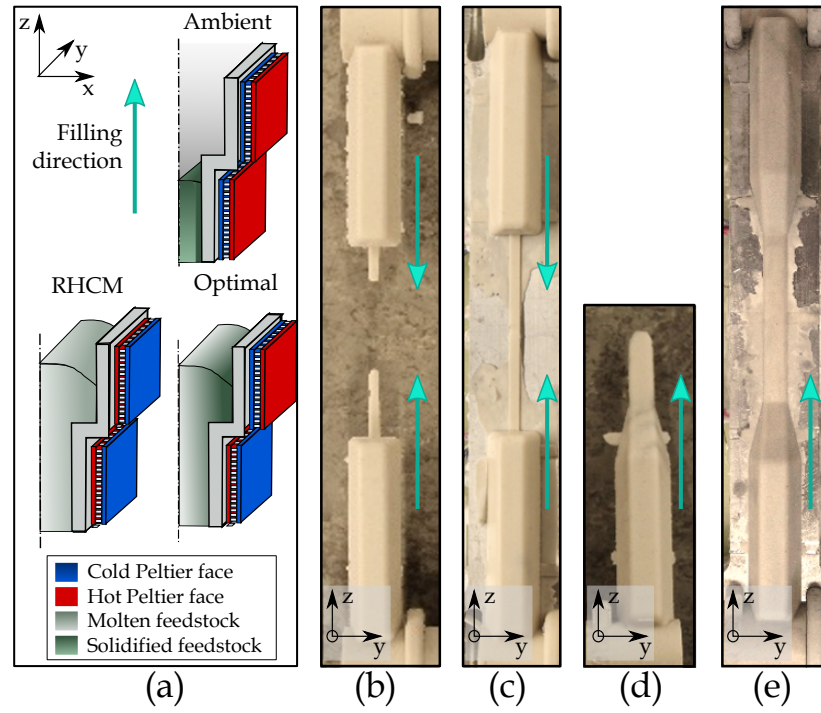


Figure 6.17: Enhancement of feature replication capability using RHCM and regional control approach. (a) Schematics of the phenomenon. (b) Cavity A DS,  $T_m = 35^\circ\text{C}$ . (c) Cavity A DS, RHCM and optimal cases. (d) Cavity B SS,  $T_m = 35^\circ\text{C}$ . (e) Cavity B SS, RHCM and optimal cases. Note: as the same flow length, during filling, was achieved in the RHCM and optimal case, only one picture for both approaches is displayed for simplicity.

high pressure drop in the channel and to the fact that feature thickness starts being comparable to particle size. This behaviour shows the effect of viscosity, which, for the employed feedstock, drops to values as low as approximately 2 Pa·sec at a temperature of approximately 62 °C, with very low dependence on the shear rate: due to this, when mould temperature is kept constant (ambient) throughout the process, the material solidifies before reaching the end of the channel; differently, as the thinnest feature temperature is increased above the "viscosity drop" level, lower pressures and subsequent shear stresses are enough to fill the thinnest channels (Figure 6.17a). This implies that only the use of a higher pressure (of approximately 25 Bar, if calculated through the Hagen-Poiseuille equation) would allow for the complete filling of the channel with a heated mould.

#### 6.7.2.2 Dimensional control

One of the main advantages of the proposed regional control approach against the employment of a uniform mould temperature is related to the dimensional control of components moulded injected using the SS configuration.

Shrinkage of the features located farther from the gate (i.e. Feature 1b, as shown in Figure 6.18a) in Cavity B was measured for parts injected with the regional and RHCM approaches. Shrinkage was evaluated by placing the sample parts on a fixture and measuring, through the Alicona InfiniteFocus optical microscope, the relative heights and widths of Feature 1b injected with the RHCM and optimised regional control (Feature 1b, as shown in Figure 6.18).

Results from these measurements (Table 6.2) show an average difference of approximately 50  $\mu\text{m}$  in height (and thus in thickness,  $\Delta th$ ) and of 130  $\mu\text{m}$

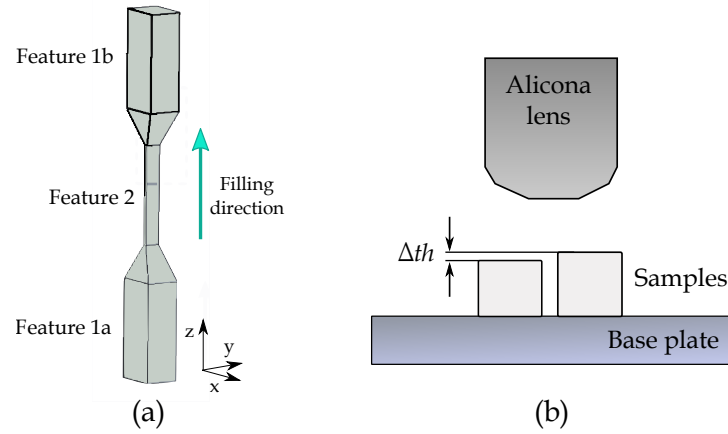


Figure 6.18: Dimensional accuracy analysis (a) Schematics of the analysed sample features (b) Schematics of the setup for dimensional accuracy measurements.

in width ( $\Delta w$ ), with the Feature 1b injected using the regional approach being larger and thicker than its equivalent injected using RHCM. Although the measured differences are quite low on an absolute value, the amount of shrinkage increases after the debinding and sintering processes, determining part warpage which, in the case of brittle ceramic materials, likely induces cracks on the final components (Mannschatz, 2011).

Table 6.2: Height difference among Feature 1 (farther from the gate) in Cavity B, moulded in SS configuration

Shrinkage in moulded samples	
Average shrinkage (Feature 1a) [%]	1
Average shrinkage (Feature 1a) [ $\mu\text{m}$ ]	125
Average $\Delta th$ (Feature 1b) (optimal - RHCM) [ $\mu\text{m}$ ]	50
Average $\Delta w$ (Feature 1b) (optimal - RHCM) [ $\mu\text{m}$ ]	130

Moreover, this difference can be compared against a measured shrinkage of about 1%, implying an increase of linear shrinkage along the thickness direction of approximately 25% in Feature 1a.

The effect on shrinkage of the regional mould temperature approach, com-



pared to the conventional RHCM, can be explained by looking at the compressible behaviour of the feedstock (Figure 6.19).

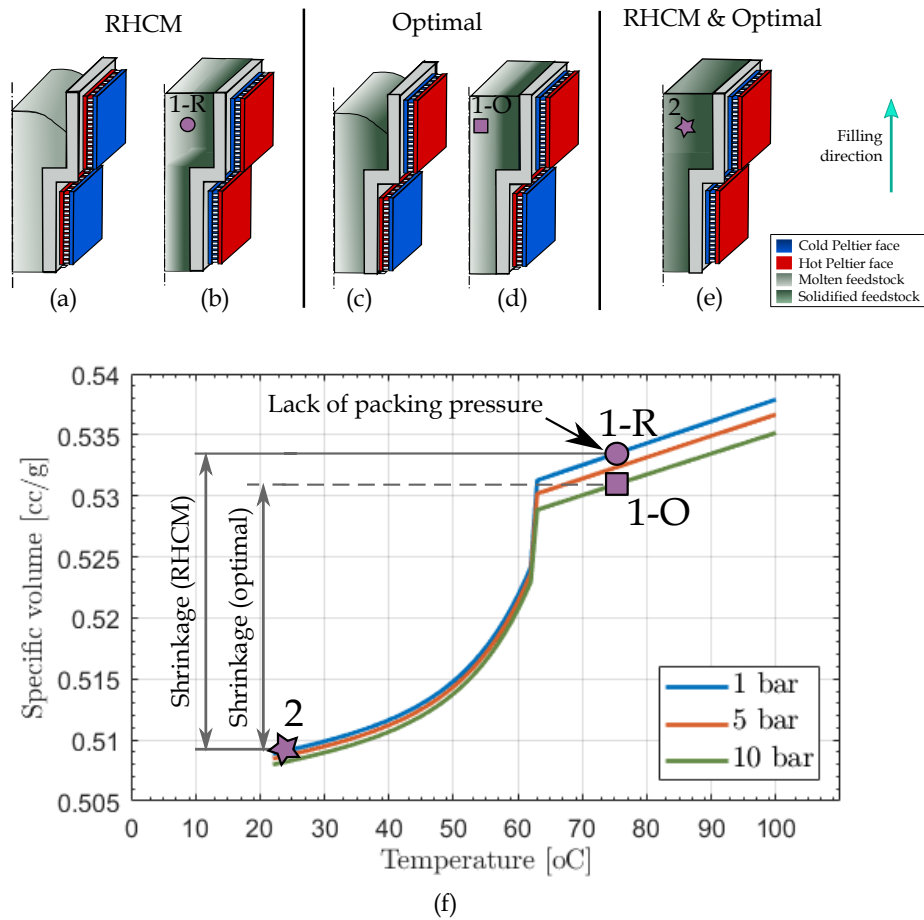


Figure 6.19: CIM outcome: Dimensional control. (a) Schematics of the phenomenon, mould filling, RHCM. (b) Schematics of the phenomenon, packing phase, RHCM. (c) Schematics of the phenomenon, mould filling, optimal. (d) Schematics of the phenomenon, packing phase, optimal. (e) Schematic of the phenomenon, part after cooling, RHCM and optimal. (f) Example of PVT behaviour.

In the RHCM case, during the filling stage, the material is molten and subjected to a higher pressure than atmospheric (Point 1-R in Figure 6.19a-b), determining an increased specific volume of the feedstock (Figure 6.19f), due to its high temperature. Once the cavity is fully filled, mould temperature is rapidly reduced uniformly, thus determining the quick solidification of the thinnest feature (as previously seen in the thermal analysis of Figures 6.13g), while the material in the thicker portion of the cavity farthest

from the gate (Feature 1b) is still in the molten state. On the other hand, in the optimised regional controlled mould temperature case, simultaneous cooling of the central portions of materials in the thin and thick part features occurs, leading to the solidification of the features farther from the gate at the imposed packing pressure (Point 1-O in Figure 6.19d and 6.19f).

The effect of this solidification behaviour in the RHCM case is threefold: first, material shrinkage in Feature 1b during cooling will not be compensated, as no extra material will be fed into this portion of the cavity due to the freezing of the thinner feature, closer to the gate (Feature 2). Second, Feature 1a will cool without any applied packing pressure, causing a higher total specific volume variation compared to solidification with higher applied pressures (Figure 6.19f): this is especially valid when high levels of packing pressure are used. Finally, in the cases of feedstocks having semi-crystalline binders, cooling rate causes a further variation of PVT behaviour of the material (Zuidema, 2001) due to the level of crystallinity obtained during undercooling. As a lower specific volume can be associated with a higher level of crystallinity (Fischer, 2013), thin and thick sections will shrink differently in the RHCM case compared to the regional control approach, causing potential further stresses and warpage in the component.

#### **6.7.2.3 Weld lines and surface quality**

Weld lines, created by the merging of multiple flow fronts of feedstock during mould filling, constitute weak areas on injected parts, as the poor blending of the different fronts determines the formation of a v-notch on the component surface where stress concentrates. Weld lines have been analysed through SEM on the moulded samples, and a clear difference in their morphology can be observed when comparing components moulded using an ambient temperature and heated mould (both RHCM and optimised re-

gional cases). In the ambient mould temperature case, poor merging of the flow fronts is achieved (Figure 6.20), due to higher viscosity of the feedstock material, approaching solidification, leading to a weld line approximately  $100\ \mu\text{m}$  below the top channel surface (Figure 6.20e).

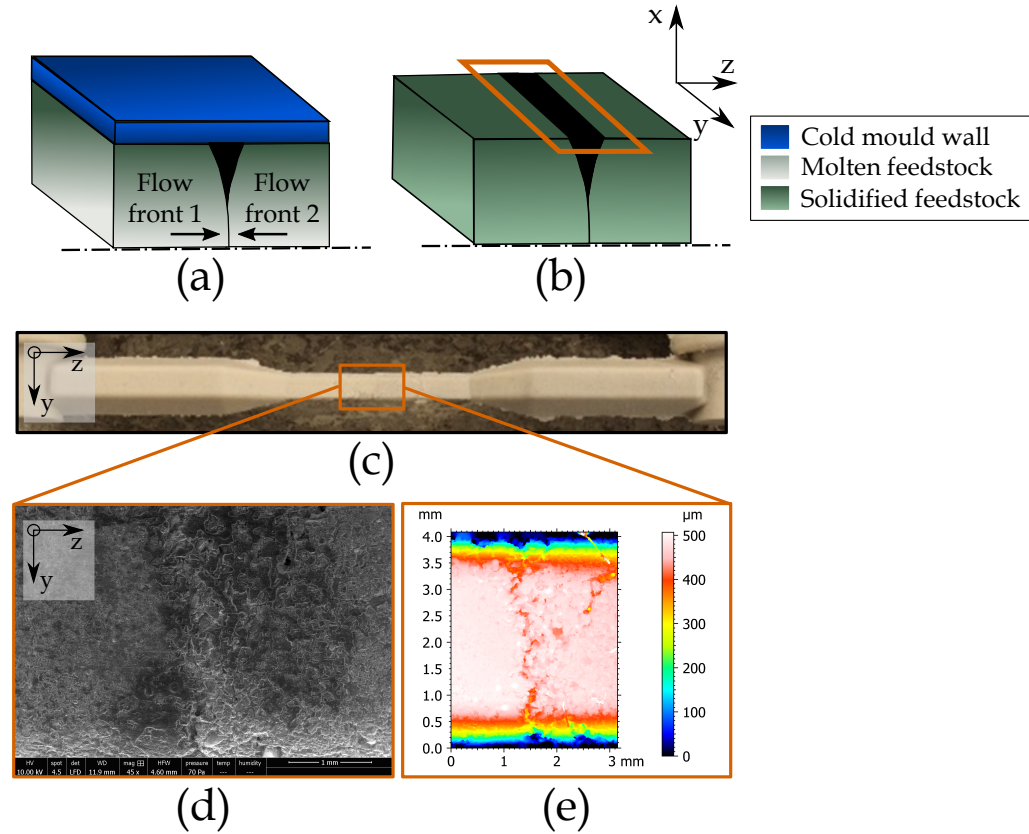


Figure 6.20: CIM outcome: Weld lines in the ambient temperature case. (a) Schematics of the phenomenon, filling phase. (b) Schematics of the phenomenon, part after ejection. (c) Example of analysed component, Cavity B in DS configuration. (d) SEM micrograph of weld line. (e) Surface topography of weld line.

On the other hand, when the surface below the weld line area is heated during mould filling, overlapping and proper merging of the flow fronts occur, with no visible weld line appearing on the surface, as shown from SEM and Alicona measurements (Figure 6.21d-e).

Analysing the samples at higher magnification (Figure 6.21f), only a V-

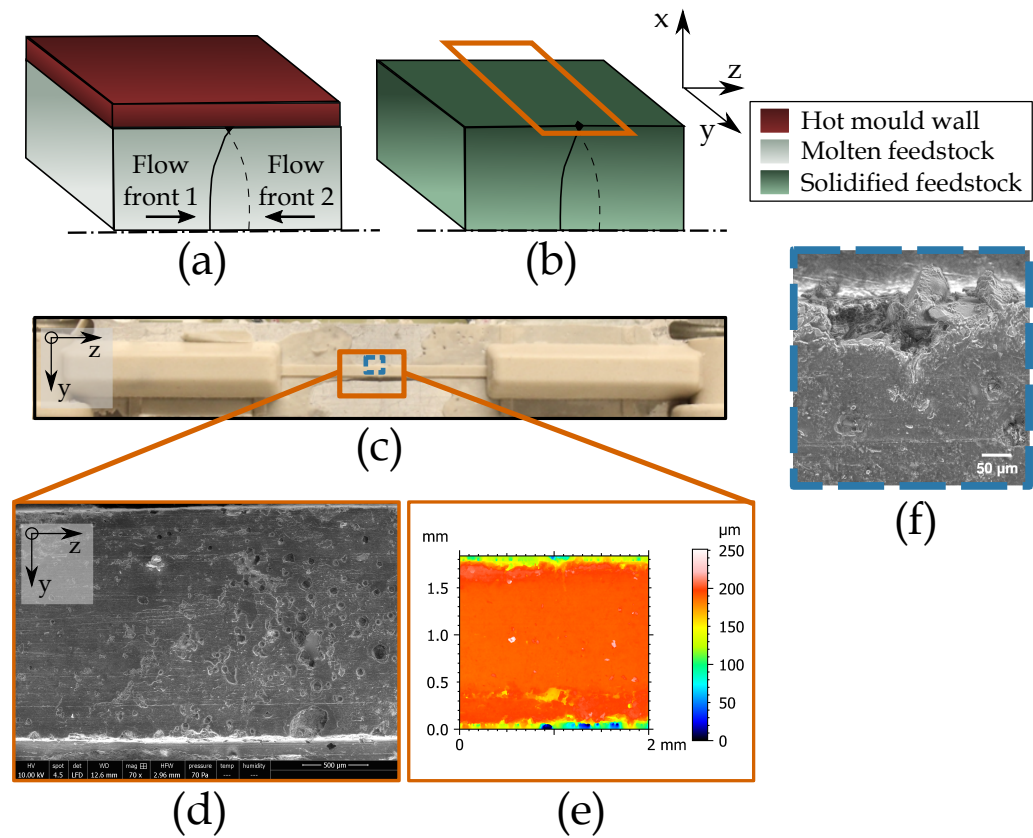


Figure 6.21: CIM outcome: Weld lines in the high temperature case. (a) Schematics of the phenomenon, filling phase. (b) Schematics of the phenomenon, part after ejection. (c) Example of analysed component, Cavity A in DS configuration. (d) SEM micrograph of weld line. (e) Surface topography of weld line. (f) SEM micrograph of the side of the top surface.

notch is visible on the side of the part: this is due to the local lower temperature on the side of the plates, not fully in contact with the Peltier modules. Considering this, while RHCM has been already proved to be an effective technique to increase weld line strength in both unfilled and fibre-filled polymer injection moulding (Wang, Zhao, and Wang, 2013b; Wang, Zhao, and Wang, 2013a; Wang, Zhao, and Wang, 2013c), also the novel approach, with a regional increase of mould temperature at weld line locations, leads to an improvement in bonding of flow fronts at the component surface. This implies a higher quality of green and subsequently sintered parts.

Considering surface quality, a clear distinction can be seen in the effect that different mould temperature approaches have on features having uneven thicknesses: in fact, when the components are injected using the ambient temperature approach, the material flowing in thin channels is subjected to high shear rate levels, which are further increased due to feedstock solidification (Bianchi et al., 2019). As seen in Chapter 5, this causes the simultaneous formation of three orientation layers – frozen, shear and core – that can separate when the external frozen one solidifies (Figure 6.22a-b). From the joint SEM-Alicona analysis it is possible to detect a 150  $\mu\text{m}$  thick frozen layer, with a smoother top surface replicating the mould cavity, which separates from the underneath shear layer, richer of particles.

A smooth surface is instead replicated when injecting components increasing mould temperature under the thinnest feature, using both the RHCM and the regional optimised control, as previously shown in Figure 6.21d-e. It is worth noticing that, as concluded from the study in Chapter 5, RHCM promotes a more uniform particle orientation in the thicker features as well. This is a drawback from the simplification of considering only two possible injection temperatures of 65°C or 35°C for the carried out optimisation,

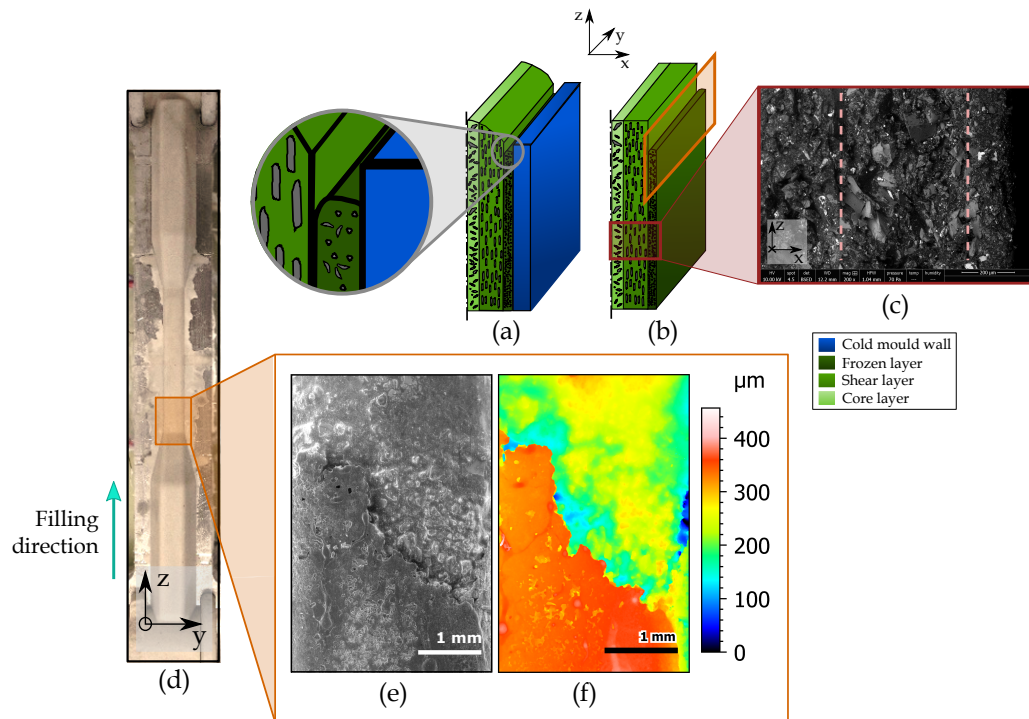


Figure 6.22: CIM outcome: surface quality on the thin feature in the ambient temperature case. (a) Schematics of the phenomenon, filling phase. (b) Schematics of the phenomenon, part after ejection. (c) SEM micrograph showing different orientation layers in the part cross section. (d) Example of analysed component, Cavity B in DS configuration. (e) SEM micrograph of shear-induced layer separation. (f) Surface topography of shear-induced layer separation.



the analysis of wax injected parts (Chapter 4), this difference in surface quality is due to the effect of mould temperature on binder surface tension. This decreases in the RHCM case, causing a higher wetting of both ceramic particles and mould cavity. When this phenomenon is coupled with high shear rate levels, separation of powder and binder can occur, which causes detrimental structural defects in moulded components. The effect of this difference in surface quality of sintered parts highly depends on geometrical tolerances of the components. In fact, while RHCM leads to a smoother surface on green parts (which is beneficial for fibre-filled polymers), the de-binding process in CIM will cause the erosion of the external surface layer (richer of binder), hence causing potential inaccuracies in the main dimensions of the sintered parts.

## 6.6 Conclusions

The employment of suitable thermal control approaches is critical for the achievement of defect-free ceramic injection moulded components. Current techniques for mould heating and cooling have not been customised to enhance the capability of moulding components characterised by features having dissimilar wall thickness, which present strong challenges due to uneven cooling rates developing in the part. To overcome these limitations, a novel mould thermal system having a regional temperature control, achieved with the employment of thermoelectric modules, was designed and manufactured. Moreover, a coupled PSO-FE thermal control model and optimisation was implemented and used to determine optimal mould temperature profiles, with the objective of minimising the differences in cooling rates developing in different cavity features, despite their dissimilar wall thicknesses. The optimisation also considers suitable profiles to allow for component ejection, and prevent strong adhesion between part and mould. To verify



the effectiveness of the developed and optimised control, an analysis of the temperature profiles and cooling rates within the component features was first carried out. Then, to analyse the performance of the novel proposed approach, its effects on the macro and micro-structural properties of the moulded parts were studied and compared to those obtained using the ambient temperature and RHCM techniques. From this work, the following conclusions can be drawn:

- The thermal control model and optimisation allowed a solution to be found, consisting of a localised-RHCM technique in proximity of the thinnest cavity feature. This approach has an enhanced performance when used on components having differential wall thickness, compared to state-of-the-art methods based on the achievement of uniform cavity temperature. This is because these approaches cause uneven cooling rates in the part, which determine defects such as differential shrinkage and lack of packing in features far from the gate.
- The optimal regional temperature control approach leads to a reduction up to 2-times in cooling rate differences between thin and thick features in the injected components and to the simultaneous solidification of the material in the thin and thick regions of the cavity.
- The optimal method allows comparable cycle times to the RHCM approach, reaching a total value of approximately 100 s with the employed setup, which has lower efficiency compared to the potential of an industry type mould.
- An enhancement in feature replication capability was achieved with the novel proposed method, comparable to a traditional RHCM approach and leading to a doubling in flow length for channels having thickness of the order of 500  $\mu\text{m}$  and width of 2 mm.

- Enhanced dimensional control was achieved with the regional thermal control approach, as features located at different distances from the gate did not exhibit significant dimensional differences. This is in contrast with the RHCM case, for which thick features far from the gate presented a further increase of approximately 25% in the volumetric shrinkage compared to those closer to the gate.
- The novel proposed method maintains the RHCM approach benefits in enhanced weld lines quality, and lack of shear induced separation at the surface of thin features.
- Comparing the regional control approach and RHCM, when moulding thick features, a difference in particle content on part surface is observed: a higher solid loading in the regional case is detected, which may lead to higher levels of dimensional accuracy after debinding and sintering processes.

The novel mould thermal system and control approach have been developed and demonstrated in the present chapter. The performed study was carried out on simple geometries, with only two features having different thicknesses. However, ceramic injection moulded components usually exhibit more complex geometries, for which the novel approach needs to be adapted. In this perspective, an application and simplification of the thermal control optimisation for a more complex geometry will be presented in the following chapter. Moreover, to conclude the work of this thesis, the design and manufacturing of an updated prototype of the novel developed tool, to be used with industrial injection moulding machined, will be presented and discussed.

# Chapter 7

## Application of the novel thermal control system to generic complex components

*In the previous chapters, the performance of different temperature systems for Ceramic Injection Moulding (CIM) die-tools has been analysed for the manufacturing of components with differential wall thickness. Moreover, a novel thermal control system, based on regional mould temperatures, has been presented and demonstrated for simple components characterised by adjoined features having uneven wall thickness. Taking these studies as a reference, it is of importance to consider how the proposed novel system and control strategy can be used in industrial applications, which present higher complexity in moulded component geometries, as well as in the employed die-tools. To address these challenges, in the present chapter, a case study is presented, and the proposed regional thermal control optimisation is applied to a ceramic core geometry, for high pressure turbine blade applications. Moreover, a prototype mould with regional temperature control, to be used with industrial Injection Moulding (IM) equipment, is presented. Finally, practical considerations and guidelines are provided for the adaptation of*

*the regional temperature system and approach to industrial IM die-tools.*

## 7.1 Introduction

The novel thermal system with regional mould temperature control for CIM, developed and described in Chapter 6, can be used to enhance the capability of manufacturing complex ceramic components having uneven wall thickness through IM. In this chapter, a demonstration of the developed control approach is provided and applied to a ceramic core geometry.

However, the application of the proposed mould thermal system and control approach to the manufacturing of generic complex components, such as ceramic cores for turbine blades, is a complex task and requires a step-wise approach. The function of the reference component and its subsequent quality requirements have to be firstly understood and related to process challenges. Then, as the mould temperature optimisation is based on the filling patterns during the injection of the components, these need to be predicted. Finally, based on this, the thermal control model and optimisation could be formulated and solved for the reference geometry (e.g. the ceramic core). To achieve this, in the present chapter, an introduction on the functionality of ceramic cores is firstly provided. Then, the filling model, developed in Moldex3D and validated in Chapter 4 for a model material, was validated for a production feedstock, to manufacture ceramic cores. This validation was performed on sample parts, similar to those employed in Chapter 7, with feature sizes extrapolated from the reference core geometry. From this, the novel thermal control optimisation was applied to the core, for which the results are be presented and discussed.

After this, a prototype mould with regional temperature control, which has

been designed and manufactured to be used within production equipment, is presented. To conclude, technical challenges to be considered in the passage from prototype to actual industrial injection moulding die-tools with the developed thermal control system are presented and discussed, and more advanced and modular concepts of moulds with regional temperature control are proposed.

## 7.2 Ceramic cores for high-pressure turbines

As previously stated in Chapter 2, Ceramic Injection Moulding (CIM) is one of the most used process to manufacture cores, to be employed in the investment casting of turbine blades and nozzle guide vanes for shaping internal cooling channels. In aeroengine applications, their function is of utmost importance in order to guarantee that the blades and nozzle guide vanes can withstand the high turbine temperatures, which can be critical for their properties, as well as to reduce the weight of turbine components. To enhance performances, cooling channels (and hence core) geometries are designed to guarantee an optimal cooling of the blades and vanes through the use of multiple passages (Figure 7.1), which follow the airfoil shape of the component, and through the introduction of *turbulators* to enhance convective heat transfer.

Despite their sacrificial nature, cores geometrical accuracy and structural integrity are critical in determining the final quality of blades and vanes. In particular, it is worth noticing that not only geometrical defects (e.g. warpage) will create inaccuracies in the casting of the turbine components, but also any other flaw in the cores will determine their equivalent "negative" in an internal, not easily inspectable, feature of the casted components. A crack or sink will result in added material in the blade, which can lead

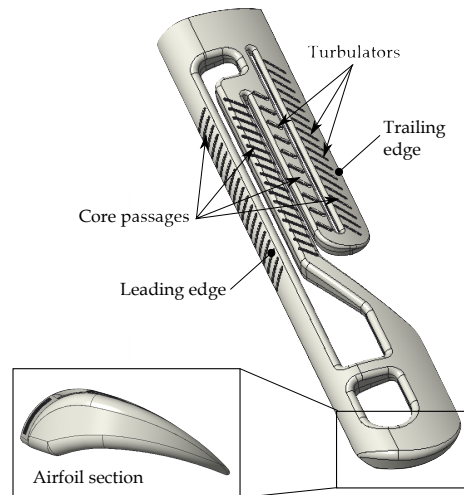


Figure 7.1: Ceramic core example geometry and main features. Note: this reference core is a model geometry provided by Rolls-Royce plc, which has representative features to real ceramic cores for high pressure turbine blades.

to blockage or reductions of cooling performances; on the other hand, sharp positive core defects (e.g. die lines) will create a notch in the metal, leading to a stress concentration area in the internal surface of the turbine blade or vane.

The complexity of core geometries brings about strong mouldability challenges: first, considering the injection process, complex filling patterns are created, due to the intricate shape of the passages, linked by bridges (called tie-bars) hence determining the creation of weld lines in the components. Also, core geometries include features having different wall thicknesses, with surface-to-volume ratios ranging from the order of  $0.1$  to  $10 \text{ mm}^{-1}$ , thus leading to uneven cooling rates in the component during the different stages of moulding. Moreover, thin sections may be filled before thicker ones, thus bringing about the risk of premature freezing of the feedstock and lack of packing at features farther away from the gate. Thus, core geometry increases the probability of non-uniform microstructure (and subsequently uneven mechanical properties) from injection moulding: considering the whole investment casting process, this is a major threat to core quality, as

it will compromise its ability to resist stresses during the wax encapsulation phase, thus increasing the chance of cracking during this stage. Having in mind these mouldability challenges, together with the functional requirements of the components, the developed model was applied to the reference core geometry.

## **7.3 Application of thermal control model to core geometry**

The simulation of the injection moulding filling stage, performed on Moldex3D, was validated for the feedstock industrially employed for the manufacturing of turbine blade cores by Rolls-Royce plc. This presents higher viscosity but same ceramic powder composition and morphology as well as similar thermodynamic properties to the model material used in the previous chapters. Due to reasons of confidentiality, the material properties are not reported in this chapter, and only a back-to-back comparison between simulation and experimental results are presented for the model validation. As previously stated in Section 7.1, the validation was carried out on sample geometries having features comparable to those of the core.

### **7.3.1 Selection of sample geometries**

The characteristic mouldability challenges presented by the geometries injected to validate the thermal control model in Chapter 6 present several commonalities with those just introduced for core geometries. Hence, in order to validate the filling model for the industrial ceramic feedstock, the same geometries and injection configurations as used in the previous chapter were employed.

The main dimensions of the reference core geometry, to which the regional thermal control optimisation was applied, were taken as a reference to design feature sizes. To do that, a representative cross section was taken into account to define both the size range and aspect ratios of the sample part features, as shown in Figure 7.2.

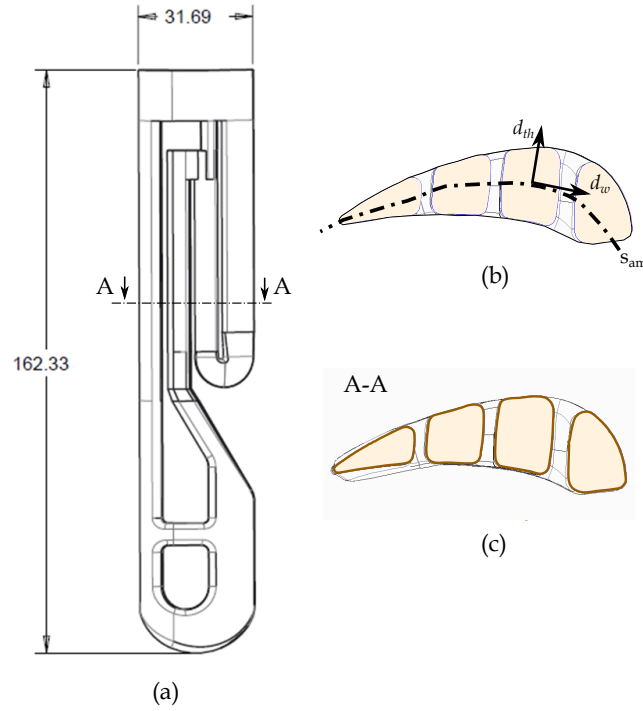


Figure 7.2: Feature thickness in a core geometry. (a) Core top view. (b) Schematics of width and thickness directions. (c) Section A.

Considering the shape of the core, within the cross section A-A, the width ( $w$ ) and thickness ( $th$ ) of each feature can be defined as the dimensions in respectively the tangent and orthogonal directions to the surface  $s_{am}$  (Figure 7.2b), taken in the middle of the airfoil core profile. In the reference section, features range from some having a thick, bulky shape (central and right hand side passages in Figure 7.2c) to thin and wide ones (trailing edge section Figure 7.2c). Thickness dimensions range from 0.5 mm to approximately 12 mm, while representing transition angles (i.e. tapers) between features having different thicknesses go from gradual to abrupt (approximately  $0^\circ$  to  $60^\circ$ ).



With the intention of selecting representative geometries, three dimensions were selected for the thicker features (6 mm, 9 mm and 12 mm), three for the thinner ones (0.5 mm, 1 mm and 2 mm) and three for the draft angles ( $0^\circ$ ,  $30^\circ$  and  $60^\circ$ ), as for the aspect ratios ( $th/w$ ), they were fixed to 0.75 for thick features and 4 for thin ones. A full factorial experimental design for this set of parameters and levels would have led to a total number of 27 cavity geometries: hence, to limit this, an optimised Taguchi design was selected, with nine cavities, which are shown in Figure 7.3.

Cavity #	$t_1$ [mm]	$t_2$ [mm]	$\alpha$ [°]
1	6	0.5	60
2	6	1	30
3	6	2	0
4	9	0.5	30
5	9	1	0
6	9	2	60
7	12	0.5	0
8	12	1	60
9	12	2	30

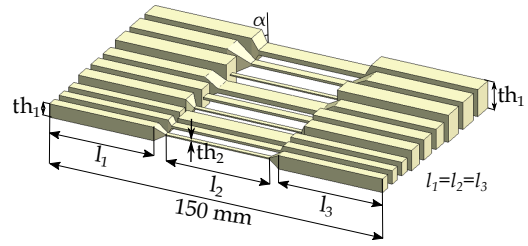


Figure 7.3: Isometric view of cavity features

Table 7.1: Main dimensions of cavity features

### 7.3.2 Filling model validation

The filling model, implemented in Moldex3D, was set up for the nine sample geometries shown in Figure 7.3, in the same way as for the simulations shown in Chapter 4, with the exception of the material properties, which were modified to fit the production material. In particular, a Cross-WLF model was used to simulate feedstock viscosity behaviour, instead of a Cross-Exp model (data are not reported here for confidentiality reasons).

The sample geometries were also employed for validating the filling model,

developed in the Moldex3D software package. The validation experiments were carried out on an MPI SA56-25-24 IM machine, using the silica-zircon "V200" production feedstock introduced in Chapter 3.

To inject the nine reference geometries, two mould cavity inserts (one top and one bottom) were manufactured and designed to be adapted to a die-tool property of Rolls-Royce plc, having straight-drilled cooling channels.

The cavity inserts (Figure 7.4), consisting, as previously shown, of nine parallel channels 150 mm long, was made in aluminium (Al 7075-T651), and their main dimensions are shown in Figure 7.4.

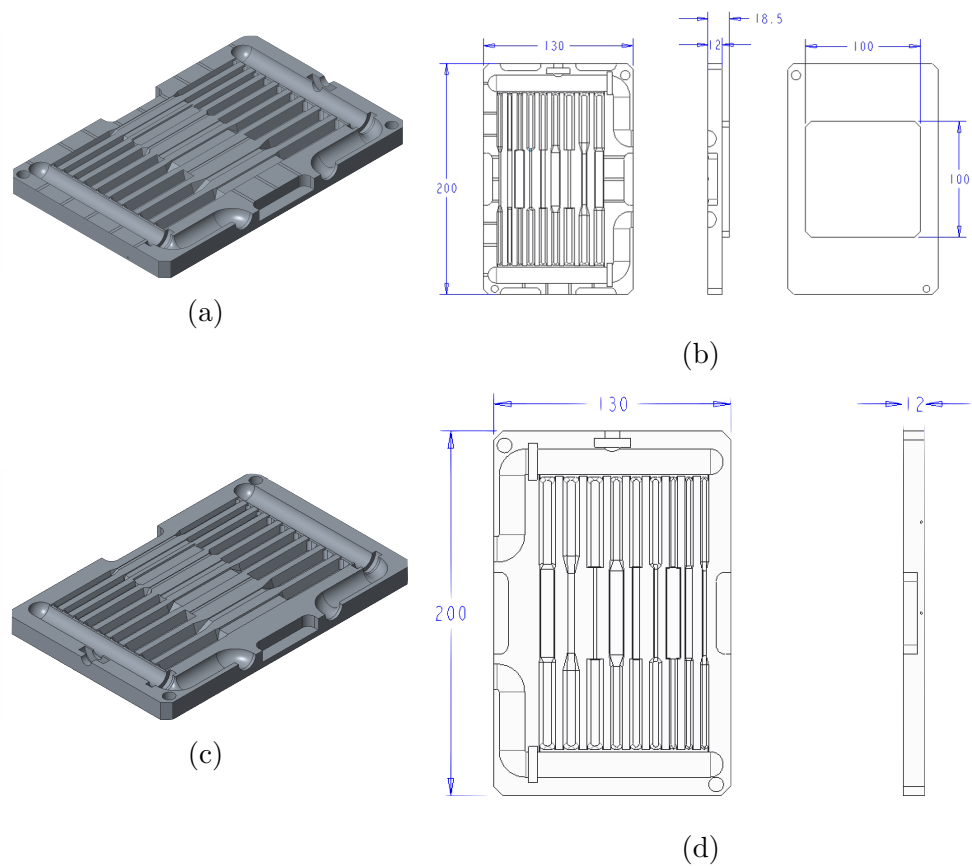


Figure 7.4: Mould inserts for injection moulding experiments. (a) Bottom plate, isometric view. (b) Bottom plate, main dimensions. (c) Top plate, isometric (d) Top plate, main dimensions.

As with the mould used for the thermal model validation (Chapter 6), a two-

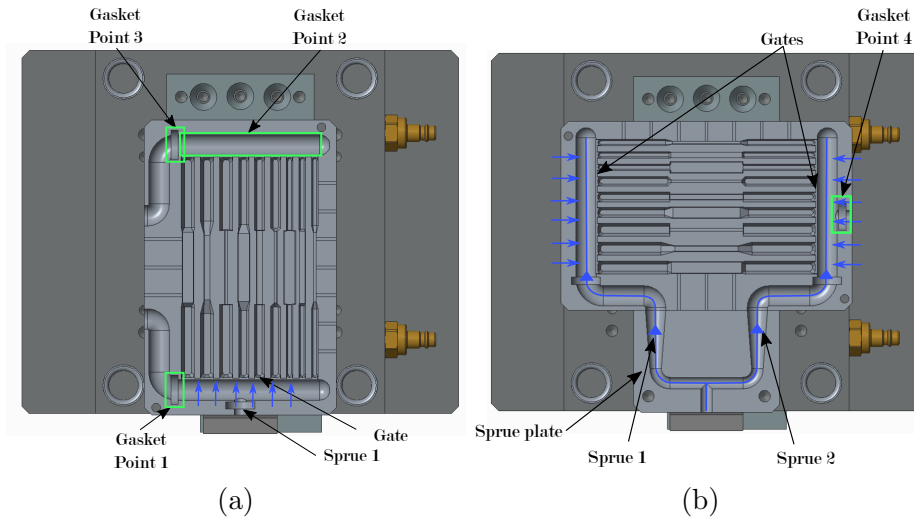


Figure 7.5: Injection configurations: (a) single sprue injection (b) double sprue injection

configurations injection setup was designed, with single and double sprue. In the first case, material was injected from one of the short sides of the mould through an edge gate, as shown in Figure 7.5a; in the double gating case, the feedstock was injected in a plate where the flow was split (Figure 7.5b) to access the mould through two sprues and then the cavity through two opposite edge gates. In order to forbid the material to leak from the mould through points 1, 2 and 3 (Figure 7.5a) in the single sprue case and point 4 (Figure 7.5b) in the double sprue one, sealing inserts were used.

Mould temperature, which was regulated only through the water cooling channels of the die-tool, was monitored throughout the cavity using six K-type thermocouples with grounded junction and 1 mm diameter. Three of them were placed in each cavity insert, in housings shown in Figure 7.6.

As for the experimental procedure (for which, the used process parameters are displayed in Table 7.2), a two-step approach was followed: first, a set of preliminary trials was carried out, in order to determine suitable values

of flow rate and injection pressure; in particular, levels of velocity and pressure were selected to enhance flow length and feature replication capability, within ranges of values that were recommended by Rolls-Royce.

Table 7.2: Injection moulding process parameters

Process parameter	Values
Melt temperature [ $^{\circ}\text{C}$ ]	80
Packing time [s]	10
Cooling time (excl. packing) [s]	20
Clamping force [kN]	110
Flow rate [ $\text{cm}^3/\text{s}$ ]	80, 150
Max pressure [bar]	5, 20, 40
Mould temperature [ $^{\circ}\text{C}$ ]	35, 50

From this set of trials, a suitable combination of values of pressure and flow rate was selected and the model was validated using the chosen process parameters at two different mould temperatures.

In the first set of trials (i.e. for pressure and flow rate calibration), a con-

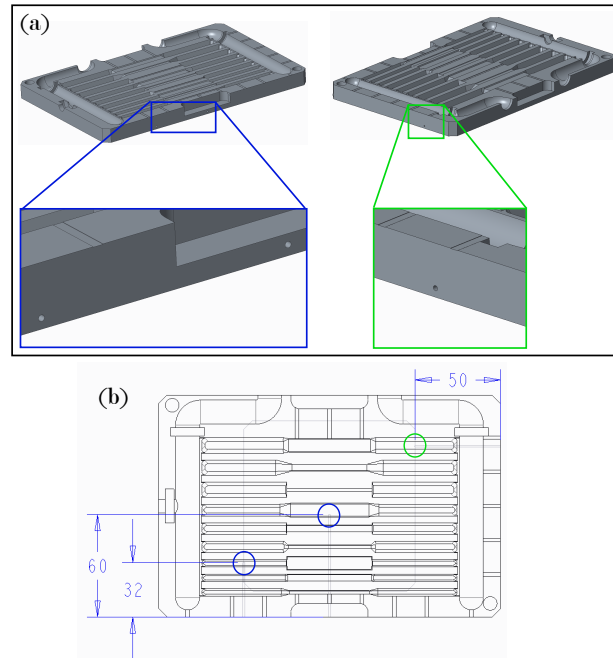


Figure 7.6: Thermocouple locations in the mould: (a) holes location, (b) thermocouple probe location

sistent increase in flow length with injection pressure was, as expected, observed in both single and double sprue injection configurations. On the other hand, looking at the effect of flow rate at the filling of the features, an opposite effect was observed for the two injection configurations (Figure 7.7): in fact, while in the single sprue case feature replication capability increases with flow rate (Figure 7.7a-b), the opposite happens in the double sprue configuration (Figure 7.7c-d).

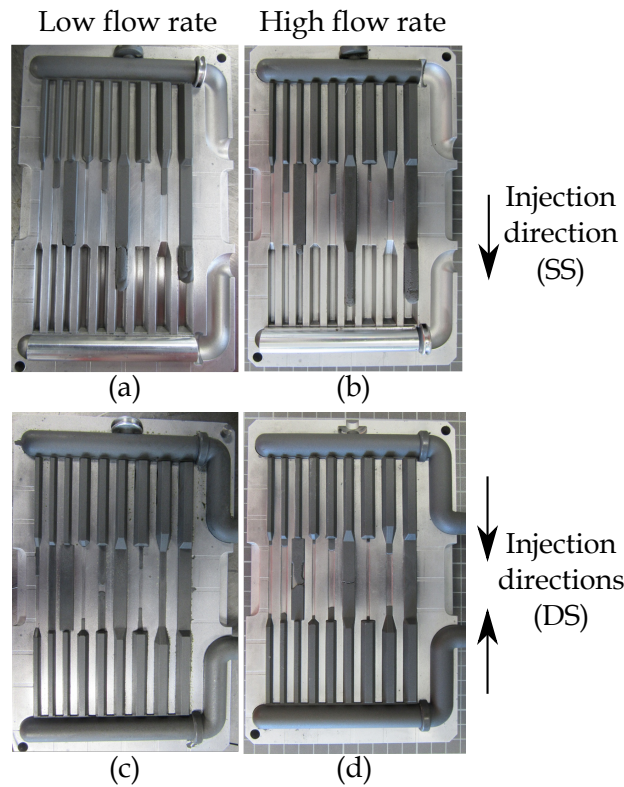


Figure 7.7: Flow length vs flow rate in calibration experiments. (a) Low flow rate, SS configuration. (b) High flow rate, SS configuration. (c) Low flow rate, DS configuration. (d) High flow rate, DS configuration.

What observed in the first case is expectable, as the feedstock has a higher velocity and hence manages to fill a longer flow length before solidification; the same should happen with the double sprue injection, however, as no venting channels are present in the centre of the features, air back-pressure is higher than in the first case as the increase of feedstock speed does not give enough time for it to escape.

From these results, for the second set of trials and the model validation, the higher values of pressure and flow rate (40 Bar and 150 cm<sup>3</sup>/s), were employed for the single sprue injection configuration. However, the assumption of cavity venting causes too high differences between the model and the actual injection moulding experiments, given the die-tool design, for which the nine features are jointly injected. Therefore, the second part of the validation, at different temperatures, was not carried out for the DS case.

The comparison between filling model and experimental results (Figure 7.8) show that the simulation is sensitive to variations of mould temperature and gives a total error (in volume%) of 0.54% in the 35°C temperature case (Figure 7.8a-b) and of 0.03% in the 50°C one (Figure 7.8c-d).

Looking at the flow length prediction per each of the channel, in both high and low temperature cases, the simulation gives a higher estimation of the cavity filling, compared to the experimental observations: this is reasonably related to the assumption that the cavity is perfectly vented, hence no back pressure from the air is taken into account in the model.

Considering this, the developed model can be used to predict the filling using the case study production material and can be used for the application of the thermal control optimisation to a case study core geometry, which is described and discussed in the following section.

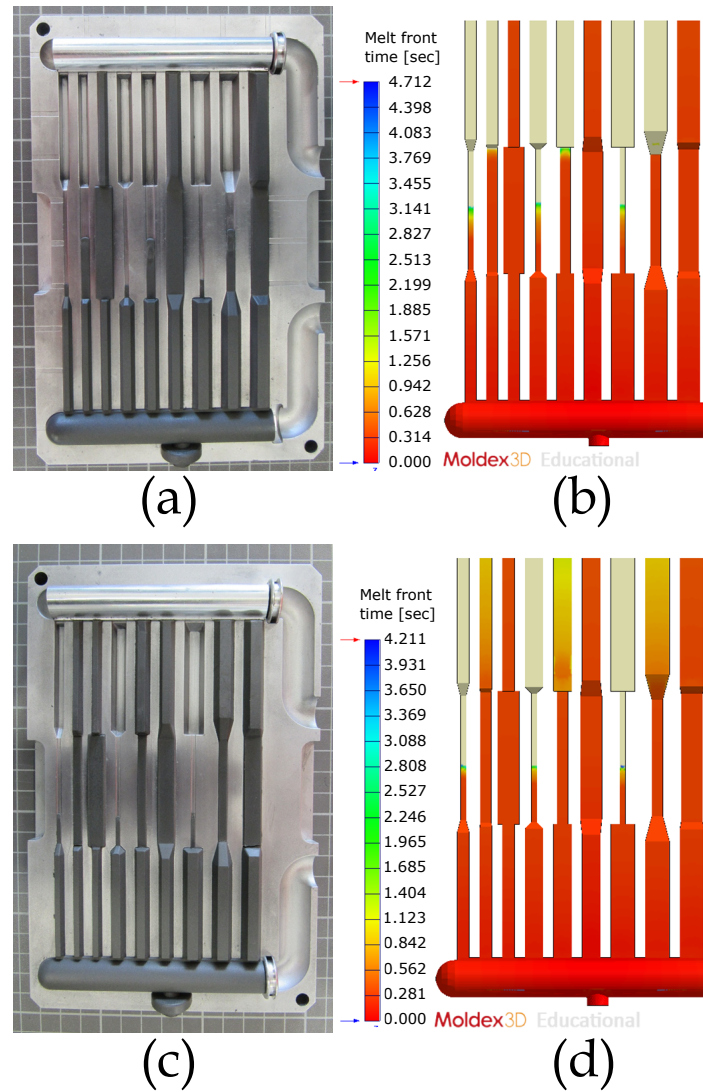


Figure 7.8: Experimental vs modelled flow length for the 9 cavities injected in SS configuration. (a) Mould temperature 35°C, experimental. (b) Mould temperature 35°C, simulation. (c) Mould temperature 50°C, experimental. (d) Mould temperature 50°C, simulation.

### 7.3.3 Thermal control model and optimisation setup for core geometry

After having validated the filling simulation, the thermal control model and optimisation was applied to a case study core geometry (Figure 7.9).

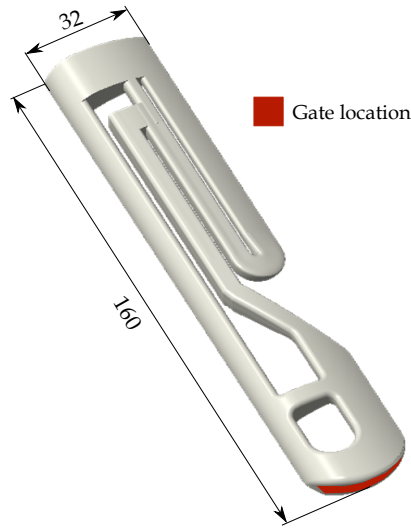


Figure 7.9: Reference core geometries used for the application of thermal control model and optimisation.

As opposite to the features used in Chapter 6, for the complex geometry of the core it is not straightforward to determine where to place Peltier modules in the cavity (also in this case, the cavity is assumed to be fully covered by thermoelectric modules), therefore, the following steps have been followed:

1. Application of the filling model to core geometry.
2. Definition of filling patterns and weld line locations.
3. Application of the thermal control model and cooling rate optimisation to the geometry.

The placement of the Peltier modules is based on the first two points of this procedure: in fact, all the features having the same thickness and that



are adjoined (in terms of filling patterns) have one Peltier module placed underneath and one above. Moreover, the filling simulation, performed in the Moldex3D software using the input process parameters displayed in Table 7.3, allowed identification of weld line locations, which need a corresponding active Peltier, in order to ensure the bonding of merging flow fronts.

Table 7.3: Main dimensions of core features

Parameter	Value 1
Melt temperature [ $^{\circ}\text{C}$ ]	75
Mould temperature [ $^{\circ}\text{C}$ ]	65
Flow rate [ $\text{cm}^3/\text{s}$ ]	40
Maximum pressure [bar]	20

It is worth noting that the filling simulation was carried with a uniform mould temperature of  $65^{\circ}\text{C}$ , assuming that the filling patterns would not have been much affected by different mould temperatures, allowing complete cavity filling. Based on the core geometry and filling simulation results (Figure 7.10a), twelve different features, corresponding to Peltier locations have been identified (Figure 7.10b) and numbered according to the order at which they are filled: for example, Feature 3 is filled after Feature 1 and Feature 2a and 2b are filled simultaneously. The main dimensions of each core feature are shown in Table 7.4.

Table 7.4: Main dimensions of core features

Feature	1	2a	2b	3	4a	5a	6	7a	7b	8	9	10
$t$ [mm]	8	4	8.5	8	4	6	8	6.5	8	7	5	3
$w$ [mm]	8.3	13.2	7.5	6.7	9.8	7	6.3	6.4	7.5	25	8	9.2

The numbering, related to filling patterns, has been done in order to understand the relative distance of each feature from the gate. This was to achieve optimal temperature profiles which ensured portions of the core closer to the gate not to solidify earlier than those farther away, thus preventing their

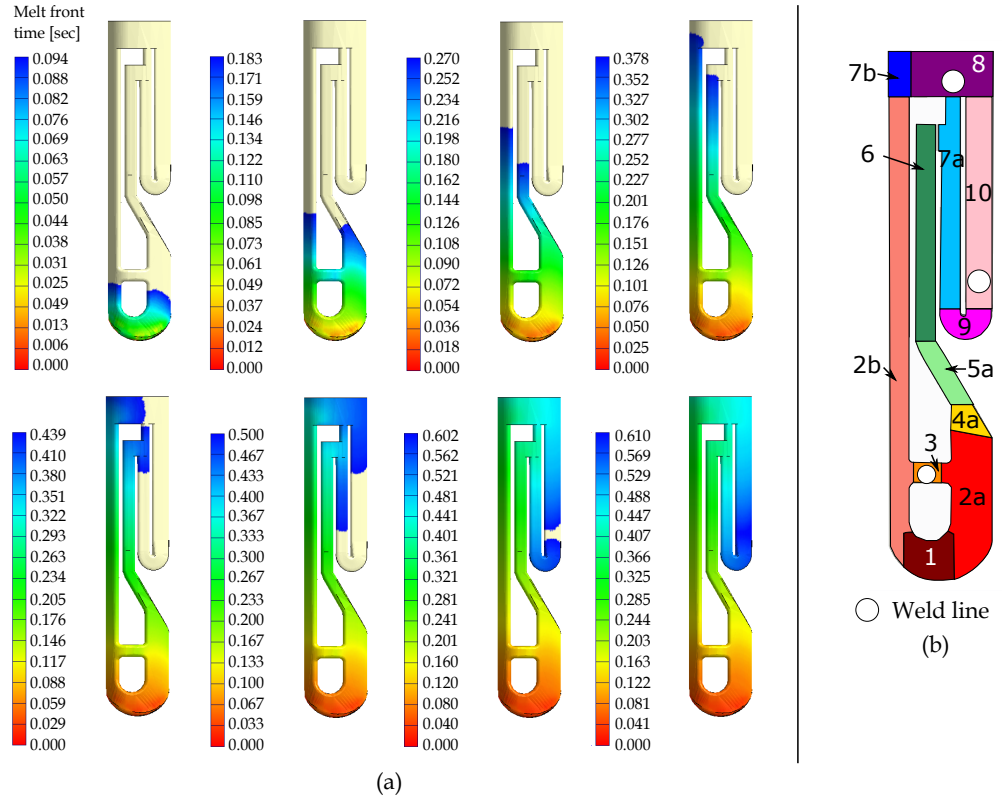


Figure 7.10: Application of filling model to core geometry and determination of Peltier and weld line locations. (a) Prediction of cavity filling over time. (b) Peltier regions in the core, based on filling patterns and features thickness, and location of weld lines.

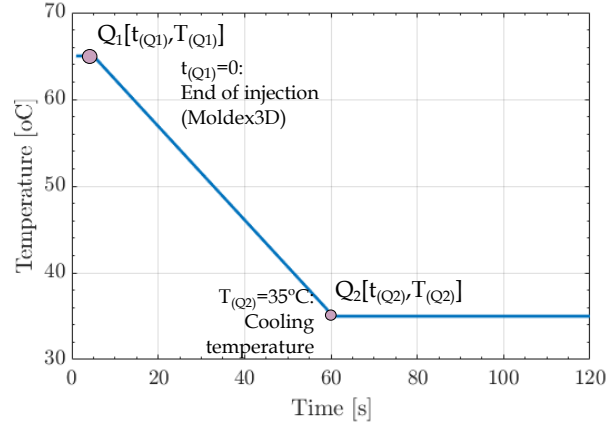


Figure 7.11: Example process window for each Peltier, used for the implementation of the thermal control model and optimisation to core geometry.

packing.

After this, the thermal control model and optimisation were applied to the core geometry: to do that, the first step was to redefine the optimisation variables, which, also this time, were based on a subdivision of the injection moulding process window. However, due to the higher number of Peltier modules with respect to the reference geometries of Chapter 6 (twelve instead of three), a lower number of control points were considered, as shown in Figure 7.11.

The two process phases are, in fact, those going from points  $Q_1 - Q_2$  and from point  $Q_2$  to the end of the process; the optimisation variables for the model, hence, correspond to the time and temperature coordinates of the two control points, per each Peltier. This would give a total of 48 optimisation variables (four per Peltier): therefore, as in the case of the first model formulation, some simplifications and assumptions have been applied in order to limit the number of variables and the subsequent required computation time. These have been selected based on the following:

- The initial time, corresponding to the end of injection and the be-

ginning of the packing and cooling phase is the start of the analysis:

$$t(Q_1) = 0.$$

- The initial mould temperature could only assume two values (RHCM or ambient):  $T(Q_1) = T_{low} \vee T(Q_1) = T_{high}$ .
- The final cooling temperature must be equal to the lower level of Peltier temperature  $T(Q_2) = T_{low}$ .
- Each Peltier located corresponding to a feature where a weld line occurs needs to be at a temperature higher than glass transition of the material during ejection ( $T(Q_1) = T_{high}$ ).
- All the temperature values were bonded to lower and upper limits coincident to the two possible values assumed at the beginning of the analysis:  $T(Q_i) = [T_{low}, T_{high}], \forall i$ .

In this way, only two variables per Peltier had to be optimised ( $T(Q_1)$  and  $t(Q_2)$ ), and only one ( $t(Q_2)$ ) in the case of Peltier modules corresponding to a weld line location. It is worth noticing that this reduced problem definition implies that, if the initial Peltier temperature is  $T_0 = 35^\circ\text{C}$ , the time variable  $t(Q_2)$  is redundant. However, this just increases computing time and should not create inconsistencies in the PSO solution search algorithm.

The fitness function  $f_c$ , to be minimised with the PSO method, was defined as:

$$f_c = \alpha(\sigma(\dot{T})_{max} + \sigma(\dot{T})_{ave}) + \beta T_{bool} + \gamma t_{step} + \delta pRes \quad (7.1)$$

In this case,  $\sigma(\dot{T})_{max}$  and  $\sigma(\dot{T})_{ave}$ , which represent respectively the maximum and the average differences in cooling rates in the centre of the twelve features of the channels, throughout the packing and cooling phases, are

calculated as the maximum and average standard deviations of the 12 cooling rate profiles.  $T_{bool}$  is a boolean variable, used to ensure that all the features of the part are solid at the end of cooling;  $t_{step}$  is the total packing and cooling time, corresponding to the cycle time of the process;  $pRes$  is instead an integer variable, used to ensure that features closer to the gate do not solidify before others, more distant from the gate. Finally,  $\alpha$ ,  $\beta$ ,  $\gamma$  and  $\delta$  are weighting coefficients. The value of the fitness function is calculated for each PSO iteration, based on the temperature distribution in the part, resulting from the ABAQUS thermal model, using the workflow implemented and described in Chapter 6.

### 7.3.4 Results and discussion

The temperature profiles resulting from the optimisation results can be summarised as in Table 7.5. When comparing the optimal temperature profiles

Table 7.5: Optimal injection temperature ( $T(Q_1)$ ) and time for the cavity to cool down to 35°C ( $t(Q_2)$ ) for each core feature and Peltier module.

Feature	1	2a	2b	3	4a	5a	6	7a	7b	8	9	10
$T(Q_1)$ [°C]	65	35	35	65	65	65	35	65	65	65	65	65
$t(Q_2)$ [s]	60	n.a.	n.a.	75	135	120	n.a.	90	110	130	90	135

with the feature dimensions, it can be seen that the optimal filling temperature ( $T(Q_1)$ ) is defined as  $T_{low}$  (35 °C) only for the thickest features. Moreover, for the features needing a higher injection temperature ( $T(Q_1)=T_{high}$ ) the time at which the cavity (i.e. Peltier) has to be at  $T_{low}$  increases with feature size, meaning that the cooling rate of the cavity surface is inversely proportional to the regional wall thickness. This is to ensure a uniform cooling rate in the centre of the whole component.

To verify this, temperature evolution in the centre of the cavity at different features, obtained when employing a constant ambient mould temperature approach (Figure 7.12b) and the Rapid Heat Cycle Moulding (RHCM) technique (Figure 7.12c) can be compared to that obtained by using the optimal Peltier temperature profiles and regional approach (Figure 7.12d).

From this, it can be observed that, by using the constant ambient temperature and the RHCM approaches, the thinner features in the cavity cool down quicker than thick ones, with maximum difference in solidification times of 30 seconds for the ambient temperature case and of 50 seconds for the RHCM one. This, with the assumption that in the ambient temperature case the cavity can get complete cavity filling, which may not be achievable, because of the fast cooling rate of features close to the gate (e.g. Feature 2a cools from 75 °C to 60 °C in less than 5 seconds). On the contrary, when using the regional temperature system and optimised control, fairly uniform cooling rates can be observed for all the features, despite their different thicknesses, with total difference in solidification time from thinnest to thickest features is of less than 20 s. This leads to a uniform cooling and subsequent lower warpage (due to achieved packing in regions farther from the gate) in the moulded part.

Even more noticeable are the differences in undercooling time between thin and thick features in the three cases. Considering the ambient temperature case, quickest undercooling time in the parts are of less than 5 seconds, while slowest ones are of about 80 s (for an undercooling time difference  $\Delta t_{UC}$  of 75 s). This is 30 s in the RHCM case and shortened down to 5 s in the regional optimised case. As discussed in Chapter 6, a similar undercooling time among features will cause more uniform level of polymer crystallinity in the part, which promotes more even part shrinkage.

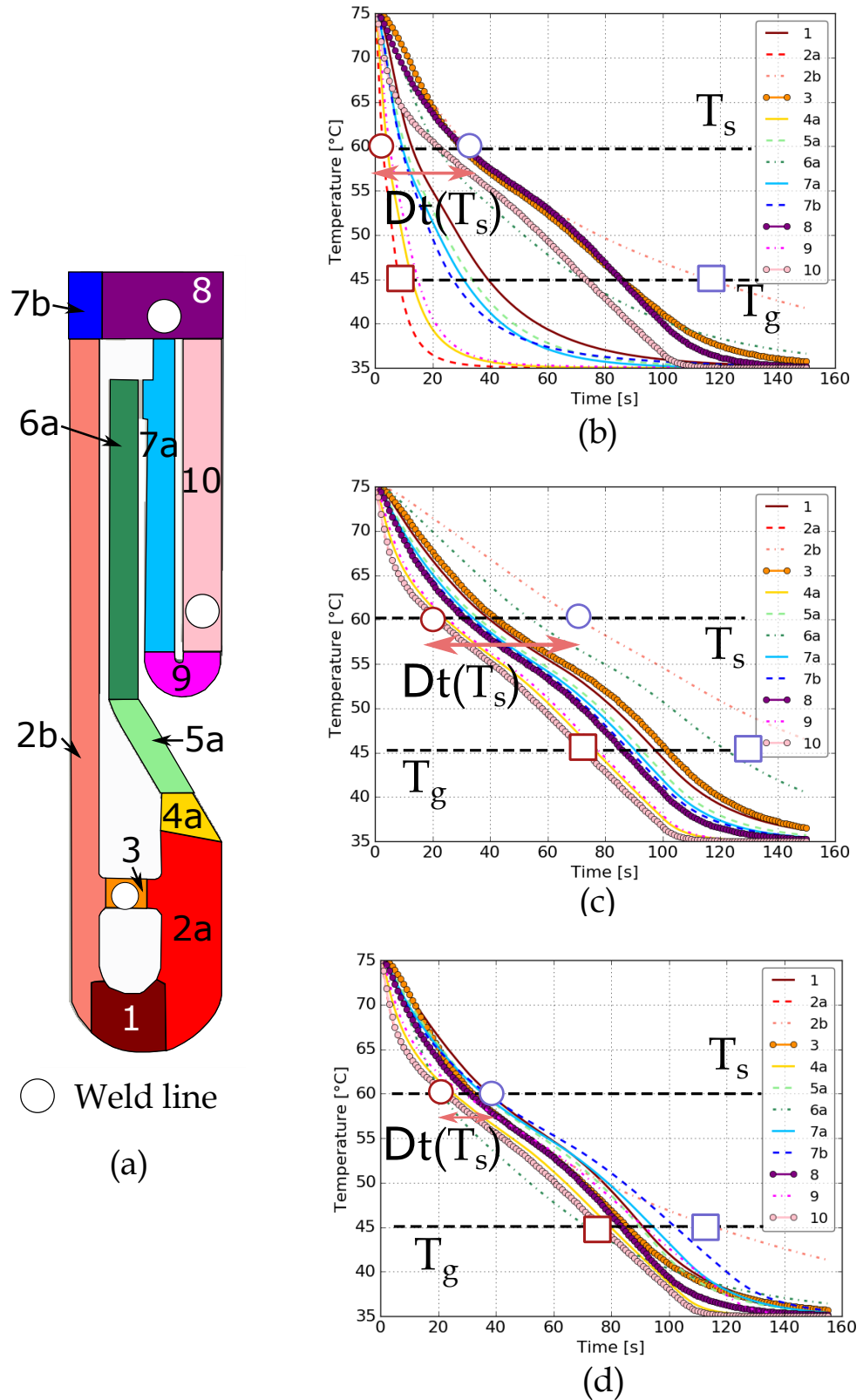


Figure 7.12: Temperature profiles at the centre of each core feature using different thermal control approaches. (a) Core feature mapping. (b) Temperature profiles using constant ambient mould temperature. (c) Temperature profiles using RHCM. (d) Temperature profiles using the regional optimised temperature control.

Considering this, the novel proposed approach can also be used to optimise mould temperature profiles when injecting complex geometries, such as ceramic cores for turbine blades and vanes.

## 7.4 Novel prototype mould for a production machine

After the demonstration of the mould with regional temperature control on a laboratory rig and the validation of its related thermal control model for both simple features and more complex geometries, it is possible to start developing a prototype die-tool to be used within production injection moulding machines. The prototype mould (Figure 7.13) was designed and manufactured for two of the geometries used for the model validation (Section 7.3).

The mould includes the following components:

- Four (two separate top and two bottom) aluminium (Al 7075-T651) cavity inserts, to allow for the drilling of thermistor housings between the Peltier modules and cavity surface. The same method of using inserts to block feedstock flow, as in the previously used moulds, has been employed to alternatively inject with single or double sprue configuration.
- Two (one top and one bottom) aluminium (Al 7075-T651) runner inserts (as for the mould used in Section 7.3).
- Two (one top and one bottom) aluminium (Al 6061) base heatsink inserts, with rectangular protrusions where Peltier modules were placed on (Figure 7.13c). As for the mould used within the test rig, the base



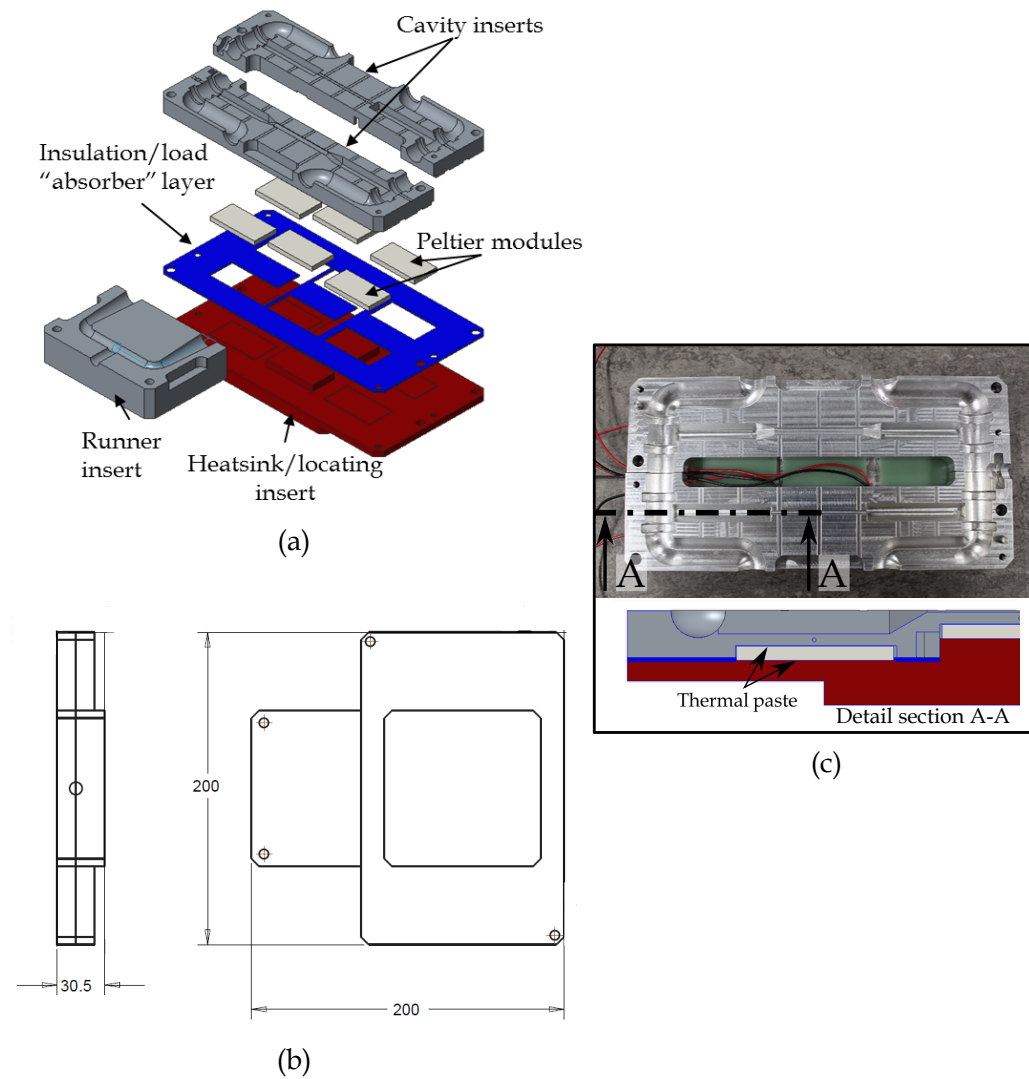


Figure 7.13: Prototype mould for production IM machine with regionally controlled temperature. (a) Exploded assembly for the bottom half of the mould. (b) Main dimensions of the whole assembly. (c) Cross section of the bottom cavity showing Peltier module location.

insert was also used as a reference for relatively locate the two cavity inserts.

- Two (one top and one bottom) glass-fibre laminated plastic insulating inserts. For their design, considering the higher amount of clamping forces (of the order of 110 kN) needed to compensate filling pressures of 20 to 40 Bar, a strong technical challenge arises: the maximum allowable pressure on the Peltier modules available in commerce is of the order of 1.5 MPa, which could then crack under such high loading conditions. To cope with that, taking into account that the overall approximate Peltier Young's modulus is 50 GPa (calculated from the elastic moduli of the ceramic and thermoelectric materials, provided by the supplier), a layer of insulating material with a modulus of approximately 400 GPa would be needed to sustain the load. Hence, an alternative solution was implemented to guarantee both the thermal insulation and load absorption requirements for this layer of material, while using a glass-fibre laminated plastic sheet (Young's modulus: 17.7 GPa). A 200  $\mu\text{m}$  tolerance gap between the Peltier faces and the base/cavity plate surfaces was placed and filled with a conductive paste, in order to maintain thermal contact between the thermoelectric cooler and the mould components (Figure 7.13c). This means that a gap exists between the mould and the Peltier face: to preliminarily verify that the clamping and injection pressures would not induce any substantial elastic or plastic deformation on the mould material, a static elastic analysis was performed with the assembly geometry, taking into account the clamping and injection pressures applied on the assembly. From this, results predict maximum stresses of approximately 80 MPa on the mould cavity (well below the 500 MPa yield strength of the Al 7075-T651 material), leading maximum

deformations of approximately  $10\text{ }\mu\text{m}$  (Figure 7.14) and peak stresses of approximately 10 MPa on the insulating layer, compared to maximum compressive strength of 410 MPa.

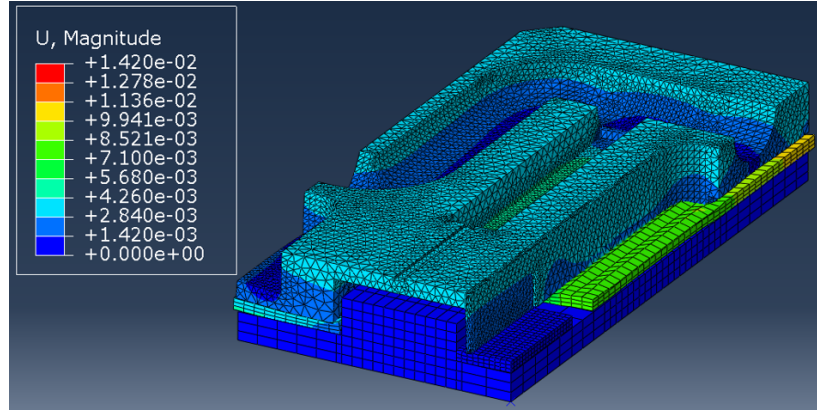


Figure 7.14: Results from the FE simulation, to verify stresses and displacements on the insulation sheet of the mould.

Due to production constraints, the injection moulding machine where the prototype should have been validated was not available: hence in this work the prototype design is presented and its validation is left to future development efforts. However, based on the use of similar moulds for tests performed both in a laboratory rig and in a production machine, it can be concluded that the present work has been able to prove the proposed mould and thermal control system up to a prototype-level manufacturing stage to be used on a production injection moulding machine.

To make the further step from a prototype to an actual production mould a number of additional technical challenges need to be addressed, which are related to the complex assembly systems and components required for die-tool design and manufacturing: to conclude this work, an effort has been made in providing an insight on these challenges and on how to overcome them, as well as in proposing more advanced concepts to design and operate regional thermal control systems for die-tools for industrial application.

This is presented in the following section, after which the key conclusions drawn from this chapter are going to be outlined.

## 7.5 Industrialisation of die-tools with regional temperature control

The development of production injection moulding die-tools requires the design and integration of mould sub-assemblies, which need to be developed in accordance to the proposed regional thermal control system. In particular, in the development of the mould prototypes presented in the previous chapters, the interaction between the novel proposed system and the following die-tools components has not been addressed, as these sub-assemblies were not designed in the employed moulds.

- **Runner system.** The importance of achieving a sufficient packing pressure throughout the moulding cavity has been often highlighted in this work: however, premature gate solidification is, even in the moulding of components having uniform wall thickness, one of the most common causes of warpage and cracks related to lack of packing in moulded parts. To prevent this, large gates, with comparable sizes to moulding features and runners, have been designed in the employed prototypes; this is often not possible when developing industrial die-tools, as this causes significant gate marks, which can affect both the aesthetic and the functionality of the moulded parts. Hence, the option of using hot runners or specific Peltier modules, to locally control mould temperature at gate locations, should be considered.
- **Cooling channel system.** The working principle of Peltier modules requires high heat dissipation on their hotter face: for this reason, the use of baffles in proximity of Peltier locations, could be a way

of improving the efficiency of thermoelectric elements during cooling. Moreover, health and safety regulations have to be accounted for, in order to couple electric elements with a water-based cooling system: this is a minor challenge, as it is already faced and overcome in the design and development of moulds equipped with cartridge heaters (Wang, Zhao, and Wang, 2014b).

- **Ejection system.** In the employed prototype moulds, components were manually ejected from die-tools: this is often not suitable in a production environment, due to the higher probability of damaging the part during a manual demoulding. Hence, room for ejector pins has to be accounted for: this brings about the challenges of placing Peltier modules, which can be overcome by using hollowed thermoelectric modules, as those employed for the adhesion tests in Chapter 5. Further analysis on thermal expansion around ejector pins in close proximity to the Peltier modules are, however, required to validate this design solution.

Moreover, when thermal cycles with higher temperature variations have to be achieved, using different materials to achieve both insulation between the two opposite faces of Peltier modules and efficient heat transfer on the bolster and cavity sides of the mould, create the risk of thermal stresses arising because of their dissimilar Coefficients of Thermal Expansion (CTE). Therefore, a suitable selection of materials, in terms of CTE, is essential for the long-term use of die-tools with such a "layered" structure.

It is also worth noting that the employment of free-form cavity geometries may also create the need of similarly shaped Peltier modules: this is a challenge related to the development of thermoelectric coolers with more advanced geometries, which is compatible to their working principle, based

on arrays of semiconductors that could potentially be arranged in curved or free-form shapes. However, considering currently available flat Peltier modules, suitable (and possibly optimal) locations must be selected, in order to ensure the required temperature distribution in the cavity. In this regard, the demonstration of the die-tool with regional controlled temperature has been performed using a mould having a bespoke "base" insert with rectangular protrusions to adjust Peltier heights in order to be at a fixed distance to the cavity face, despite the different feature depths. This special-purpose design can be compared to that of moulds having conformal cooling channels, in which the water ducts are shaped to follow the cavity geometry. However, alternative, more modular designs can be proposed, in which Peltier modules of an arbitrary size (to achieve different levels of temperature control resolution) can be arranged in arrays and independently controlled (Figure 7.15).

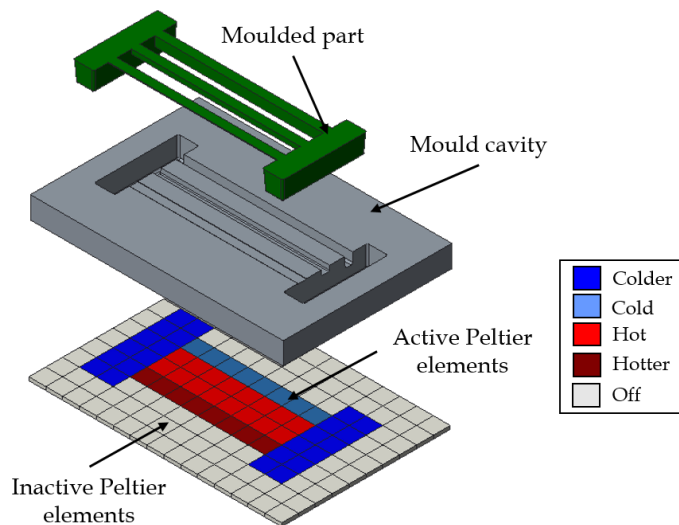


Figure 7.15: Example concept of mould with arrays of Peltier modules, selectively controlled.

Another way of achieving arbitrarily high temperature control resolution, instead of using smaller Peltier modules, to mould complex components with fine features, consists of exploiting a layer made by inserts of materials

having different thermal conductivities (Figure 7.16) to flexibly facilitate heat transfer underneath some features, while insulating others. This design, however, needs to account for the requirement of heat dissipation on the hot side of the Peltier, which must not be thermally isolated by the layer of the low conductive materials.

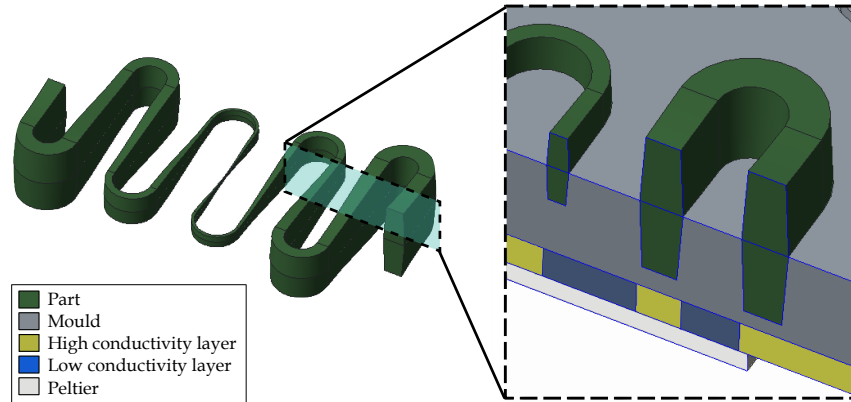


Figure 7.16: Example concept of mould with layer of multi-conductivity materials.

These proposed concepts would allow for a more flexible mould layout in comparison with conformal heating and cooling technologies, which constraint the use of a bolster for a single cavity, thus bringing a cost advantage in the industrialisation of the proposed tools, with fully tailored temperature control. The validation of this proposed approach in an industrial environment would then broaden the mouldability boundaries of components, by enhancing the capability of manufacture geometries characterised by uneven wall thickness by injection moulding.

## 7.6 Conclusions

In this chapter, a more industrial-oriented set of guidelines has been presented to operate regional mould thermal control systems in injection moulding die-tools, based on the understanding developed from the previous chapters. To generate these guidelines, a further step in the development of

regionally controlled mould tools has been performed, by applying the thermal control model and optimisation to a case study core geometry, employed within the investment casting of aeroengine turbine blades. Then, an effort has been made to provide design recommendations to deploy industrial injection moulding die-tools with the proposed regional approach, considering the integration of the developed solution with specific components, such as ejection and cooling systems. Finally, an insight into more advanced and modular design concepts has been provided, to extend the potential capability and flexibility of mould tools realised with the demonstrated concept. The key findings from this study can be summarised as follows:

- The thermal control optimisation was successfully applied to a sample core geometry with results showing a reduction in maximum variation of solidification temperatures within the component of approximately 33% compared to the ambient temperature case and of 60% compared to the Rapid Heat Cycle Moulding case. Undercooling time differences are instead 94% lower compared to the ambient temperature case and of 83% lower compared to RHCM.
- Although the final mould tool prototype has not been tested in an actual industrial injection moulding machine, from the validation of the proposed concept in a laboratory environment achieved in Chapter 6, the application of the model to a core geometry and the prototype design presented in this chapter, it can be concluded that the proposed thermal control approach has been brought to a *prototype-level* manufacturing readiness stage.
- The employment of thermoelectric modules for the achievement of regional heating and cooling of injection moulding die-tools broadens the possibility to modularise mould designs, in contrast with other state-of-the-art approaches of conformal heating and cooling. Two types of



design concepts have been provided: the first one involves the employment of arrays of selectively operated Peltier modules; the second is a "sandwich" mould with layers of materials having differential conductivities, to cope with limitations of currently available thermoelectric modules, which may be incompatible to achieve regional cooling in complex cavity geometries.

# Chapter 8

## Conclusions

The aim for the present work has been to develop and demonstrate a novel thermal system and control approach for die-tools, to enhance the capability of manufacturing complex components having uneven wall thickness, through Ceramic Injection Moulding (CIM). To achieve this, a comprehensive review of the current literature regarding the CIM process, outcomes, die-tools and control approaches has been carried out (Chapter 2). From this, several research challenges emerged, which have been addressed in the present thesis work.

The first major gap is related to the fact that very limited research has been carried out on the application of advanced mould thermal control systems to CIM. This implies that no systematic methodology is in place to assess the performance of thermal systems and control approaches applied to the Injection Moulding (IM) of ceramic components. To address this issue, in Chapter 4, a methodology was developed to evaluate the performance of these systems in CIM applications, through the investigation of the effect of different thermal conditions on the quality of green and sintered components. Having a methodological framework in place, it was possible to analyse the performance of state-of-the-art thermal systems, such as Rapid

Heat Cycle Moulding (RHCM), currently used for plastic IM, applied to CIM. In particular, in Chapter 5, the effect of RHCM was studied on the phenomena of particle orientation and packing and on the adhesion behaviour between mould and part in CIM. Having gained an understanding of the performances of current thermal systems, it was possible to develop a novel approach for mould temperature management and control in CIM. This has been addressed in Chapter 6, where a novel mould, having regionally controlled temperatures, achieved through the employment of Peltier modules, was presented and demonstrated. This also included the development of a thermal control system, performed by an optimisation of local mould temperatures. The aim of this was to minimise differences in cooling rates throughout the moulded components, despite their uneven wall thickness. The novel thermal system and control approach were demonstrated on reference geometries that presented strong mouldability challenges, and using laboratory equipment. In Chapter 7, an effort was made to apply the newly developed thermal control approach to a generic complex component, using a ceramic core for high-pressure turbine blades as case study geometry. Moreover, a prototype of the novel die-tool with regionally controlled temperatures was designed and manufactured, to be used with an industrial IM machine, and general guidelines were provided to use the newly developed system in real production applications.

To conclude the present work, in the following sections, the main contributions from each research stage (corresponding to thesis chapters) are summarised. Then, future work needed to build upon the carried out investigations on thermal control approaches for CIM die-tools are presented and discussed.

## 8.1 Methodology for the evaluation of thermal systems performances in CIM

A methodological framework for the performance evaluation of thermal control systems for CIM die-tools was developed through a step-wise approach. This includes (i) the development of a model of the IM filling process stage and its use to support the understanding of the effect of different thermal conditions on (ii) green and (iii) sintered components. The main conclusions from this study can be summarised as follows:

- To help evaluate the performance of thermal control systems for CIM, a model of the IM filling stage was developed to enable the prediction of temperature distribution in the part during IM. The simulation was validated for a wax and a ceramic feedstock and can be used as support tool to correlate observed quality outcomes from moulded components to the thermal phenomena occurring during IM.
- To develop an understanding of the effect of different thermal conditions on the quality of as-moulded (i.e. green) parts, the influence of varying melt temperatures was investigated upon the integrity of wax injected components. The wax feedstock was selected with similar properties to the binder of the reference CIM feedstock used within the present work.
- Results from the research on the quality of as-moulded (wax) parts show that higher temperatures throughout the component during the filling process enhance feature replication capability, weld line morphology and surface quality, but promote shrinkage-related defects and increase mould-part adhesion. Fillers packing was also analysed in as-moulded wax components, and differential distribution in the part was observed, due to shear rate variations.

- In the study of wax parts, the developed filling simulation was successfully employed to support the understanding of the observed microstructural outcomes, and hence to evaluate the influence of different thermal conditions on the quality of green components.
- A second study was carried out on a sintered ceramic block, to investigate the possibility to track the origin of defects and microstructural outcomes observed in sintered components, back to the IM process. This was performed by use of scanning electron microscopy and with the support of the developed filling model. From this study, some defects arising from the injection moulding process could be tracked; however, variations in the component microstructure during debinding and sintering did not allow to univocally correlate other observed post-sintering defects to the IM process.
- From the study on the sintered ceramic block, it was concluded that, in order to evaluate the performance of current and newly developed thermal systems for CIM die-tools, the quality of green parts needs to be analysed.

## **8.2 Application of rapid thermal cycling to CIM**

Rapid Heat Cycle Moulding (RHCM) offers the opportunity of broadening the IM process capability, as it enhances features replication and surface quality of moulded components. However, since this mould temperature control approach had not been applied to ceramic applications, a study was carried out to evaluate the performances of rapid thermal cycling in CIM. In particular, the performance of RHCM was evaluated by analysing particle orientation and packing in green parts, and adhesion behaviour between

part and mould, which affects ejection forces. The investigation was carried out using green reference components characterised by features having different wall thicknesses, moulded with a silica-zircon ceramic feedstock, and following the methodological framework developed in Chapter 4. From this study, the following conclusions can be drawn:

- The phenomena of particle orientation and packing, which are critical for the integrity and dimensional control of ceramic moulded components, are affected by the RHCM approach. This promotes a favourable microstructure, characterised by a more uniform particle orientation and packing in green parts, which is likely to reduce differential sintering defects.
- In green moulded parts, a banded microstructure was observed, having different layers of particle orientation (frozen, shear and core). The filling simulation, previously developed, was used as a support to understand how RHCM influences the thickness of these layers. From this, a correlation was observed between degree of particle orientation across part thickness and maximum shear rates which, in turn, depend on temperature gradients developing during the mould filling stage of the IM process. In particular, RHCM leads to an enlargement of the core layer, characterised by randomly oriented particles, and a reduction of the shear layer, having preferentially aligned particles. This is particular relevant in thicker features, subject to lower shear rates, compared to thinner ones. However, in both thinner and thicker features, the use of RHCM determines the disappearance of the outer frozen layer, which further helps achieve a less stratified microstructure, thus preventing differential sintering.
- Homogeneity in particle packing between features having different wall thickness is also promoted by the employment of RHCM. However,

within thinnest features, having high length-to-thickness ratios, differential packing throughout their length could be still observed, due to the high shear rate gradients developing during filling.

- A novel methodology was proposed for the analysis of particle packing and orientation, based on *in-situ* compression tests under the SEM. Results from these experiments confirm the findings from microstructural analyses and density measurements and show the potential of this method to analyse particle orientation and packing in green parts.
- A test rig was developed to measure ejection forces as a function of different temperature profiles employed during IM. From this, a significant increase of part-mould mechanical interlocking and subsequent ejection forces was observed when employing the RHCM technique, due to the higher contact area between the part and mould cavity.
- A reduction in ejection forces was observed when using the RHCM approach, followed by an increase of mould temperature up to approximately the glass transition point of the feedstock during part ejection. This is due to local decreases of cohesive forces in the binder portions that are interlocked with cavity roughness features.
- Effective temperature control approaches for CIM needs to be designed with thermal cycles which account for lowering adhesion between part and mould and ensuring components integrity after ejection.

## 8.3 Novel thermal control system for CIM die-tools

State-of-the-art IM thermal control approaches, such as RHCM, are based on the achievement of a uniform mould cavity temperatures throughout the process. This is not tailored to the IM of components characterised by features having dissimilar wall thickness, which present strong challenges due to uneven cooling rates developing in the part. To overcome these limitations, a novel mould thermal system having a regional temperature control, was designed and developed. Local heating and cooling was achieved with the employment of thermoelectric modules, placed corresponding to features having different thicknesses. To determine optimal thermal profiles for each thermoelectric (Peltier) module, a coupled PSO-FE thermal control model and optimisation was implemented, with the objective of minimising cooling rate gradients developing in different cavity features with dissimilar wall thicknesses. Moreover, based on previous findings, the optimisation considers temperature profiles that facilitate part ejection, by preventing strong adhesion between part and mould. To assess the performance of the newly developed thermal system, and optimised control, temperature profiles and solidification rates during IM were analysed, and then the effect of the novel system on the quality of green moulded parts was studied. From this work, the following conclusive remarks can be drawn:

- A prototype mould incorporating Peltier modules, placed in close vicinity to mould cavity features having specific thickness was designed and manufactured. This enabled a local and independently controlled temperature profile per each moulded feature of the reference components.
- A thermal control model was implemented, in order to optimise local



mould temperatures during the CIM process. Results from the optimisation confirm the importance of differentially controlling mould temperatures in proximity of cavity features having different thicknesses. This approach promotes the achievement of uniform cooling rates in the part, which help prevent defects such as differential shrinkage and lack of packing in features far from the gate.

- The application of the novel mould tool with the optimised temperature profiles demonstrates a reductions up to 2-times in cooling rate differences between thin and thick features in the injected components was promoted by the regional optimised thermal control approach. Moreover, simultaneous solidification of the material in the thin and thick regions of the cavity occurs, thanks to the regional control of mould temperatures.
- The optimised regional method leads to comparable cycle times to the RHCM approach, from a thermal efficiency point of view. The achieved cycle times, of the order of 100 s, are competitive to industry-standards and have the potential of being improved when the novel system is implemented on production die-tools, having cooling channels that enhance heat dissipation. Differences in undercooling time between thin and thick features are also reduced by the regional control approach, hence promoting uniform crystallinity levels throughout the parts, that avert differences in shrinkage upon cooling.
- The novel proposed method also led to improved component macro- and micro-structural quality. An enhancement in feature replication capability was observed, comparable to what can be achieved by using the RHCM approach. The components manufactured with the novel approach exhibited improved dimensional control compared to those injected using the RHCM technique. In terms of weld lines and surface

quality, the novel proposed method maintains the RHCM approach benefits in enhanced weld lines bonding, and reduces hesitation during mould filling, which is due to shear induced separation at the surface of thin features.

## 8.4 Application of the novel system to generic complex components

The investigation and demonstration of the novel thermal control system, reported in the section above, has only been applied to relatively simple reference geometries, with only two features having different thicknesses. However, since ceramic injection moulded parts can exhibit much more complex geometries (e.g. ceramic cores for turbine blades and vanes), it is of importance to assess the adaptability of the novel proposed method to more generic components and to understand the challenges to allow for its use in industrial applications. Therefore, the thermal control optimisation was modified to be applied to a reference ceramic core geometry. Moreover, a prototype die-tool with the novel regional thermal control system was designed and manufactured, to be used with production equipment. Finally, an effort has been made to provide a more industrial-oriented set of guidelines and design recommendations to deploy industrial injection moulding die-tools with the proposed regional temperature approach, considering the complexity brought by die-tool sub-assemblies (e.g. ejection and runner systems), often neglected in academic research. The main conclusions from this study can be summarised as follows:

- The thermal control optimisation model was successfully applied to a sample core geometry, leading to a reduction in cooling rate variations in the part and simultaneous feature solidification, when compared to

state-of-the-art thermal control approaches (e.g. RHCM and ambient temperature). This method was demonstrated capable of achieving uniformity in undercooling time across features having different thicknesses, thus enabling a more uniform part shrinkage.

- A prototype mould tool with regional thermal control, to be used within a production-type IM machine was designed and manufactured, responding to the more challenging requirements of industrial equipment (e.g. higher clamping forces and injection pressure), hence demonstrating the feasibility of the novel method in real world industrial scenarios.
- In an effort to demonstrate the flexibility of the proposed localised temperature system from a design perspective, two alternative design concepts were proposed, enabled by the employment of a pixelated layer of Peltier modules: in the first, the local control is achieved by selectively operating the modules, and the second, by having a layer of materials having different thermal diffusivities, to locally control heat transfer from the Peltier to the cavity. These design concepts demonstrate the possibility to realise modular die-tool designs, which are not achievable with alternative thermal control approaches, such as conformal cooling channels.

## 8.5 Future work

The work reported in the present thesis significantly contributes to the understanding of heat transfer phenomena during the CIM process and, in particular, of their effect on the quality of ceramic moulded components. Moreover, the development of a novel thermal system with regional temperature control broadens the capability of the IM process, both for ceramic

and polymer applications.

Despite these advances, still work needs to be carried out to further improve the achievements and deployed methods of the present thesis. The main points, which call for further improvement and investigation are highlighted in the following:

- Due to the limitations of univocally tracking detected defects on sintered components to the IM process, only the quality of green parts was analysed in the present work. This was also caused by the fact that any development work on the debinding and sintering processes was out of the scope of this thesis, and hence, observed defects in fired components may have arisen from flaws in these thermal processes. However, in order to achieve a more complete understanding of the whole process chain, the effects of mould temperature on the quality of fired ceramic components have to be evaluated.
- A methodology has been developed for the evaluation of particle orientation and packing in green parts, through in-situ micromechanical testing, and good correlation was observed comparing the results from these experiments, microstructural analyses and density measurements. However, a more extensive validation of the proposed methodology is needed, with a more comprehensive analysis of the statistical error from these measurements, carried out across a higher number of experiments.
- As mentioned in Chapter 6, the developed thermal control optimisation accounts only for two levels of injection temperatures, thus leading to optimal profiles that include ambient local mould temperatures during the filling phase of IM, corresponding to thick features of the components. However, from the findings of Chapter 5, RHCM

was demonstrated to be an effective technique to promote a more uniform microstructure for thick features. Therefore, more work on the optimisation of regional mould temperatures is needed, to account for more possible injection temperature levels that guarantee both even cooling rates in the parts and the filling at temperatures closer to the glass transition point of the feedstock.

- Advances in thermoelectric module design and efficiencies are needed to fully exploit the potential of localized mould heating and cooling. This is particularly valid when the proposed thermal control system has to be applied to high-pressure and high temperature IM, in contrast to the proposed Low-Pressure CIM application.

# Bibliography

- Ab, S. (2003). “Using a Finite Volume Approach to Simulate the Mould Filling in”. In: 22.6, pp. 499–515. DOI: 10.1106/073168403023290.
- Agazzi, A., V. Sobotka, R. LeGoff, and Y. Jarny (2013). “Optimal cooling design in injection moulding process – A new approach based on morphological surfaces”. In: *Applied Thermal Engineering* 52.1, pp. 170–178. ISSN: 13594311. DOI: 10.1016/j.applthermaleng.2012.11.019. URL: <http://www.sciencedirect.com/science/article/pii/S1359431112007326>.
- Allen, T. (1981). *Particle Size Measurement*. Powder technology series. Chapman and Hall. ISBN: 9780412154102. DOI: 10.1007/978-1-4899-3063-7. URL: <https://books.google.co.uk/books?id=AMFRAAAAMAAJ>.
- Amorós, J., V. Cantavella, J. Jarque, and C. Felú (2008). “Green strength testing of pressed compacts: An analysis of the different methods”. In: *Journal of the European Ceramic Society* 28.4, pp. 701–710. ISSN: 0955-2219. DOI: 10.1016/J.JEURCERAMSOC.2007.09.040. URL: <https://www.sciencedirect.com/science/article/pii/S0955221907005079>.
- Babenko, M. et al. (2018). “Evaluation of heat transfer at the cavity-polymer interface in microinjection moulding based on experimental and simulation study”. In: *Applied Thermal Engineering* 130, pp. 865–876. ISSN: 1359-4311. DOI: 10.1016/J.APPLTHERMALENG.2017.11.022. URL: <https://www.sciencedirect.com/science/article/pii/S1359431117313534>.

- Bai, Y., B. Yin, X.-r. Fu, and M.-g. Yang (2006). “Heat transfer in injection molding of crystalline plastics”. In: *Journal of Applied Polymer Science* 102.3, pp. 2249–2253. ISSN: 0021-8995. DOI: 10.1002/app.24398. URL: <http://doi.wiley.com/10.1002/app.24398>.
- Bianchi, M. F. et al. (2019). “On the effect of mould temperature on the orientation and packing of particles in ceramic injection moulding”. In: *Journal of the European Ceramic Society* 39.10, pp. 3194–3207. ISSN: 1873619X. DOI: 10.1016/j.jeurceramsoc.2019.03.049. URL: <https://doi.org/10.1016/j.jeurceramsoc.2019.03.049>.
- Boenig, J. M. and R. R. Kunts (1995). *Flash removal system for a mold, US Patent 5,454,708*.
- Carter Barry & Norton, M. G. (2007). *Ceramic Materials, Science and Engineering*. Springer.
- Chang, E., S. Shin, and H. Chung (2016). “Identification of Controlling Parameters on Thermal Deformation of Mobile Device by Injection Molding Process”. In: 135. February 2013, pp. 1–9. DOI: 10.1115/1.4023284.
- Chen, S. C., W. R. Jong, and J. A. Chang (2006). “Dynamic mold surface temperature control using induction heating and its effects on the surface appearance of weld line”. In: *Journal of Applied Polymer Science* 101.2, pp. 1174–1180. ISSN: 00218995. DOI: 10.1002/app.24070.
- Chen, Y. Y. X. and N. L. F. Gao (2016). *Injection Molding Process Control, Monitoring, and Optimization*. Hanser. ISBN: 9781569905920.
- Chung, T.-s. (1985). “Pressure Build-Up During the Packing Stage of Injection Molding”. In: *Polymer Engineering & Science* 25.11, pp. 772–777.
- Chung, Y., K. Kato, and N. Otake (2001). “Melt front surface asperity and welding-defect generation in ceramic injection molding”. In: *Journal of Materials Processing Technology* 111.1-3, pp. 219–224. ISSN: 09240136.

- DOI: 10.1016/S0924-0136(01)00543-X. URL: <http://www.sciencedirect.com/science/article/pii/S092401360100543X>.
- Collomb, J. et al. (2017). "Thermo-mechanical simulations for the comparison of heating channels geometries for composite material injection tools". In: *Applied Thermal Engineering* 126, pp. 204–211. ISSN: 1359-4311. DOI: 10.1016/J.APPLTHERMALENG.2017.07.125. URL: <https://www.sciencedirect.com/science/article/pii/S1359431117326601>.
- Cross, M. M. (1965). "Rheology of non-Newtonian fluids: A new flow equation for pseudoplastic systems". In: *Journal of Colloid Science* 20.5, pp. 417–437. ISSN: 0095-8522. DOI: [https://doi.org/10.1016/0095-8522\(65\)90022-X](https://doi.org/10.1016/0095-8522(65)90022-X). URL: <http://www.sciencedirect.com/science/article/pii/009585226590022X>.
- Dang, X.-P. and H.-S. Park (2011). "Design of U-shape milled groove conformal cooling channels for plastic injection mold". In: *International Journal of Precision Engineering and Manufacturing* 12.1, pp. 73–84. ISSN: 1229-8557. DOI: 10.1007/s12541-011-0009-8. URL: <http://link.springer.com/10.1007/s12541-011-0009-8>.
- De Santis, F., R. Pantani, V. Speranza, and G. Titomanlio (2010). "Analysis of shrinkage development of a semicrystalline polymer during injection molding". In: *Industrial and Engineering Chemistry Research* 49.5, pp. 2469–2476. ISSN: 08885885. DOI: 10.1021/ie901316p.
- Delaney, K., G Bissacco, and D Kennedy (2012a). "A structured review and classification of demolding issues and proven solutions". In: *International Polymer Processing* 27.1, pp. 77–90.
- Delaney, K. D., G. Bissacco, and P Kennedy (2012b). "A structured review and classification of demolding issues and proven solutions". In: *International Polymer Processing*.
- Demers, V., S. Turenne, and O. Scalzo (2015). "Segregation measurement of powder injection molding feedstock using thermogravimetric analysis,



- pycnometer density and differential scanning calorimetry techniques”. In: *Advanced Powder Technology* 26.3, pp. 997–1004. ISSN: 09218831. DOI: 10.1016/j.appt.2015.04.005. URL: <http://www.sciencedirect.com/science/article/pii/S0921883115000813>.
- Enescu, D. and E. O. Virjoghe (2014). “A review on thermoelectric cooling parameters and performance”. In: *Renewable and Sustainable Energy Reviews* 38, pp. 903–916. ISSN: 13640321. DOI: 10.1016/j.rser.2014.07.045. URL: <http://dx.doi.org/10.1016/j.rser.2014.07.045>.
- Evans, J. (1997). “Particle contact before firing”. In: *Journal of the European Ceramic Society* 17.2-3, pp. 161–169. ISSN: 09552219. DOI: 10.1016/S0955-2219(96)00126-4. URL: <http://www.sciencedirect.com/science/article/pii/S0955221996001264>.
- Fernandes, C., A. J. Pontes, J. C. Viana, and A. Gaspar-Cunha (2016). “Modeling and Optimization of the Injection-Molding Process: A Review”. In: *Advances in Polymer Technology* 00.0, pp. 1–21. ISSN: 10982329. DOI: 10.1002/adv.21683.
- Fischer, J. M. (2013). *Handbook of molded part shrinkage and warpage*. William Andrew, p. 261. ISBN: 9781455725977.
- Fu, G. et al. (2006). “Analysis of demolding in micro metal injection molding”. In: *Microsystem Technologies* 12.6, pp. 554–564. ISSN: 09467076. DOI: 10.1007/s00542-005-0071-1.
- Gao, F, W. I. Patterson, and M. R. Kamal (1996). “Cavity pressure dynamics and self-tuning control for filling and packing phases of thermoplastics injection molding”. In: *Polymer Engineering & Science* 36.9, pp. 1272–1285. ISSN: 1548-2634. DOI: 10.1002/pen.10521.
- Gebelin, J. C. et al. (2004). “Simulation of die filling for the wax injection process: Part II. Numerical simulation”. In: *Metallurgical and Materials Transactions B* 35.August, pp. 761–768. ISSN: 1073-5615. DOI: 10.1007/s11663-004-0016-6.

- German, R. and B. A. (1997). *Injection molding of metals and ceramics*. Metal Powder Industries Federation. ISBN: 187895461X. URL: <http://www.techstreet.com/mpif/products/41057#product>.
- Giboz, J., T. Copponnex, and P. Mélé (2007). “Microinjection molding of thermoplastic polymers: morphological comparison with conventional injection molding”. In: *J. Micromech. Microeng. J. Micromech. Microeng* 17.17, pp. 96–109. ISSN: 0960-1317. DOI: 10.1088/0960-1317/17/6/R02. URL: <http://iopscience.iop.org/0960-1317/17/6/R02>.
- Greco, L. (1997). *Process for determining the changeover point when producing plastic injection mouldings and die-castings, US Patent 5,665,283*.
- Greiner, A. et al. (2011). “Simulation of micro powder injection moulding: Powder segregation and yield stress effects during form filling”. In: *Journal of the European Ceramic Society* 31.14, pp. 2525–2534. ISSN: 09552219. DOI: 10.1016/j.jeurceramsoc.2011.02.008.
- Gromada, M. et al. (2015). “Ceramic cores for turbine blades via injection moulding”. In: *Journal of Materials Processing Technology* 220, pp. 107–112. ISSN: 09240136. DOI: 10.1016/j.jmatprotec.2015.01.010. URL: <http://linkinghub.elsevier.com/retrieve/pii/S0924013615000126>.
- Guevara-Morales, A. and U. Figueroa-Lopez (2014). “Residual stresses in injection molded products”. In: *Journal of Materials Science* 49.13, pp. 4399–4415. ISSN: 00222461. DOI: 10.1007/s10853-014-8170-y.
- Gupta, V. and G. S. (2012). *Fluid Mechanics and its Applications*. New Academic Science.
- Hassan, H., N. Regnier, C. Le Bot, and G. Defaye (2010). “3D study of cooling system effect on the heat transfer during polymer injection molding”. In: *International Journal of Thermal Sciences* 49.1, pp. 161–169. ISSN: 12900729. DOI: 10.1016/j.ijthermalsci.2009.07.006.

- Heaney, D. (2012). *Handbook of Metal Injection Molding*. Elsevier, pp. 29–49. ISBN: 9780857090669. DOI: 10.1533/9780857096234.1.29. URL: <http://www.sciencedirect.com/science/article/pii/B9780857090669500029>.
- Hidalgo, J., A. Jiménez-Morales, and J. Torralba (2012). “Torque rheology of zircon feedstocks for powder injection moulding”. In: *Journal of the European Ceramic Society* 32.16, pp. 4063–4072. ISSN: 09552219. DOI: 10.1016/j.jeurceramsoc.2012.06.023. URL: <http://www.sciencedirect.com/science/article/pii/S0955221912003834>.
- Hobson, G. R. (2004). *Method and apparatus for in mold trimming, US Patent 6,719,554 B2*.
- Holm, E. and H. Langtangen (1999). “A unified finite element model for the injection molding process”. In: *Computer Methods in Applied Mechanics and ...* 178.0045, pp. 413–429. URL: <http://www.sciencedirect.com/science/article/pii/S0045782599000298>.
- Huang, M.-S. (2007). “Cavity pressure based grey prediction of the filling-to-packing switchover point for injection molding”. In: *Journal of Materials Processing Technology* 183.2-3, pp. 419–424. ISSN: 09240136. DOI: 10.1016/j.jmatprotec.2006.10.037. URL: <http://www.sciencedirect.com/science/article/pii/S092401360600896X>.
- Hurst, C. W. (1970). *Apparatus for in-mold removal of flash, US Patent 3,499,071*.
- Janardhana Reddy, J., N. Ravi, and M. Vijayakumar (2000). “A simple model for viscosity of powder injection moulding mixes with binder content above powder critical binder volume concentration”. In: *Journal of the European Ceramic Society* 20.12, pp. 2183–2190. ISSN: 09552219. DOI: 10.1016/S0955-2219(00)00096-0.
- Jansen, K. M. B., D. J. Van Dijk, and M. H. Husselman (1998). “Effect of processing conditions on shrinkage in injection molding”. In: *Polymer*

- Engineering & Science* 38.5, pp. 838–846. ISSN: 0032-3888. DOI: 10.1002/pen.10249. URL: <http://doi.wiley.com/10.1002/pen.10249>.
- Jeng, M.-C. et al. (2010). “Rapid mold temperature control in injection molding by using steam heating”. In: *International Communications in Heat and Mass Transfer* 37.9, pp. 1295–1304. ISSN: 07351933. DOI: 10.1016/j.icheatmasstransfer.2010.07.012. URL: <http://www.sciencedirect.com/science/article/pii/S0735193310001764>.
- Kamal, M. R. and S. Kenig (1972). “The injection molding of thermoplastics part I: Theoretical model”. In: *Polymer Engineering & Science* 12.4, pp. 294–301. ISSN: 15482634. DOI: 10.1002/pen.760120408.
- Karataş, Ç., A. Sözen, E. Arcaklioglu, and S. Erguney (2008). “Investigation of mouldability for feedstocks used powder injection moulding”. In: *Materials & Design* 29.9, pp. 1713–1724. ISSN: 02613069. DOI: 10.1016/j.matdes.2008.03.021. URL: <http://www.sciencedirect.com/science/article/pii/S0261306908000587>.
- Kennedy, J. and R. Eberhart (1995). “Particle Swarm Optimization”. In: *Proceedings of the IEEE International Conference on Neural Networks* 4.1, pp. 1942–1948. ISSN: 13594311. DOI: <http://dx.doi.org/10.1109/ICNN.1995.488968>.
- Kennedy, P. (2013). *Flow analysis of injection molds*. Carl Hanser Verlag.
- Kim, B. H. and R. R. Wadhwa (1987). “A New Approach to Low Thermal Inertia Molding”. In: *Polymer-Plastics Technology and Engineering* 26.1, pp. 1–22. ISSN: 0360-2559. DOI: 10.1080/03602558708070089. URL: <http://www.tandfonline.com/doi/abs/10.1080/03602558708070089>.
- Koh, C. J., P. Hookham, and L. Leal (1994). “An experimental investigation of concentrated suspension flows in a rectangular channel”. In: *Journal of Fluid Mechanics* 266, pp. 1–32. DOI: <https://doi.org/10.1017/S0022112094000911>.

- Kostic, B., T. Zhang, and J. Evans (1992). "Measurement of residual stress in Injection-Molded Ceramics". In: *Journal of the American Ceramic Society* 75.10, pp. 2773–2778.
- Krug, S., J. R. G. Evans, and J. H. H. Ter Maat (2000). "Residual stresses and cracking in large ceramic injection mouldings subjected to different solidification schedules". In: *Journal of the European Ceramic Society* 20, pp. 2535–2541. ISSN: 09552219. DOI: 10.1016/S0955-2219(00)00120-5.
- (2002a). "Differential sintering in ceramic injection moulding: Particle orientation effects". In: *Journal of the European Ceramic Society* 22.2, pp. 173–181. ISSN: 09552219. DOI: 10.1016/S0955-2219(01)00259-X.
- (2002b). "Solidification of large section ceramic injection mouldings under low hold pressures". In: *Journal of Materials Science* 37.13, pp. 2835–2841. ISSN: 00222461. DOI: 10.1023/A:1015897806699.
- Krug, S. and J. R. G. Evans (2001). "Effect of Polymer Crystallinity on Morphology in Ceramic Injection Molding". In: *Journal of the American Ceramic Society* 84.12, pp. 2750–2756. ISSN: 00027820. DOI: 10.1111/j.1151-2916.2001.tb01090.x.
- Kyprianidis, K. (2012). "Future Aero Engine Designs: An Evolving Vision". In: *Advances in Gas Turbine Technology* June. DOI: 10.5772/19689.
- Lee, S., D. Yang, J. Ko, and J. Youn (1997). "Effect of compressibility on flow field and fiber orientation during the filling stage of injection molding". In: *Journal of Materials Processing Technology* 70.1-3, pp. 83–92. ISSN: 09240136. DOI: 10.1016/S0924-0136(97)00041-1. URL: <http://www.sciencedirect.com/science/article/pii/S0924013697000411>.
- Ling, D, M Gupta, P. R. Myers, and R. K. Upadhyay (2006). "Simulation of Core Deflection in Powder Injection". In:

- Liu, D. M. (1997). "Influence of solid loading and particle size distribution on the porosity development of green alumina ceramic mouldings". In: *Ceramics International* 23.6, pp. 513–520. ISSN: 02728842.
- Liu, Y. and M. Gehde (2015). "Evaluation of heat transfer coefficient between polymer and cavity wall for improving cooling and crystallinity results in injection molding simulation". In: *Applied Thermal Engineering* 80, pp. 238–246. ISSN: 13594311. DOI: 10.1016/j.applthermaleng.2015.01.064. URL: <http://linkinghub.elsevier.com/retrieve/pii/S1359431115000897>.
- Loebbecke, B., R. Knitter, and J. Haußelt (2009). "Rheological properties of alumina feedstocks for the low-pressure injection moulding process". In: *Journal of the European Ceramic Society* 29.9, pp. 1595–1602. ISSN: 09552219. DOI: 10.1016/j.jeurceramsoc.2008.11.001.
- Lucchetta, G., M. Sorgato, S. Carmignato, and E. Savio (2014). "Investigating the technological limits of micro-injection molding in replicating high aspect ratio micro-structured surfaces". In: *CIRP Annals - Manufacturing Technology* 63.1, pp. 521–524. ISSN: 00078506. DOI: 10.1016/j.cirp.2014.03.049. URL: <http://www.sciencedirect.com/science/article/pii/S0007850614000523>.
- Malloy, R. A. (2010). *Plastic Part Design for Injection Molding*. Hanser. ISBN: 9781569904367.
- Mannschatz, A., S. Höhn, and T. Moritz (2010). "Powder-binder separation in injection moulded green parts". In: *Journal of the European Ceramic Society* 30.14, pp. 2827–2832. ISSN: 09552219. DOI: 10.1016/j.jeurceramsoc.2010.02.020. URL: <http://www.sciencedirect.com/science/article/pii/S0955221910001081>.
- Mannschatz, A., A. Müller, and T. Moritz (2011). "Influence of powder morphology on properties of ceramic injection moulding feedstocks". In: *Journal of the European Ceramic Society* 31.14, pp. 2551–2558. ISSN:

09552219. DOI: 10.1016/j.jeurceramsoc.2011.01.013. URL: <http://www.sciencedirect.com/science/article/pii/S0955221911000276>.
- Massé, H. et al. (2004). "Heat transfer with mechanically driven thermal contact resistance at the polymer-mold interface in injection molding of polymers". In: *International Journal of Heat and Mass Transfer* 47.8-9, pp. 2015–2027. ISSN: 00179310. DOI: 10.1016/j.ijheatmasstransfer.2002.04.001.
- Menotti, S. et al. (2015). "Comparison of two setups for induction heating in injection molding". In: *The International Journal of Advanced Manufacturing Technology* 81.9-12, pp. 1863–1870. ISSN: 0268-3768. DOI: 10.1007/s00170-015-7224-x. URL: <http://link.springer.com/10.1007/s00170-015-7224-x>.
- Merz, L. et al. (2002). "Feedstock development for micro powder injection molding". In: *Microsystem Technologies* 8.2-3, pp. 129–132. ISSN: 09467076. DOI: 10.1007/s00542-002-0166-x.
- Michaeli, W. and R. Gärtner (2006). "New Demolding Concepts for the Injection Molding of Microstructures". In: *Journal of Polymer Engineering* 26.2-4, pp. 161–178. ISSN: 0334-6447. DOI: 10.1515/POLYENG.2006.26.2-4.161.
- Morris, J. F. and F. Boulay (1999). "Curvilinear flows of noncolloidal suspensions: The role of normal stresses". In: *Journal of Rheology* 43.5, pp. 1213–1237. ISSN: 0148-6055. DOI: 10.1122/1.551021. URL: <http://sor.scitation.org/doi/10.1122/1.551021>.
- Navabpour, P., D. Teer, D. Hitt, and M. Gilbert (2006). "Evaluation of non-stick properties of magnetron-sputtered coatings for moulds used for the processing of polymers". In: *Surface and Coatings Technology* 201.6, pp. 3802–3809. ISSN: 02578972. DOI: 10.1016/j.surfcoat.2006.06.042. URL: <http://www.sciencedirect.com/science/article/pii/S0257897206005123>.

- Neto, V., R. Vaz, M. Oliveira, and J. Grácio (2009). "CVD diamond-coated steel inserts for thermoplastic mould tools—Characterization and preliminary performance evaluation". In: *Journal of Materials Processing Technology* 209.2, pp. 1085–1091. ISSN: 09240136. DOI: 10.1016/j.jmatprotec.2008.03.012. URL: <http://www.sciencedirect.com/science/article/pii/S0924013608002331>.
- Nian, S.-C., M.-S. Huang, and T.-H. Tsai (2014). "Enhancement of induction heating efficiency on injection mold surface using a novel magnetic shielding method". In: *International Communications in Heat and Mass Transfer* 50, pp. 52–60. ISSN: 07351933. DOI: 10.1016/j.icheatmasstransfer.2013.11.017. URL: <http://www.sciencedirect.com/science/article/pii/S0735193313002376>.
- Nian, S.-C., C.-Y. Wu, and M.-S. Huang (2015). "Warpage control of thin-walled injection molding using local mold temperatures". In: *International Communications in Heat and Mass Transfer* 61, pp. 102–110. ISSN: 07351933. DOI: 10.1016/j.icheatmasstransfer.2014.12.008. URL: <http://linkinghub.elsevier.com/retrieve/pii/S0735193314002954>.
- Nian, S.-C. et al. (2014). "Key parameters and optimal design of a single-layered induction coil for external rapid mold surface heating". In: *International Communications in Heat and Mass Transfer* 57, pp. 109–117. ISSN: 0735-1933. DOI: 10.1016/J.ICHEATMASSTRANSFER.2014.07.019. URL: <https://www.sciencedirect.com/science/article/pii/S0735193314001766>.
- Niewels, J. J. (2005). *Method and apparatus for mold component locking using active material elements, US Patent 2005/0236727 A1*.
- Nikolic, S., S. Randelovic, and M. Milutinovic (2014). "Effect of mold temperature on melt front temperature of thermoplastic resin at injection molding". In: *Journal for Technology of Plasticity* 39.2.



- Ohsaka, S., H. Takahashi, N. Shinohara, and M. Okumiya (1995). "Characterization of particle packing in an injected molded green body". In: 78.78, pp. 3107–109.
- Oliveira, R. V. B., V. Soldi, M. C. Fredel, and A. T. N. Pires (2005). "Ceramic injection moulding: Influence of specimen dimensions and temperature on solvent debinding kinetics". In: *Journal of Materials Processing Technology* 160.2, pp. 213–220. ISSN: 09240136. DOI: 10.1016/j.jmatprotec.2004.06.008.
- Ostwald, W. (1925). "Quantitative Filtrationsanalyse als dispersoidanalytische Methode". In: *Kolloid-Zeitschrift* 36.1, pp. 46–55. ISSN: 1435-1536. DOI: 10.1007/BF01526868. URL: <https://doi.org/10.1007/BF01526868>.
- Ozcelik, B., E. Kuram, and M. M. Topal (2012). "Investigation the effects of obstacle geometries and injection molding parameters on weld line strength using experimental and finite element methods in plastic injection molding". In: *International Communications in Heat and Mass Transfer* 39.2, pp. 275–281. ISSN: 07351933. DOI: 10.1016/j.icheatmasstransfer.2011.11.012. URL: <http://dx.doi.org/10.1016/j.icheatmasstransfer.2011.11.012>.
- Ozcelik, B. and I. Sonat (2009). "Warpage and structural analysis of thin shell plastic in the plastic injection molding". In: *Materials & Design* 30.2, pp. 367–375. ISSN: 02613069. DOI: 10.1016/j.matdes.2008.04.053. URL: <http://www.sciencedirect.com/science/article/pii/S0261306908001568>.
- Özkan, N. and B. J. Briscoe (1997). "Characterization of die-pressed green compacts". In: *Journal of the European Ceramic Society* 17.5, pp. 697–711. ISSN: 0955-2219. DOI: 10.1016/S0955-2219(96)00090-8. URL: <https://www.sciencedirect.com/science/article/pii/S0955221996000908>.

- Pantani, R., F. De Santis, V. Speranza, and G. Titomanlio (2015). “Modeling morphology evolution during injection molding of thermoplastic polymers”. In: *AIP Conference Proceedings* 1664, pp. 1185–1222. ISSN: 15517616. DOI: 10.1063/1.4918410.
- Park, H.-S. and X.-P. Dang (2010). “Optimization of conformal cooling channels with array of baffles for plastic injection mold”. In: *International Journal of Precision Engineering and Manufacturing* 11.6, pp. 879–890. ISSN: 1229-8557. DOI: 10.1007/s12541-010-0107-z. URL: <http://link.springer.com/10.1007/s12541-010-0107-z>.
- Piorkowska, E. and A. Galeski (2013). “Overall Crystallization Kinetics”. In: *Handbook of Polymer Crystallization*, pp. 215–236. DOI: 10.1002/9781118541838.ch7. URL: <http://dx.doi.org/10.1002/9781118541838.ch7>.
- Pontes, A. J., R. Pantani, G. Titomanlio, and A. S. Pouzada (2000). “Solidification criterion on shrinkage predictions for semi-crystalline injection moulded samples”. In: *International Polymer Processing* 15.3, pp. 284–290. ISSN: 0930777X. DOI: 10.3139/217.1594.
- Powers, M. C. (1953). “Journal of Sedimentary Research Volume Vol. 23 issue 1953 [doi 10.1306%2FD4269567-2B26-11D7-8648000102C1865D] M. C. Powers, – A New Roundness Scale for Sedimentary Particles.pdf”. In: 23.2, pp. 117–119.
- Rahaman, M. (2007). *Ceramic Processing*. Taylor & Francis.
- Rolls-Royce (2015). *The Jet Engine*. Wiley. ISBN: 9781119065999. URL: <https://books.google.co.uk/books?id=QUQxBwAAQBAJ>.
- Rosato, D. V., D. V. Rosato, and M. G. Rosato (2000). *Injection molding handbook*. Ed. by Springer. 3rd. ISBN: 9781461370772.
- Sardarian, M., O. Mirzaee, and A. Habibolahzadeh (2017). “Numerical simulation and experimental investigation on jetting phenomenon in low pressure injection molding (LPIM) of alumina”. In: *Journal of Materi-*

- als Processing Technology* 243, pp. 374–380. ISSN: 02728842. DOI: 10.1016/j.ceramint.2016.11.208. URL: <http://dx.doi.org/10.1016/j.jmatprotec.2016.12.014>.
- Selden, R (1997). “Effect of Processing on Weld Line Strength in Five Thermoplastics”. In: 37.1. ISSN: 00323888.
- Shayfull, Z et al. (2014). “Potential of Conformal Cooling Channels in Rapid Heat Cycle Molding: A Review”. In: *Advances in Polymer Technology* 33.1, n/a–n/a. ISSN: 1098-2329. DOI: 10.1002/adv.21381. URL: <http://dx.doi.org/10.1002/adv.21381>.
- Shi, Z. (2009). *Crack Analysis in Structural Concrete Theory and Applications*. Elsevier. ISBN: 978-0-7506-8446-0. URL: <https://app.knovel.com/hotlink/toc/id:kpCASCTA05/crack-analysis-in-structural/crack-analysis-in-structural>.
- Somé, S. C. et al. (2015). “Modeling of the thermal contact resistance time evolution at polymer–mold interface during injection molding: Effect of polymers’ solidification”. In: *Applied Thermal Engineering* 84, pp. 150–157. ISSN: 13594311. DOI: 10.1016/j.applthermaleng.2015.03.037. URL: <http://linkinghub.elsevier.com/retrieve/pii/S1359431115002604>.
- Sommer, F. et al. (2014). “Influence of feedstock preparation on ceramic injection molding and microstructural features of zirconia toughened alumina”. In: *Journal of the European Ceramic Society* 34.3, pp. 745–751. ISSN: 09552219. DOI: 10.1016/j.jeurceramsoc.2013.09.020. URL: <http://dx.doi.org/10.1016/j.jeurceramsoc.2013.09.020>.
- Speranza, V., S. Liparoti, G. Tosello, and G. Titomanlio (2017). “Replication of micro and nano-features on iPP by injection molding with fast cavity surface temperature evolution”. In: *Materials & Design* 133, pp. 559–569. ISSN: 0264-1275. DOI: 10.1016/J.MATDES.2017.08.016.

URL: <https://www.sciencedirect.com/science/article/pii/S0264127517307621>.

Suresh, S., P. B. Sujit, and A. K. Rao (2007). "Particle swarm optimization approach for multi-objective composite box-beam design". In: *Composite Structures* 81.4, pp. 598–605. ISSN: 02638223. DOI: 10.1016/j.compstruct.2006.10.008.

Tait, P. (1888). "Physics and Chemistry of the Voyage of HMS Challenger". In: *Vol. II, Part IV, SP LXI*.

Thornagel, M. (2012). "Injection moulding simulation : New developments offer rewards for the PIM industry". In: *Powder Injection Moulding International* 6.1, pp. 64–68.

Turng, L. S. and H Kharbas (2003). "Effect of Process Conditions on the Weld-Line Strength and Microstructure of Microcellular Injection Molded Parts". In: *Polymer Engineering and Science* 43.1, pp. 157–168. ISSN: 00323888 (ISSN). DOI: 10.1002/pen.10013. URL: <http://www.scopus.com/inward/record.url?eid=2-s2.0-1542396982{\&}partnerID=40{\&}md5=3504def6be41ee2a6e8550e1b34fd2f2{\%}5Cninternal-pdf://polymengsci2003-43-157-3780960768/PolymEngSci2003-43-157.pdf>.

Uematsu, K., S. Ohsaka, N. Shinohara, and M. Okumiya (1997). "Grain-Oriented Microstructure of Alumina Ceramics Made through the Injection molding process". In: *Journal of the American Ceramic Society* 15.191539, pp. 1313–1315.

Van Der Beek, M. H. E., G. W. M. Peters, and H. E. H. Meijer (2006). "Classifying the combined influence of shear rate, temperature, and pressure on crystalline morphology and specific volume of isotactic (poly)propylene". In: *Macromolecules* 39.26, pp. 9278–9284. ISSN: 00249297. DOI: 10.1021/ma060768p.

- Wang, G.-l., G.-q. Zhao, and X.-x. Wang (2014a). “Heating/cooling channels design for an automotive interior part and its evaluation in rapid heat cycle molding”. In: *Materials & Design* 59, pp. 310–322. ISSN: 02613069. DOI: 10.1016/j.matdes.2014.02.047. URL: <http://linkinghub.elsevier.com/retrieve/pii/S0261306914001654>.
- Wang, G., Y. Hui, L. Zhang, and G. Zhao (2018). “Research on temperature and pressure responses in the rapid mold heating and cooling method based on annular cooling channels and electric heating”. In: *International Journal of Heat and Mass Transfer* 116, pp. 1192–1203. ISSN: 0017-9310. DOI: 10.1016/J.IJHEATMASTRANSFER.2017.09.126. URL: <https://www.sciencedirect.com/science/article/pii/S0017931017336426{\#}f0010>.
- Wang, G., G. Zhao, H. Li, and Y. Guan (2010). “Research of thermal response simulation and mold structure optimization for rapid heat cycle molding processes, respectively, with steam heating and electric heating”. In: *Materials and Design* 31.1, pp. 382–395. ISSN: 02641275. DOI: 10.1016/j.matdes.2009.06.010. URL: <http://dx.doi.org/10.1016/j.matdes.2009.06.010>.
- (2011). “Multi-objective optimization design of the heating/cooling channels of the steam-heating rapid thermal response mold using particle swarm optimization”. In: *International Journal of Thermal Sciences* 50.5, pp. 790–802. ISSN: 12900729. DOI: 10.1016/j.ijthermalsci.2011.01.005.
- Wang, G., G. Zhao, and X. Wang (2013a). “Effects of cavity surface temperature on reinforced plastic part surface appearance in rapid heat cycle moulding”. In: *Materials & Design* 44, pp. 509–520. ISSN: 02613069. DOI: 10.1016/j.matdes.2012.08.039. URL: <http://www.sciencedirect.com/science/article/pii/S026130691200578X>.

- Wang, G., G. Zhao, and X. Wang (2013b). “Effects of cavity surface temperature on mechanical properties of specimens with and without a weld line in rapid heat cycle molding”. In: *Materials & Design* 46, pp. 457–472. ISSN: 02613069. DOI: 10.1016/j.matdes.2012.10.054. URL: <http://www.sciencedirect.com/science/article/pii/S0261306912007522>.
- (2014b). “Development and evaluation of a new rapid mold heating and cooling method for rapid heat cycle molding”. In: *International Journal of Heat and Mass Transfer* 78, pp. 99–111. ISSN: 00179310. DOI: 10.1016/j.ijheatmasstransfer.2014.06.062. URL: <http://www.sciencedirect.com/science/article/pii/S0017931014005341>.
- Wang, J., C. Hopmann, M. Schmitz, and J. Wipperfurth (2019). “Modeling of pvT behavior of semi-crystalline polymer based on the two-domain Tait equation of state for injection molding”. In: *Materials and Design* 183. ISSN: 18734197. DOI: 10.1016/j.matdes.2019.108149.
- Wang, J. and Q. Mao (2009). “Rapid Thermal Cycling of Injection Molds: An Overview on Technical Approaches and Applications”. In: *Advances in Polymer Technology* 27.4, pp. 233–255. ISSN: 07306679. DOI: 10.1002/adv.
- Wang, T.-H. and W.-B. Young (2005). “Study on residual stresses of thin-walled injection molding”. In: *European Polymer Journal* 41.10, pp. 2511–2517. ISSN: 00143057. DOI: 10.1016/j.eurpolymj.2005.04.019.
- Wang, W., G. Zhao, X. Guan, and Y. Hui (2015). “Effect of rapid heating cycle injection mold temperature on crystal structures, morphology of polypropylene and surface quality of plastic parts”. In: *Journal of Polymer Research* 22.5, p. 84. ISSN: 1022-9760. DOI: 10.1007/s10965-015-0731-5. URL: <http://link.springer.com/10.1007/s10965-015-0731-5>.

- Wang, X., G. Zhao, and G. Wang (2013c). “Research on the reduction of sink mark and warpage of the molded part in rapid heat cycle molding process”. In: *Materials & Design* 47, pp. 779–792. ISSN: 02613069. DOI: 10.1016/j.matdes.2012.12.047. URL: <http://linkinghub.elsevier.com/retrieve/pii/S026130691200876X>.
- Wang, Y., K.-M. Yu, C. C. Wang, and Y. Zhang (2011). “Automatic design of conformal cooling circuits for rapid tooling”. In: *Computer-Aided Design* 43.8, pp. 1001–1010. ISSN: 00104485. DOI: 10.1016/j.cad.2011.04.011. URL: <http://www.sciencedirect.com/science/article/pii/S0010448511001060>.
- White, J. L. (1975). “Fluid mechanical analysis of injection mold filling”. In: *Polymer Engineering and Science* 15.1, pp. 44–50. ISSN: 1548-2634. DOI: 10.1002/pen.760150108.
- Worgull, M., J. F. Héту, K. K. Kabanemi, and M. Hecke (2008). “Hot embossing of microstructures: Characterization of friction during demolding”. In: *Microsystem Technologies* 14.6, pp. 767–773. ISSN: 09467076. DOI: 10.1007/s00542-007-0492-0.
- Wright, J. K., M. J. Edirisinghe, J. G. Zhang, and J. R. Evans (1990). “Particle packing in ceramic injection moulding”. In: *Journal of the American Ceramic Society* 73.9, pp. 2653–2658. ISSN: 0002-7820. DOI: 10.1111/j.1151-2916.1990.tb06742.x. URL: <http://discovery.ucl.ac.uk/730828/>.
- Wu, C. H. and W. J. Liang (2005). “Effects of geometry and injection-molding parameters on weld-line strength”. In: *Polymer Engineering and Science* 45.7, pp. 1021–1030. ISSN: 00323888. DOI: 10.1002/pen.20369.
- Xiao, C.-L. and H.-X. Huang (2014a). “Development of a rapid thermal cycling molding with electric heating and water impingement cooling for injection molding applications”. In: *Applied Thermal Engineering* 73.1, pp. 712–722. ISSN: 13594311. DOI: 10.1016/j.applthermaleng.2014.

- 08.027. URL: <http://www.sciencedirect.com/science/article/pii/S1359431114006899>.
- Xiao, C.-L. and H.-X. Huang (2014b). “Optimal design of heating system for rapid thermal cycling mold using particle swarm optimization and finite element method”. In: *Applied Thermal Engineering* 64.1-2, pp. 462–470. ISSN: 13594311. DOI: 10.1016/j.applthermaleng.2013.12.062. URL: <http://www.sciencedirect.com/science/article/pii/S1359431113009599>.
- Xie, L. and G. Ziegmann (2008). “A visual mold with variotherm system for weld line study in micro injection molding”. In: *Microsystem Technologies* 14.6, pp. 809–814. ISSN: 09467076. DOI: 10.1007/s00542-008-0566-7.
- (2009). “Influence of processing parameters on micro injection molded weld line mechanical properties of polypropylene (PP)”. In: *Microsystem Technologies* 15.9, pp. 1427–1435. ISSN: 09467076. DOI: 10.1007/s00542-009-0904-4.
- Yang, S., R. Zhang, and X. Qu (2013). “X-ray tomographic analysis of powder-binder separation in SiC green body”. In: *Journal of the European Ceramic Society* 33.15-16, pp. 2935–2941. ISSN: 09552219. DOI: 10.1016/j.jeurceramsoc.2013.06.011. URL: <http://www.sciencedirect.com/science/article/pii/S0955221913003117>.
- Yao, D. and B. Kim (2002). “Development of rapid heating and cooling systems for injection molding applications”. In: *Polymer Engineering & Science* 42.12, pp. 2471–2481. ISSN: 0032-3888. DOI: 10.1002/polb.11133. URL: <http://www.scopus.com/inward/record.url?eid=2-s2.0-0036956846&partnerID=tZ0tx3y1>.
- (2004). “Scaling Issues in Miniaturization of Injection Molded Parts”. In: *Journal of Manufacturing Science and Engineering* 126.November, p. 733. ISSN: 10871357. DOI: 10.1115/1.1813479.



- Zhang, N., Q. Su, S. Y. Choi, and M. D. Gilchrist (2015). "Effects of gate design and cavity thickness on filling, morphology and mechanical properties of microinjection mouldings". In: *Materials & Design* 83, pp. 835–847. ISSN: 02641275. DOI: 10.1016/j.matdes.2015.06.012. URL: <http://www.sciencedirect.com/science/article/pii/S0264127515003627>.
- Zhang, T, S Blackburn, and J Bridgwater (1996). "Debinding and sintering defects from particle orientation in ceramic injection moulding". In: *Journal of Materials Science* 31.22, pp. 5891–5896. ISSN: 0022-2461. DOI: 10.1007/BF01152138.
- Zhang, T., S. Blackburn, and J. Bridgwater (1997). "The orientation of binders and particles during ceramic injection moulding". In: *Journal of the European Ceramic Society* 22.96, pp. 101–108. ISSN: 0955-2219. DOI: 10.1016/S0955-2219(96)00070-2. URL: [http://dx.doi.org/10.1016/S0955-2219\(96\)00070-2](http://dx.doi.org/10.1016/S0955-2219(96)00070-2).
- Zhang, T., J. R. G. Evans, and M. J. Bevis (1996). "The control of fibre orientation in ceramic and metal composites by open-ended injection moulding". In: *Composites Science and Technology* 56.8, pp. 921–928. ISSN: 02663538. DOI: 10.1016/0266-3538(96)00055-3.
- Zhao, D. and G. Tan (2014). "A review of thermoelectric cooling: Materials, modeling and applications". In: *Applied Thermal Engineering* 66.1, pp. 15–24. ISSN: 13594311. DOI: 10.1016/j.applthermaleng.2014.01.074.
- Zhao, G., G. Wang, Y. Guan, and H. Li (2011). "Research and application of a new rapid heat cycle molding with electric heating and coolant cooling to improve the surface quality of large LCD TV panels". In: *Polymers for Advanced Technologies* 22.5, pp. 476–487. ISSN: 10427147. DOI: 10.1002/pat.1536.

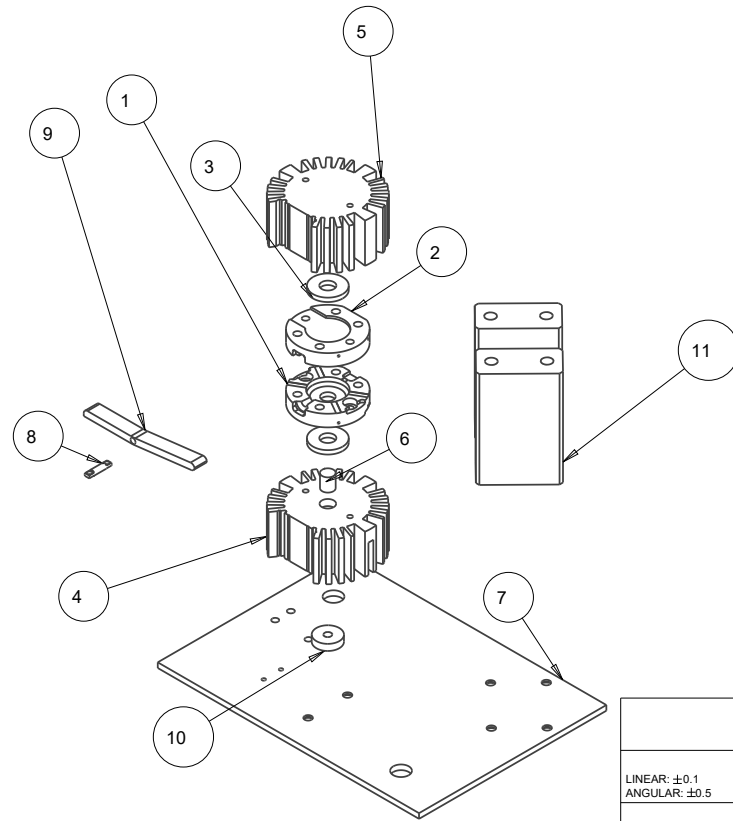
- Zheng, R., P. Kennedy, N. Phan-Thien, and X. J. Fan (1999). “Thermoviscoelastic simulation of thermally and pressure-induced stresses in injection moulding for the prediction of shrinkage and warpage for fibre-reinforced thermoplastics”. In: *Journal of Non-Newtonian Fluid Mechanics* 84.2-3, pp. 159–190. ISSN: 03770257. DOI: 10.1016/S0377-0257(98)00148-7.
- Zheng, R., R. I. Tanner, and X.-J. Fan (2011). *Injection Molding: Integration of theory and modeling methods*. Springer. ISBN: 9783642212628.
- Zhou, H. (2013). *Computer modeling for injection molding*. Wiley. ISBN: 9780470602997.
- Zuidema, H., G. W. M. Peters, and H. E. H. Meijer (2001). “Influence of cooling rate on pVT-data of semicrystalline polymers”. In: *Journal of Applied Polymer Science* 82.5, pp. 1170–1186. ISSN: 00218995. DOI: 10.1002/app.1951.

# Appendix A

## Engineering Drawings

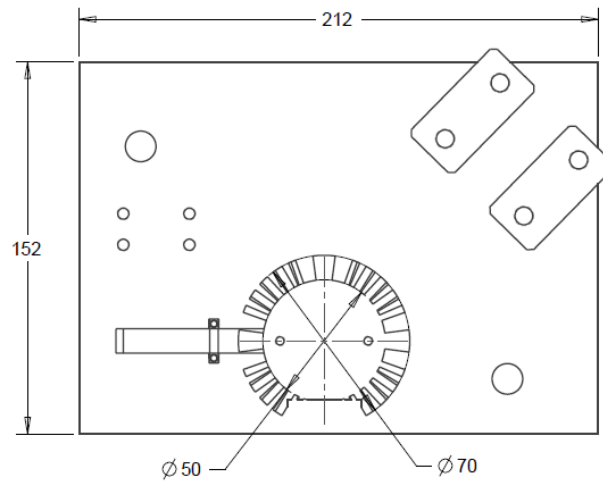
The following engineering drawings are shown in the present Appendix:

- General assembly of the adhesion test mould (Pages 304-305)
- Main components of the adhesion tests mould (Pages 306-309)
- General assembly of laboratory rig for injection moulding tests and regional controlled mould (Pages 310-311)
- Main components of the laboratory rig (Pages 312-316)
- Main components of the regional controlled mould (Pages 317-322)

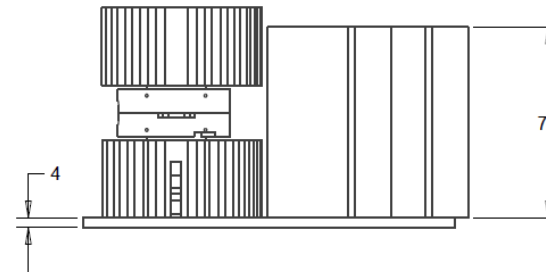
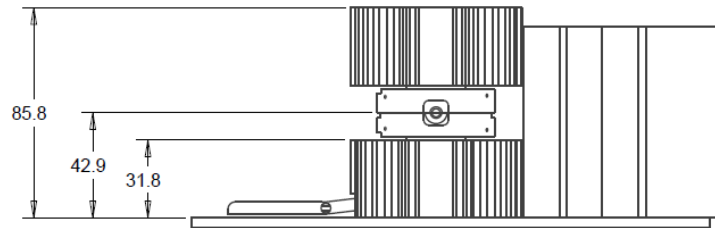


ITEM	DWG or PART NO.	DESCRIPTION	MATERIAL	QTY
1	001	Cavity Plate	Aluminium	1
2	002	Core Plate	Aluminium	1
3	003	Peltier elements	-	2
4	004	Bottom Heatsink	-	1
5	005	Top Heatsink	-	1
6	008	Pin	Aluminium	1
7	011	Base	Aluminium	1
8	006	Pivot	Aluminium	1
9	007	Wedge	Aluminium	1
10	010	Plate	Aluminium	1
11	012	Toggle clamp support	Aluminium	2

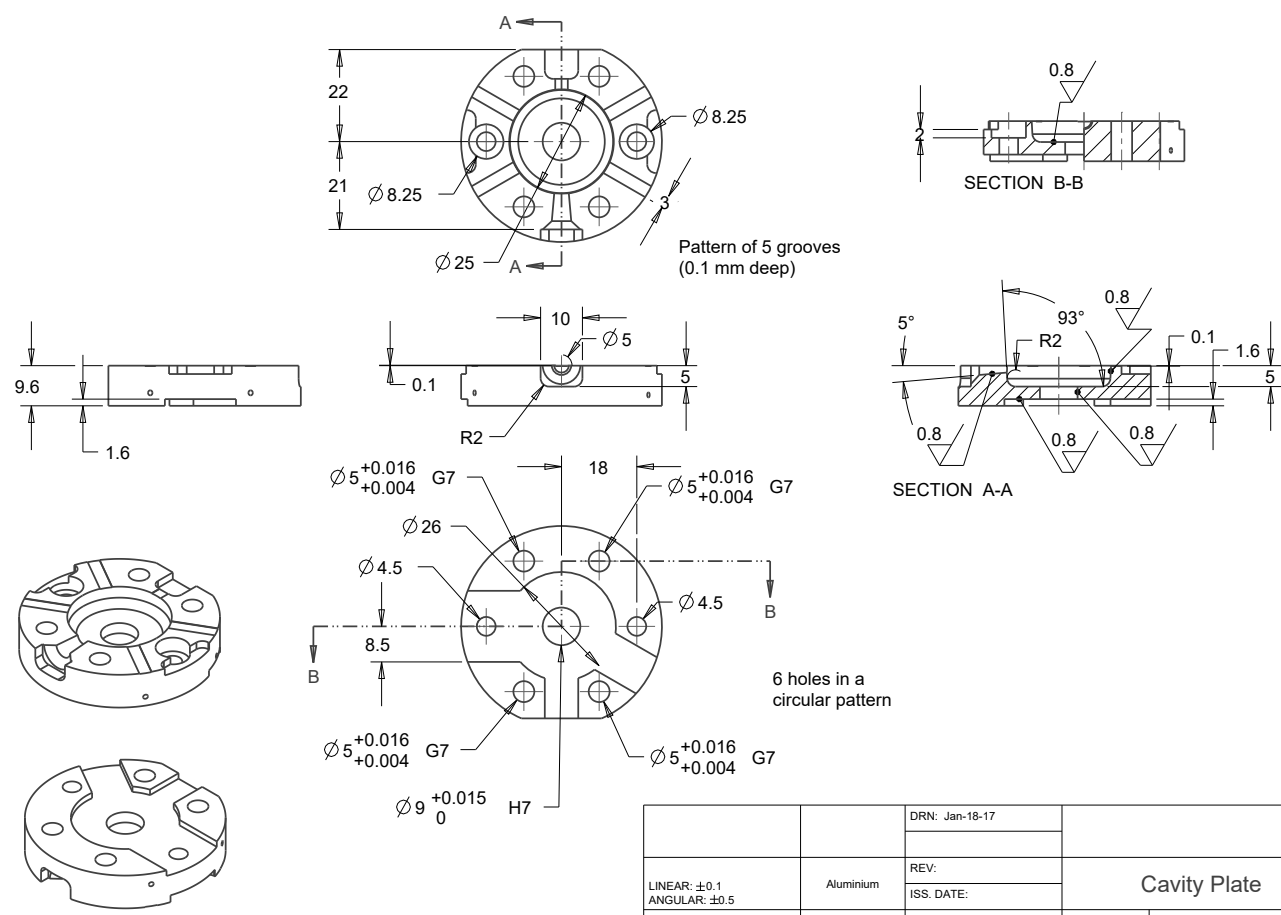
		DRN: Jul-18-17		
LINEAR: ±0.1 ANGULAR: ±0.5		REV:	Mould Assembly	
		ISS. DATE:		
			SIZE A3	DWG NO.
			SCALE 0.500	SHEET 1 of 2



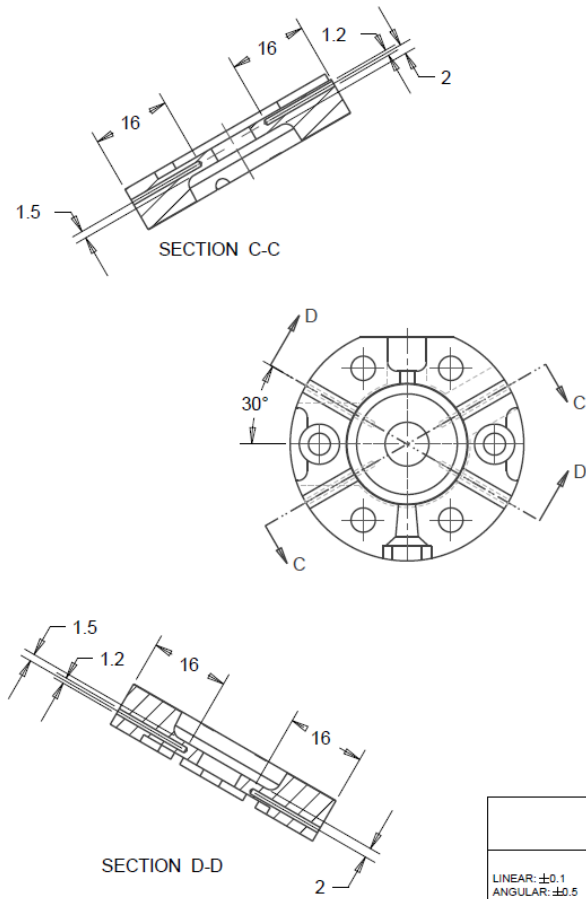
ITEM	DWG or PART NO.	DESCRIPTION	MATERIAL	QTY
1	001	Cavity Plate	Aluminium	1
2	002	Core Plate	Aluminium	1
3	003	Peltier elements	-	2
4	004	Bottom Heatsink	-	1
5	005	Top Heatsink	-	1
6	008	Pin	Aluminium	1
7	011	Base	Aluminium	1
8	006	Pivot	Aluminium	1
9	007	Wedge	Aluminium	1
10	010	Plate	Aluminium	1
11	012	Toggle clamp support	Aluminium	2



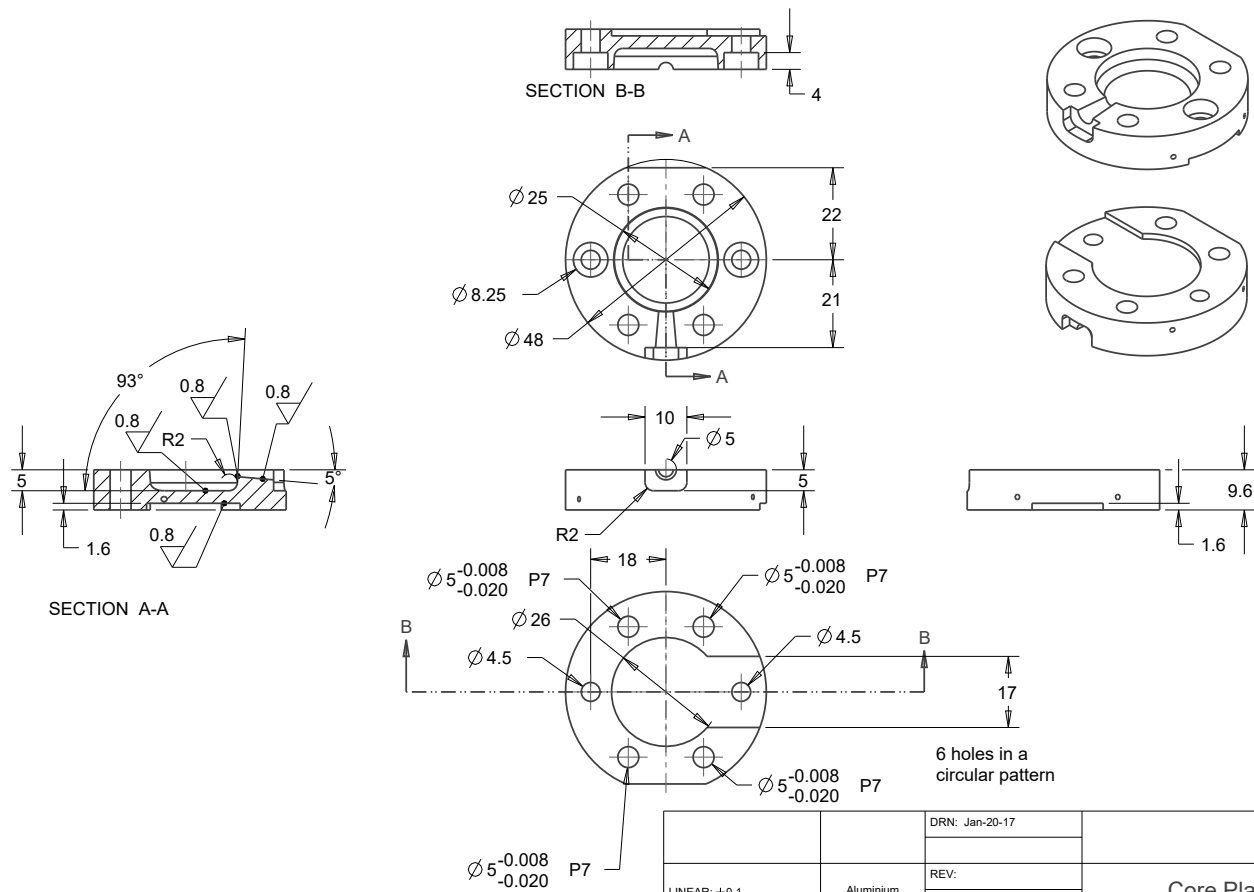
		DRN: Jan-18-17	Mould Assembly	
LINEAR: ±0.1 ANGULAR: ±0.5		REV:		
		ISS. DATE:		
			SIZE A3	DWG NO.
			SCALE 0.700	SHEET 2 of 2



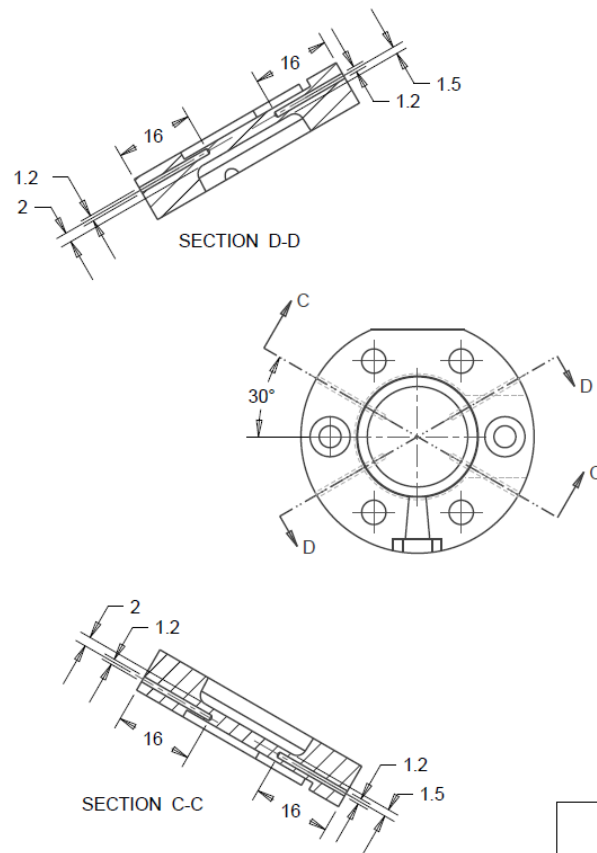
LINEAR: $\pm 0.1$ ANGULAR: $\pm 0.5$	Aluminium	DRN: Jan-18-17	Cavity Plate	
		REV:		
		ISS. DATE:		
Unless otherwise stated 1.6 Ra			SIZE A3	DWG NO. 001
			SCALE 1.200	SHEET 1 of 2



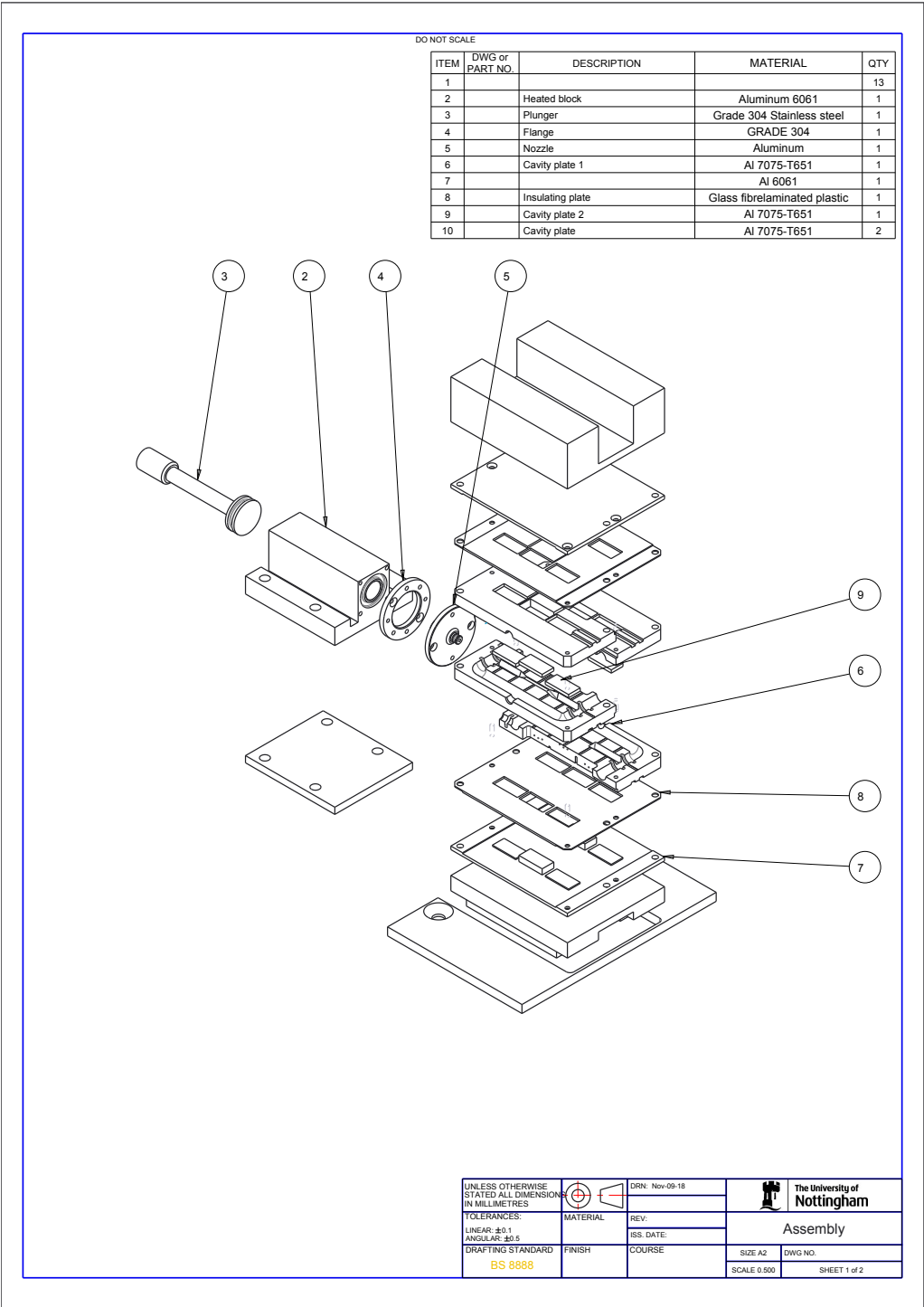
		DRN: Jul-18-17	Cavity Plate	
LINEAR: $\pm 0.1$ ANGULAR: $\pm 0.5$	Aluminium	REV:		
		ISS. DATE:		
			SIZE A3	DWG NO. 001
			SCALE 1:400	SHEET 2 of 2

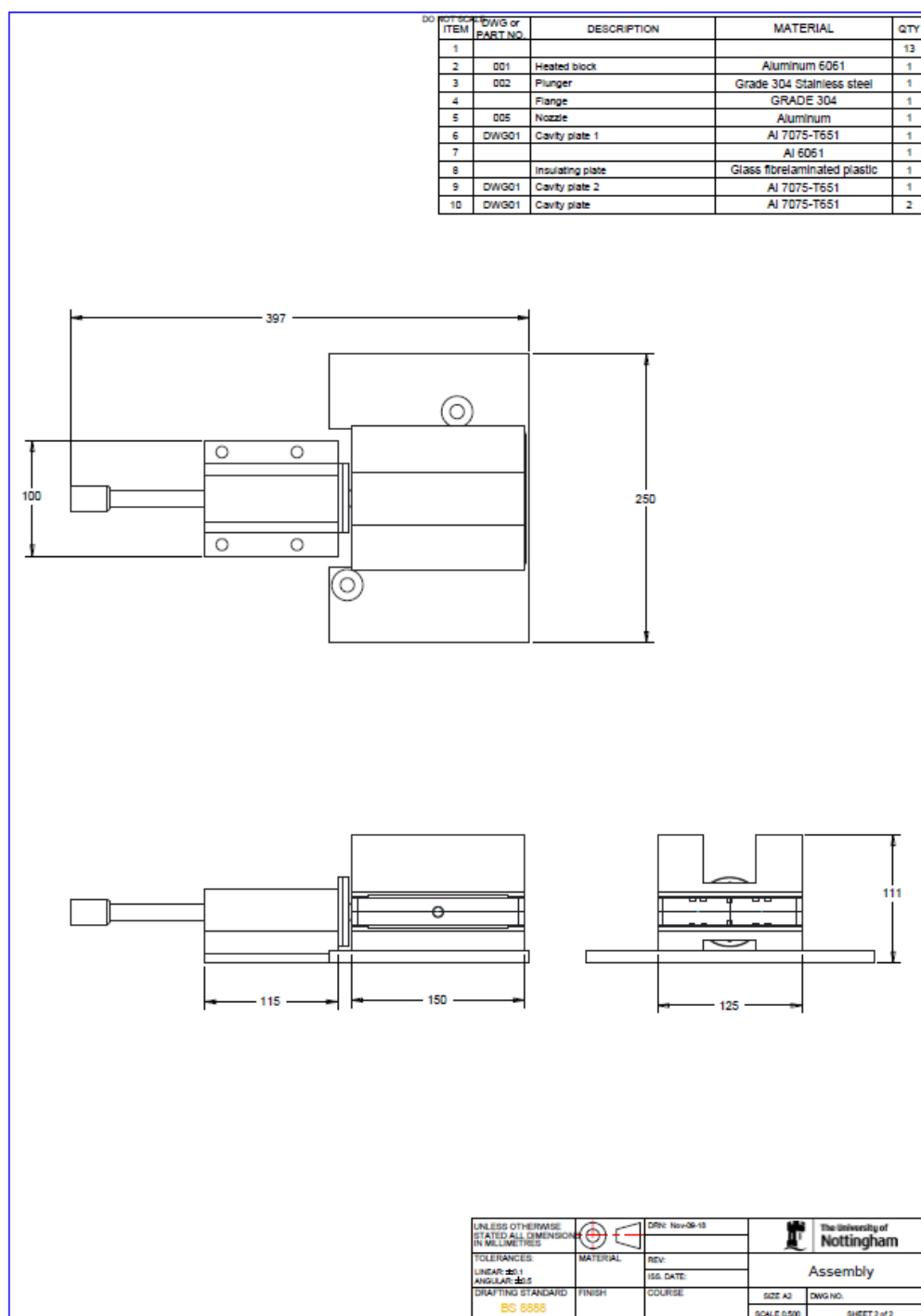


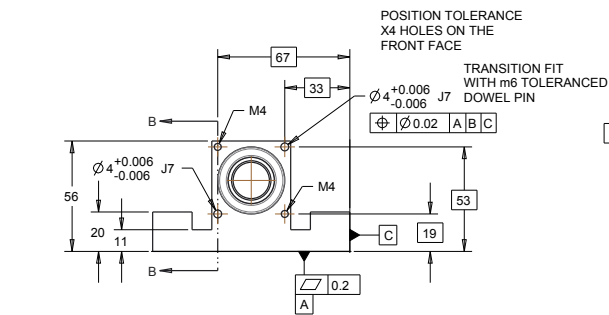




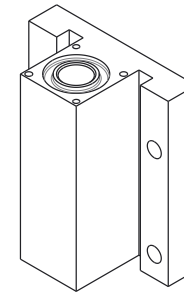
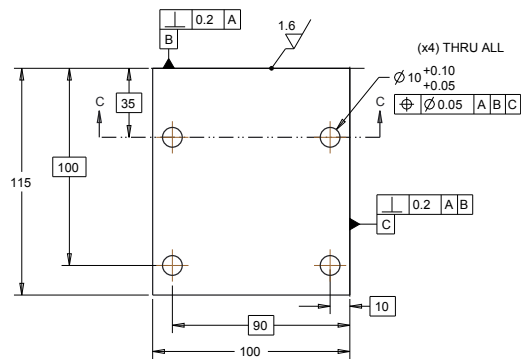
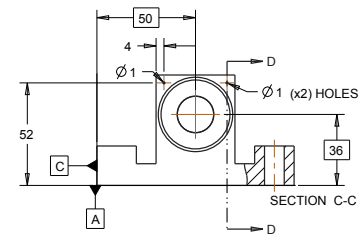
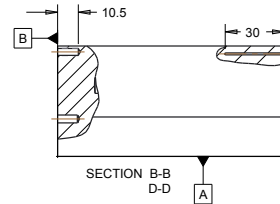
		DRN: Jul-19-17	Core Plate	
LINEAR: $\pm 0.1$ ANGULAR: $\pm 0.5$	Aluminium	REV:		
		ISS. DATE:		
			SIZE A3	DWG NO. 002
			SCALE 1:400	SHEET 2 of 2





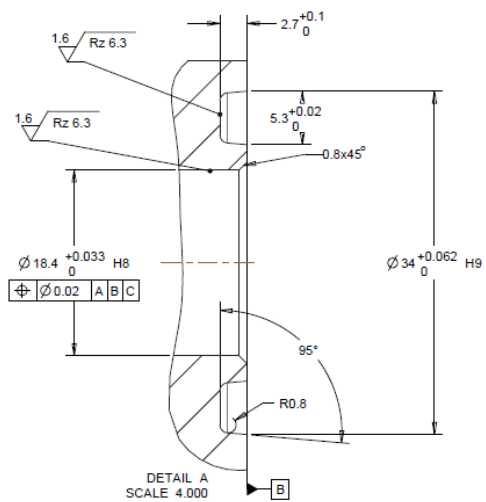


DO NOT SCALE

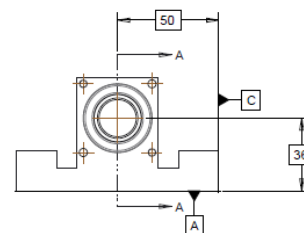
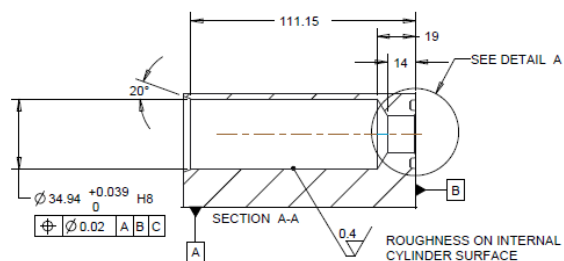
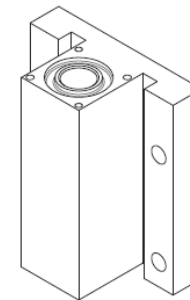
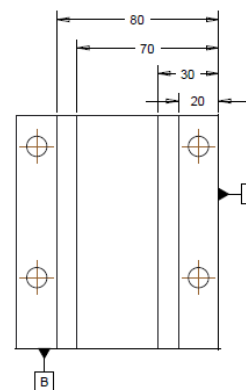




3.2 / ( 1.6 / ) ( 0.4 / )

UNLESS OTHERWISE STATED ALL DIMENSIONS IN MILLIMETRES	DRN: Oct 29-18	The University of Nottingham
TOLERANCES: LINEAR: $\pm 0.1$ ANGULAR: $\pm 0.5$	MATERIAL: Aluminum 6061	
DRAFTING STANDARD BS 8888	FINISH: 3.2 RA UNLESS OTHERWISE STATED	Heated block
	COURSE	SIZE A2 DWG NO. 001
		SCALE 0.800 SHEET 1 of 2

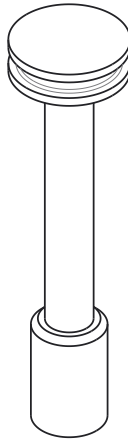
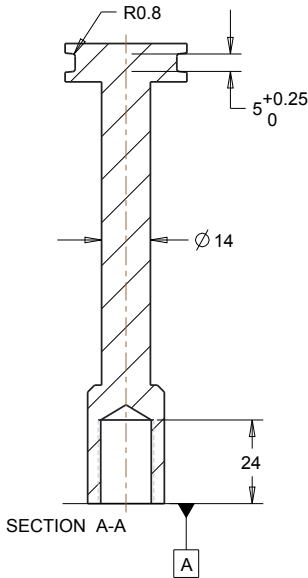
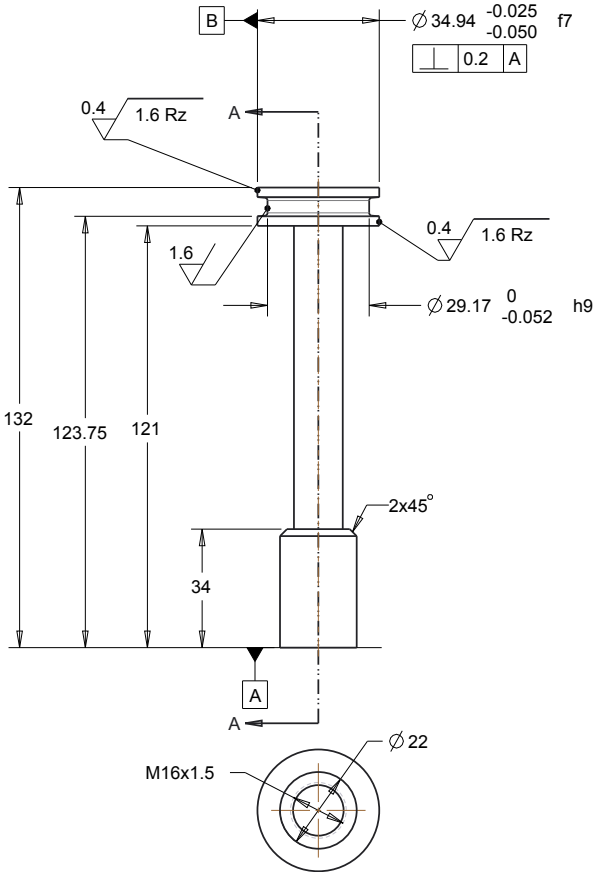




DO NOT SCALE


$$\frac{3.2}{\nabla} \left( \frac{1.6}{\nabla} \right) \left( \frac{0.4}{\nabla} \right)$$

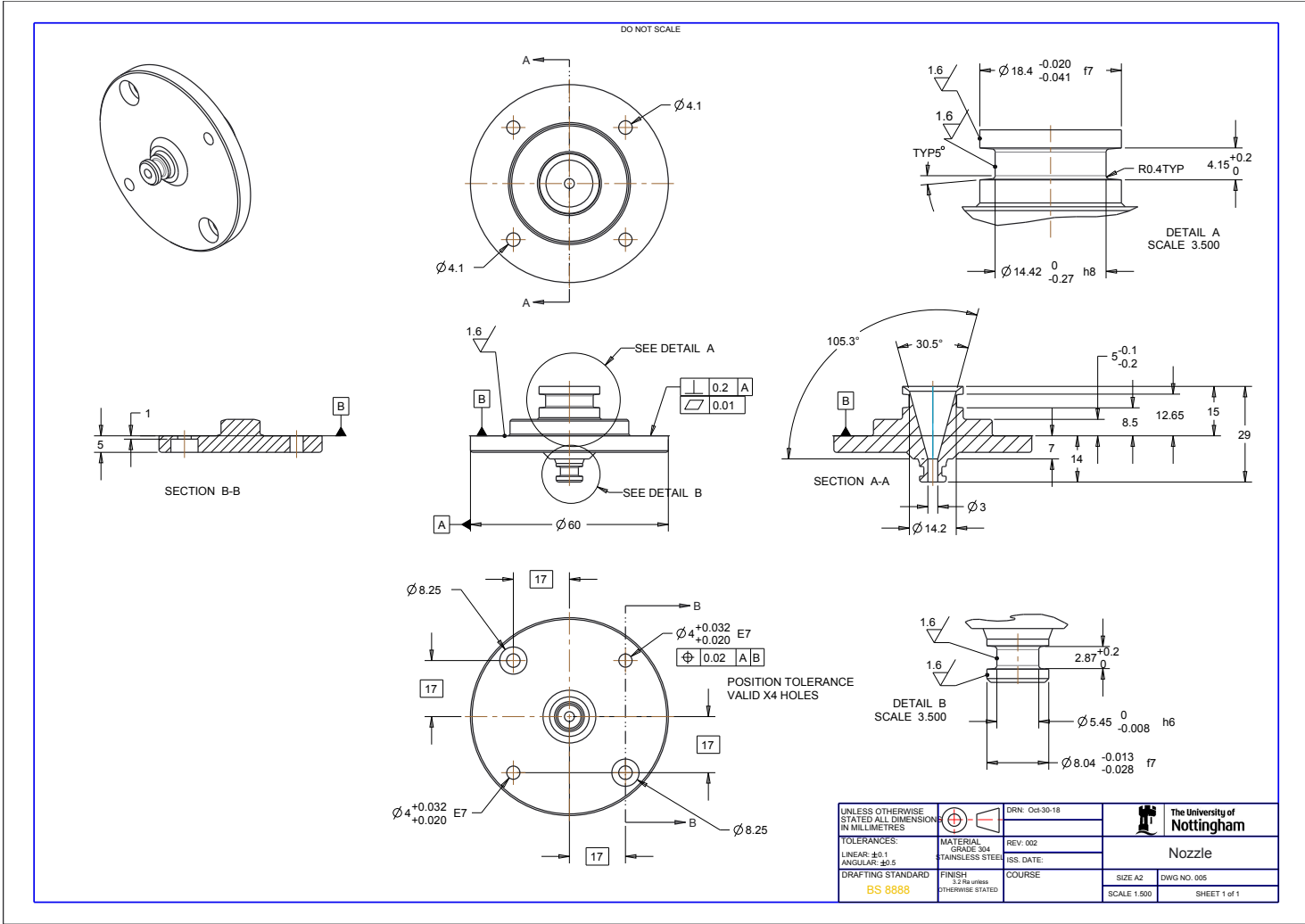
UNLESS OTHERWISE STATED ALL DIMENSIONS IN MILLIMETRES		 DRN: Oct-20-18		 The University of Nottingham	
TOLERANCES:		MATERIAL		REV:002	
LINEAR: $\pm 0.1$		Aluminium 6061		ISS. DATE:	
ANGULAR: $\pm 0.5$				Heated block	
DRAFTING STANDARD		FINISH		COURSE	
BS 8888		UNLESS OTHERWISE STATED			
				SIZE A2	
				DWG NO. 001	
				SCALE 0:800	
				SHEET 2 of 2	

DO NOT SCALE



UNLESS OTHERWISE STATED ALL DIMENSIONS IN MILLIMETRES				DRN: Oct-30-18		 <b>The University of Nottingham</b>	
TOLERANCES:		MATERIAL Grade 304 Stainless Steel		REV: 002		Plunger	
LINEAR: $\pm 0.1$ ANGULAR: $\pm 0.5$				ISS. DATE:			
DRAFTING STANDARD <b>BS 8888</b>		FINISH 3.2 Ra OTHERWISE STATED		COURSE		SIZE A3	DWG NO. 002
						SCALE 1:000	SHEET 1 of 1





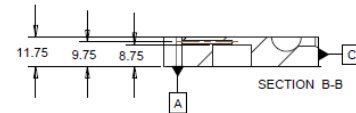
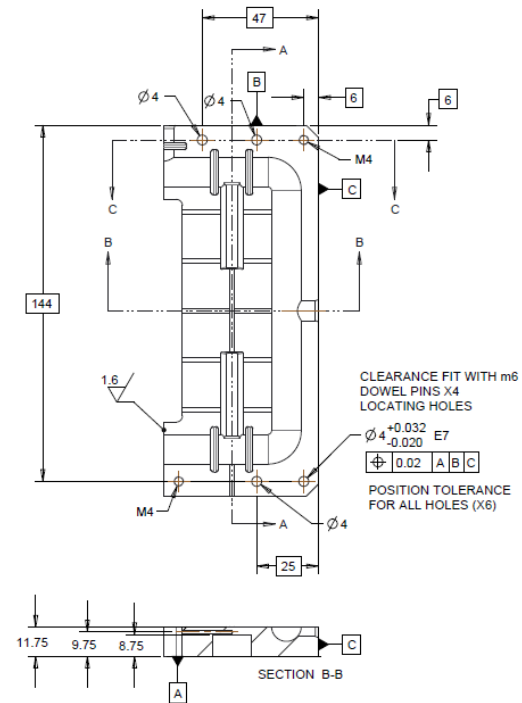
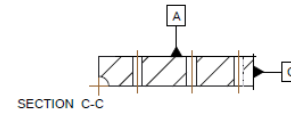
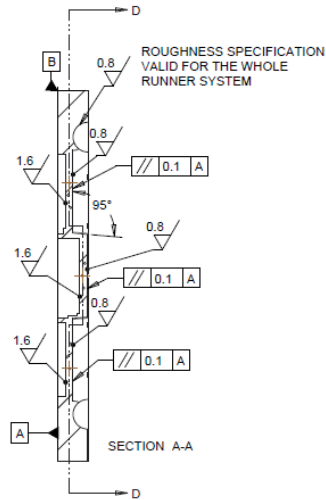
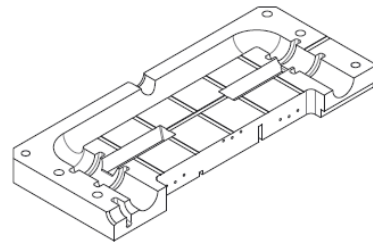
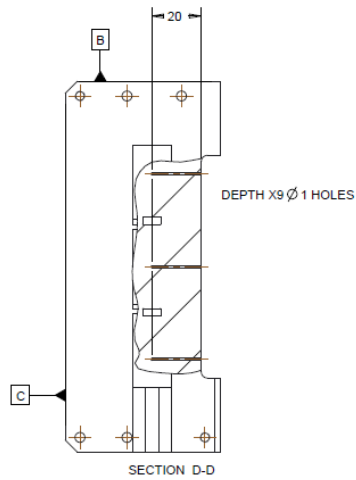




DO NOT SCALE

LOCATING HOLES: THE TWO  $\varnothing 4$ MM HOLES DISTANT 25MM FROM DATUM C WILL NEED A CLEARANCE FIT ON THE TWO BOTTOM PLATES, WHILE A TRANSITION FIT ON THE TOP CAVITY PLATES, AS THEY ARE FOR RELATIVE LOCATION BETWEEN TOP AND BOTTOM MOULD PLATES.

THE OTHER  $\varnothing 4$ MM HOLES WILL BE FOR LOCATION BETWEEN MOULD AND BASE PLATES AND WILL BE CLEARANCE FIT FOR ALL THE FOUR MOULD PLATES



UNLESS OTHERWISE STATED ALL DIMENSIONS IN MILLIMETRES		DRN: Oct31-18		Cavity plate 1
TOLERANCES:	MATERIAL	REV:004	SIZE A2	DWG NO: DW001
LINEAR: $\pm 0.1$	AI 7075-T651	ISS. DATE:		
ANGULAR: $\pm 0.5$	FINISH	COURSE	SCALE 1:200	SHEET 2 of 3
DRAFTING STANDARD	3.2Ra unless otherwise stated			
BS 8888				

